The Thesis Committee for Stefanie Naoko Frelinger
Certifies that this is the approved version of the following thesis:

Chronology of Laramide Magmatism and Stockwork Fracture Filling at the Red Hills Porphyry Mo-Cu Deposit, Presidio County, Texas

APPROVED BY
SUPERVISING COMMITTEE:

James Richard Kyle, Supervisor

Brent A. Elliott, Co-Supervisor

James E. Gardner

Chronology of Laramide Magmatism and Stockwork Fracture Filling at the Red Hills Porphyry Mo-Cu Deposit, Presidio County, Texas

by

Stefanie Naoko Frelinger, B.S.

Thesis

Presented to the Faculty of the Graduate School of

The University of Texas at Austin

in Partial Fulfillment

of the Requirements

for the Degree of

Master of Science in Geological Sciences

The University of Texas at Austin

May 2015

Dedication

I’d like to dedicate this to my father, Rick and my dear friend, Wolfgang.

Acknowledgements

Thank you to my advisors Dr. J. Richard Kyle, Dr. Brent Elliott, and Dr. James Gardner for serving on my committee and for their support, guidance, and invaluable insight on the completion of this thesis. I'd like to extend my gratitude to Steve Glass of Gault Group LLC and Tosca Resources Corp. who facilitated access to the Red Hills property and the 31 drill cores. Thank you Dr. Daniel Stockli for conducting the U-Pb zircon analyses.

I would like to thank the Jackson School of Geosciences, the Society of Economic Geologists, the Association of Environmental and Engineering Geologists, and the West Texas Geological Society for providing funding for my research.

Thanks to my office mates Christine O'Neil, Matthew Ledvina, Mackenzie Hinds, and Nathan Williams for their support and encouragement throughout graduate school. And finally, thank you to my family for their support.

Abstract

Chronology of Laramide Magmatism and Stockwork Fracture Filling at the Red Hills Porphyry Mo-Cu Deposit, Presidio County, Texas

Stefanie Naoko Frelinger, M.S. Geo. Sci

The University of Texas at Austin, 2015

Supervisors: J. Richard Kyle and Brent A. Elliott

The Red Hills intrusive complex is the easternmost porphyry Mo-Cu system of Laramide age in southwestern North America. This study constrains the timing between igneous phases, and compares their geochemical characteristics with dikes from the Shafter silver deposit in order to support a possible link to a similar magmatic source. In addition, this study is the first to utilize SEM-CL techniques to document veining in a porphyry Mo system, comparing those to porphyry Cu systems.

The high-K calc-alkaline igneous complex consists of early biotite porphyry (BP), biotite quartz monzonite porphyry (BQMP), quartz monzonite porphyry (QMP), quartz latite porphyry (QLP), and granodiorite porphyry (GP) with microgranular mafic enclaves. These magmas intruded Permian sandstones, siltstones, and dolostones, resulting in an extensive hornfels zone with local garnet skarn. U-Pb ages of zircon from the QLP and BQMP are 62.54 ± 0.49 Ma and 66.08 ± 0.31 Ma ages, respectively. When integrated with Gilmer's (2001) 60.2 $\pm$ 0.3 Ma molybdenite Re-Os age and $^{40}Ar/^{39}Ar$ sericite age of 61.58 $\pm$ 0.34 Ma, magmatism and

hydrothermal activity may have spanned at least 6 My at Red Hills. Whole-rock and trace-element geochemistry suggest the Red Hills intrusions are sourced from an intermediate crustal melt and share a similar geochemical parent as dikes found in the Shafter carbonate-replacement-silver deposit.

Potassic alteration is found in deep BP intercepts as mm-scale K-spar alteration halos and as shreddy biotite, which is pervasively overprinted by phyllic alteration. Intermediate argillic alteration caps the phyllic alteration zone and propylitic alteration extends east of the western mineralized part at Red Hills. Mo-Cu mineralization at Red Hills is confined to stockwork quartz veins and as disseminations within hydrothermally altered wallrock. The Red Hills intrusions have similar vein styles and, from youngest to oldest, the stockwork veining sequence involves: A veins (A1 and A2), B veins, D veins (D1 and D2), and hypogene alunite veins. Mo mineralization is confined to B veins and copper mineralization occurs later from phyllic overprinting in the form of copper sulfide inclusions in pyrite in wallrock and in D veins.

SEM-CL of hydrothermal quartz reveals intricate quartz textures in relation to sulfide deposition within complex stockwork veins where fracture overprinting is common. A sequence of three stages of main-stage vein development and has been developed: 1) Fracturing in a semi-plastic magma formed sinuous veins filled with granular quartz that has internal wavy growth zones or homogenous CL texture. 2a) Fracturing under brittle conditions formed planar veins with euhedral, inward-oriented quartz that has oscillatory growth zones and bright luminescence. 2b) molybdenite deposition sites are associated with local dark-CL quartz in early quartz, while retaining primary growth textures. 3a) Dissolution of early quartz by retrograde solubility formed embayments along quartz grain boundaries. Following dissolution, euhedral, dark-CL quartz precipitated coevally with pyrite enriched in copper. When the hydrothermal activity ends, tectonic activity resulted in dark-CL microfractures and partial recrystallization may affect the stockwork veins.

Table of Contents

List of Tables

List of Figures

Chapter 1: Introduction

The Red Hills deposit is the easternmost, Laramide porphyry molybdenum-copper (Mo-Cu) in southwestern North America. Mo and Cu mineralization styles broadly follow models of arc-related porphyry Mo deposits (Taylor et al., 2010) or transitional, syenite- and monzonite-related porphyry Mo deposits associated with high K calc-alkalic and alkali-calcic magmas (Westra and Keith, 1981). These porphyry molybdenum models are similar to classic porphyry Cu deposits, except that stockwork vein-hosted Mo mineralization precedes Cu mineralization.

The goals of this study is to constrain the timing between igneous phases, and compare their geochemical characteristics with dikes from the Shafter silver deposit in order to support a possible link to a similar magmatic source. In addition, this study is the first to utilize SEM-CL techniques to document veining in a porphyry Mo system, comparing those to porphyry Cu systems.

OVERVIEW OF PORPHYRY DEPOSITS

Porphyry deposits contribute approximately 65% of world copper production and are important sources of gold, molybdenum, tungsten, and silver (Sillitoe, 2010). Large tonnage and relatively low grade are characteristic of these kinds of deposits. The South-West Cordilleran type porphyry deposits are situated along a linear belt of andesitic magmatism related to subduction of oceanic crust from the Farrallon plate along the North American continental margin (Titley, 1975; Seedorff et al., 2005; Sinclair, 2007). They derive from granitic to intermediate composition magmas, where their emplacement at shallow crustal levels is dependent upon deep-seated strike-slip, pull-apart structures at the regional to local scale, which provide pathways for magmatic stocks to ascend from large batholiths below (Cloos and Sapiie, 2013). Transient pulses of magmatic fluid

accumulate at the top of a crystallizing magmatic stock from which the fluids are exsolved. Cloos and Sapiie (2013) argue that stockwork fracturing in porphyry systems occur from increased seismogenic movement on the semi-solidified stock, which forms downward propagating fractures, in turn draining the systems of the magmatic fluid. Decompression of the hydrothermal system causes the fluids to ascend into extensional stockwork fractures above and to precipitate out minerals within them. In contrast, other researchers have proposed a hydraulic fracturing model which involves the build-up of extreme fluid over-pressure at the top of the cupola as magmatic fluids continue to exsolve from the crystallizing stock (Gruen et al., 2010; Klemm et al., 2007; Sillitoe, 2010; Weis et al., 2012; Landtwing and Pettke, 2005). When the fluid pressure exceeds the confining strength of the wallrocks, the chamber will catastrophically fail and release the accumulated water (Proffett, 2003). According to the latter model, the drop in internal pressure of the magma chamber causes much of the water dissolved in the melt to be suddenly released and increases the effective melting temperature of the magma. The loss of heat from the rapidly escaping water causes the temperature of the melt to fall. This combination causes the melt to quickly quench, releasing still more water and resulting in a fine-grained groundmass and a porphyritic texture, if large crystals are present in the melt (Gustavson and Hunt, 1975; Gruen et al., 2010; Proffett, 2003).

The release of fluids enriched in metals and silica make their passage through these fractures, which alters the wallrock by fluid-rock interactions and precipitates minerals within the conduit fractures, eventually filling the fracture to form veins. The *throttling cupola* mechanism first described by Cloos et al. (2005) explains that these systems will experience multiple cycles of fluid release and clogging of the fractures as long as tectonic activity is sustained, much like opening and closing of a valve, ejecting fluid and magma simultaneously by repeated porphyry dike injection (Proffett, 2003).

The fluid supply needs to be continually replenished to generate economic hypogene mineralization of porphyry deposits. As a result, these systems typically display unique alteration halos that are temperature and pressure dependent of the hydrothermal fluids as well as the reactive wall rock (Gustavson and Hunt, 1975; Cooke et al., 2005; Hemley and Jones, 1964). The core of the magmatic stock lacks metal enrichment because the temperature and pressure conditions within its dynamic interior are too high for ore precipitation to occur. This region is inhabited by high temperature, early barren quartz veins that form by a lithostatically pressured, single phase supercritical fluid that is injected into the host rock in the heart of the porphyry system where the highest vein volumes and densities occur (Gustafson and Quiroga, 1995; Proffett, 2003; Cannell et al., 2005; Sillitoe, 2010).

As this fluid makes its ascension to the top of the cupola, the drop in temperature (caused by heat removal by interaction of colder wall rocks and possibly by meteoric water) and pressure (by transition from lithostatic to hydrostatic stress regime) will cause the fluid to separate into two phases: a low salinity vapor phase and a high salinity liquid phase (Cline and Bodnar, 1991; Bodnar, 1995). Precipitation of ore minerals can occur at this fluid phase transition or in lower temperature conditions which is also due in part to the change in stress regime from lithostatic to hydrostatic pressures. An ore shell will form as a result above and lateral to the stock which resembles an inverted tea cup geometry (Westra and Keith, 1981). The shape of the ore shell is dependent upon the original porosity of the host rock and preexisting fractures that can facilitate fluid migration based on the throughput of hydrothermal fluids released from the pluton (Gruen et al., 2010; Mercer and Reed, 2013). The oreshell will be narrower and vertically extensive but more enriched in metals in host rocks with higher permeabilities and larger

source volumes compared to those with lower permeablities and sources, which will result in a wider and less enriched cap (Sillitoe, 2010; Weis et al., 2012).

LOCATION

The Red Hills porphyry Mo-Cu deposit is located in Presidio County in Trans-Pecos Texas, approximately 40 km (25 miles) north-northwest from the town of Presidio (Figure 1.1). Red Hills occurs in the western part of the famous Shafter silver mining district and on the south-eastern corner of the Chinati Mountain caldera complex (Gilmer et al., 2003; Tietz, 2012). The district follows a west-to-east trend of Mo-Cu at Red Hills to the west and multiple Zn-Pb and Pb-Ag occurrences eastward. Figure 1.2 shows abandoned Zn-Pb and Pb-Ag mines and prospects along this trend including the Gleim, Stauber, Mac Daniel (Leland), Perry, Chinati, Montezuma, Last Chance (Young), Cibolo, Ross, Carr (Sullivan), and Shafter (Presidio/Shafter extension). Red Hills owes its name to the Fe-oxide-rich leached cap that is exposed at the surface (Figure 1.3). The Red Hills proper roughly covers a 39 km^2 (15 mi^2) surface area and is reported to contain an open-pit, indicated resource of 26.7 Mt (24.7 Mtonne equivalent) at 0.08% MoEq which was calculated from a 0.025% MoEq grade cutoff. This resource totals 14.4 Kt of Mo, averaging 0.054% Mo, and 38.5 Kt of Cu, averaging 0.14% Cu, based on a 850 m (2,800 ft) bottom elevation constraint approximately 370 m (1,200 ft) below surface elevation (Tietz, 2012).

PREVIOUS WORK

Gilmer's (2001) extensive work on the Red Hills concluded, from zircon U-Pb analyses, that the Red Hills intrusive center is the easternmost Laramide porphyry deposit (64.2 $\pm$ 0.2 Ma) in the North American Cordillera, and therefore distinctly older in age than the nearby Tertiary Chinati Mountains Caldera complex (32 Ma) with which the Red

Hills previously was thought to be genetically linked (Price and Henry, 1982). Re-Os analyses indicated molybdenite mineralization to be 60.2 $\pm$ 0.3 Ma (Gilmer, 2001), while sericite $^{40}Ar/^{39}Ar$ analyses produced dates of approximately 61 Ma (Gilmer et al., 2003). Fluid inclusion analyses in hydrothermal vein quartz from phyllically altered samples had 399°C $\pm$ 58°C mean homogenization temperatures with halite, sylvite, chalcopyrite, hematite, pyrite and bixbyite daughter minerals identified by scanning electron microscopy - energy dispersive spectrometry (SEM-EDS). Estimated salinities ranged from 33 to 47 wt. % NaCl equiv which, when applying mean homogenization temperatures for boiling phases, corresponded to 2-3 km depth of exhumation. Supergene alunite dated by the $^{40}Ar/^{30}Ar$ method at roughly 3.8 to 5.8 Ma (Kyle, 2012), which may suggest Red Hills was rapidly exhumed and eroded during the Pliocene, while the Presidio Bolson was the southern terminus of the Rio Grande system.

GOALS OF THIS STUDY

The recent drilling campaign conducted by Canadian junior mining company Tosca in 2012 resulted in the extraction of over 7315 m (24,000 ft) of core from 31 drill holes at Red Hills. This provided a unique opportunity to collect and analyze samples deep within the Red Hills intrusive center in which previous studies (Gilmer, 2001; Gilmer et al., 2003) were lacking by limitations to surface samples. Analysis of drill core samples were necessary to ascertain if the Red Hills is a multi-phase igneous system and to identify if multiple episodes of Mo-mineralization occurred throughout the life of the system.

Restricted access only allowed for 3 days of field mapping on the Red Hills proper to measure stress orientations of faults and joints exposed at the surface and to expand Gilmer's (2001) field work dataset to evaluate if east-west trending structures

which may have facilitated the transport of hydrothermal fluids exsolved from the Red Hills intrusions might ultimately be the source for Shafter silver orebody. This endeavor proved difficult due to extensive alluvial cover. An additional 4 days were spent logging and sampling the Tosca drill cores in preparation for other research.

Whole-rock major oxide and trace-element geochemistry of new phases were conducted to examine if these intrusive stocks derived from the same parental melt as well as compare their geochemical characteristics with pre-existing geochemical data from Gilmer (2001) and nearby intrusions from the Chinati Mountains, Shafter, and Pinto Canyon areas (Cepeda, 1977). In addition, zircon U-Pb geochronology was conducted to identify crystallization ages of these phases. Detailed observations of vein types present at the Red Hills were catalogued, and veins, which are quartz-bearing, were imaged with scanning-electron microscopy, and cathodoluminescence (SEM-CL) to help identify quartz textures not observable by other techniques to provide insight into the formation of these veins. Trace element analyses of hydrothermal vein quartz were conducted to provide a holistic view of changes in the physio-chemical conditions, particularly thermal gradients, which occur during vein growth especially in conditions for molybdenum and copper precipitation.

EXPLORATION HISTORY

Exploration in Trans-Pecos Texas began with silver exploration and exploitation of the Mina Grande deposit in the Shafter district during the early 1800s (Smith, 2011). The first evaluation of the Red Hills began with Phelps Dodge Corp. in the 1950s. In 1955, American Smelting and Refining Company (ASARCO) drilled 12 holes and conducted subsequent geologic mapping, geochemical sampling, and geophysical and magnetic surveying in the 1960s (Long, 1992). They targeted drill holes in the main area

of mineralization in 1965. In 1966, Amax leased the property and drilled one deep hole within the south-center portion of the deposit in 1967. In 1970 and 1971, Duval leased the Red Hills property and drilled 70 holes into the Red Hills stock and outlined the Cu-Mo porphyry zone in 1971 to 1973 (Peterson, 1972).

Gold Fields Mining Corporation conducted exploration regional mapping and drilling west of Shafter up to the Sullivan mine, located roughly 483 m (0.3 miles) west of the Red Hills, from 1977 to 1982 after the purchase of the Shafter property from Amax in 1977. Peterson (1973) reported two carloads of malachite and azurite were the only copper minerals mined at the Shafter district. Gold Fields and Duval participated in a joint venture from 1980 to 1983 to target precious metal occurrences west and south of the Red Hills, specifically near the Sullivan mine which contained veins with high grade concentrations of lead, silver, and gold (Naylor, 1982a, 1982b; Whitney, 1982a, 1982b).

Duval estimated the Red Hills contained over 5.5 Mt of 0.5% Cu and that 21 drill holes contained drill-intervals greater than 31 m (100 ft) in length averaged 0.06% Mo (Peterson, 1973). Gold Fields dropped their lease and purchase option for the surface right in March 1983 and also terminated their joint venture with Duval in March 1983 (Fitz-Gerald, 1983). The joint venture prompted EM Technology of Boulder, Colorado to conduct controlled-source AMT (audio-magnetotellurics) surveys in the Shafter and Red Hills areas in early 1983 (Knox, 1983). An anomaly was identified that coincided with the Shafter silver deposit. A resistivity survey was run across the Livingston Ranch property in early 1983, including two north-south lines run over the Red Hills.

A total of 89 holes were drilled in the Red Hills copper-molybdenum porphyry mineralization by prior Tosca operators. Duval quitclaimed the mineral rights of the five sections comprising the Red Hills property to Gold Fields in April 1984. Siltex Resources, Inc, who merged with Belcor, Inc. in early 1994, acquired the mineral rights

from Gold Fields in July 1994. Rio Grande Mining Company acquired all of Gold Fields' mineral holdings in October 1994, and acquired the surface rights to 16,871 acres on the Livingston ranch in 1998 (Belcor Corp, 1997). No exploration had been done on the Red Hills since 1983. After purchasing the Red Hills drilling information from Pennzoil in 1995, Rio Grande conducted pre-feasibility studies to determine the viability of extracting the shallow copper resource at the Red Hills in 1997 (Rio Grande Mining Company, 1995, 1997a, 1997b). Silver Assets Inc. acquired Rio Grande, which in turn, was acquired by Silver Standard Resources in 2000.

Silver Standard Resources sold the mineral rights to five sections at the Red Hills over the span of 5 years to Red Hills Copper, Inc. in February 2008 (Rozelle and Tschabrun, 2008). Tosca purchased all stock of Red Hills Copper, Inc by 2011 which was promptly followed by an extensive drilling and evaluation program by Tosca Mining Corporation in 2012 (Tietz, 2012). Due to the poor economic climate, particularly low Mo prices and relatively low copper grade and tonnage estimated during the evaluation program, Tosca dropped their option in the Red Hills property in January 2013, returning the minerals rights to Red Hills Copper, Inc.

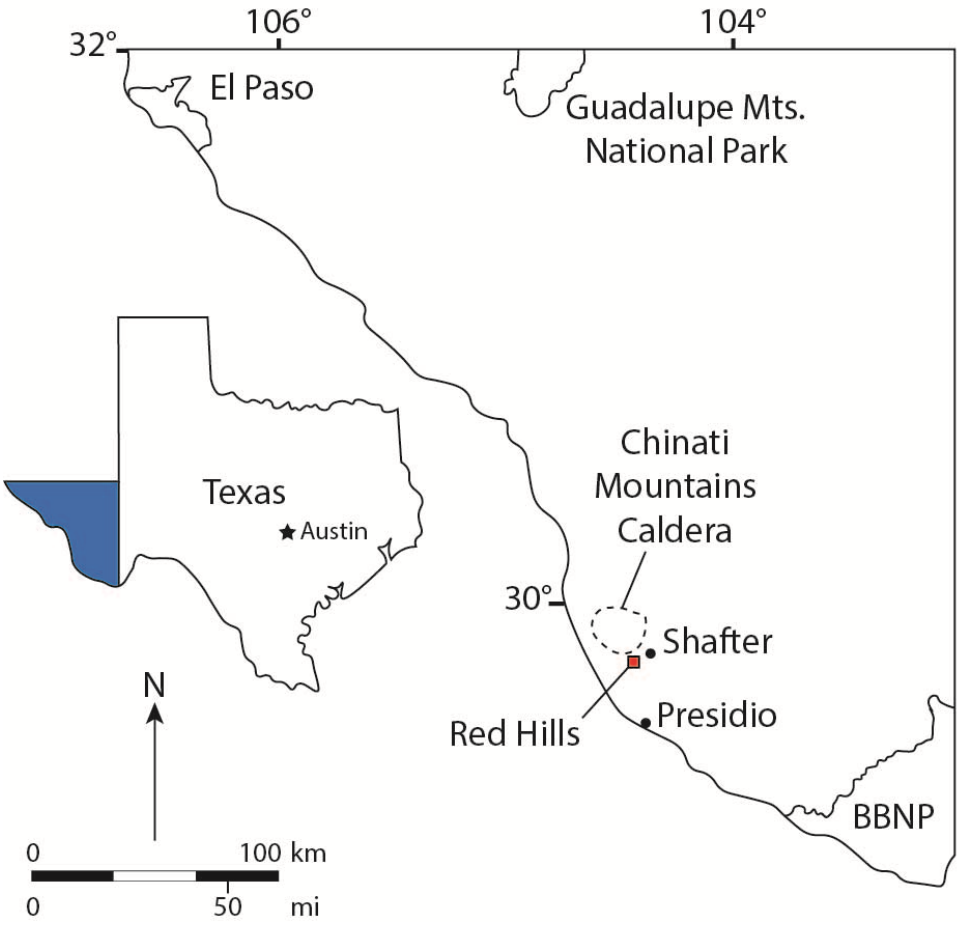

Figure 1.1. Location of the Red Hills research area. Figure modified after Evans (1975).

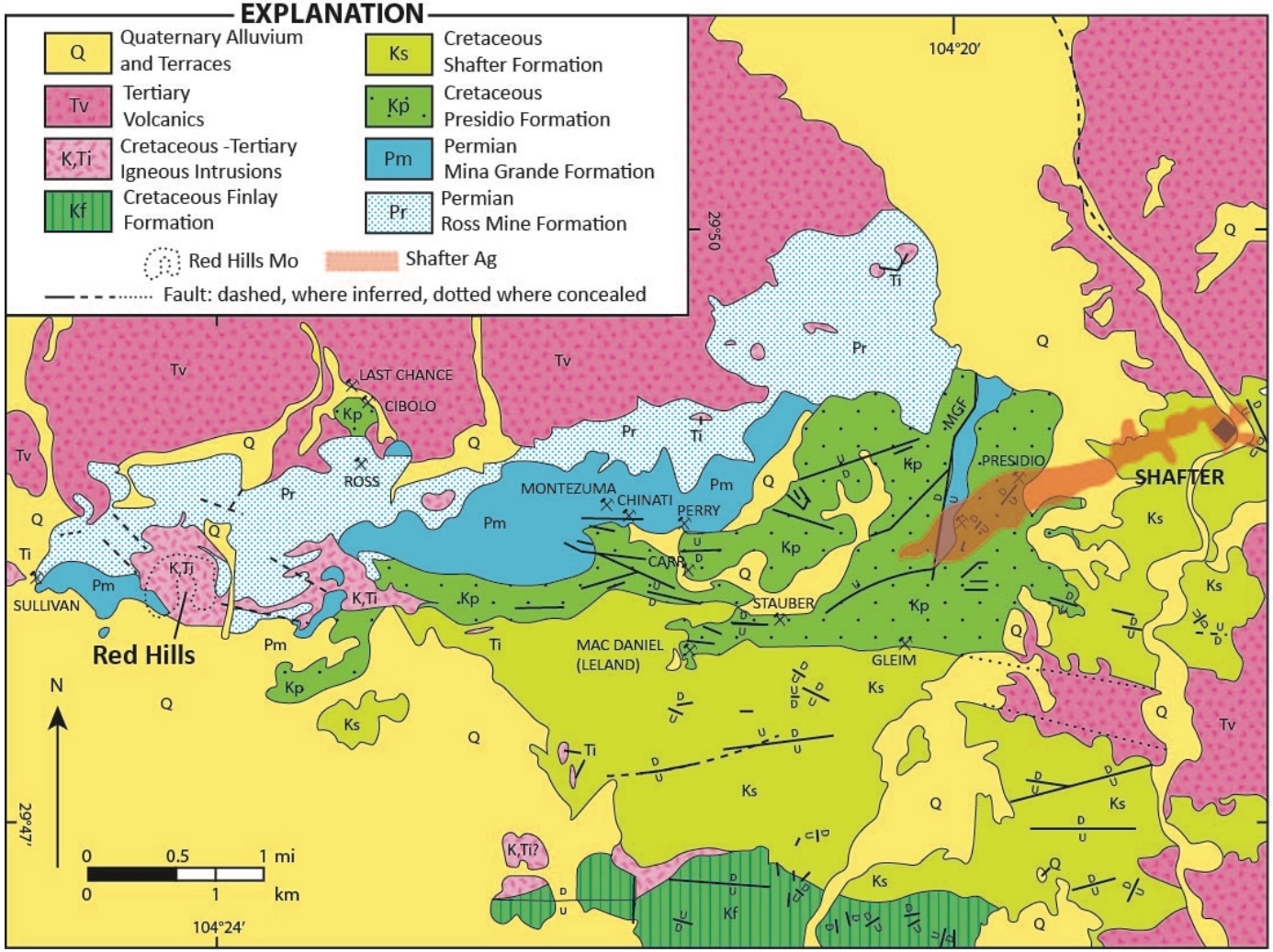

Figure 1.2. Geologic map of the Shafter mining district. Modified after Evans (1975).

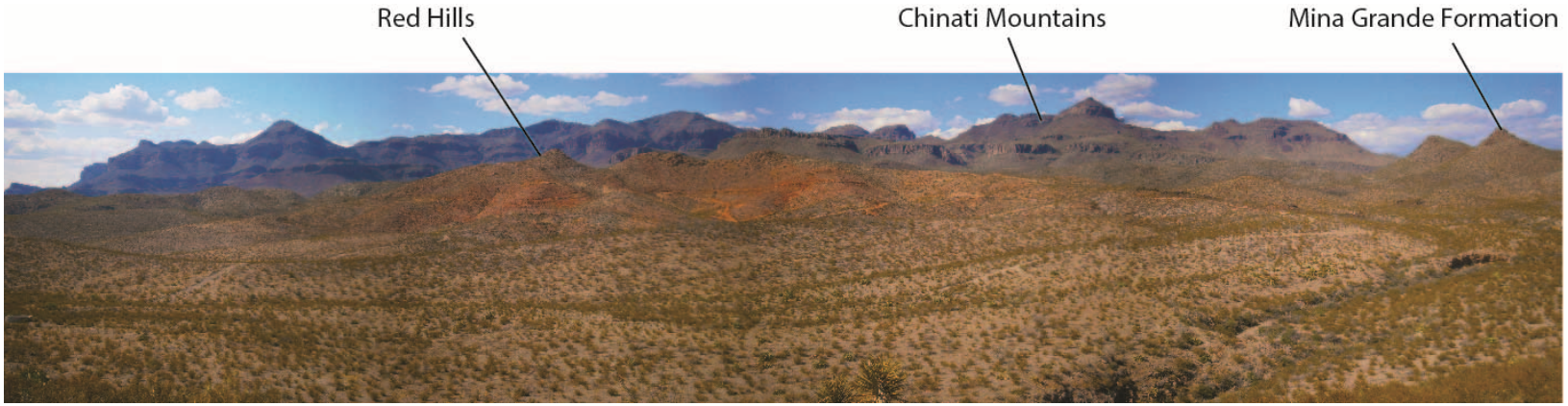

Figure 1.3. Field location panoramic photograph. The Red Hills sits south of the Chinati Mountains in the background with the tilted strata of the Mina Grande Formation apparent to the east. View is looking North-West.

Chapter 2: Geologic Setting

INTRODUCTION

The geologic history of Trans-Pecos Texas is complex due to superimposed tectonic deformation events (Figure 2.1). The Red Hills porphyry system is contained within the boundary of the intensely deformed Chihuahua tectonic belt to the west and the relatively stable Diablo Platform to the east (Figure 2.2). Tertiary volcanics, approximately 1 km (0.62 mi) north, and the eastern flank of the Presidio Bolson bound the Red Hills to the north and west to south, respectively (Figure 2.3).

REGIONAL TECTONIC SETTING

Trans-Pecos lies at the intersection of three major orogenic belts: the Precambrian Van Horn mobile belt, the Paleozoic Ouachita thrust belt, and the late Mesozoic Cordilleran tectonic belt (Shepard and Walper, 1982). During the middle Proterozic, this area was a site of regional scale thrusting and orogenic activity. The west Texas basement, comprised of deformed and metamorphosed accretionary island-arc and interarc sediments and volcanics, formed a northwest-trending structural grain that includes the Texas Lineament and defines the southwestern edge of the North American margin (Muehlberger and Dickerson, 1989; Muehlberger, 1980). During the Grenville orogeny (1100-1400 Ma), the northwest-southeast plate convergence acted in a strike-slip manner in west Texas (Mosher, 1998) and is coincident with the formation of the Van Horn Mobile Belt (Horak, 1985), where the oldest rocks in this region are found. Formation of the Delaware Aulocogen occurred near the same time as the Grenville orogeny, preceding Late Precambrian to early Cambrian rifting that separated the proto-Pangean supercontinent into the North American and proto-Afro-South American plates locally (Adams and Keller, 1996). By Mid-Ordovician, a passive margin succession was

formed by shallow-marine cratonic deposition as a product of sagging from the divergent continental margin (Goetz and Dickerson, 1985) during the early Paleozoic postrift and drift phases of Laurentia, following the breakup of the late Precambrian supercontinent (Sarg et al., 1999).

While Cambrian to Pennsylvanian transgressive and regressive marine sequences were being thrust over Precambrian crystalline basement during the Ouachita Orogeny. A synorogenic foreland succession, represented by the Val Verde foreland basin, was being formed in front of the Marathon thrust belt, which was filled with clastic, carbonate, and evaporite packages into the Permian as the basin continued to deepen (Ammon, 1981; Ross, 1986; Sarg et al., 1999). Near the same time, the Tobosa Basin was segmented into northwest-aligned foreland basins, such as the Delaware Basin, the Central Basin Platform, and the Midland Basin, by Precambrian fault reactivation while the Central Basin Platform became a positive feature from uplift. In Wolfcampian time, the Marfa Basin was formed by normal faulting of the Wolfcamp foreland basin (Ammon, 1981).

According to Dickerson (1980), the Chalk Draw and Tescotal Mesa faults formed en echelon systems of grabens in west Texas, which resulted in left-lateral strike-slip stress orientations along WNW-trending basement faults of the Texas Lineament. Left-lateral movement along the Chalk Draw fault due to Ouachita convergence took place in the Early Permian (Wolfcampian) (Muehlberger and Dickerson, 1989). The Diablo Platform became a separate structural feature when its southern end buttressed the Marfa Basin against the Marathon thrust sheets. Late Permian carbonate accumulations as much as 6000 ft (1800 m) thick became completely eroded locally during post-Permian uplift (Luff, 1981). Deformation of the Diablo Platform and Marathon structures divided the Marfa Basin into western and eastern parts, the Val Verde/South Delaware Basins respectively, whose only connection to the other Permian basins was the Hovey Channel

(Ammon, 1981), as evidenced by the reef deposits found prograding west from the former Ouachita-Marathon front into the Marfa Basin. Frontal overthrusts of the Ouachita-Marathon Foldbelt pushed northwest buttressing against the Diablo Platform, separating the Marfa Basin from the Delaware Basin and forming a salient into the graben located between the Walnut Draw and Chalk Draw faults.

During the Mesozoic, extensional rifting and breakup of Pangea occurred with the subsequent opening of the Gulf of Mexico during crustal plate reorganization (Shepard and Walper, 1982). Late Triassic to Early Jurassic normal faulting formed the Chihuahua trough, which parallels the Rio Grande (Silver and Anderson, 1974; Berge, 1982; Goetz and Dickerson, 1985). High-angle normal faulting in the late Paleozoic was followed by episodes of uplift, intense compressional deformation and magmatism starting in Early Cretaceous, collectively referred to the Laramide orogeny (Coney, 1978). Sediments deposited within the Chihuahua Trough/Basin were deformed against the buttress of the stable Mesozoic platform, coinciding with the Late Paleozoic Diablo Platform edge which created the Chihuahua tectonic belt (Muehlberger and Dickerson, 1989; Shepard and Walper, 1982). N- and NW-oriented structural features found in the Chihuahua fold and thrust belt (Horak, 1985) are the result of early NE and later ENE Laramide compression (Price and Henry, 1985). ENE-shortening continued until at least 32 Ma until the transition to an extensional regime (Price and Henry, 1984; Barker, 1987). Laramide contraction reactivated WNW-striking basement faults with left-lateral strike-slip displacement, and produced some folds, high-angle reverse faults and low-angle thrusts. Extension also reactivated basement faults, producing pull-apart grabens terminating against WNW-striking right-lateral strike-slip faults bounded by NNW-striking normal faults (Barker, 1987; Muehlberger and Dickerson, 1989). Laramide

convergence also resulted in elevating west Texas, thus again allowing the area to be eroded (Ammon, 1981).

The Basin and Range extensional tectonic episode was initiated when the Pacific plate came into contact with the North American plate along the growing San Andreas transform margin. Widespread block faulting, right-lateral divergent wrenching, and northwest dip slip superimposes all earlier structures but is influenced by the pre-existing structural grain formed by earlier tectonic episodes (Shepard and Walper, 1982; Muehlberger and Dickerson, 1989). Previous deformation events and on-going Basin and Range extension have most likely reactivated numerous faults during these different tectonic episodes which obscures the exact nature of fault movement in the Red Hills research area.

LOCAL STRATIGRAPHY

The more calcareous Cibolo, Ross Mine and Mina Grande Formations were deposited throughout the later Permian as transgressive/regressive reef/forereef cycles. These reefs are the source of the forereef and talus debris that make up the ore-hosting Mina Grande limestone (Luff and Pearson, 1988; Bogle, 2000). The Late Permian Ross Mine (Word equivalent) and Mina Grande (Capitan equivalent) Formations are the oldest units (Guadalupian) exposed at Red Hills (Rix, 1953). Bogle (2000) interpreted that these units were deposited as basin margin/platform edge mixed carbonate-clastic sequence in the Marfa Basin during transgressive/regressive reef/forereef cycles (Rix, 1953; Bogle, 2000) (Figure 2.4). The older Ross Mine is described as interbedded bioclastic packstone to wackestone at its base, carbonate mudstones and bedded quartz sandstones, siltstones and shales (Bogle, 2000). This unit is described as series of transgressive and regressive cycles that ultimately ends in a transgressive system tract and continuous deposition of

the Mina Grande that conformably overlies the Ross Mine formation. Chert nodules located at the top of the section are characteristic of the Ross Mine, which were useful in defining contacts between the Mina Grande formation during field mapping and core logging.

The upper Ross Mine and Mina Grande formations represent a transgresssive/regressive platform margin environment with essentially continuous deposition throughout the Permian. Deposition of the Mina Grande reflected the progradation of a carbonate platform as the marked increase in carbonaceous material grew over time (Bogle, 2000). Reefs are the source of the forereef and talus debris the Mina Grande (host to the Shafter silver orebody; Head, 2002) which is composed of massive to thin bedded wackestone to packstone and carbonate mudstone, deposited as turbidites, debris flows, and mud flows as seen by normal grading (Bogle, 2000). After burial, the Permian units were uplifted, which exposed the Mina Grande to erosion and karstification before Cretaceous deposition took place. Due to variations in erosion, thicknesses of the Mina Grande measured by Rix (1953) in outcrop ranged from 15 m (50 ft) to 90 m (300ft). Together, the greatest thickness of the Ross Mine and Mina Grande total 305 m (1000 ft) according to Bogle (2000).

At Red Hills, the Ross Mine is the largest Permian exposure in the map area and according to Gilmer (2001), also occurs as roof pendants above the Red Hills intrusion. The Ross Mine is typically altered to light tan-colored hornfels and silicified siltstones along intrusion contacts. Localized breccias zones are typically concentrated near high-density fault zones. Along with the Ross Mine, the Mina Grande bounds the western Red Hills stock to the west and is cut by the eastern stock. Gilmer (2001) states that the exoskarns from both the Ross Mine and Mina Grande are primarily composed of

grossular-andradite-garnet and are both affected by retrograde alteration, the Ross Mine more so because of its closer proximity to the Red Hills intrusions (Figure 2.9).

In the Late Cretaceous, inundation of the Cretaceous Seaway into the Marfa Basin allowed renewed deposition (Presidio and Shafter Formations) unconformably on Permian strata in Trans-Pecos Texas, which thin against the Diablo platform. Increased subsidence of the Chihuahua Trough/Basin resulted in deposition of more than 4,000 m (13,000 ft) of Cretaceous sediments southwest of the basin edge fault, whereas a maximum of only 300 m (1000 ft) is present in the Marfa region (Luff, 1981). The Presidio Formation is the dominant Cretaceous unit that bounds the Red Hills intrusive complex to the east, consisting of basal sandstone and conglomerate (clasts from underlying Permian units) with fossiliferous limestone interbeds. This unit varies from 15 m (50 ft) to 90 m (300 ft) in thickness, depending on the intensity of erosion (Bogle, 2000). Gilmer (2001) reported that the Shafter formation to the south of the study area, dips more steeply and is covered by thicker alluvium and gravel cover. Exposures of the Shafter Formation are limited to the SE corner of the study area where it appears to be contained within a series of NE-trending faults (Figure 2.9). This unit is described as alternating beds of fossiliferous, nodular limestone and sandstone (Rix, 1953). The Presidio and Shafter Formations show no signs of alteration compared to the Permian units.

Triassic to Mid-Cretaceous strata within the Chihuahua Basin were locally deformed by compression induced by the Farallon plate subducting under the North American plate during the Laramide Orogeny, followed by large scale ignimbritic Tertiary volcanism (Figure 2.3). Approximately 1 km (~0.62 mi) north of the Red Hills, Tertiary volcanics from the Chinati Mountains Caldera lay unconformably on Permian and Cretaceous strata (Cepeda and Henry, 1983).

Erosion of these extensional Basin and Range fault grabens filled the Quaternary Presidio Bolson with as much as 1,500 m of sediments at the southern boundary of the ancestral Rio Grande Drainage (Figure 2.3). During the Pleistocene, the Rio Grande system was reintegrated when the southern boundary of the Presidio Bolson was breached. As a result, progradation of the western Gulf of Mexico continental margin began forming as a fluvial-deltaic depocenter associated with the modern Rio Grande (Kyle, 2012).

TRANS-PECOS MAGMATISM

Compressional stresses and plutonism formed as a result of the Farallon plate subducting under the North American plate, beginning at 75 until 58 Ma, by the progressive flattening of the Farallon plate. Detachment of the flattened plate and its subsequent sinking into the mantle triggered Mid-Tertiary sweep from SW to NE of crustal extension, magmatism, and explosive volcanism (Coney, 1978; Shepard and Walper, 1982; Coney, 1987). Residual NNW-oriented compressional stress from the Laramide orogeny induced widespread, alkaline magmatism. Prominent east-trending dikes formed most likely in a continental arc setting during the middle Eocene to early Oligocene, 48 to 32 Ma, Basin and Range crustal extension followed at approximately 31 Ma (Price et al., 1986). From 30 to 27 Ma, prior to the onset of extensional faulting, volcanism consisted mainly of ash-flow tuffs, rhyolite domes, and silica-undersaturated suites (alkali basalt to trachyte) (Price et al., 1987). The youngest igneous activity in Trans-Pecos, Texas, occurred between 24 and 17 Ma as small amounts of alkali basalts and hawaiites associated with Basin and Range faulting. These dikes are oriented NNW due to ENE extension (Price et al., 1987; Price and Henry, 1982). The dominant style of

deformation during this time was right-lateral divergent wrenching and northwest dip slip due to Basin and Range extension (Muehlberger and Dickerson, 1989).

Gentle tilting (~15°) of the strata towards the south at Red Hills has been attributed to the development of the Chinati Mountains by swelling, eruption, collapse and subsequent resurgence (Rix, 1953). This caldera covers a 30 x 20 km area, which is filled by 1300 m of lower and middle trachyte lavas, lower rhyolite lavas, upper trachyte lavas, and upper peralkaline rhyolite ash-flow tuffs (Figure 2.5). This caldera was the source of the widespread Mitchell Mesa Rhyolite, with at least 1000 km^3 as outflow and 700 km^3 ponded in the caldera (Price et al., 1986).

The Cretaceous and Permian units dip away from the caldera, which is bordered with high angle normal faults along the caldera rim. The Chinati Mountains caldera follows the previous Laramide structural trends near the intersection of the east-west Chalk Draw Fault and NNW and WNW structures like the Texas Lineament (Cepeda and Henry, 1983). East and northeast-trending normal faults in the Permian and Cretaceous strata generally parallel the caldera collapse boundary and may control the orientation of mineralized structures in the Shafter area (Cepeda and Henry, 1983; Muehlberger and Dickerson, 1989). Basin and Range extensional tectonics followed by Laramide compression formed large basins filled with thick sequences of gravel and sand (Henry and Price, 1986).

LOCAL STRUCTURES

Prominent, large-scale structures in the Red Hills and Shafter mining district include the Proterozoic, N-NW to NW-WNW Texas Lineament structures, late Proterozoic, E-W-trending structural grain proposed as a western extension of the Chalk-Draw Fault, Cenozoic NW-trending West and East Chinati faults, Cenozoic E to E-ENE

trending caldera faults south of the Chinati Mountains caldera, and the Mina Grande fault west of the Shafter deposit (Muehlberger and Dickerson, 1989; Goetz and Dickerson, 1985; Henry, 1998; Price et al., 1986; Muehlberger, 1980). Local structures include en echelon faults, dikes and sills, and joints.

The doming of the Chinati Mountains caldera tilted Permian and Cretaceous units away from the volcanic center and formed ENE-striking normal faults (termed strike or tangential faults) along the caldera rim (Ross, 1943; Udden, 1904). The Mina Grande Fault System (Figure 1.2) is a set of interconnected faults oriented N10°E that borders the eastern margin of the Shafter orebody. It is part of the high-angle, normal faulting associated with caldera collapse, and is responsible for uplifting the mineralized Permian limestone which hosts the Presidio mine. This fault has a 60 to 90 m (~200 to 300 ft) throw and is responsible for uplifting Mina Grande strata to the surface (Head, 2002). The Chinati Mountains horst is a late Tertiary to early Quaternary structure that is defined by the West Chinati fault and the East Chinati fault. The West Chinati fault is a down-to-the-west, normal fault and the East Chinati fault and Burton fault is a down-to-the-east, normal fault (Rix, 1953).

In order to gain a better understanding of the local structures and their relationship to the Red Hills mineralizing system, mapping in the Red Hills study area (Figure 2.6) allowed the collection of additional field samples and data across the map area (Figure 2.7) with a focus on the unaltered portion for U-Pb geochronology work that will be discussed in Chapter 4. Gilmer (2001) documented N-S and E-W trend of quartz veins (Figure 2.8c) within the intrusion, but found random orientations for secondary alunite veins and joints within the Permian units (Figure 2.8d).

NW-striking, en echelon faults in the western, mineralized stock curve to an E-W orientation in the eastern, unaltered stock. The en echelon faults at Red Hills cut through

Permian strata and the Red Hills intrusion and continue to the west past the Mina Grande Fault System transitioning to a NE trend. The NW-striking, en echelon structures are interpreted to be reactivated basement, Texas lineament structures during Tertiary Laramide contraction. The E-W en echelon faults mimic a similar orientation as the late Proterozoic Chalk Draw strike-slip fault, which further suggests the continuation of superimposed deformation (Muehlberger and Dickerson, 1989). Although reactivated, E-W-striking structures may have controlled the ascension of the Red Hills stock, based on the west to east elongation of the intrusive complex at the surface (Figure 2.9). Field relationships suggest that gentle folds to the north of the study area with E-W trending fold-axes and NE-striking faults appear to be radial faults related to caldera development and collapse.

Fifty-nine joints and faults and 68 bedding attitudes were mapped in the Permian strata located between 29 48’0”N and 29 48’45”N. Most of the joints are open mode fractures showing little to no displacement while faults are silica flooded and appear oxidized. Joints in the Permian strata show a weak NW orientation (Figure 2.8a), which differs from Gilmer’s (2001) observation of weakly E-W trending joints (Figure 2.8b). This discrepancy may be due to the limited amount of field work in somewhat different areas rather than a true difference in joint orientation. Figure 2.9 shows an updated geologic structure map at Red Hills with new attitude measurements.

Many faults observed in drill core appear to be blind faults, that is faults that do not reach the surface. Access to drill core was vital in the interpretation of the subsurface geology at Red Hills in which multiple igneous phases were observed (Figure 2.10) and will be discussed in chapter 3. Quartz veins in drill core were observed to occur in three forms: stockwork veins, high-angle veins, and shallow, concentric veins. Delineation of

the structural orientations of these groups of veins could not be done as the cores were not oriented.

SUMMARY AND DISCUSSION

The Red Hills intrusive complex intruded into Permian siliciclastic and carbonate units that dip south as a result of caldera collapse and resurgence of the 32-Ma Chinati Mountains caldera that lies approximately 1 km north from the Red Hills deposit. Hornfels have developed along the contact aureoles of the intrusive suite with minor skarn development to the west of the mineralized, western stock. Joints in and around the Red Hills intrusion display a weak NW orientation, which contradicts previous E-W trending orientations by Gilmer (2001). This may be due to the limited amount of structural information that could be collected during the restricted field time.

Orientations of map-scale, en echelon faults in the field area have distinct NNW- and E-striking trends, which are discordant to the ENE-dominant structure orientations that Head (2002) observed at Shafter. She suggested that the Mina Grande Fault System and the en echelon faults at Shafter were fluid conduits responsible for the mineralization of the Shafter silver deposit, even though none of these structures correspond to the orientations of large-scale structures in the region. Exploration drilling by Aurcana in 2013 along the Mina Grande Fault found no evidence that the Mina Grande Fault System served as a pathway for mineralizing fluids, which formed the orebody. Perhaps then, the E-trending en echelon structures are of primary importance for the transportation of mineralizing fluids from a cooling magmatic source at depth under the Shafter orebody (Head, 2002).

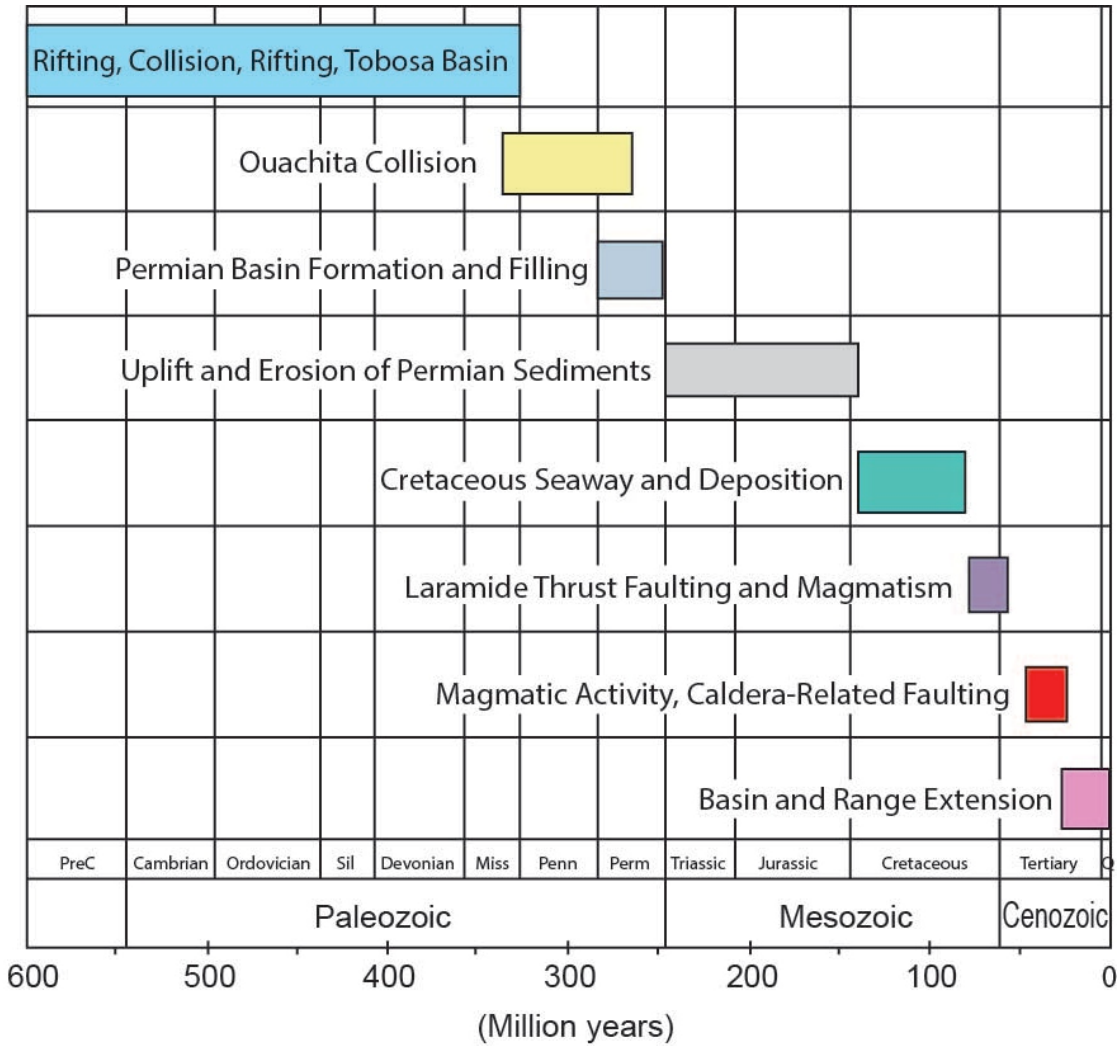

Figure 2.1. Timeline of major tectonic events in southern Trans-Pecos Texas. Figure modified after Horak (1985).

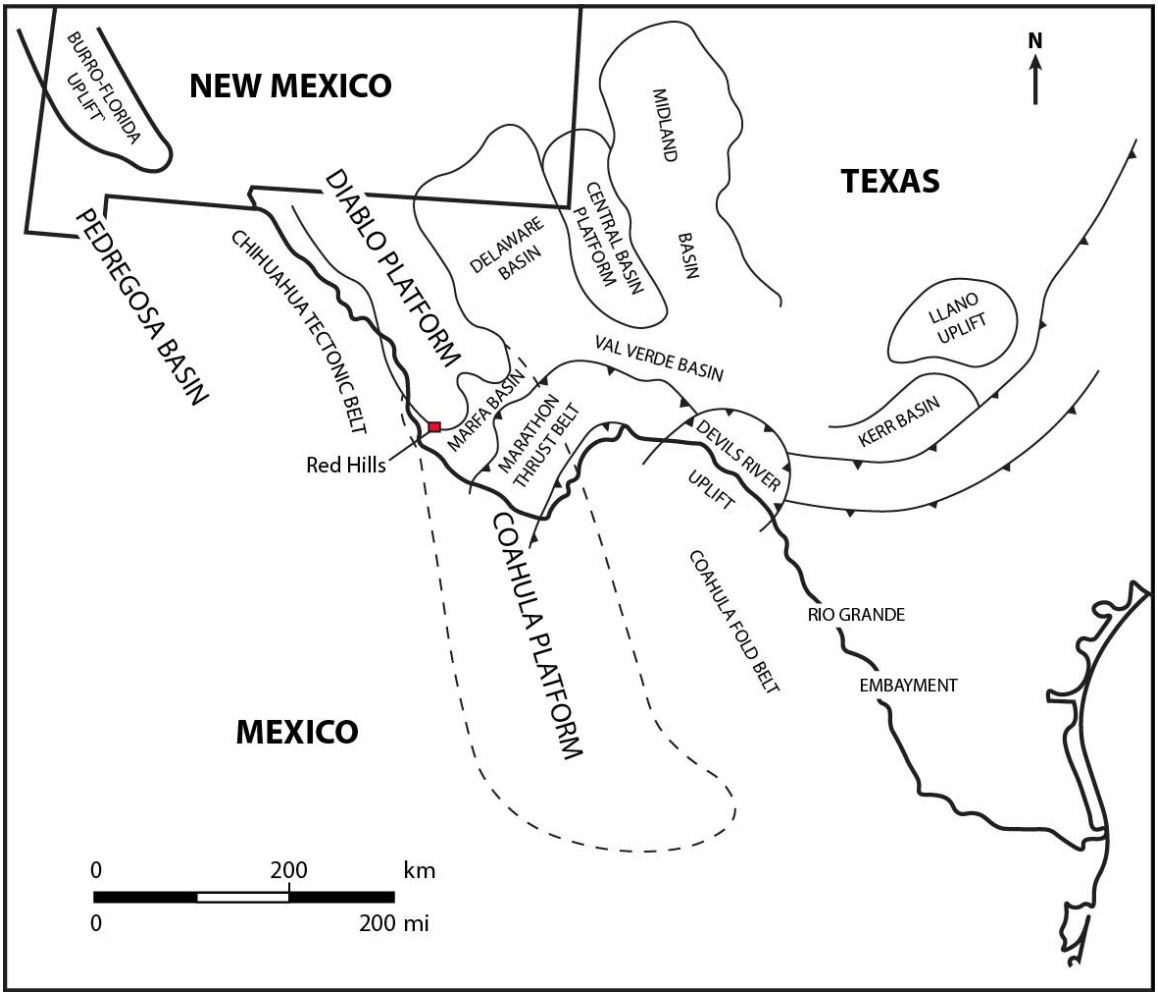

Figure 2.2. Tectonic elements of Trans-Pecos Texas. Figure modified after Shepard and Walper (1982).

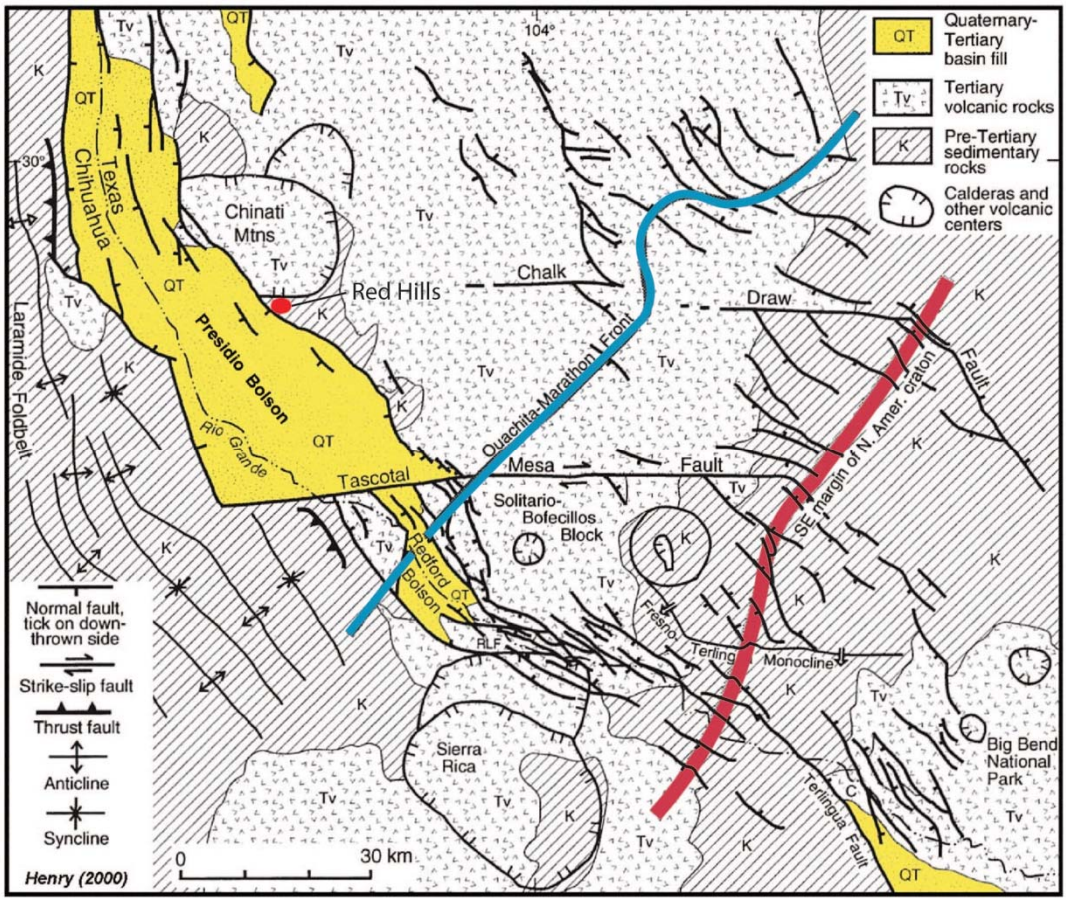

Figure 2.3. Regional structural geology map of Trans-Pecos Texas. Highlighted major tectonic structures are the Ouachita-Marathon Front (in blue), the South-East margin of the North America craton (in red), and the Presidio Bolson (in yellow). The Red Hills study area is circled in red. Figure modified from Henry (1998).

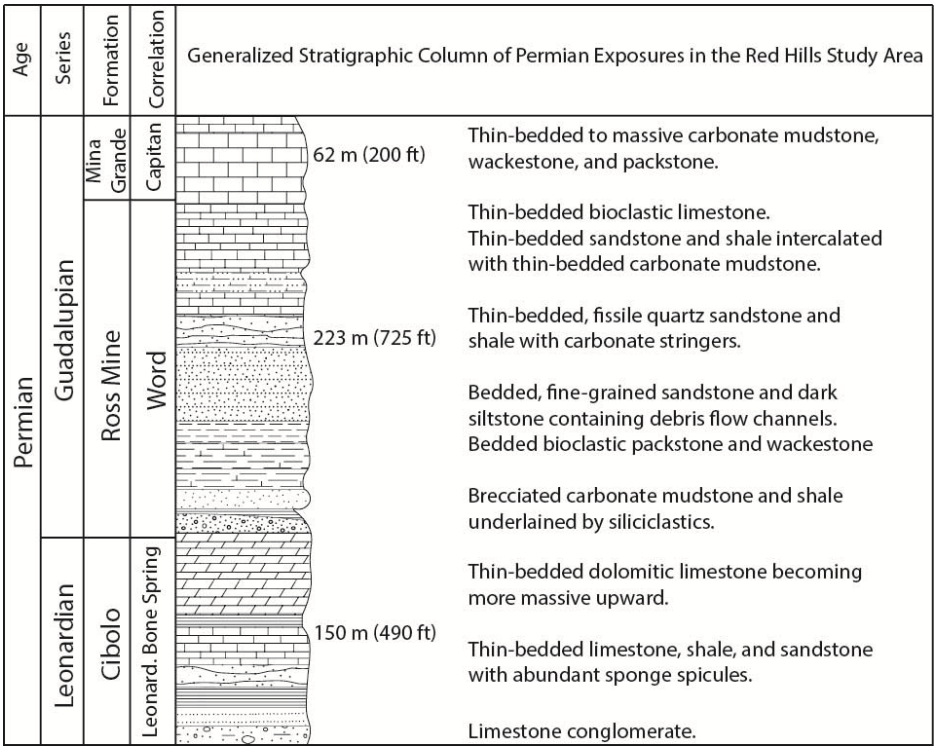

Figure 2.4 Generalized Permian stratigraphic units in the Red Hills area. From Bogle (2000).

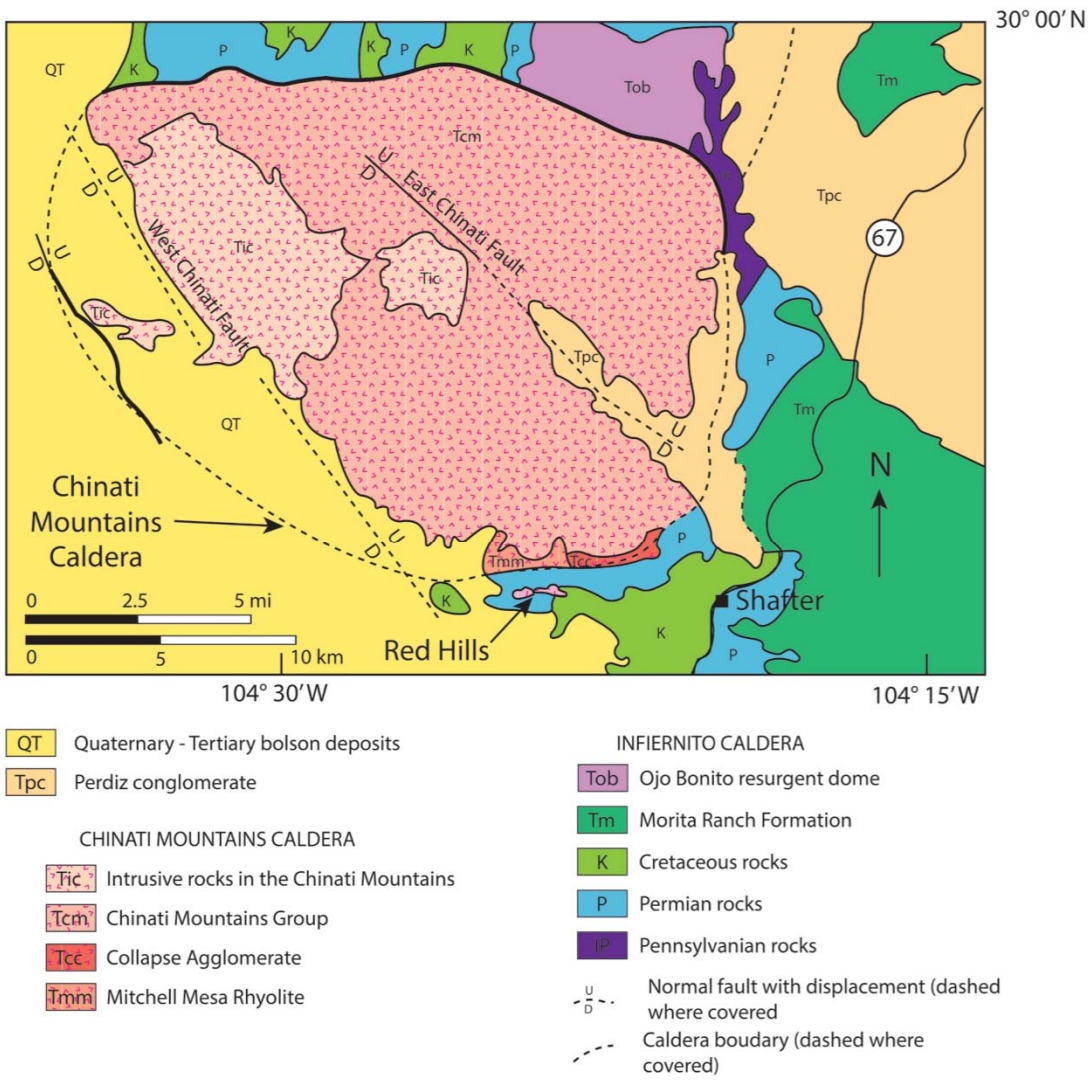

Figure 2.5. Geologic map of the local geology of the Chinati Mountains Caldera showing the location of the Red Hills intrusive complex and the town of Shafter. Figure modified from Cepeda & Henry (1983).

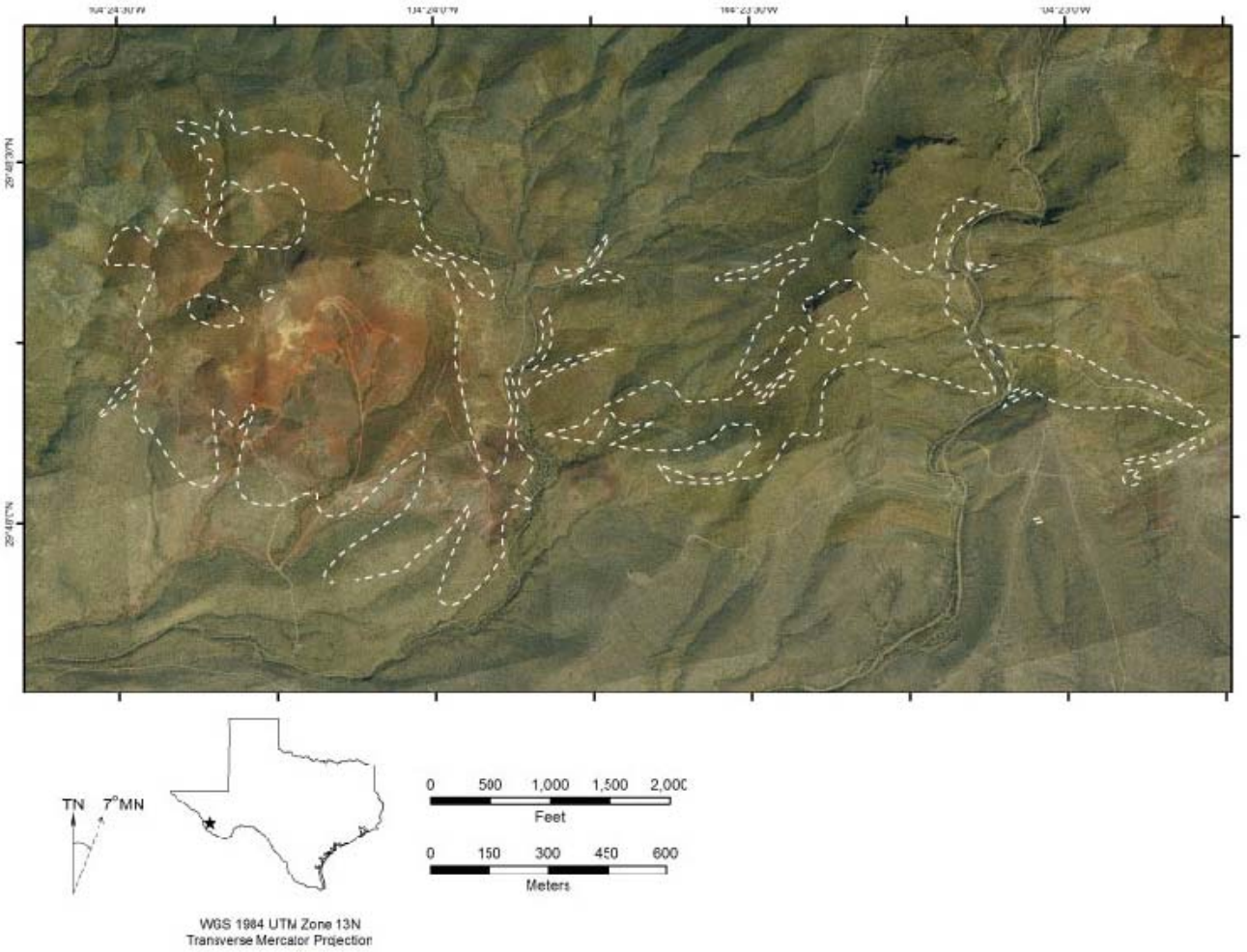

Figure 2.6. Aerial photograph of the Red Hills study area. Dashed-white line represents the outline of Red Hills intrusions.

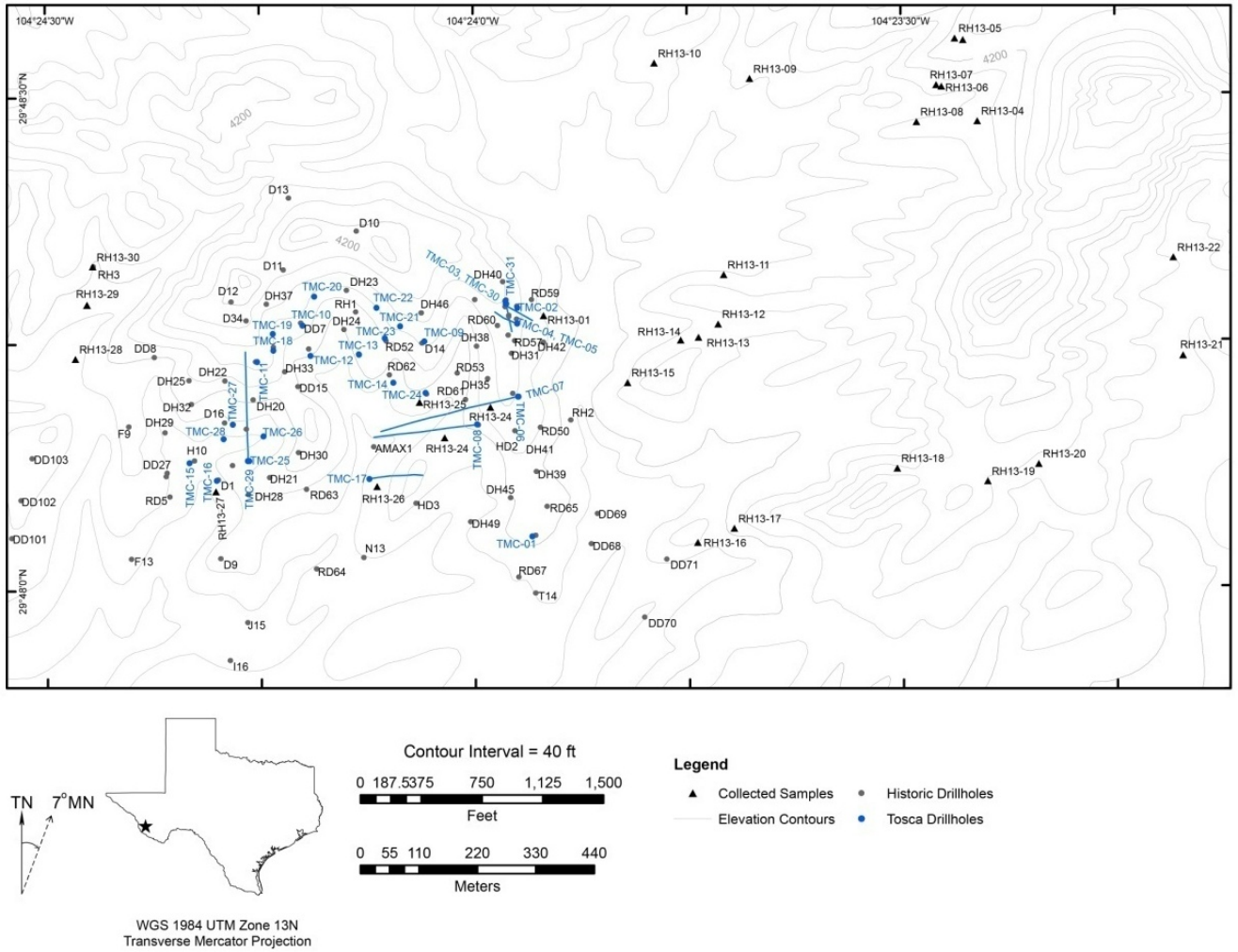

Figure 2.7. Collected field sample and drill hole location map in the Red Hills study area.

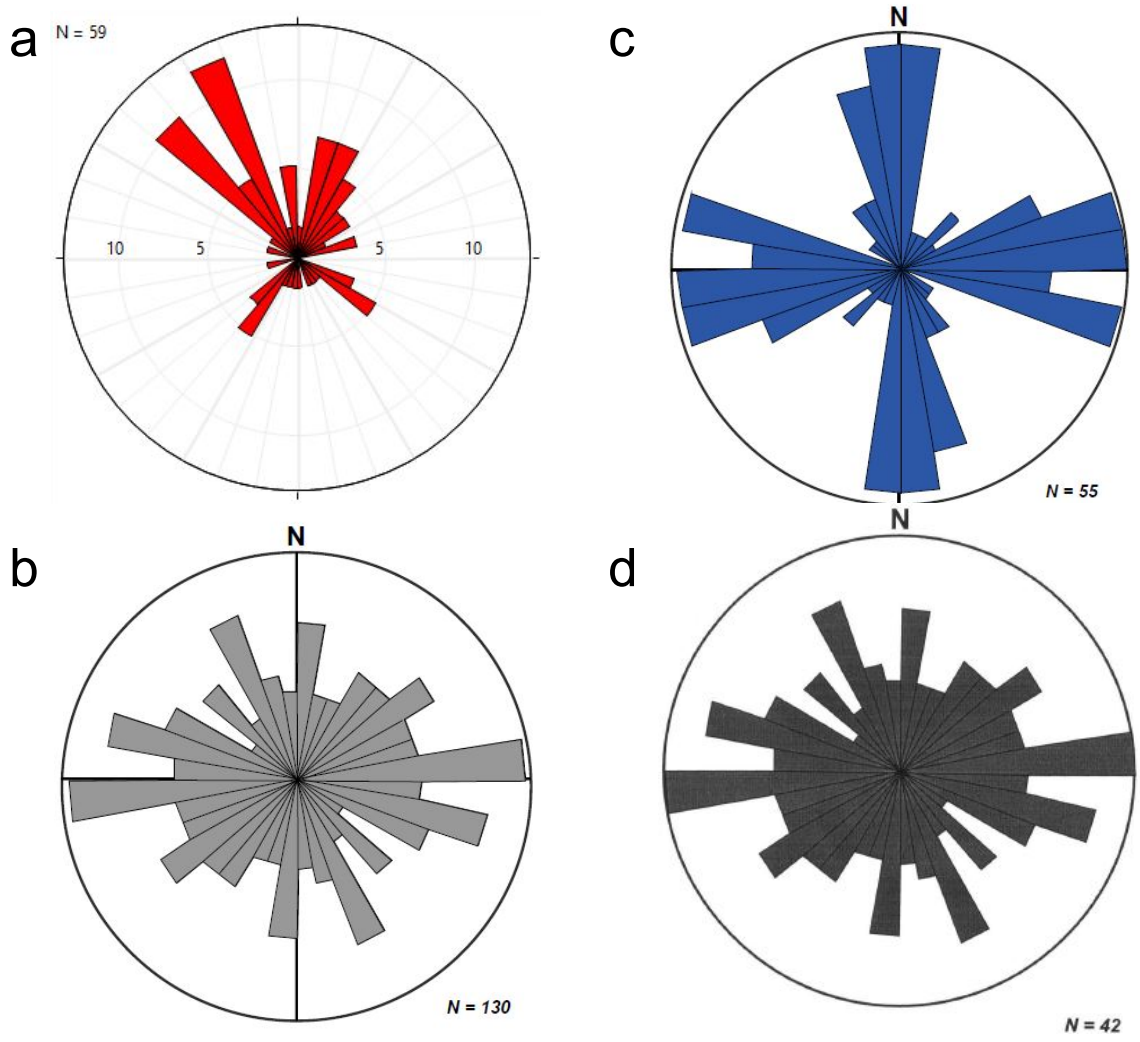

Figure 2.8. Rose diagrams of joint orientations. Each petal represents 10°. a.) Joint orientations in and around the Red Hills Study area showing a weak NW orientation. b.) Gilmer's (2001) orientations in and around the Red Hills study area showing a weak EW preferred orientation. Largest petal is 14°. c.) Gilmer's (2001) quartz vein orientations at Red Hills showing a weak EW and NS preferred orientation. Largest petal is 11°. d.) Gilmer's (2001) alunite vein orientations showing a weak E-W preferred orientation where the circle represents 11° of total alunite veins.

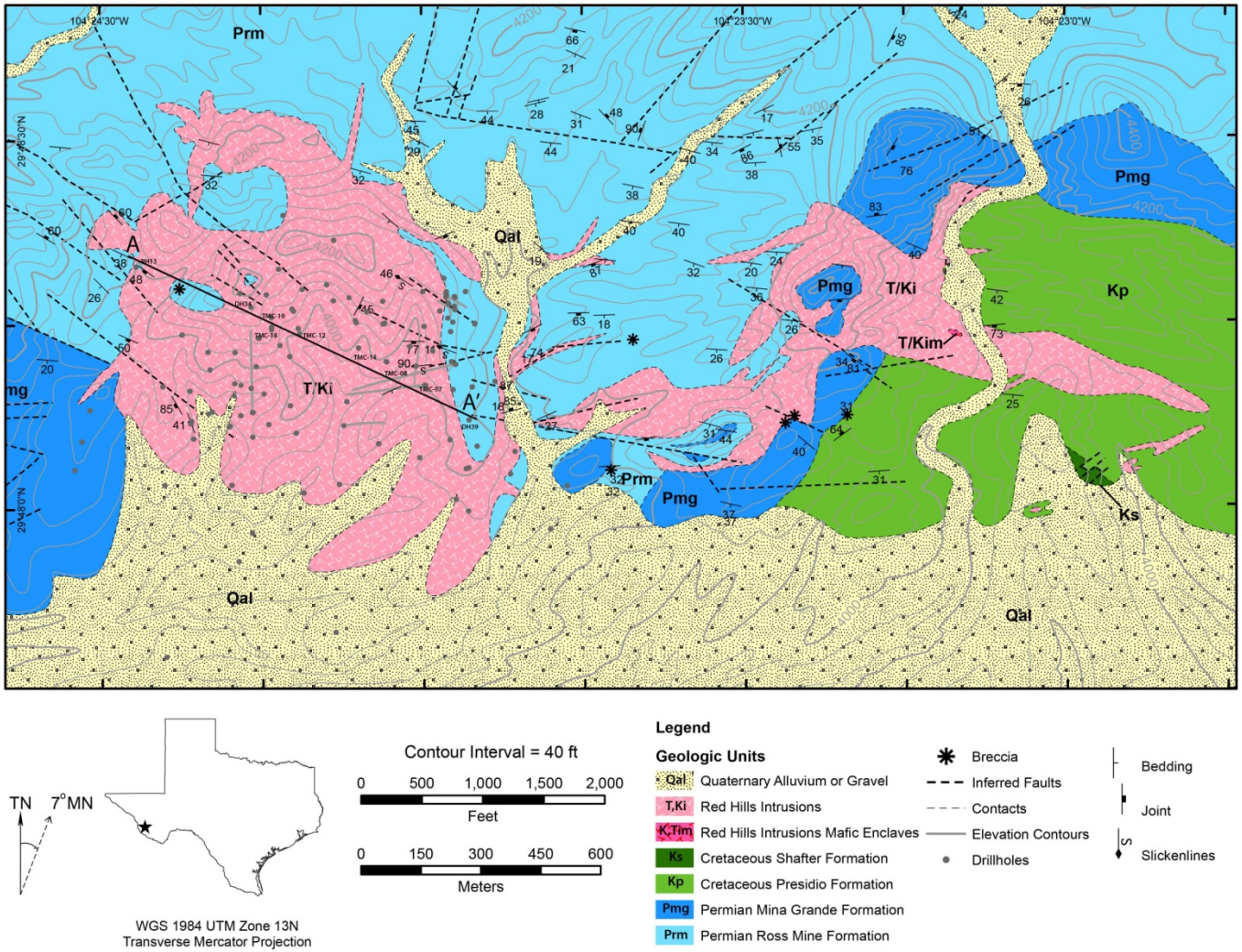

Figure 2.9. Local geologic structure map of the Red Hills study area. Figure modified from Gilmer (2001).

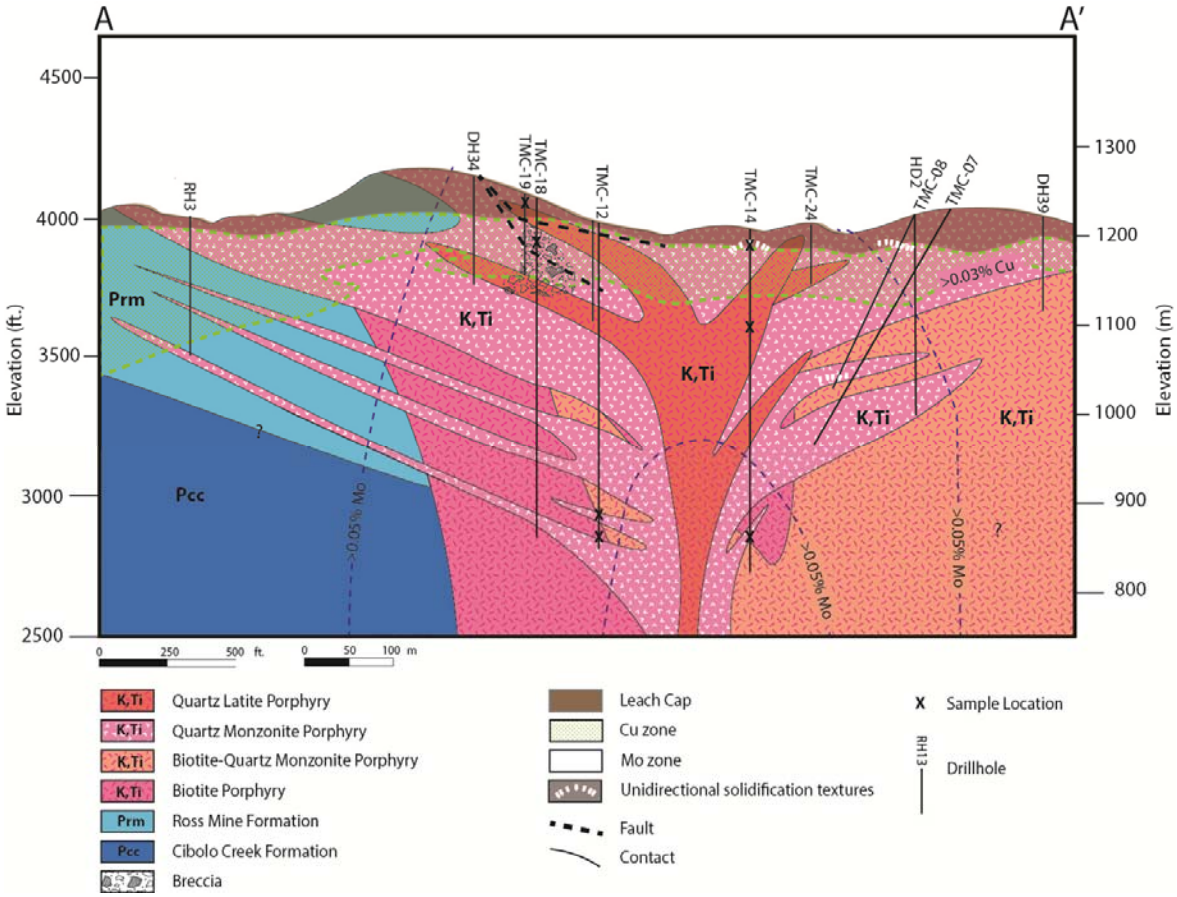

Figure 2.10. NW to SE cross section of the western area of the Red Hills deposit. Cross section A-A' shows multi-phase igneous intrusions having cylindrical geometries with a series of younger porphyry dike injections intruding into the Permian Ross Mine Formation and the Cibolo Creek Formation. The dashed green outline represent the thin chalcocite blanket of > 0.03% Cu and the blue dashed line represent the horse-shoe shaped molybdenum zone of > 0.05% Mo.

Chapter 3: Igneous Phases, Mineralogy, and Petrography

INTRODUCTION

The Red Hills porphyry Mo-Cu deposit is centered on an intrusive complex composed of ore-related Laramide porphyries. These porphyries range in composition from biotite-rich (BP) to biotite-quartz monzonite (BPQMP) to quartz monzonite (QMP) and quartz latite (QLP) phases, which are temporally and spatially linked to Cu-Mo mineralization. Granodiorite porphyry (GP) with mafic enclaves are unmineralized phases of the eastern Red Hills stock, and are temporally related to the western Red Hills stock. These intrusions were emplaced as massive stocks, dikes, and sills into an overlying Permian sedimentary sequence of siliciclastic and calcareous units of the Permian Ross Mine and Mina Grande Formation, as well as the Cretaceous Presidio Formation. Hornfels and local garnet skarns are located around the contact aureoles of the igneous bodies and are weakly enriched in Zn with trace amounts of Pb and Ag. Tertiary intrusions and volcanics of the Chinati Mountains Caldera bound the map area to the north and west.

Each porphyry intrusion has undergone a similar sequence of veining, whereby phyllic alteration has significantly overprinted early potassic alteration associated with all phases. This hypogene vein sequence, from early to late, consists of biotite veinlets (only in the BP), A quartz veins, B quartz-molybdenite veins, D pyrite veins, and late hypogene alunite veins. Detailed descriptions of these vein styles are covered in chapter 6.

All samples recovered from deep drill core were affected by hydrothermal alteration, so unaltered samples for each porphyry phase could not be obtained, except for the granodiorite porphyry and mafic enclave (Appendix A, Table A-2 and Table A-3).

Least altered samples were only found in outcrop, east of the mineralized complex (Figure 3.1). Descriptions of unaltered and altered phases are combined in this chapter. Biotite veinlets and A veins are associated with potassic alteration, where thin mm-scale K-feldspar alteration halos exist outside the margins of the vein. These K-feldspar halos are commonly altered to sericite by phyllic alteration overprint. Rare occurrences of this style of alteration have been found in B-veins as well. Coincident to potassic alteration is propylitic alteration, which extends laterally from the potassic core. Later stage phyllic alteration largely overprints and associated D-veins largely overprint potassic alteration.

SURPAC 3-D MODELLING OF IGNEOUS PHASES

Tosca's TMC drill holes were re-logged primarily using drill core photographs. Older drill holes were also re-logged based on lithologic descriptions due to the lack of drill core photographs available, which inherently allows for greater error in lithologic distribution across the intrusive body. These data were input into Surpac 3-D modelling software to examine the crude distribution of separate phases within the intrusive solid that extends 853 m (2,800 ft) north to south, 1400 m (4,600 ft) east to west, cut off at a 610 m (2,000 ft) maximum depth elevation, which Tosca previously outlined during reconnaissance studies. Tonnage and Mo/(Mo+Cu) values were not constrained to an ore-shell during estimation. Composite strings were created at 1-ft intervals based on numeric coding assigned to specified lithologies. Composite strings for Mo and Cu distribution among phase types were also created at 20-ft sample depths similar to Tosca's methodology according to their NI 43-101 report. A 20 ft x 20 ft x 20 ft block model of the intrusion and altered sedimentary units was created using the inverse distance estimation method applying a power of 2 and discretization values of 3 in the x, y, and z directions. The parameters of the search ellipse include: 500 ft maximum search distance

of the major axis, 300 ft maximum vertical search distance of the major axis, 1:3 semi-major to minor axis ratio, and a 12 and 2 maximum and minimum number of samples, respectively. Densities of the intrusions were averaged from the limited specific gravity measurements Tosca conducted during reconnaissance studies so constraining densities for each phase and alteration type could not be completed. Bulk specific gravity values from the NI 43-101 report for hypogene copper, the enrichment blanket, and hypogene molybdenum include 2.75 (average between the given range 2.13 to 3.37), 2.67, and 2.49 respectively. Based on the locations of available drilling information, the spatial extents for each phase are outlined in Figure 3.1, and Figure 3.2 shows a plan map of the intrusive phases at 3200 ft. The average Mo/(Mo+Cu) is 0.62 from ~5Bt of rock.

BIOTITE RICH PORPHYRY

The biotite-rich porphyry (BP) appears to be the oldest intrusive phase at the Red Hills (Figure 3.3a) and is the only phase that contains early flaky, hydrothermal biotite veinlets with K-feldspar halos indicative of potassic alteration, a feature unwitnessed by Gilmer (2001). This phase is only present at subsurface levels at deepest drill hole intercepts. Phenocryst modal percentages are 5-10% K-feldspar, 15-20% plagioclase, 2-3% magmatic biotite, 25% secondary biotite, and rare quartz with rutile, monazite, sphene, and xenotime accessory phases in 60-70% groundmass (Table 3.1). Sulfide phases from higher to lower abundances include pyrite, molybdenite, pyrrhotite, chalcopyrite, covellite, and bismuthinite.

BP and associated veins are typically truncated by BQMP and QMP phases where numerous xenoliths are typically found in younger porphyry phases (Figure 3.3b and Figure 3.5a). Contacts between these porphyries are sharp, with no chilled margins.

This dike is red-brown in color compared to other porphyries due to the presence of abundant phenocrystic and groundmass biotite (Figure 3.4 a, b).

At subsurface levels, BP extends 427 m (1,400 ft) from east to west and 344 m (1,130 ft) from north to south at 610 m (2,000 ft) maximum depth elevation, which is the deepest elevation of the intrusion 3-D solid. This phase likely extends deeper in the system. In plan view, it is continuous for 563 m (1,846 ft) along a 120° strike. All BP core intercepts appear mineralized and altered from phyllic overprinting or silicification. According to the crude Surpac block model, the BP contains the highest Mo grades with the largest tonnages, which correlate to the high densities of quartz veins, and the second lowest average copper grades for the largest tonnage. The BP makes up ~63% of the total volume of the intrusion at 0.74 Mo/(Mo+Cu) ratio. Vein truncation relationships and 10-45% decrease in grades at contact with later porphyries indicate the high grades in BP are not the result of overprinting by magmatic-hydrothermal fluids from a younger porphyry intrusion.

BIOTITE QUARTZ MONZONITE PORPHYRY

Biotite-quartz monzonite porphyry (BQMP) vaguely mimics the Mo outline of the Red Hills stock at subsurface levels, but similar to the Mo outline, this may be due to a lack of drilling. This phase appears to be dipping to the NE along a 156° strike. BQMP dikes span from approximately 640 m (2,100 ft) from east to west and 579 m (1,900 ft) from north to south at a 808 m (2,650 ft) maximum elevation. BQMP is found near sharp or gradational contacts of BP (Figure 3.5a). BQMP contains 50-70 vol. percent of medium to coarse grained phenocrysts, comprised of 10-20% K-feldspar, 20-25% plagioclase, 5% biotite, and 1-2% quartz occasionally in the form of quartz eyes with rutile, xenotime, monazite, apatite, zircon, and ankerite accessory phases in 30-50%

groundmass (Table 3.1). Feldspar phenocrysts have been altered to green sericite by phyllic alteration, except for megacrystic K-feldspar that remain moderately unaltered (Figure 3.5b). Most biotite phenocrysts have inclusions of quartz, rutile, apatite, magnetite, hematite, and sulfides along basal cleavage planes. The edges of phenocrystic biotite are commonly frayed and are partially recrystallized or altered to chlorite (Figure 3.6 a, b).

The matrix is largely composed of anhedral quartz, feldspar, and calcite, clusters of secondary biotite, sericite, apatite, monazite, rutile, and sphene. Sulfide phases present in the BQMP from increasing to decreasing order include pyrite, molybdenite, chalcopyrite, bornite, covellite, and sphalerite. Disseminated pyrite (300 – 50 μm) and rare chalcopyrite (150 - 50 μm) exist within phyllically altered groundmass and along cleavage planes in magmatic biotite. Chalcopyrite and pyrrhotite inclusions (10-30 μm) with rutile exist in disseminated pyrite and pyrite veins. Disseminated chalcopyrite contains bornite exsolution lamellae and rims of covellite and sphalerite. The Surpac block model reported this phase maintains lowest average copper grades and tonnages and the second lowest molybdenum grade at higher tonnages. The BQMP contributes 16% of the total intrusive volume at a ratio of 0.78 Mo/(Mo+Cu).

Xenoliths of silicified BQMP with truncated quartz-molybdenite veinlets within phyllically altered BQMP have been observed, which may suggest at least two pulses of BQMP injections. Because biotite phenocrysts are homogenous, this suggests that crystallization of igneous biotite occurred over a limited range of conditions. The biotite that last crystallized from the melt is represented by the protrusions of biotite phenocrysts, interpreted as overgrowths that crystallized contemporaneous with the aplitic groundmass of the porphyry. The overgrowths on biotite phenocrysts may have formed under conditions different from the main part of the phenocryst. Based on the

amount of biotite present, the dissolved water content in the melt would roughly be 4 to 6 weight percent (Holland, 1972). Biotite geochemistry modelling in porphyry environments by Jacobs and Parry (1979) concluded that resilient, fresh magmatic biotite can bypass hydrothermal destruction if phenocystic biotite reequilibrates with the hydrothermal solution within the annite-phlogopite-eastonite-siderophyllite solid solution stability field. In order for this to happen, a low pH solution must have varying concentrations of Fe and Mg to compensate for the loss of H^+ ions during the initial destruction of biotite while the solution is in equilibrium with muscovite. Thus, the composition of the hydrothermal fluid is the controlling factor for biotite stable phases assuming isothermal and isobaric conditions.

QUARTZ MONZONITE PORPHYRY

Quartz monzonite porphyry (QMP) is a non-biotite-bearing phase of BQMP, and is the second most voluminous phase within the Red Hill stock. This phase spans from 823 m (2,700 ft) from east to west and 838 m (2,750 ft) at a maximum elevation of 792 m (2,600 ft). Surface exposure of QMP in the western, mineralized part of the research area has been altered by phyllic and argillic alteration with local zones of intense silicification that is usually concentrated around wallrock contacts and faults. This phase extends to the eastern lobe that is generally unmineralized beyond the extent of the barren propylitic alteration zone. QMP contains 40-60% groundmass and 45-60% phenocrysts of 12-15% K-spar, 35-40% plagioclase, and 2-3% quartz in the classic form of quartz eyes found in hydrothermal systems (Table 3.1). Rims of coarse K-spar and plagioclase phenocrysts are often corroded (Figure 3.7a). Accessory phases include apatite, monazite, xenotime, rutile, and zircon.

Magmatic biotite is virtually absent, but where present is compositionally similar to BQMP. Contacts between the BQMP are gradational and based on drill hole cross section interpretations, the QMP appears to be a series of repeated dike injections that cut through the BP and BQMP. Dikes and sills exposed on the surface are interpreted to be part of the QMP or the quartz latite porphyry.

The QMP contains the second largest average copper and molybdenum grades. Despite the relatively higher molybdenum grade, the lowest tonnage of all porphyry phases. However, the QMP has the second largest tonnages for copper. This phase contributes roughly 13% of the total volume of the intrusive solid at a ratio of 0.58 Mo/(Mo+Cu).

QUARTZ LATITE PORPHYRY

Quartz latite porphyry (QLP) dikes cut through all previous porphyry phases and appear to be the volumetrically largest porphyry intrusion, although this may be a product of different logging styles of historic drill holes. This phase also displays a horse-shoe shape geometry, and is abundant near the eastern and western margins of the western stock, as well as the shallow levels of the deposit. According to the Surpac block model, this phase covers an area spanning 1,417 m (4,650 ft) from east to west and 884 m (2,900 ft) from north to south at a maximum elevation of 838 m (2,750 ft). The Surpac block model revealed that this phase contains the highest average copper grade compared to the older phases. It must be noted, however, that this phase is at the shallowest levels of the deposit, where supergene Cu enrichment may account for the elevated copper grades within the defined boundaries of the Surpac intrusive solid. The QLP has the lowest average molybdenum grade and contributes 8.5% of the total intrusive volume at a ratio of 0.37 Mo/(Mo+Cu).

The QLP consists of 30-40 vol. percent phenocrysts and 60 to 70 vol. percent matrix (Figure 3.7b). Relative abundances of phenocrysts display 20-35% fine-grained feldspars (predominantly plagioclase as noted by Gilmer (2001)) with rare quartz eye ocelli and rare biotite (Table 3.1). Although weakly altered by propylitic alteration, sample RH13-20 shows concentrically zoned orthoclase with chloritic reaction rims. Plagioclase appears to display sieve textures within the core of the grains, but this may be a product of sausseritization. Feldspar phenocrysts and ground mass phenocrysts appear randomly oriented with no apparent flow pattern. Gilmer (2001) described the QLP as an earlier phase that chilled quickly and was recombined with the protrusion of QMP. Based on cross cutting relationships in drill core, the QLP instead appears to be a late phase that concludes the trend of increasing groundmass abundance through the succession of porphyry intrusions at Red Hills.

QLP in shallow levels of the deposit (1,219 to 1,127 m elevations or 4,000 to 3,700 ft elevations) contain disseminated pyrite and copper sulfides. Copper sulfides are commonly anhedral chalcopyrite cores with bornite exsolution lamellae and chalcocite rims, a likely result of supergene alteration. Euhedral pyrite disseminations contain polymetallic sulfide inclusions, such as sphalerite, galena, bismuthinite, covellite, and molybdenite.

GRANODIORITE PORPHYRY

The barren, granodiorite porphyry (GP) crops out only at the surface in the unaltered zone, east of the propylitic alteration halo. Phenocrysts and megacrysts comprise approximately 40-55% of the rockmass, compared to the pink-brown groundmass (Figure 3.9a). Mineral modal percentage estimates include 25-30% plagioclase, 5-10% K-feldspar, 2-3% quartz, 3-5% biotite (book biotite), 2-3%

hornblende, and 1% magnetite, all within a 45-60% matrix (Table 3.1). The groundmass is composed of quartz, feldspars, disseminated magnetite and hematite. Feldspars ranges in size from 3 mm to 4 cm. Poikilitic textures occur in subhedral K-feldspar megacrysts that contain anhedral K-feldspar oikocrysts with embayed grain boundaries (Figure 3.10a). Euhedral plagioclase is characterized by albite twinning, while quartz is partially resorbed and embayed with fine-grained mafic rims (Figure 3.10b and Figure 3.11a). The fine-grained groundmass points to a high nucleation rate triggered by strong undercooling of the acidic magma. This phase is mostly unaltered except at contacts with mafic enclaves that are affected by propylitic alteration. Mafic phases, such as hornblende and biotite, have been partially replaced by epidote and calcite. This phase may represent the unaltered BQMP based on similar mineralogies and phenocryst to groundmass ratio.

Vernon (1984) interpreted the formation of K-feldspar oikocrysts to derive from delayed crystallization after magma mixing, reflecting that the quenching temperature was higher than the saturation temperature for a given mineral and that growth rates became considerably slower. Castro et al. (1991) conclude that the oikocrysts imply a time gap between magma mixing and the onset of their recrystallization as well as recording the attainment of thermal equilibrium between felsic and mafic phases.

MAFIC ENCLAVES

Ovoid, approximately 8 cm in diameter, dark mafic microgranular enclaves (MME) are interpreted to be a product of comingling and quenching of a mafic melt with the granodiorite porphyry magma. The rounded, cuspate shapes of the enclaves appear to be primary, rather than from rounding of angular, solid fragments, globules of magma while the granodiorite magma was flowing. Contacts between the two units are sharp with no apparent chilled margins. This unit is composed of fine-grained, mafic-dominate

phases, such as hornblende and biotite with rare quartz ocelli (Figure 3.9b). Modal compositions of the mafic enclaves include rare K-feldspar, 10-20% plagioclase, 15-20% hornblende, up to 2-4% biotite, and 1% quartz within a groundmass which comprises 60 to 80 vol. percent of the rock mass. The relatively fine-grained microstructures (Figure 3.11b) indicate relatively rapid crystallization from quenching of magma in the plutonic environment. Vernon (1984) explains that the more mafic magma with crystallize more rapid (forming finer-grained aggregates) than the felsic magma, because it is more undercooled. Once the two have reached equilibrium, a marked increase in nucleation rate and marked decrease in growth rate will occur. The presence of apatite needles, indicative of magma quenching, also supports this idea. Fe-rich chlorite, calcite, and Fe-oxides also exist largely within the groundmass, but these are likely secondary alteration minerals by propylitic alteration.

The distribution of MME's is irregular and not widely abundant. They appear concentrated in swarms located in the eastern, unaltered portion of the study area. The mineral assemblages in the enclaves are generally the same as those in the host granodiorite, but the proportions and compositions of the minerals are different. Samples from this unit have been affected by propylitic alteration as seen by the conversion of biotite to Fe-rich chlorite and hornblendes to Fe-oxides. All feldspars have been texturally obliterated and the matrix has been replaced by actinolite, calcite, and epidote with magnetite and hematite disseminations.

UNIDIRECTIONAL SOLIDIFICATION TEXTURES

Unidirectional solidification textures (UST) are primarily observed within QLP and QMP. "Brain rock" is the most common UST at Red Hills, and comprise of rhythmic, crenulate layering of comb quartz and aplitic material (Figure 3.8 a and b).

These textures are restricted to the lower SE corner of the western Red Hills stock, spanning from 76 m (250 ft) east to west and from 214 m (700 ft) from north to south along a 185° strike. UST textures have been identified at 884 m (2,900 ft) elevations, 930 m (3,050 ft) elevations, 1,006 m (3,300 ft) to 1,047 m (3,435 ft), and 1198 m (3,930 ft) to 1,192 m (3,910 ft) elevations. Occurrences of UST's have been observed in the BQMP, QMP, and QLP, but not in the BP, which suggests that this texture is not restricted to any particular phase at Red Hills. Reasons for their spatial distribution at Red Hills is unclear because they show no relationship to lithology, structure, or alteration.

UST textures commonly form near the upper contact of crystallizing plutons and are interpreted to form by pressure fluctuations during the magmatic to hydrothermal transition (Cannell et al., 2005; Kirkham and Sinclair, 1988; White et al., 1981). White et al. (1981) first reported the occurrence of UST's from the Henderson porphyry-Mo deposit, which represented marker beds for high-grade ore just below the UST's. This feature is not the case at Red Hills. UST's are interpreted to represent the boundary between the magmatic to hydrothermal transition from crystallizing porphyry stocks near the apex of the cupola. The C-axes of euhedral quartz layers are reported to point toward the direction of the crystallizing pluton.

UST's at Red Hills occur as discontinuous pods and lenses which may be as thin as a meter in thickness. The thickest occurrence of UST's was 7.5 m at 382-389.5 m (1,252-1,276 ft) down hole of TMC-7. No obvious spatial relationship exists between UST occurrences and phases at Red Hills, but the fact that UST's appear to occur in thin, alternating contacts between QMP and QLP could argue that these textures occur near the transition to volumetrically higher groundmass phases.

Aplitic layers mostly contain fine-grained muscovite and feldspar with disseminated pyrite. Pyrite commonly contains micron-sized inclusions of anhydrite. bismuthinite, chalcopyrite, molybdenite, apatite, rutile, zircon, monazite, and xenotime.

DISCUSSION AND CONCLUSION

Like many porphyry systems in the southwestern United States, the Red Hills porphyry deposit is a multiphase igneous system that became increasingly felsic with more abundant groundmass with each successive intrusion. The proportion of biotite also decreases with the younger porphyries. UST's found at Red Hills are irregular, discontinuous lenses or pods that are largely restricted to the west-central area of the mineralized stock in narrow drill intercepts. Their occurrences do not appear to be significant in terms of metal sulfide concentrations. Mafic enclaves within the granodiorite do not appear to contribute to mineralization based on the lack of sulfides as seen in thin section. This suggests that the granodiorite and associated enclaves were emplaced after Mo and Cu mineralization.

Based on crude block modelling of the lithologies present at Red Hills, the BP contained the largest average molybdenum grade with the largest tonnage, while the highest average copper grade was found in the QLP within the intrusive solid and did not include the copper enrichment blanket. Geometries of these phases appear obscure and unusual, but this is likely due to a lack of control on lithologic conversions of older drill core and a lack of drill coverage in certain areas of the deposit.

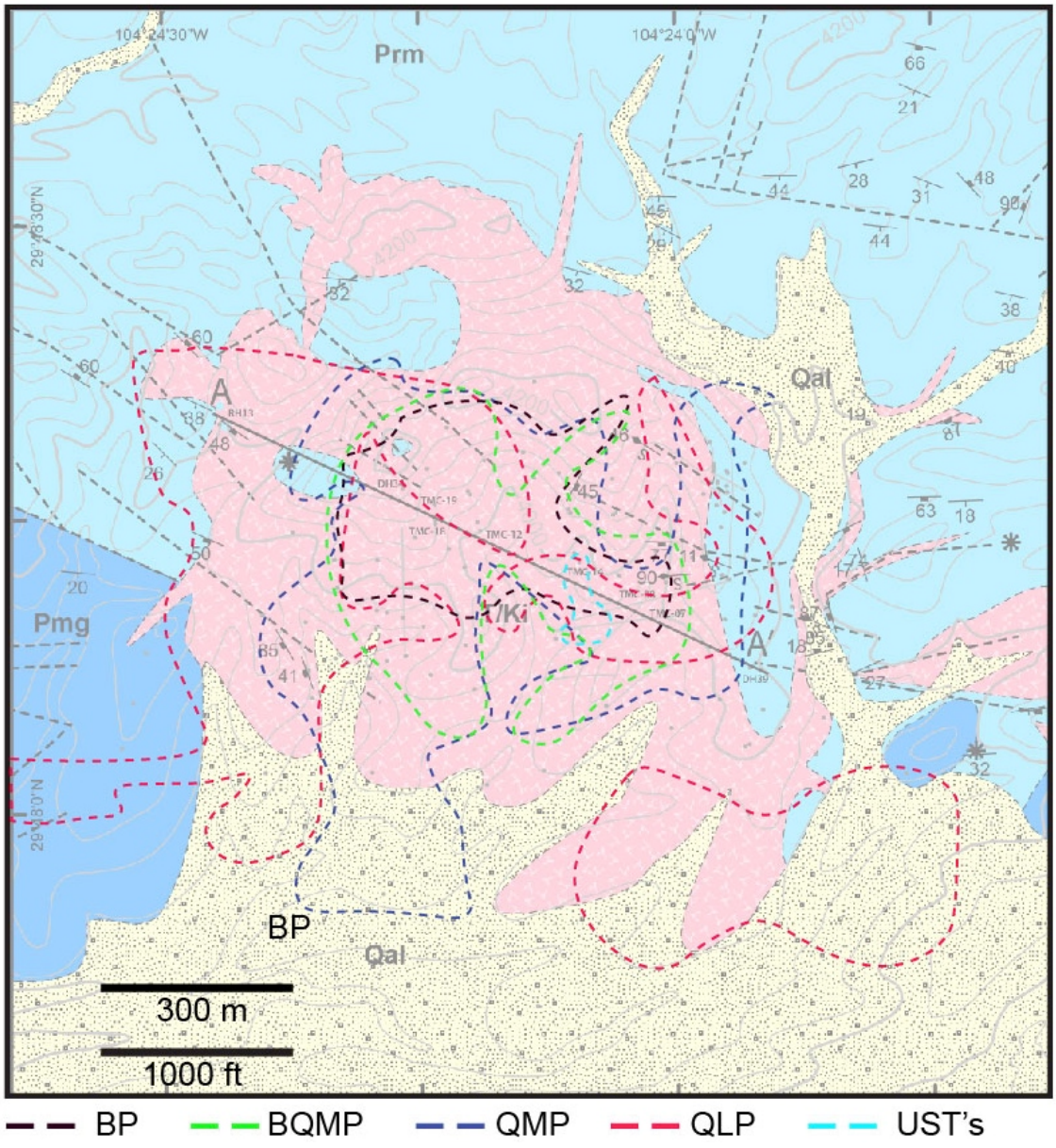

Figure 3.1. Outlines of the porphyry phases at Red Hills. Outlines of each phase are stacked on top of each other and projected onto the surface. Modified from Gilmer (2001).

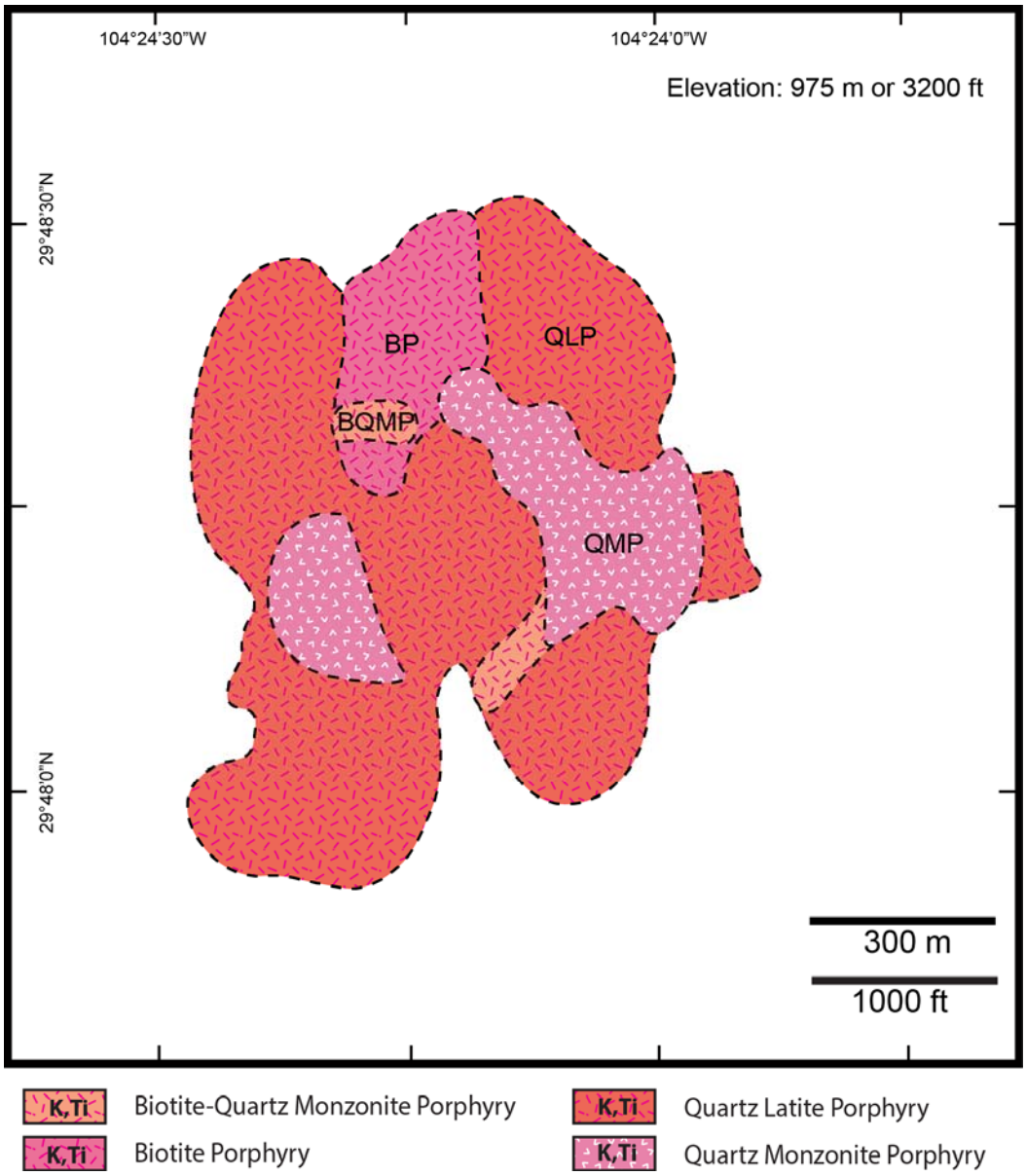

Figure 3.2. Plan map of intrusive phases at 975 m (3,200 ft).

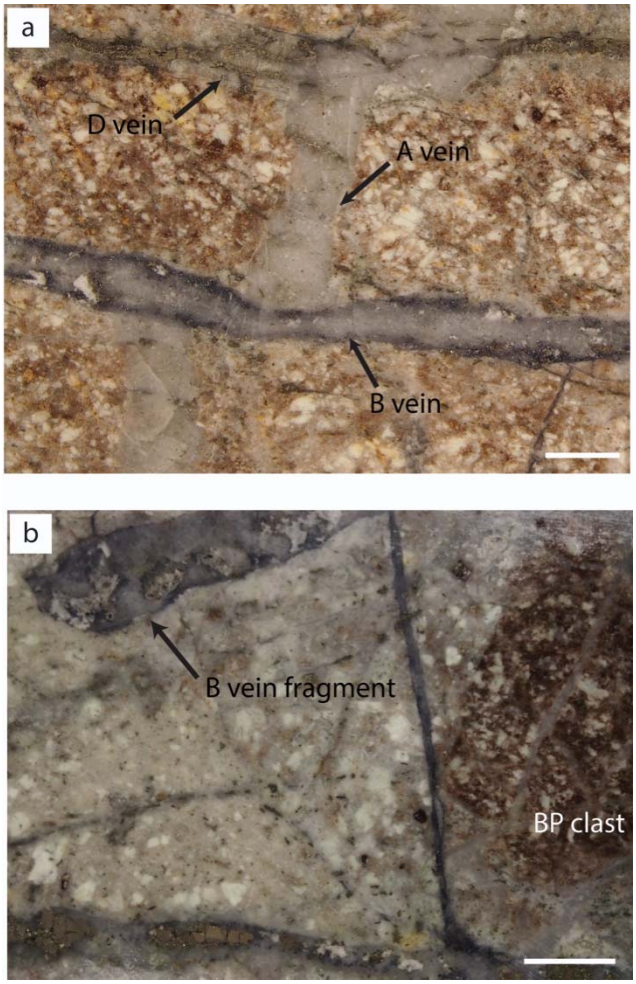

Figure 3.3a. Slab of biotite porphyry (BP) from sample TMC12-1075 displaying pervasive hydrothermal biotite groundmass and feldspar phenocrysts which have been altered to sericite by phyllic alteration. An early quartz A-vein is offset by a quartz-molybdenite B vein and a pyritic D vein. White scale bar represents 1 cm.

Figure 3.3b. Slab of biotite quartz monzonite porphyry (BQMP) from sample TMC12-1075 displaying fresh, coarse biotite phenocrysts with corroded feldspars altered to sericite embedded within a quartz-feldspar-sericite groundmass with disseminated pyrite. A BP xenolith is encased within the BQMP indicating that the BP is inherently older in age. A B vein fragment is floating within the QMP indicating that the magma continued to circulate after quartz-molybdenite stockwork fracturing occurred. White scale bar represents 1 cm.

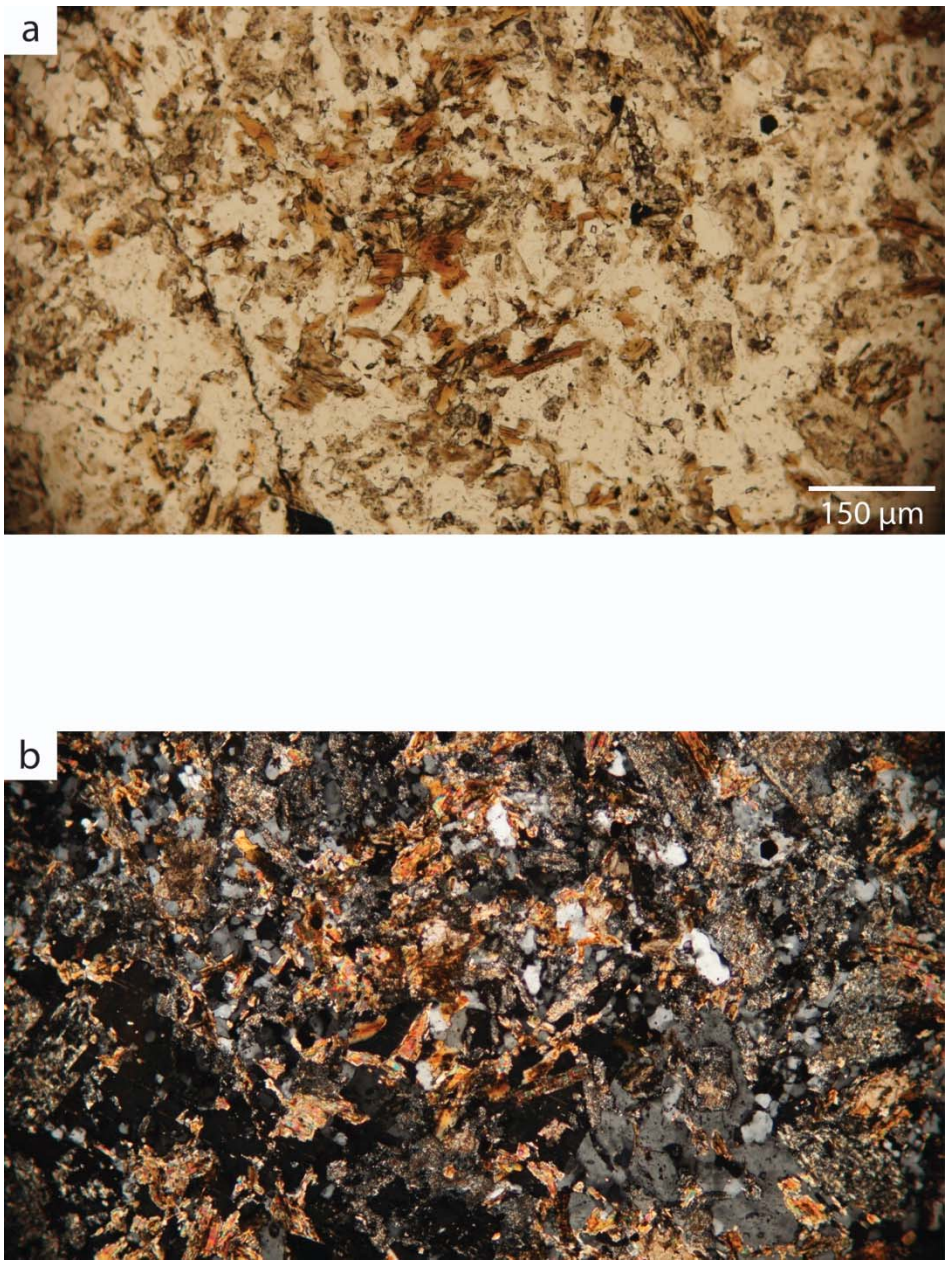

Figure 3.4a. Photomicrograph in plane-polarized light of hydrothermal biotite phenocrysts in BP from sample TMC12-964.

Figure 3.4b. Photomicrograph in cross-polarized light showing sericite, quartz, and feldspar groundmass in BP from sample TMC12-964.

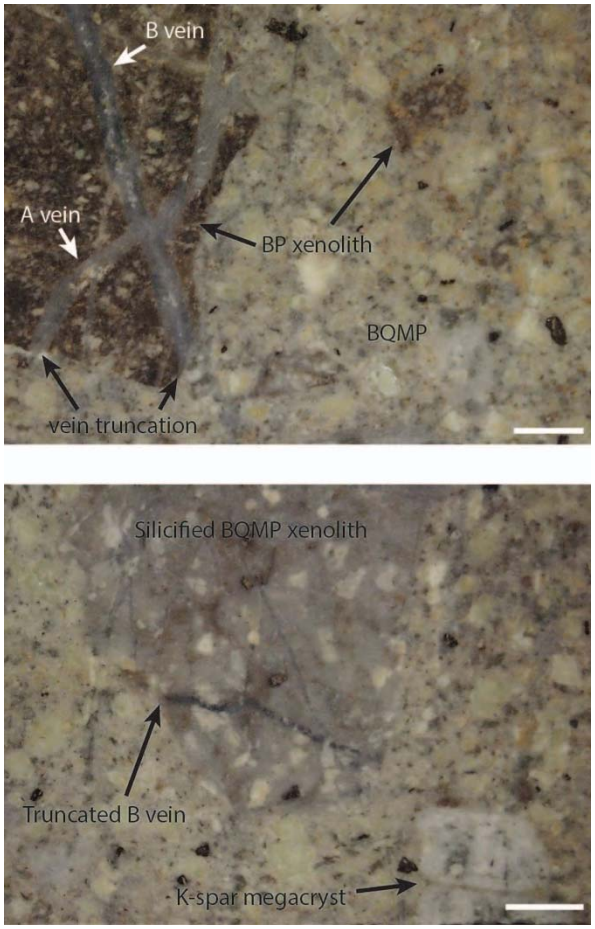

Figure 3.5a. Slab of BP xenoliths within BQMP from sample TMC12-964. BP xenolith to the left of the image contains a barren quartz A vein and a quartz-molybdenite B vein which is truncated at the contact of BQMP. This indicates BP experienced a separate mineralization episode prior to the emplacement of BQMP. White scale bar represents 1 cm.

Figure 3.5b. Slab of rounded, silicified BQMP xenoliths within phyllically altered BQMP from sample TMC12-964. A quartz-molybdenite B vein within the silicified BQMP xenolith suggests this phase experienced mineralization associated with silicification, perhaps near a large structure, but maintained plasticity for continued circulation within the crystal mush as more solid, silicified fragments are dislodged and transported from their original position in the magmatic stock K-feldspar megacrysts within the BQMP are relatively fresh compared to smaller feldspar phenocrysts which have been altered to green sericite by phyllic alteration. White scale bar represents 1 cm.

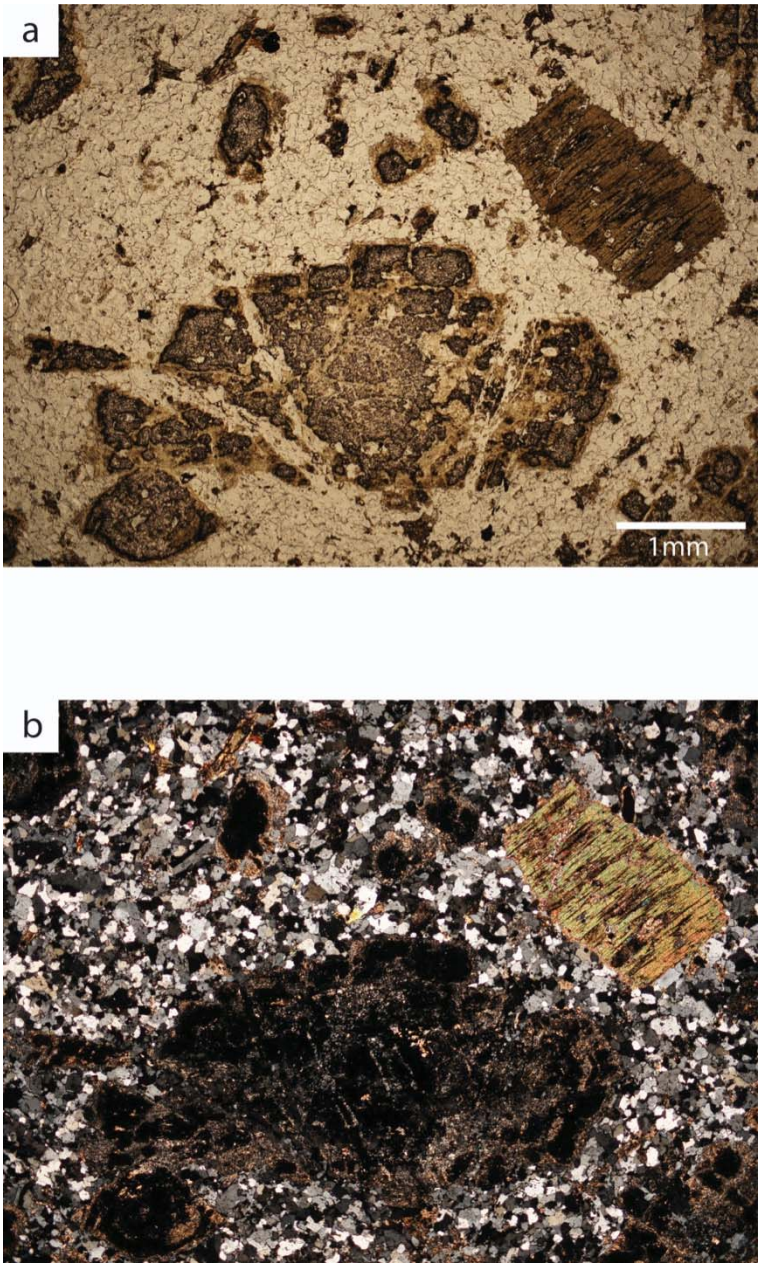

Figure 3.6a. Photomicrograph in plane-polarized light of silicified BQMP in phyllically altered and silicified sample TMC17-1245. Feldspar phenocrysts are fragmented with corroded edges rimmed by green sericite.

Figure 3.6b. Photomicrograph in cross-polarized light of figure 3.4a in sample TMC17-1245 displaying fine-grained quartz groundmass. Coarse-grained, euhedral biotite to the upper right of the image is slightly altered with calcite, hematite, precipitating along cleavage planes.

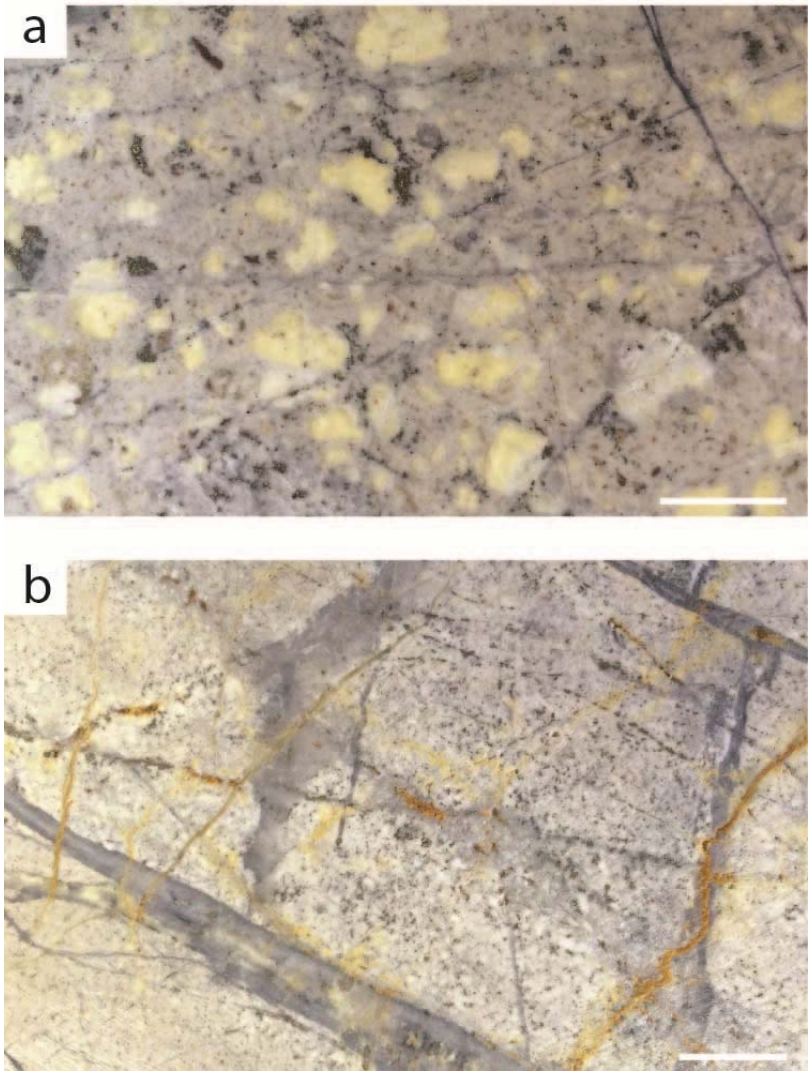

Figure 3.7a. Slab of QMP from sample TMC15-196 showing corroded rims on feldspars. White scale bar represents 1 cm.

Figure 3.7b. Slab of QLP from sample TMC19-32a. White scale bar represents 1 cm.

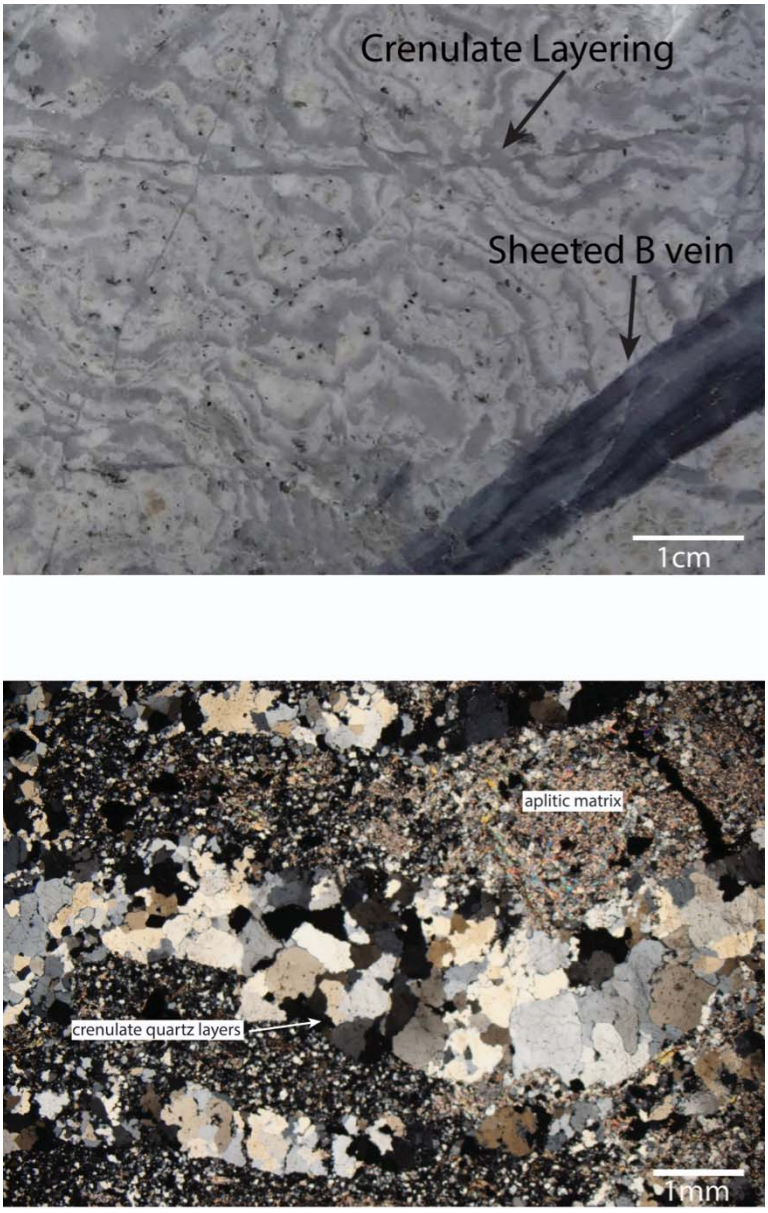

Figure 3.8a. Slab of brain rock from sample TMC14-31b. Rhythmic layering of crenulate quartz and aplite bands with disseminated pyrite are cut by a sheeted quartz-molybdenite B vein.

Figure 3.8b. Photomicrograph in cross-polarized light from sample TMC14-31b displaying comb textures in the upper portion of the crenulate quartz layers with coarser-grains on the other end projecting into the aplitic groundmass composed of fine grained quartz, feldspar, and sericite.

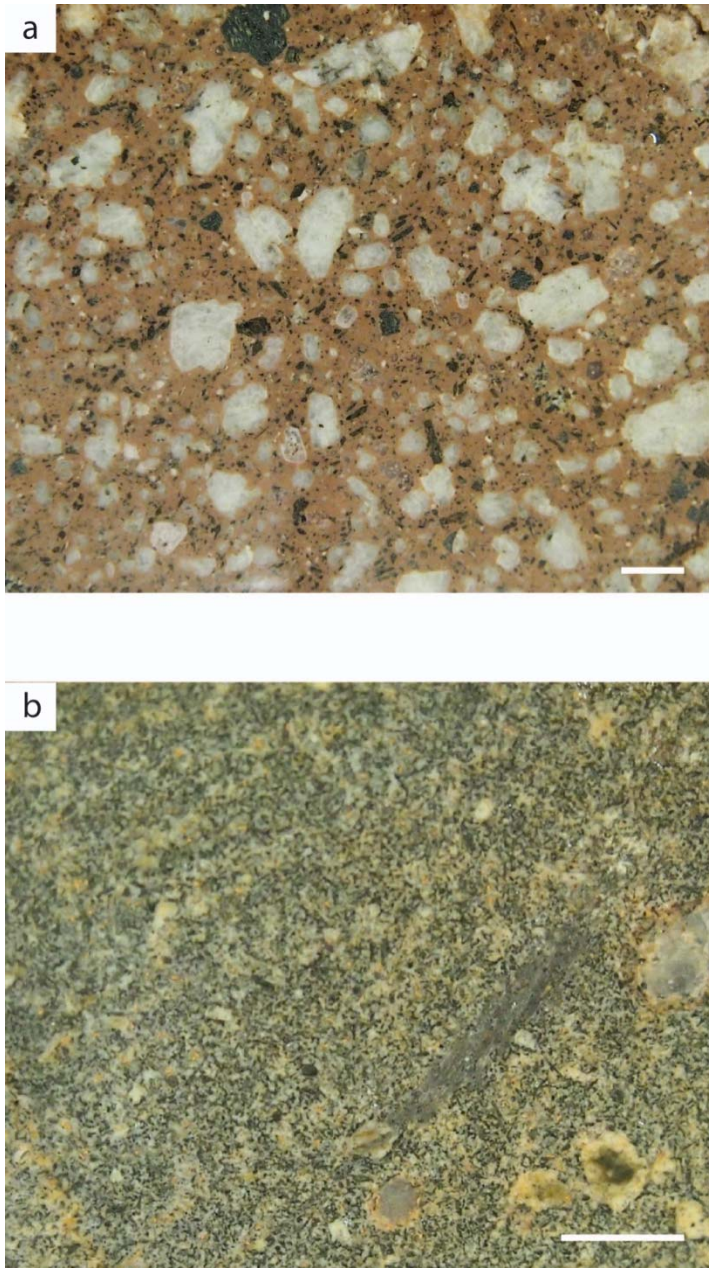

Figure 3.9a. Slab of unaltered granodiorite porphyry from sample RH13-21. Subhedral feldspar, hydrothermal (book) biotite, hornblende, and anhedral quartz eye phenocrysts are encased within a red-brown fine-grained groundmass. White scale bar represents 1 cm.

Figure 3.9b. Slab of microgranular mafic enclave from sample RH13-21b which has been affected by propylitic alteration. White scale bar represents 1 cm.

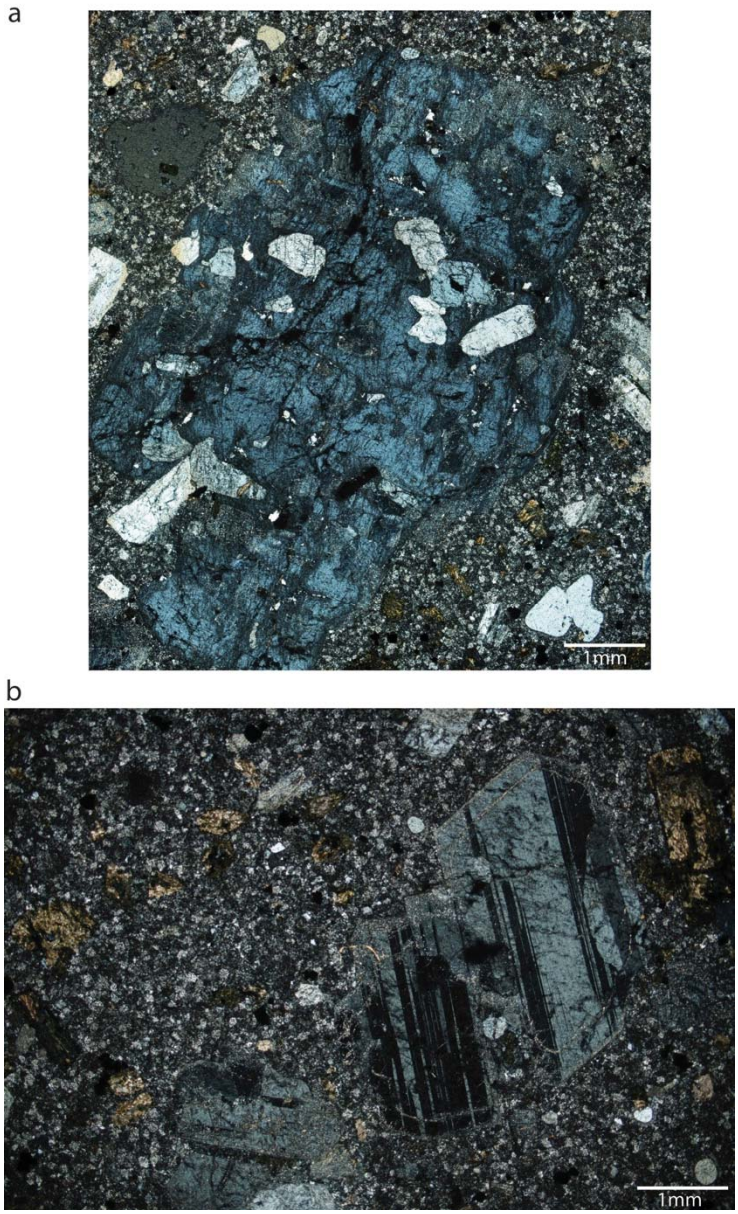

Figure 3.10a. Photomicrograph in cross-polarized light from sample RH13-21 displaying poikilitic texture of K-spar megacrysts encapsulating anhedral, k-spar oikocrysts. Amoeboid quartz grains in the lower right corner of the image display significant embayments along grain boundaries which are rimmed by fine-grained feldspar.

Figure 3.10b. Photomicrograph in cross-polarized light from sample RH13-21 displaying albite twinning in weakly altered plagioclase phenocrysts and minor epidote encased within a quartz-rich groundmass.

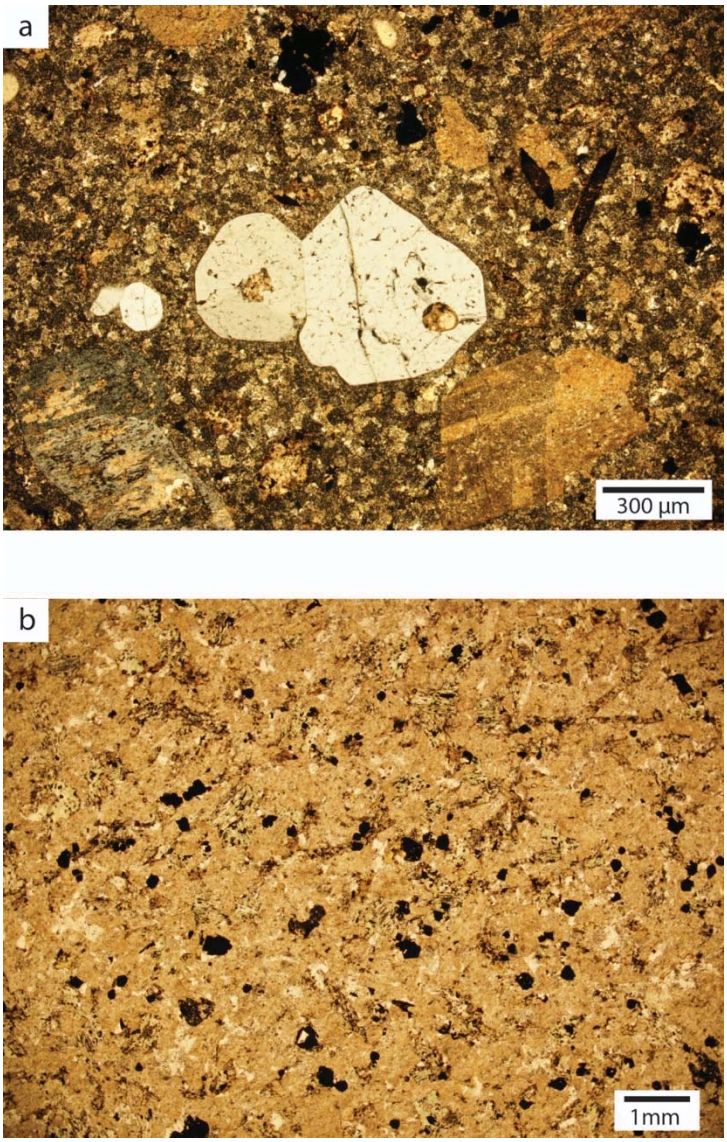

Figure 3.11a. Photomicrograph in cross-polarized light of intergrown quartz-eye phenocrysts with embayed grain boundaries in mildly unaltered QMP from sample RH13-31. Corroded feldspars are partially altering to sericite and hornblende has been replaced by iron oxides.

Figure 3.11b. Photomicrograph in plane-polarized light of mafic enclave from sample RH13-21b. Fine-grained mafic minerals have been converted to green chlorite, calcite, and epidote by propylitic alterations. Anhedral opaque minerals are magnetite.

Table 3.1. Mineralogical Characteristic of the Red Hills Intrusive Phases

Mineralogical Characteristics of Red Hills Intrusive Rock-Types

	Phenocryst vol. %						
	K-feldspar	Plagioclase	Hornblende	Biotite[1]	Quartz	Pheno vol.%	GM vol.%
BP	5-10	15-20	1-3	2-3, 25 hydrothermal	Rare	30-40	60-70
BQMP	10-20	30-35	Rare	5	1-2	50-70	30-50
QMP	12-15	35-40	Rare	Rare	2-3	45-60	40-60
QLP	5-10	15-25	3-5	Rare	Rare	30-40	60-70
GP	5-10	25-30	2-3	3-5	2-3	40-55	45-60
MME	Rare	10-20	15-20	2-4	1	20-40	60-80

Percentage charts were used to visually estimate mineral abundances in sawn slabs and thin sections: no point counting was carried out

Abbreviations: BP = biotite porphyry, BQMP= biotite quartz monzonite porphyry, GM = groundmass, MME = mafic enclave, Pheno = phenocryst, GP= granodiorite porphyry, QLP= quartz latite porphyry, QMP = quartz monzonite porphyry

[1]Magmatic, book biotite

Chapter 4: Geochemistry and Geochronology

INTRODUCTION

Whole rock and trace element geochemical analyses were carried out by ICP-MS (Inductively Coupled Plasma – Mass Spectromer) by third party, ACME labs (Appendix C). Six altered and unaltered samples from the newly identified phases, including phyllically altered biotite porphyry (BP) and biotite quartz monzonite porphyry (BQMP), brain rock, and unaltered granodiorite porphyry and mafic enclave xenoliths were analyzed. Two igneous samples from Shafter, one surface sample and one drill core sample, were also analyzed with the Red Hills samples (Appendix C, Table 1). This was carried out to compare and contrast Gilmer's 2001 data on surficial Red Hills samples as well as neighboring igneous units from the Tertiary Chinati Mountains Caldera, Pinto Canyon, and Shafter areas (Cepeda, 1977; Price et al., 1986; Cameron and Cameron, 1986; Henry, 1992; Cepeda and Henry, 1983; James and Henry, 1993; Gilmer, 2001). All geochemical data was input into Reflex ioGAS software for plotting purposes.

The identification of new igneous phases within the new drill core prompted the question of temporal differences among these units versus the previous crystallization age of Gilmer (2001). Using the U-Pb method on zircons from phyllically altered surface samples of the Red Hills quartz monzonite porphyry, RH24, and yielded an age of 64.2 $\pm$ 0.2 Ma Gilmer (2001). Gilmer et al.'s (2003) reported a sericite $^{40}Ar/^{39}Ar$ age of 61.58 $\pm$ 0.34 Ma and Re-Os age for molybdenite at 60.2 $\pm$ 0.3 Ma (Gilmer, 2001), suggesting that magmatism at Red Hills was sustained for at least 4 Ma. Zircons for U-Pb dating were separated from the phyllically altered BQMP in sample TMC17-1245 and the unaltered QLP surface sample, RHS-105, located east of the deposit (Appendix A, Table A-2) to compare the results of Gilmer (2001) and Gilmer et al.'s (2003) geochronology data.

WHOLE ROCK GEOCHEMISTRY

Previous work by Gilmer (2001) showed that the western and eastern parts of the Red Hills intrusive complex were part of the same geochemical affinity, which was initially obscured by thick alluvial cover between the two. In order to distinguish the degree of alteration of available sample data, these data were plotted on the Ishikawa alteration index (AI) versus advanced argillic alteration index (AAAI) diagram (Figure 4.1). Phyllically altered samples, as well as brain rock (UST), at Red Hills follow the trend line within the muscovite domain, while Pinto Canyon samples support silicic alteration. All Pinto Canyon samples and Chinati Mountain samples outside the unaltered box contain elevated AAI values relative to AI.

Normative mineralogies plotted on the QAP diagram in Figure 4.2 display a myriad of lithologies of unaltered Red Hills samples. Gilmer (2001) reported lithologies of unaltered phases at Red Hills ranging from granodiorite, granite, quartz monzonite, quartz syenite, quartz monzodiorite, to monzonite, whereas altered phases plotted in the alkali feldspar granite and quartz alkali feldspar syenite fields. The phyllically altered BP and BQMP plot in the syeno-granite and monzogranite field, respectively, while the brain rock plots within the quartz-rich granitoid field. The GP, located in the eastern part of Red Hills, plot in the granodiorite field and the MME, also part of the eastern zone, plots along the boundary between monzodiorite-monzogabbro and quartz monzodiorite-quartz monzogabbro fields. Shafter samples SH12-14 (drill core) and SD-253 (outcrop) plot in the monzodiorite-monzogabbro field, respectively, similar to the BQMP and MME phases. Cepeda's (1977) Shafter intrusions plot in the granodiorite and quartz monzodiorite-monzogabbro field. Finally, the Pinto Canyon samples plot exclusively within the monzogranite field.

Figure 4.3 shows the alumina saturation index (ASI) of unaltered samples from Red Hills, Shafter, Chinati Mountains, and Pinto Canyon. Unaltered Red Hills samples fall into the weakly peraluminous to metaluminous categories, while altered samples lie within strongly peraluminous field. The dominantly metaluminous character of the Red Hills intrusions suggests minor crustal contribution and hence unlikely is to be from a crustal melt source. Shafter samples dominantly lie within the metaluminous field. The Chinati Mountains volcanics, however, dominantly fall into the metaluminous field, while Pinto Canyon intrusions trend toward the weakly peraluminous to strongly peraluminous fields. The Peccerillo-Taylor K_2O versus SiO_2 diagram, Figure 4.4, illustrates the high K calc-alkaline to shoshonite series affinities of all samples with their respective localities. The Chinati Mountains volcanics, however, remain largely in the shoshonite series rather than the high K calc-alkaline fields.

Pearce et al.'s 1984 Granite Y+Nb versus Rb diagram, Figure 4.5, reveals that the unaltered Red Hills intrusions have a tectonomagmatic affinity with a volcanic arc environment, likely from the Laramide orogeny, while one altered outlier fits into the syn-collision field. Perhaps this is due to the mobilization of Rb during hydrothermal alteration. The Chinati Mountains samples fall within the within-plate domain, which is likely from Basin and Range extension. Drill core sample SH12-14 falls within the within-plate field similar to the Chinati Mountain samples while outcrop sample SD-253 is part of the volcanic arc domain.

Harker variation diagrams, Figure 4.7, were compiled to visualize the differences of whole rock oxides of unaltered intrusions from Red Hills, Shafter, Chinati Mountains, and Pinto Canyon versus SiO_2. The Red Hills intrusions display intermediate compositions overall, based on the alkali content versus silica, silica contents ranging from 48 to 66 wt%, whereas the Chinati Mountains displays a wide range in silica and

alkali content. This may be a product of magmatic differentiation between the Tertiary units as the melt evolved. The Pinto Canyon intrusions display a distinct felsic signature compared to the other locations The Shafter samples appear sporadic, likely a product of small sample density. Al_2O_3, Fe_2O_3, MgO, MgO, CaO, and P_2O_5 linearly correlate with silica on Harker diagrams at all locations.

TRACE ELEMENT COMPOSITIONS

Rare-earth-element (REE) concentrations from Red Hills, Shafter, and Chinati Mountain samples were normalized against Sun and McDonough's (1995) C1 Chondrite and Weaver and Tarney's (1984) average crust to compare and contrast the REE trends, which are intimately linked to melt source and evolution. Red Hills shows a relatively flat curve within the C1 chondrite normalized plot in Figure 4.8. The lack of a negative Eu anomaly and low La/Yb ratio suggests that very little feldspar fractionation occurred and all phases are derived from a primary melt with little to no fractional crystallization at Red Hills. The relatively depleted heavy REE concentrations suggest that the residual liquids from the Red Hills melt are dominated by both hornblende and clinopyroxene crystallization phases. The decrease in dip on Dy, however, is most likely due to analytical variation because there is no reason why Dy would be more compatible.

In order to substantiate the C1 chondrite normalized REE signature at Red Hills, the intermediate phases were normalized against the REE values of the mafic enclave (Figure 4.9). Comparatively, the REE signatures normalized against the mafic enclave are similar to the C1 chondrite normalized values which grants greater confidence in the chondrite normalized curves. The Chinati Mountains samples, except one sample, which follows the Red Hills pattern, display very different REE signatures. A negative Eu anomaly exists which is due to fractionation of calcium-rich plagioclase. Eu has a similar

ionic radius as Ca and can carry either 2^+ or 3^+. Due to its similar charge with Ca, Eu^{2+} will partition into plagioclase more easily than Eu^{3+}. Because plagioclase preferentially incorporates Eu^{2+} from the melt, the residual liquid will be more enriched in other REE's, resulting in a negative Eu^{2+} anomaly. This signature suggests that the Chinati Mountains derive from an evolved melt by either magmatic differentiation or melt fractionation. Shafter dike samples follow similar trends as the Red Hills, suggesting that both Shafter and Red Hills had the same source and may have been responsible for contributing metal-rich hydrothermal fluids that formed the Shafter orebody.

Figure 4.10 is the REE and trace-element normalized plot against average crust. The Red Hills trends suggest that this melt was not very mafic and derived from an intermediate crust rather than a more mafic lower crust. Sr is typically comparable to Eu behavior so if plagioclase is a dominant phase, a negative Sr and Eu anomaly should exist. Because the Red Hills displays a small negative Sr anomaly, plagioclase was only a minor fractionating phase. Although some samples on these diagrams are phyllically altered, the REE concentrations was not affected by alteration because it is expected that Rb and Sr are to be more mobile than K, which is apparent on the Red Hills plots. Anthony and Titley (1994) state elements residing in the major minerals, i.e. the feldspars, oxides and ferromagnesian minerals, were mobile during alteration, i.e. Sr resides primarily in plagioclase and K, which Rb follows, in potassium feldspars and biotite. They proposed that element mobility is dependent on different complexing ligands, such as chloride and SO_4^{2-}.

Variation diagrams of precious and base metals versus SiO_2 at Red Hills and Shafter dike samples are plotted in Figure 4.11. Copper (Cu) concentrations of most igneous phases are very low, ranging from 15.6 to 2.7 ppm, the lowest being the GP and MME in the eastern part of Red Hills. The highest copper concentration was found in

phyllically altered brain rock with a value of 105.5 ppm Cu. Shafter samples display elevated Cu values, 68.7 and 35.2 ppm, compared to most of the Red Hills intrusive phases. Brain rock and QMP showed the highest values of molybdenum (Mo) relative to silica, 199 and 116 ppm Mo, respectively, whereas Shafter samples displayed trace amounts of Mo compared to Red Hills samples. Elevated Zn and Pb concentrations were found in the Red Hills MME and Shafter samples Zn concentrations are up to ten times higher than Pb. The MME and Shafter sample SH12-14 showed trace concentrations of gold, 0.8 and 0.5 ppb Au respectively. Silver (Ag) is virtually absent in all analyzed samples. Antimony (Sb) concentrations appear to decrease successively with younger igneous phases present within the western part of the intrusive complex.

U-PB GEOCHRONOLOGY PRINCIPLES

The uranium-lead system is unique among isotopes because two different isotopes of uranium decay to two different isotopes of lead (^{238}U to ^{206}Pb and ^{235}U decays to ^{207}Pb) at very different rates. This provides a built-in way to check for both system disturbance and presence of original daughter product. ^{238}U has a half-life of 4.47×10^9 yrs and ^{235}U has a half-life of 0.704×10^9 yrs. Wetherill (1965) developed a method that measures both isotopes of U and Pb in order to determine two ages from isochron diagrams based on decay equations in which $^{207}Pb/^{235}U$ and $^{206}Pb/^{238}U$ will evolve such that both ratios will follow the concordia curve. If the system has remained closed (ie. no parent or daughter has been gained or lost by any process other than radioactive decay), then the two ages would be identical and follow a concordant curve. If the system experiences a single episode of Pb loss, the lead leaving the system has a $^{207}Pb/^{206}Pb$ composition of the mineral at that time, which corresponds to its Pb–Pb date. The initial common lead trapped in the zircons must be corrected in order to calculate accurate U-Pb zircon ages.

The slope of the isochron, created by plotting the $^{206}Pb/^{204}Pb$ composition against their respective $^{238}U/^{204}Pb$ compositions, corresponds to crystallization age and the intercepts represent the initial $^{206}Pb/^{204}Pb$ compositions of the zircons when they formed. The equations for $^{207}Pb/^{235}U$, $^{206}Pb/^{238}U$, and $^{207}Pb/^{206}Pb$ are as follows:

(a) $(^{206}Pb/^{204}Pb) = (^{206}Pb/^{204}Pb)_0 + (^{238}U/^{204}Pb)(e^{\lambda 238t} - 1)$

(b) $(^{207}Pb/^{204}Pb) = (^{207}Pb/^{204}Pb)_0 + (^{235}U/^{204}Pb)(e^{\lambda 235t} - 1)$

(c) $(^{207}Pb/^{204}Pb) - (^{207}Pb/^{204}Pb)_0 / (^{206}Pb/^{204}Pb) - (^{206}Pb/^{204}Pb)_0 =$

$(^{235}U/^{238}U)((e^{\lambda 235t} - 1)/(e^{\lambda 238t} - 1) = (^{207}Pb/^{206}Pb)^*$

0: initial

*: radiogenic

U-PB ANALYTICAL METHODS AND RESULTS

Samples of phyllically altered BQMP yielded subhedral to euhedral, medium-sized (80-160 μm) zircons that were dated by LA-ICP-MS at the University of Texas at Austin (Appendix B). All zircon fractions were pre-ablated prior to analysis. Pb-Pb analyses (Appendix D) of zircons from the BQMP yielded an age of 66.27 $\pm$ 0.5 Ma (Figure 4.12), while the U-Pb method defined an age of 66.08 $\pm$ 0.31 Ma (Figure 4.13) with a mean weighted standard deviation of 4.2 at less than 10 % discordance. Sample RHS105 from the unaltered QLP yielded an age of 62.54 $\pm$ 0.49 Ma (Figure 4.14) with a mean weighted standard deviation of 9.6 at less than 10 % discordance.

CONCLUSION

Whole rock and trace element geochemistry agrees with Gilmer's (2001) interpretation that the Red Hills is inherently different from and unrelated to the Chinati Mountains and Pinto Canyon intrusive complex. Dike samples at Shafter suggest that these intrusions are linked to the Red Hills stock. Granite Y+Nb versus Rb trace element

plots suggest that intrusions from both geographic locations are derived from a volcanic arc environment, and range from both weakly peraluminous and metaluminous melts (based on alumina saturation diagrams). Unaltered samples are mostly metaluminous, suggesting minor crustal contribution and therefore not likely sourced from a crustal melt, which agrees with the REE signatures. Metal concentrations between Red Hills and Shafter shows that the MME has the most similar character to the Shafter dikes. These intrusions could be responsible for the introduction of late-stage copper in the Red Hills porphyry system due to their elevated copper concentrations (compared to the early intrusive phases).

The integration of new U-Pb zircon crystallization ages of Red Hills igneous intrusions to Gilmer's (2001) and Gilmer et al.'s (2003) geochronology data suggest that magmatism and hydrothermal activity at Red Hills may have occurred over 6 million years. The BQMP is the oldest phase dated (66.27 $\pm$ 0.5 Ma) so far, but the Red Hills in its entirety may be even older based on relative timing from cross cutting relationships that the BP precedes the BQMP. Gilmer's U-Pb zircon age (2001) of phyllically altered QMP (64.02 $\pm$ 0.3 Ma) and Gilmer et al.'s (2003) sericite $^{40}Ar/^{39}Ar$ age of 61.58 $\pm$ 0.34 Ma falls within the range of the BQMP and QLP (62.54 $\pm$ 0.49 Ma). Gilmer (2001) also interpreted that the eastern unaltered portion of the intrusive complex was genetically linked to the western portion, but thick surface alluvium covering the boundary between the two parts made this interpretation somewhat vague. The new date (62.54 $\pm$ 0.49 Ma) of the eastern lobe proves that the two parts are related in time and space. Stockwork mineralization of molybdenum and copper are not strictly contemporaneous with crystallization of porphyry magmas (Moore and Lanphere, 1971) and postdate at least part of the emplacement of the Red Hills stock. The single Re-Os mineralization age of molybdenite by Gilmer (2001) yielded the youngest age of 60.2 $\pm$ 0.3 Ma from the

phyllically altered QMP and based on mineral paragenesis, molybdenite appears to be the first sulfide to precipitate out of solution. These data suggest that molybdenum mineralization occurred approximately 2.5 Ma after the emplacement of the last igneous phase. Because molybdenum stockwork veining is apparent in all intrusive phases, older mineralization episodes must exist compared to Gilmer's (2001) molybdenite Re-Os age. Future work should analyze mineralization ages from each igneous phases and veins where there is an obvious difference in relative timing based on cross cutting relationships.

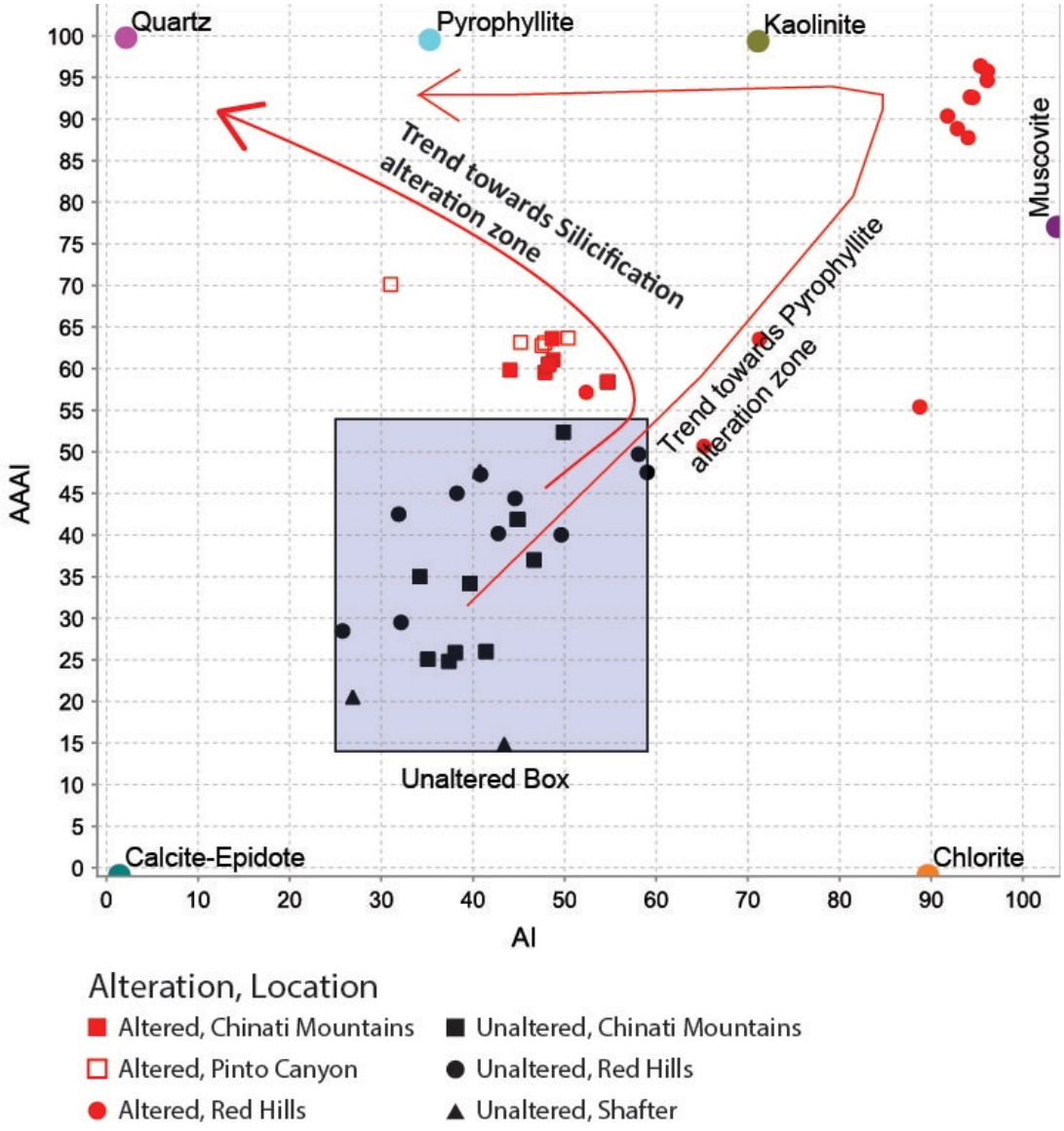

Figure 4.1. Ishikawa Alteration Index (AI) versus Advanced Argillic Alteration Index (AAAI) (Ishikawa et al., 1976) plot to differentiate altered samples from unaltered samples from Red Hills, Shafter, and the Chinati Mountains. All samples that lie outside the unaltered box in purple are considered altered samples.

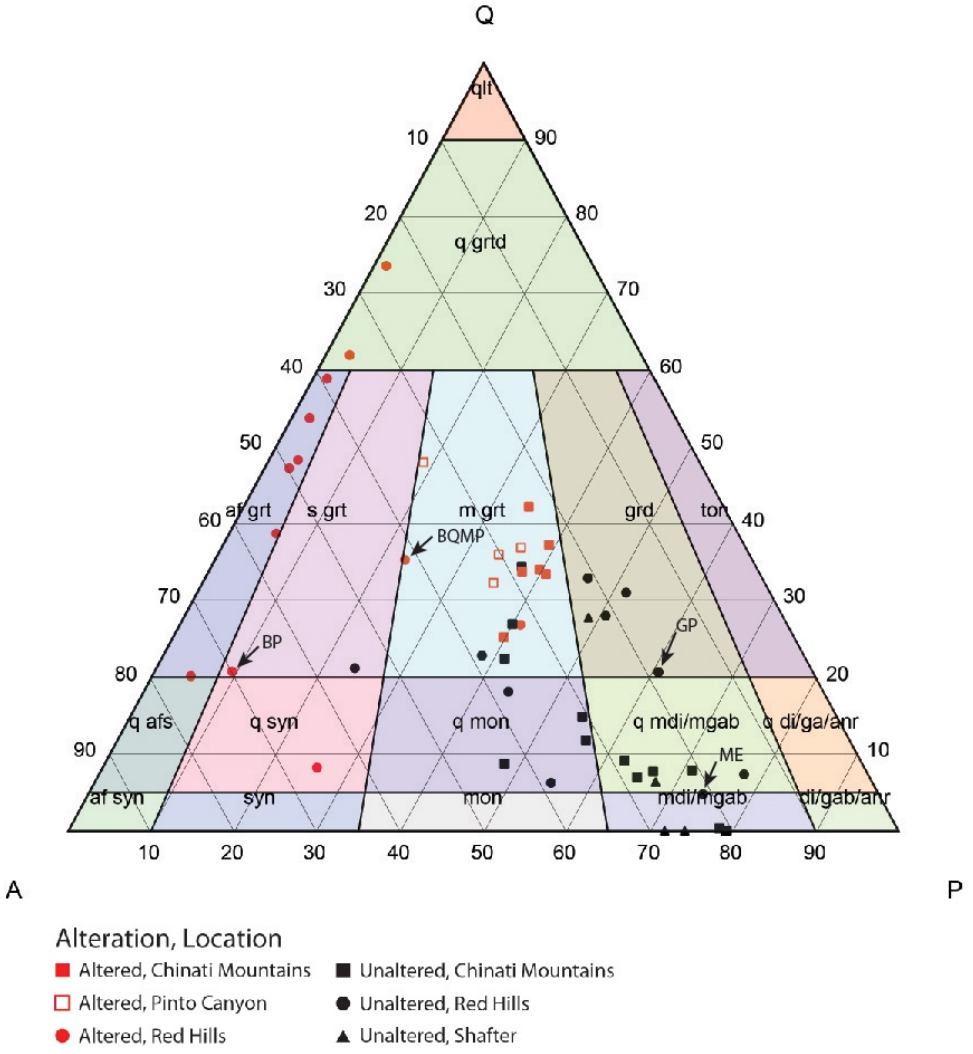

Figure 4. 2. Streckeisen's (1976) QAP diagram of normalized samples from Red Hills, Shafter, Chinati Mountains, and Pinto Canyon.

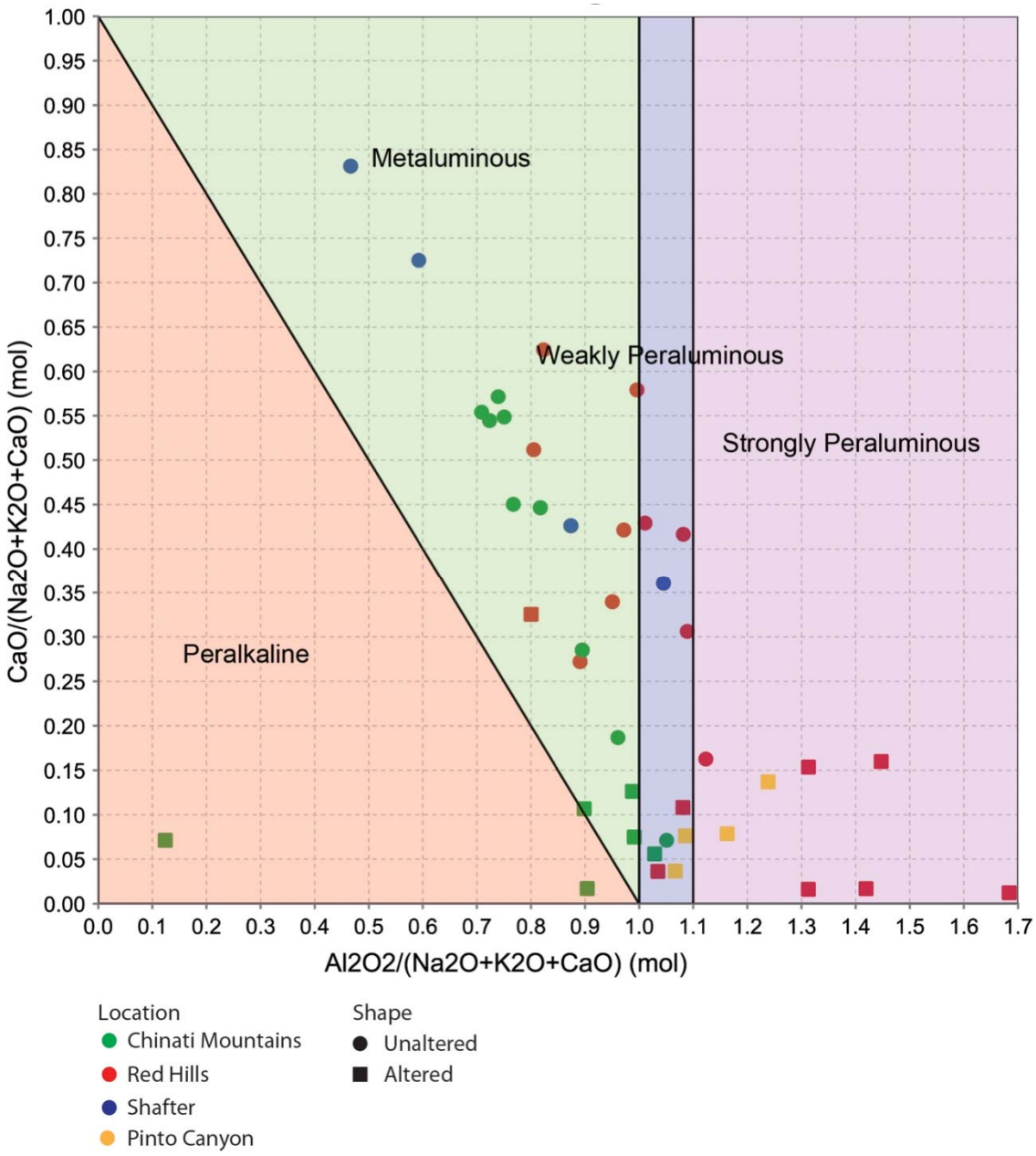

Figure 4.3. Barton and Young's (2002) Alumina Saturation plot of Red Hills, Shafter, Chinati Mountains, and Pinto Canyon intrusive samples.

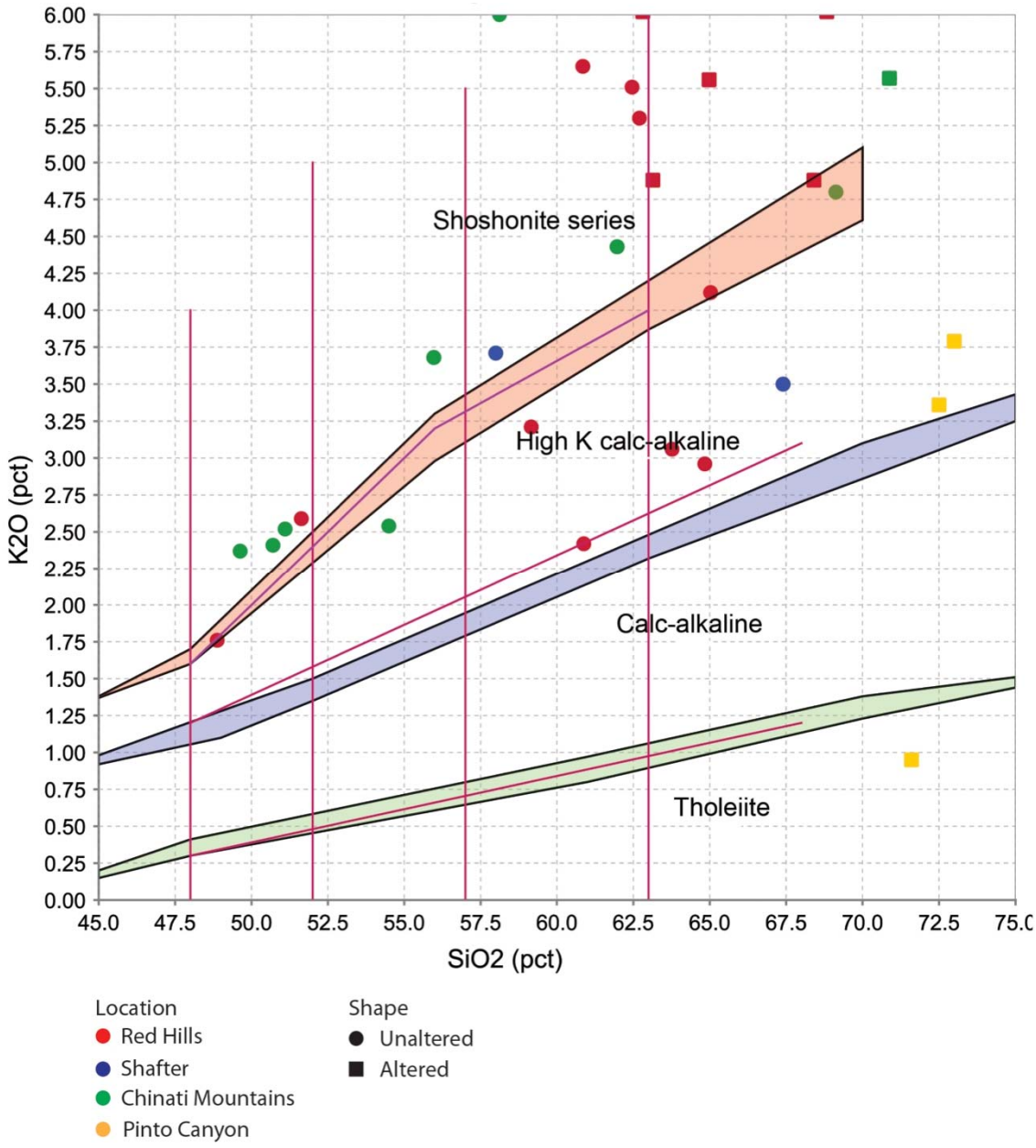

Figure 4.4. Peccerillo-Taylor's (1976) K_2O versus SiO_2 subalkalic subdivisions plot of the Red Hills, Shafter, Chinati Mountains, and Pinto Canyon intrusive samples.

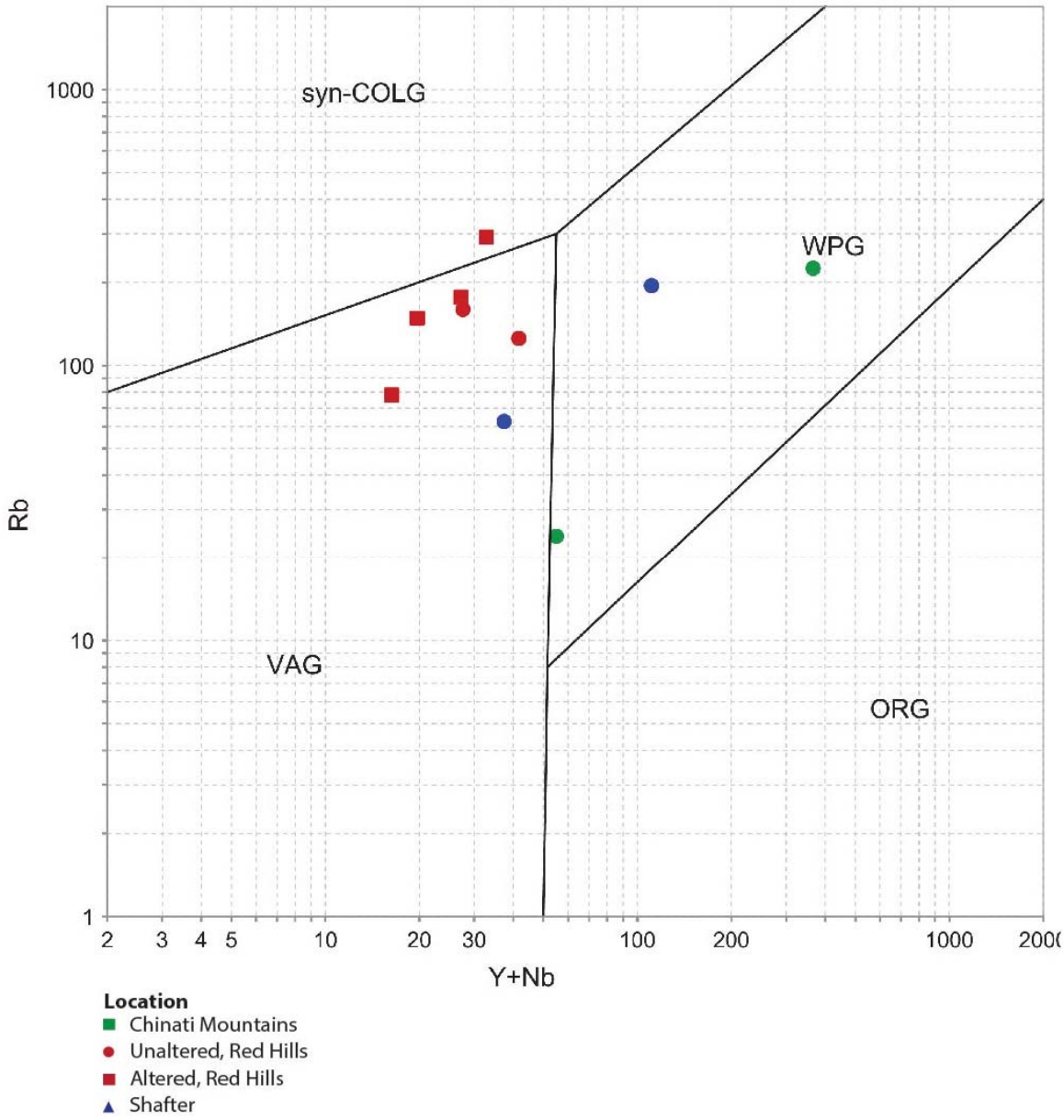

Figure 4.5. Pearce et al.'s (1984) granite Y+Nb versus Rb tectonic interpretation diagram. Plotted samples are intrusions from Red Hills, Shafter, and Chinati Mountains. ORG = orogenic granites, syn-COLG = syn-collision granites, VAG = volcanic arc granites, WPG = within-plate granites.

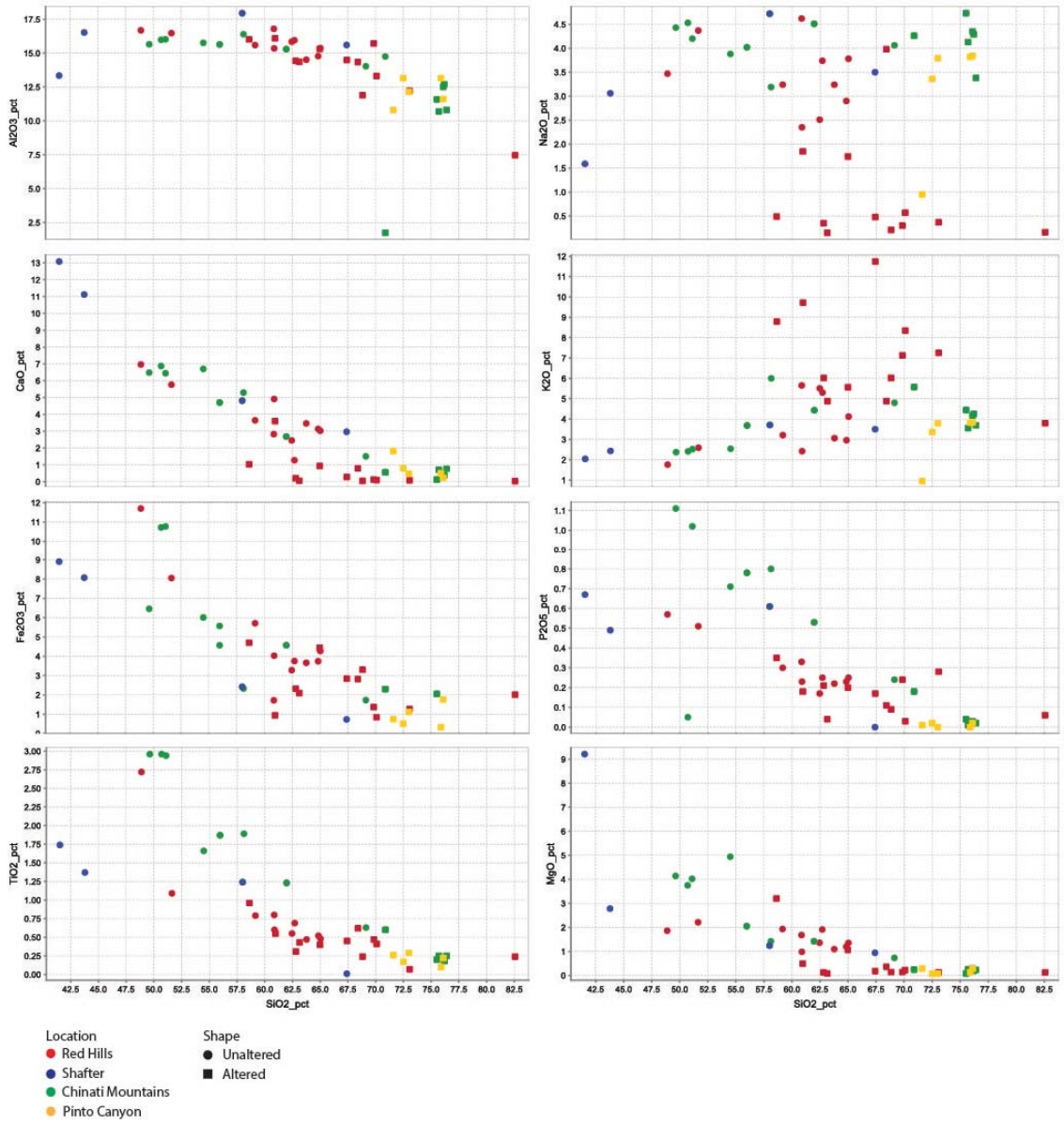

Figure 4.6. Harker (1909) variation diagrams. Major oxides are compared to unaltered intrusive samples from Red Hills, Shafter, Chinati Mountains, and Pinto Canyon showing the differences in elemental concentration and distribution.

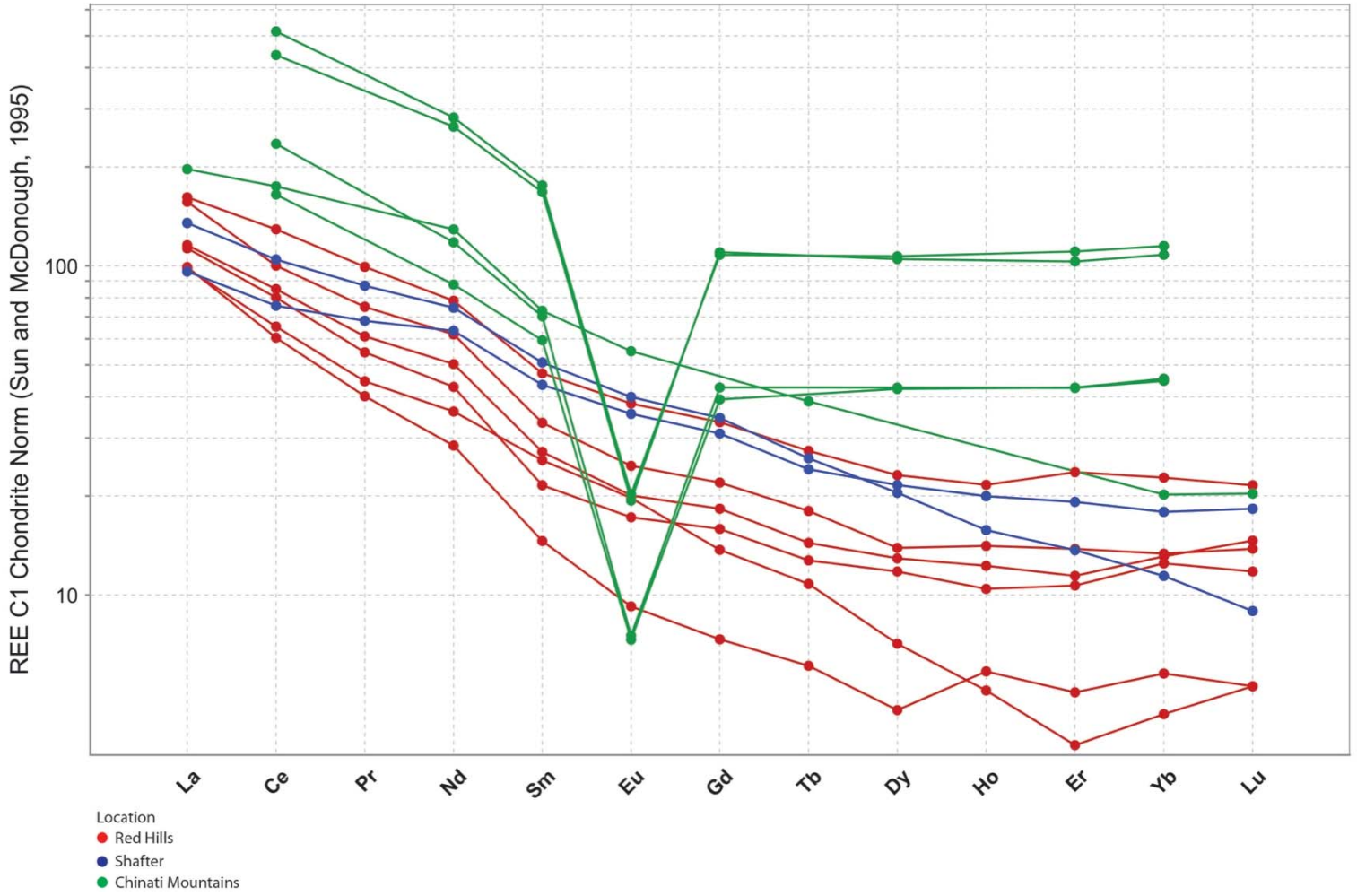

Figure 4.7. REE C1 Chondrite Normalized spider diagram from McDonough and Sun (1995). Samples are located from Red Hills, Shafter, and the Chinati Mountains.

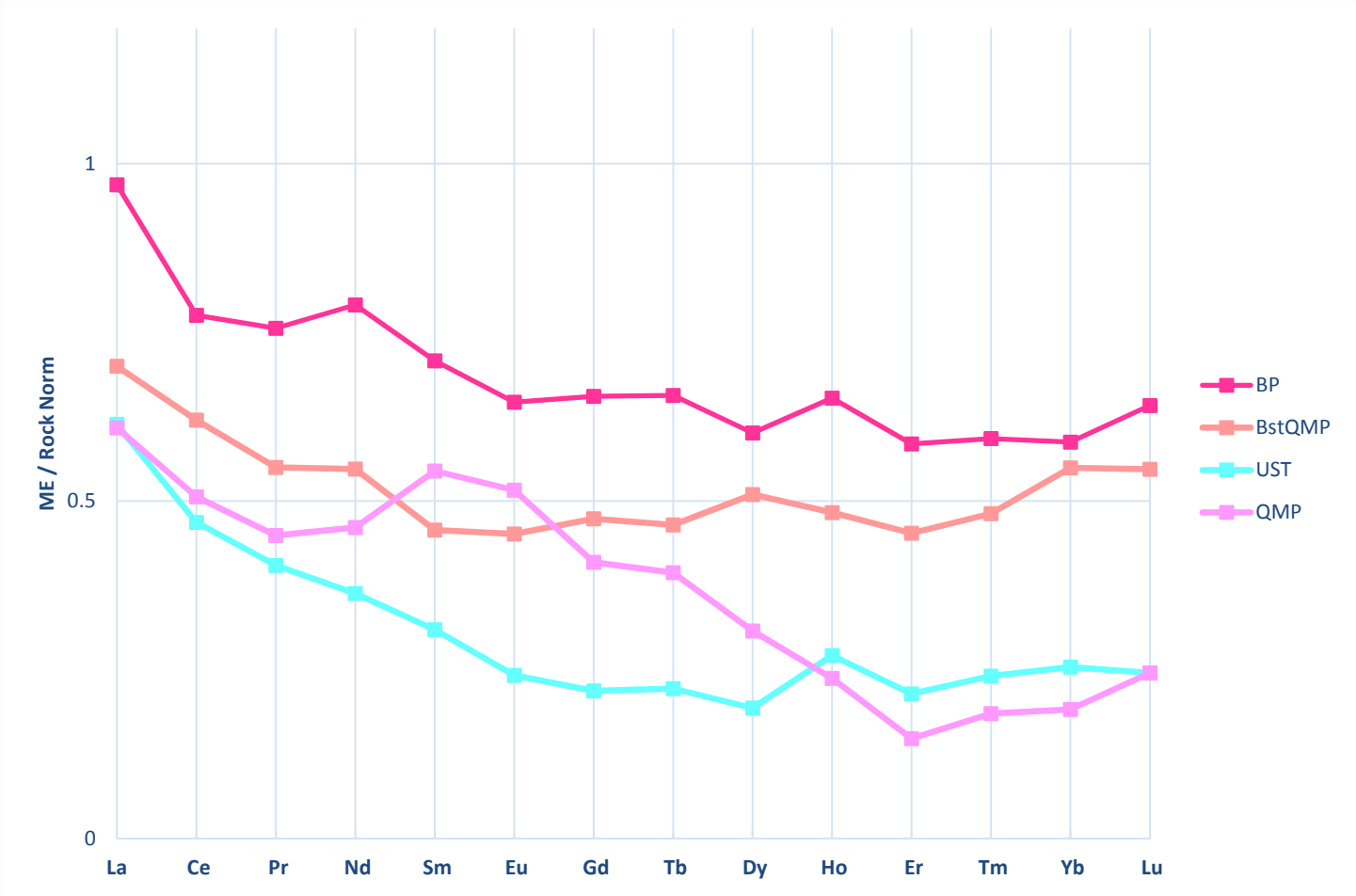

Figure 4.8. REE Red Hills mafic enclave-normalized plot of the Red Hills igneous samples.

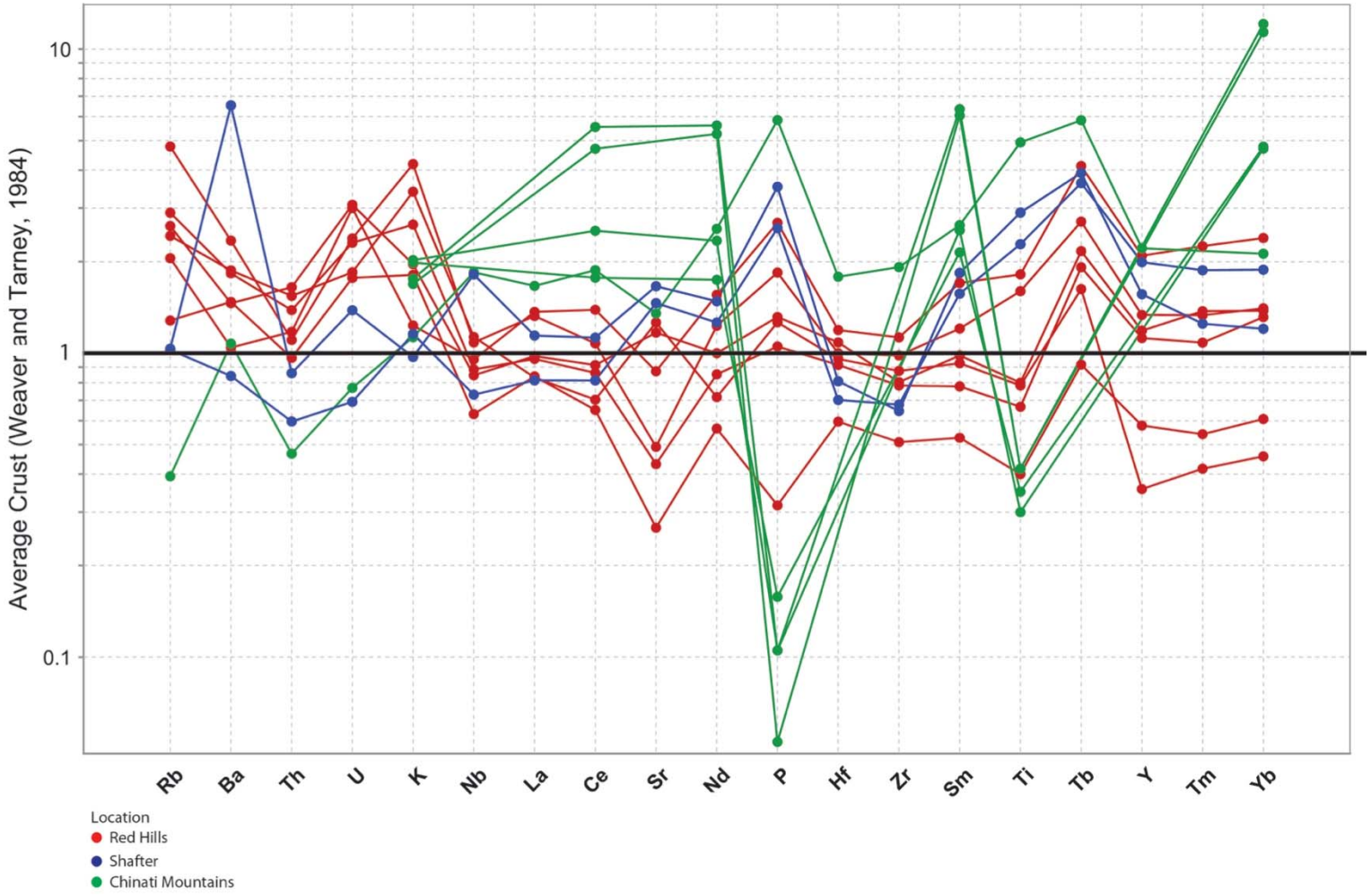

Figure 4.9. REE average crust normalized spider diagram by Weaver and Tarney (1984) for igneous samples from Red Hills, Shafter, and Chinati Mountains.

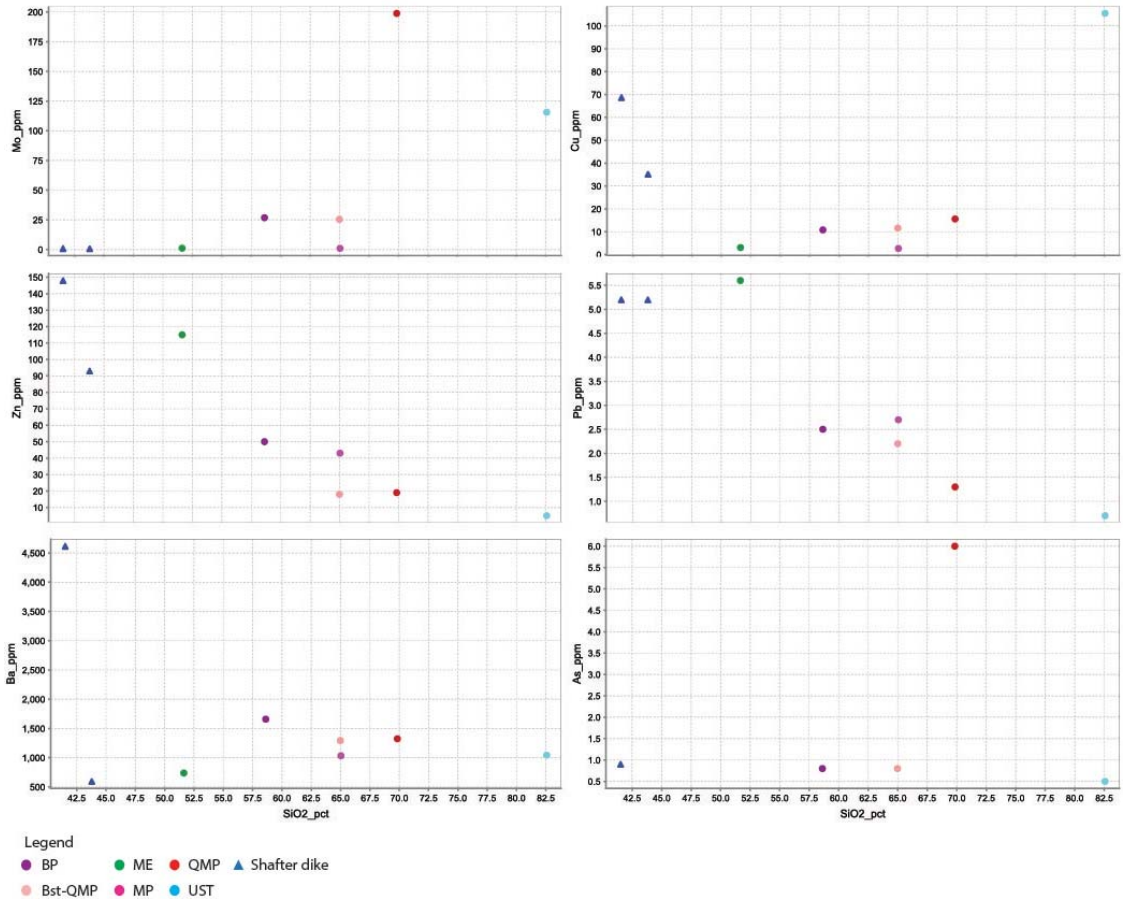

Figure 4.10. Variation diagrams of metals versus SiO_2 of Red Hills intrusive phases and Shafter dike samples.

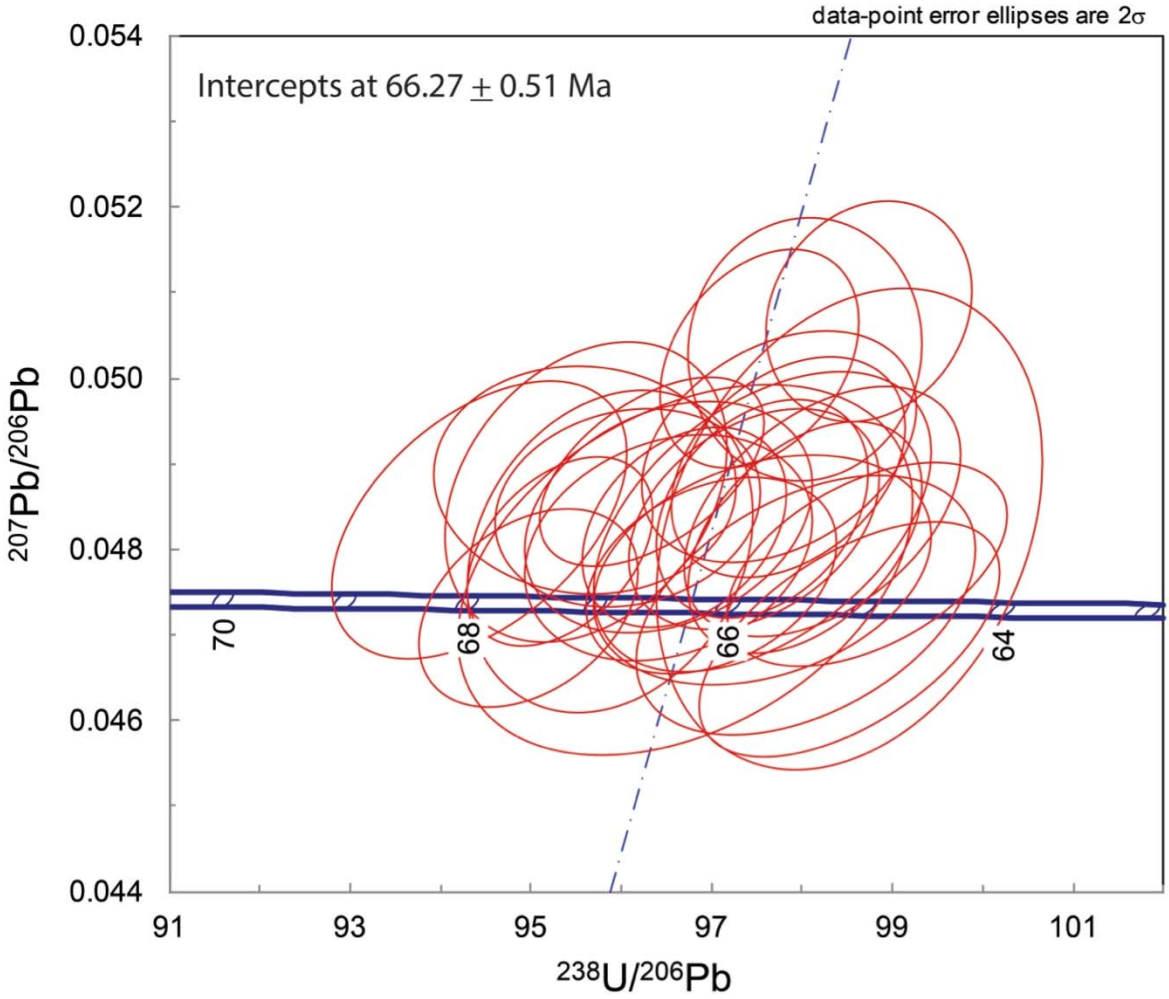

Figure 4.11. $^{238}U/^{206}Pb$ v. $^{207}Pb/^{206}Pb$ isochron plot for 27 zircons from the phyllically altered BQMP from the Red Hills intrusive complex.

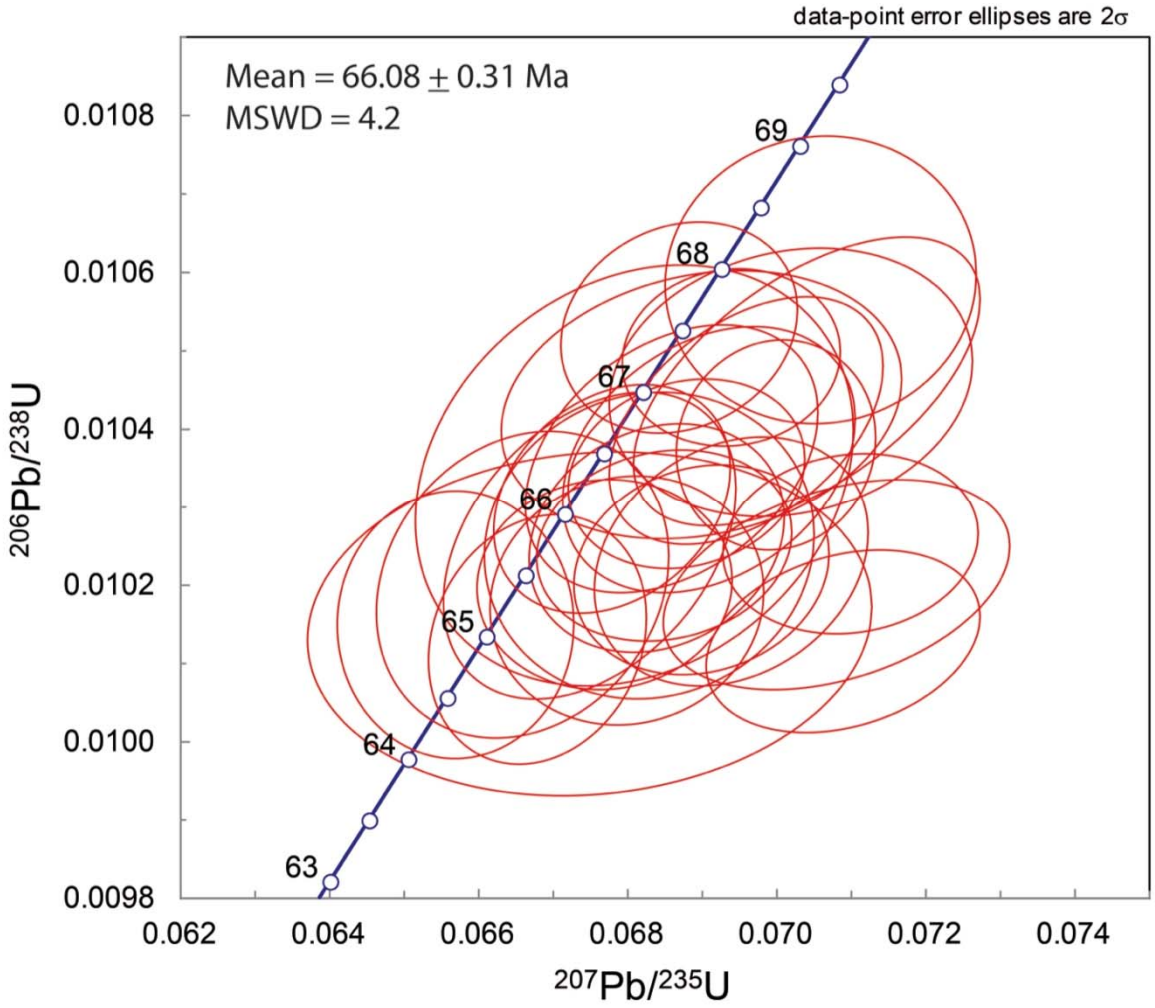

Figure 4.12. $^{207}Pb/^{235}U$ v. $^{206}Pb/^{238}U$ isochron plot for 27 zircons from the phyllically altered BQMP from the Red Hills intrusive complex.

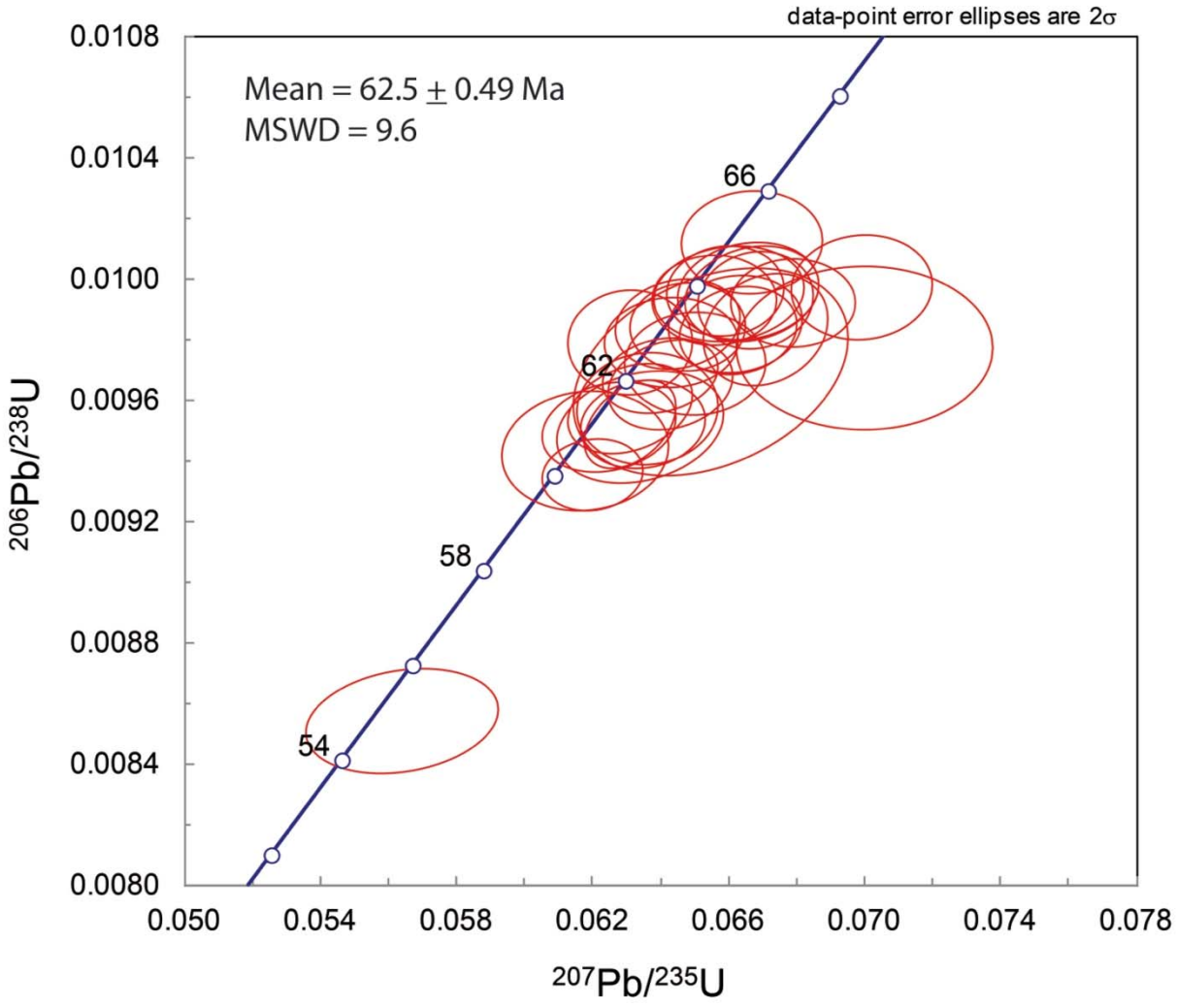

Figure 4.13. $^{207}Pb/^{235}U$ v. $^{206}Pb/^{238}U$ isochron plot for 30 zircons from the unaltered QLP from the Red Hills intrusive complex.

Chapter 5: Alteration and Mineralization

INTRODUCTION

The Red Hills displays evidence of multiple mineralizing events and changes in sulfide-silicate assemblages through time, based on progressive changes of fluid composition and temperature through time. Extensive phyllic alteration is present on the western lobe of the intrusive complex (Figure 5.1). Pods of silicification exposed near surface occur near fault zones, while propylitic alteration extends to the east projecting into the unaltered intrusion. Previous mapping by Gilmer (2001) and recent mapping identified exoskarns and hornfels weakly mineralized in Pb, Zn, and Ag near intrusive contacts with supergene argillic alteration present to the north (Figure 5.1). Copper and molybdenum outlines (Figure 5.2 and 5.3) updated by Tosca show crescent shape surface geometries, although this may be influenced by drill coverage (Tietz, 2012).

HYPOGENE

Felsic to intermediate magmas contain 1 to 2 % H_2O and experimental studies show most silicate mamas require 2 to 4 % H_2O to stabilize hornblende and biotite (Gardien et al., 2000). Therefore, sufficient H_2O will be available to separate from the melt and will be typically enriched in F, Cl, S, and metals due to their incompatibility in crystallizing minerals from the melt.

Potassic and phyllic alteration styles in porphyry systems are fracture controlled alteration zones. Mineralization consists of veinlets of silicate and sulfide minerals with some disseminated sulfide, which precipitated from an aqueous fluid. Hydrothermal solutions travelling through fractures within the deeper hypogene zone produced veining styles of molybdenite, quartz-molybdenite, and barren quartz.

Potassic

Aqueous fluid near the top of the magma chamber in the cupola generally contains potassium-dominant alkalis, silica, volatiles (CO_2, SO_4, Cl) and metals. With pressure release, fractures form in the quickly cooling magma and surrounding wallrocks. These fractures are commonly filled with hydrothermal orthoclase, biotite, quartz, and/or anhydrite as well as chalcopyrite. Potassic alteration is not widespread at Red Hills, and is commonly overprinted by pervasive phyllic alteration. This alteration style is coeval with A and B style veining, which will be explained in further detail in Chapter 6. Lack of exposure and difficulty of recognition of remnant altered zones in drill core only allowed two general forms potassic alteration to be defined. Red-brown, hydrothermal, flaky biotite in the form of veinlets, stringers, or massive aggregates has formed by the complete replacement of igneous hornblende or biotite within porphyritic groundmass is the second form of potassic alteration, Figure 5.5. The distinct color difference between black igneous biotite is related to the elevated Mg/Fe ratio in hydrothermal biotites (Beane, 1974). An interpreted type of potassic alteration is represented by mm-scale, white alteration halos bordering the margins of early quartz, A-veins, Figure 5.4. These halos are interpreted to be K-feldspar halos, which have been replaced by sericite by phyllic alteration. Molybdenite is the dominant sulfide phase in the potassic zone with minor pyrite; chalcopyrite was not seen. Intense biotization of the BP may represent early pervasive potassic alteration of the intermediate phases.

The styles of potassic alteration are heavily dependent on the chemical interaction between the wallrock and the hydrothermal fluids passing through fractures. Mo mineralization in the form of molybdenite is primarily hosted within quartz veins that do not display alteration halos. It also forms less commonly as disseminations within porphyry groundmass and as “moly-paint’ in which molybdenite coats fracture planes appearing as monominerallic veinlets. Mo mineralization occurs in the late stage of potassic alteration but before phyllic alteration at the Red Hills. It is exposed on the surface and extends to at least 594 m (1,950 ft) elevation, but

average grades decrease with depth (Tietz, 2012). In plan view, the molybdenum outline is horseshoe shaped and encompasses an area extending 594 m (1,950 ft) east to west and 732 m (2,400 ft) north to south (Figure 5.2 and 5.3).

Propylitic

Coeval with potassic alteration is CaO, MgO, Na_2O, H_2O and CO_2-enriched propylitic alteration that moves outboard from the fringes of the potassic alteration zone. Propylitic alteration extends predominantly to the east from the foci of the Red Hills stock. Surface exposure of propylitic alteration extends east of the deposit. Rocks affected by propylitic alteration commonly are pervasively green, which is attributed to the replacement of mafic phases by chlorite and calcic plagioclase partially converting to epidote and calcite (Figure 5.6). Propylitic alteration is not veinlet controlled and affects mafic minerals and feldspar. Accessory minerals in the propylitic zone at the Red Hills include tremolite, actinolite, and Fe-oxides. A specular hematite zone exists within the propylitic alteration zone near outcrops containing mafic enclaves, but no minerals of economic interest are found in this zone.

Phyllic

The upper and lateral portions of the deposit show quartz-sericite-pyrite veining cross cut by pyrite veins in the phyllic alteration zone. In porphyry systems, phyllic (sericitic) alteration assemblages are produced from lower temperature magmatic fluids (Figure 5.8), which commonly overprint potassic and propylitic alteration assemblages (Rusk, 2004; Sillitoe, 2010). However, phyllic alteration can form along the margins of the system where meteoric groundwater convection is influenced by the presence of hot igneous bodies (Harris et al., 2005; Sillitoe, 2010). At Red Hills, the wallrock is intensely sericitized and abundant pyrite is introduced. The host rocks are depleted in CaO, MgO, and Na_2O but are enriched in K_2O (Burnham, 1962). Pervasive phyllic alteration has destroyed original rock textures and contains the highest hypogene sulfide content. D-style, pyrite veining with or without quartz-sericite-

pyrite halos, veins are associated with this style of alteration. Hydrolytic alteration is the result of hydrogen ion consumption and the release of metal ions into solution. The potassic assemblage breaking down to phyllic assemblage is as follows (Hemley and Jones, 1964):

$$1.5\ KAlSi_3O_{8(ksp)} + H^+ = 0.5\ KAl_3Si_3O_{10}(OH)_{2(musc)} + 3\ SiO_{2(qz)} + K^+$$

Phyllic alteration is the most important style of alteration associated with hypogene Cu mineralization at Red Hills. Late-stage pyrite, as veins or as disseminations within porphyry groundmass, is enriched in copper, as evidenced by copper sulfide inclusions. The copper zone (Figures 5.2 and 5.3) spans an area from 4,200 ft (1,280 m) from east to west and from 2,800 ft (853 m) from north to south. Hypogene copper sulfides at Red Hills include chalcopyrite, bornite, covellite, and digenite (Figure 5.9 a, b). Because bornite is not typically found in phyllic alteration zones in most porphyry copper systems, its occurrence is probably a relict from potassic alteration. Chalcopyrite commonly is rimmed by chalcocite resulting from supergene replacement processes (Figure 3.4 and Figure 5.10 a and b). Pyrrhotite is also found as isolated inclusions within pyrite or in association with chalcopyrite inclusions.

Late-stage fluids have also introduced minor Zn, Pb, Bi, and Ba to the system. Galena, sphalerite, bismuthinite, molybdenite, and chalcopyrite have been found in euhedral pyrite grains in shallow drill core samples of the uppermost phyllic zone (Figure 5.11 a-c). Anhedral pyrite within the aplitic crenulate layers in brain rock show an abundance of ~ 1 to 2 μm bismuthinite inclusions (Figure 5.12). Barite is found as disseminations within groundmass or in vugs in B-veins in samples TMC01-114 and TMC25-733. Ca-Na-K-zeolite framboids exist within vugs in veins or in the groundmass in samples RH24, TMC7-1089, TMC12-1071, and TMC14-1173. In the Mines Gaspe porphyry Cu-Mo deposit, Shelton and Rye (1982) stated that late stage zeolite and calcite veins formed when the hydrothermal system died based on low salinity, low homogenization temperature (near 150°C) fluid inclusions of meteoric origin. This may also be the case at Red Hills.

Argillic

Argillic alteration is not well developed at Red Hills. In porphyry systems, rocks affected by phyllic alteration are susceptible to retrograde argillic alteration during the waning stages of lower temperature hydrothermal activity. Where present, massive alteration of K-feldspar to fine grained kaolinite (Figure 5.13 a and b) and chloritization and leaching of biotite consumes the host rock by K_2O metasomatism (Burnham, 1962). This alteration style may have been formed by 1) time-equivalent alteration to sericitic alteration as the outermost zone next to propylitic alteration, 2) high-level, magmatically derived hydrothermal fluids from late intrusions, or 3) later supergene alteration by weathering of pyrite-rich sericitic alteration zones. General mineralogy of the argillic alteration zone includes quartz, kaolinite, montmorillonite, local sericite, 1-2% pyrite, trace chalcopyrite, tennantite, and sphalerite. Identification of phases characteristic of advanced argillic alteration, such as pyrophyllite and/or andalusite, have not been identified in any Red Hills samples. The phyllic assemblage altered to argillic assemblage is as follows (Hemley and Jones, 1964):

$$KAl_3Si_3O_{10}(OH)_{2(musc)} + H^+ + 1.5\ H_2O = 1.5\ Al_2Si_2O_5\ (OH)_{4(kaol)} + K^+$$

The reaction path from potassic alteration to argillic alteration can be found in Figure 5.7. Dill et al. (1997) states that element ratios in kaolinite can be used to distinguish hypogene versus supergene kaolinite (P vs. S, Zr vs. Ti, Cr+Nb vs. Ti+Fe, and Ce+Y+La vs. Ba+Sr). Hypogene kaolinite will be enriched in S, Ba, and Sr during hydrothermal alteration while supergene kaolinite will be enriched in Cr, Nb, Ti and lanthanide elements during weathering. Future work should implement this technique to constrain the hypogene argillic assemblages versus the supergene argillic assemblages.

Hypogene Alunite

Alunite is typically a low-temperature hypogene constituent of epithermal alteration (Field, 1966). Pyrite dissolution will form acidic solutions that react with K-Al silicate host rocks

to produce alunite and jarosite under high acid and sulfate conditions (Blahd, 1982). Hypogene alunite exists within shallow levels of the Red Hills at elevations approximately from 1212 m to 1067m (3975 ft to 3500 ft) where alunite depths increase from north to south similar to dip of the overlying Permian and Cretaceous strata. It occurs as 0.5 mm thick veinlets up to 1.5 cm veinlets that typically dip at shallow angles. In hand sample, hypogene alunite is white, hard, and depicts a micro-crystalline, porcelain texture. XRF data showed hypogene alunite veins contain elevated SiO_2 compared to supergene alunite veins, suggesting that the hard character of hypogene alunite veins may be intergrown with quartz. In thin section, hypogene alunite displays a bladed habit (Figure 5.14). Stoffregen et al. (2000) write that deposition of hypogene alunite may be coincident with pyrite deposition, but not during the same time as ore sulfides based on acid-sulfate conditions. Further detail on these veins will be explained in Chapter 6.

SILICIFICATION

Silicification is typically concentrated along fault zones particularly to the south-east of Red Hills and may be pervasive within the wallrock of multiple porphyry units. Pervasive replacement by fine grained quartz is the most prominent feature of silicification.

SUPERGENE

Based on fluid inclusion characteristics, estimated Gilmer (2001) estimated that the present Red Hills surface represents 2-3 km of exhumation and subsequent erosion to allow for secondary copper enrichment. Phyllic alteration exposed at the paleosurface has undergone leaching and supergene enrichment beneath the paleowater table, which is overlain by a hematitic leached cap. Supergene processes have formed a thin chalcocite blanket beneath the Red Hills leach cap. Copper grades in the chalcocite blanket range from 0.3% to 1% Cu but grades exceeding 9% Cu occur in altered hornfels to the northeast where local structures host high grade copper (Figure 5.15 a and b).

Leach cap oxide zone

The thin leached cap has mm- to cm- wide alunite, hematite, and goethite veins (Figure 5.16), and overlies a weak supergene copper zone with local high-grade chalcocite typically in pyritic wall rocks. Pyrite in the phyllic alteration zone reacts with oxygen-rich ground water in the vadose zone and capillary fringe above the water table and "rusts", forming iron oxide and sulfuric acid (Chavez, 2000). Acids leached from alkali and alkaline minerals react with K-silicates to produce a distinctive suite of secondary silicate and sulfate minerals as well as hydrated iron oxides. This process removes copper and forms a "leached cap". The primary minerals at the Red Hills leach cap identified by XRD are consistent with the classic limonite assemblage (Blanchard, 1968; Anderson, 1955; Chavez, 2000): hematite, goethite, jarosite, and alunite. The acidic groundwater percolates downward and attacks copper-bearing hypogene sulfides, such as chalcopyrite, and releases the copper into the water. Reactions for pyrite and chalcopyrite decomposition in the leached zone include:

$$8\ FeS_{2(py)} + 28\ O_2 + 8H_2O = 8\ FeSO_4 + 8\ HSO_4$$

$$8\ FeSO_4 + 4\ H_2SO_4 + 2\ O_2 = 4\ Fe_2(SO_4) + 4\ H_2O$$

$$2\ CuFeS_{2(cp)} + 4\ Fe_2(SO_4)_3 = 2\ CuSO_4 + 4\ S$$

Reduced zone

Enrichment in porphyry copper deposits starts when typically low grade (0.05% to 0.35% Cu, primary pyrite and chalcopyrite mineralization is exposed to oxygenated groundwater, requiring a pyrite to chalcopyrite ratio of >4:1 (Titley and Marozas, 1995; Enders, 2000; Chavez, 2000). When the copper-rich water reacts with pyrite at depth in the phyllic zone and migrates downward to a redox (reduction/oxidation) boundary at or below the paleo-water table, the copper in solution reacts with reduced sulfur in chalcopyrite and pyrite in the reduced zone and forms secondary copper sulfides (chalcocite) in an "enriched blanket". At Red Hills, the

chalcocite blanket is thin but widespread throughout the deposit (Tietz, 2012). Replacement textures involve volume-to-volume replacement of chalcopyrite or pyrite to chalcocite or pyrite partially replaced by chalcocite (Figure 5.16 a and b). The minimum ratio of py:cpy in the body being leached to produce chalcocite must be 4:1 involving the reaction:

$$5\ FeS_{2(py)} + 14\ CuSO_4 + 12\ H_2O = 7\ Cu_2S_{(cc)} + 5\ FeSO_4 + 12\ H_2SO_4$$

Through continued weathering and lowering of the water table, by uplift of land or decrease in rainfall, the chalcocite zone will continue to move downward, becoming richer as more copper is leached and deposited. Replacement textures range from complete volume-for-volume replacement to thin coatings on primary copper sulfide grain boundaries. Copper enrichment by leach cycles typically increases copper grade by a factor of at least 2 (Enders, 2000). Chalcocite within argillically altered rock appears as thin mm-scale veinlets or massive disseminations largely reflecting the character of the replaced hypogene sulfides.

Supergene processes are reflections of cyclic and episodic vertical changes in the position of the redox boundary due to changes in tectonic, physiographic, and climatic conditions. As long as pyrite is readily available and copper mobilization is sustained by the changing water table levels, enrichment blankets can readily migrate downward. A structure map for the base of the oxide zone was created at Red Hills to document the position of the paleowater table when migration of the enrichment blanket ceased (Figure 5.17). Elevations of the base of the oxide zone were identified by Tosca drill logs, which were confirmed or corrected by drill core photographs. The structure map reflects local tilting to the south similar to the Cretaceous and Permian units that dip towards the south away from the Chinati Mountains caldera. The light-green concentration in the central area of the north-east quadrant is a reflection of steeply-dipping, high-angle structures where Cu grades reach up to 9%. Figure 5.18 shows a net-thickness isopach map of the oxidized zone. Due to surface erosion and weathering, true thicknesses could not be represented. Nevertheless, the map depicts thickness increasing from

north to south, which is likely an artifact from surface topography, i.e. greater erosion in the north.

Supergene Alunite

In environments that still retain pyrite undergoing dissolution, maintaining a low pH environment, acid-stable sulfates such as alunite and jarosite form. Jarosite is only stable in low pH conditions (<2.5) and converts to goethite (FeO(OH)) at higher pH. Supergene alunite is yellow-brown in color, microcrystalline, and typically is associated with vuggy silica (Figure 5.19). According to Titley and Marozas (1995), jarosite is a product of the immediate reaction of sulfates with K-bearing silicates, and alunite is mostly a product found beneath weathered, former enriched sulfides blankets. Alpers and Brimhall (1988), for example, concluded that supergene alunite formed beneath the water table in the relatively reducing zone. At Red Hills, supergene alunite is found as 1 mm to 3 mm veinlets within the matrices of hornfels breccia clasts and in the phyllically altered plutons.

$$4\,FeSO_4 + 3\,KAlSi_3O_{8(ksp)} + 4\,H_2O + 4\,H^+ + O_2 = KAl_3(SO_4)_2(OH)_{2(alu)} + KFe_3(SO_4)_2(OH)_{6(jar)} + K^+ + Fe^{3+}$$

Stoffregen et al. (2000) states that this stage of supergene alteration (associated with vuggy silica alteration) has the potential to create sites for later metal concentration by creating permeability within the host rock.

Transition zone

Once pyrite has been destroyed or if lithological variations of acid-consuming wall rocks, such as limestones, skarns, or feldspar and biotite-bearing intrusions, are present, oxidation of minerals occur in-situ with minor transportation of copper. Sulfuric acid and ferric sulfate react completely with chalcopyrite forming cupric sulfate and ferrous sulfate. Secondary oxide minerals, such as malachite, azurite, chrysocolla, will form depending on a myriad of factors

such as Eh, pH, P_{CO2}, P_{O2}, SO_4^{2-} and a variety of other environmental and geochemical conditions (Enders, 2000).

HORNFELS AND SKARNS

Pyritic hornfels, weakly mineralized (Zn) skarns, and jasperoids are found within the contact aureoles of the intrusive complex within the Ross Mine and Mina Grande Formations. The hornfels are light tan to brown in color, fine grained, and are highly pyritized. Hornfels xenoliths within intrusive phases are found as deep as 3785 ft elevation in drill hole TMC-15 (Figure 5.22 a-b). Gilmer (2001) noted that the calcareous hornfels and skarn bodies are discontinuous pods that represent metasomatised roof pendants above the intrusion. Massive pyrite is typically monominerallic but may contain minor chalcopyrite inclusions. Interstitial, bladed hematite between hornfels clasts is also found in the groundmass, which may contain as much as 20% in certain samples (Figure 5.23 a-b).

Exoskarns are primarily composed of massive retrograde-hydroandradite garnets which exhibit alteration coronas (Gilmer, 2001). These garnets are commonly replaced by calcite, hematite, quartz, and actinolite.

DISCUSSION AND CONCLUSION

Hydrothermal alteration at the Red Hills deposit has resulted in hypogene mineralization of the intrusions and proximal alteration of adjacent siliciclastic and carbonaceous wallrock into hornfelds, skarns, and jasperoid. Hypogene alteration and mineralization was followed by supergene enrichment processes that formed a leach cap and thin chalcocite blanket. Molybdenite mineralization associated with potassic alteration occurred first at the Red Hills, followed by the introduction of copper associated with subsequent phyllic alteration. Pyrite, chalcopyrite, pyrrhotite, bornite, covellite, and barite with rare sphalerite, galena, and bismuthite assemblages are found in phyllically altered samples. Pervasive phyllic overprinting has destroyed many primary textures of the intrusions and any remnants of potassic alteration.

Propylitic alteration, composed of calcite, epidote, chlorite, and actinolite alteration minerals, is interpreted to occur near the same time as potassic alteration, and occurs laterally toward the east from the mineralized center. Intermediate argillic alteration occurs near the center of the western stock, where feldspathic minerals are completely replaced by clays, dominantly kaolinite.

The leach cap is primarily composed of hematite, goethite, and jarosite with vuggy quartz while copper minerals transition zone are composed of chrysocolla and azurite which are typically found in fractures within hornfels. The reduced zone contains the supergene enrichment blankets that dominantly composed of chalcocite replacing pyrite which occurs predominantly as massive pods or thin veinlets.

The thin chalcocite blanket and lack of characteristic textures suggesting repeated episodes of supergene enrichment at Red Hills probably states that only one cycle of leaching and secondary enrichment occurred. Gilmer's (2001) 2-3 km exhumation estimate and Kyle's (2012) supergene alunite $^{40}Ar/^{39}Ar$ dates of 5.8 to 3.1 Ma suggest that the Red Hills was rapidly exhumed and eroded during the Pliocene. Major uplift subsequent to mid-Tertiary volcanism was caused by Basin and Range deformation, which may have been responsible for normal faulting and subsequent drop in the water table during the Pliocene.

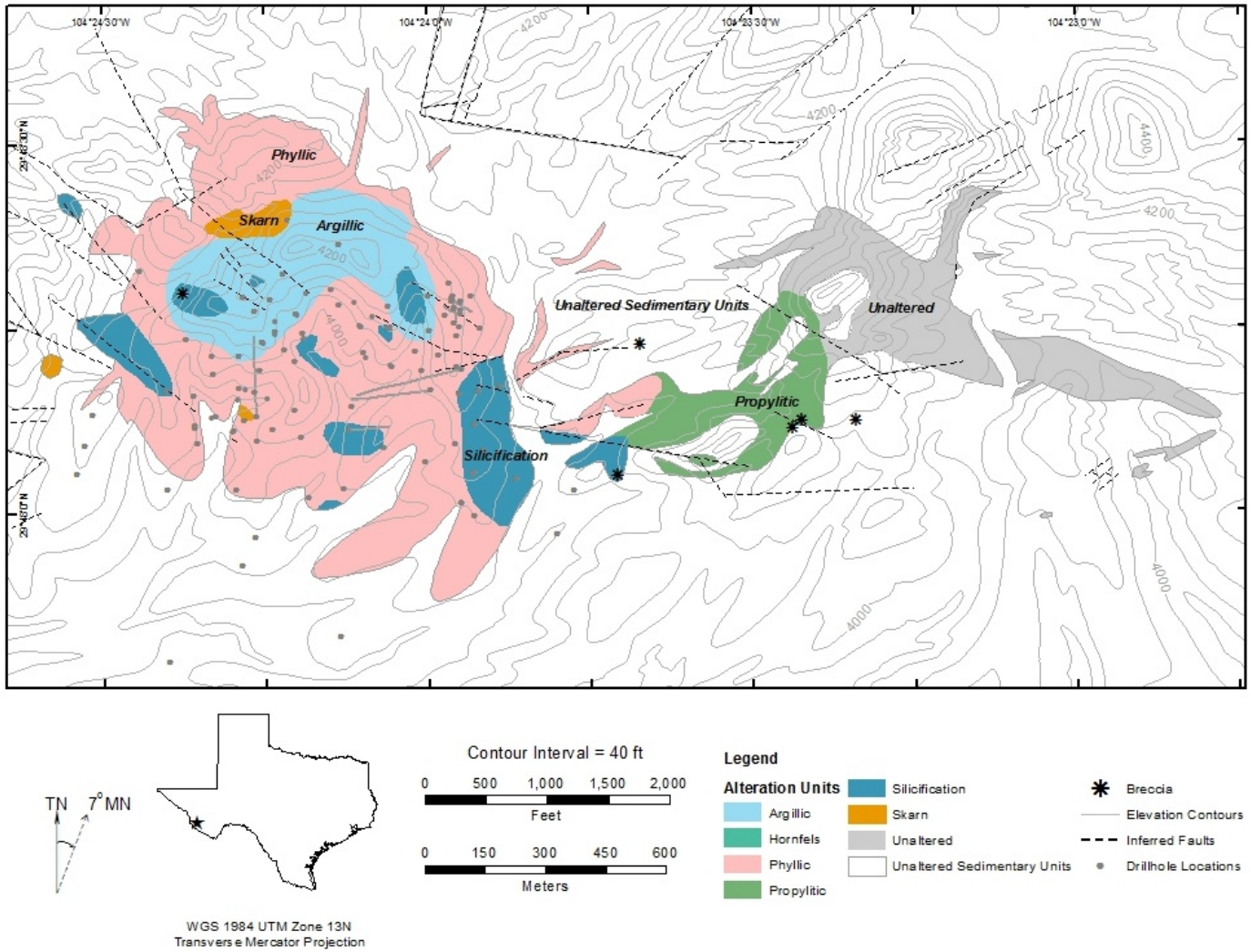

Figure 5.1. Surface alteration map at the Red Hills. Figure modified from Gilmer (2001).

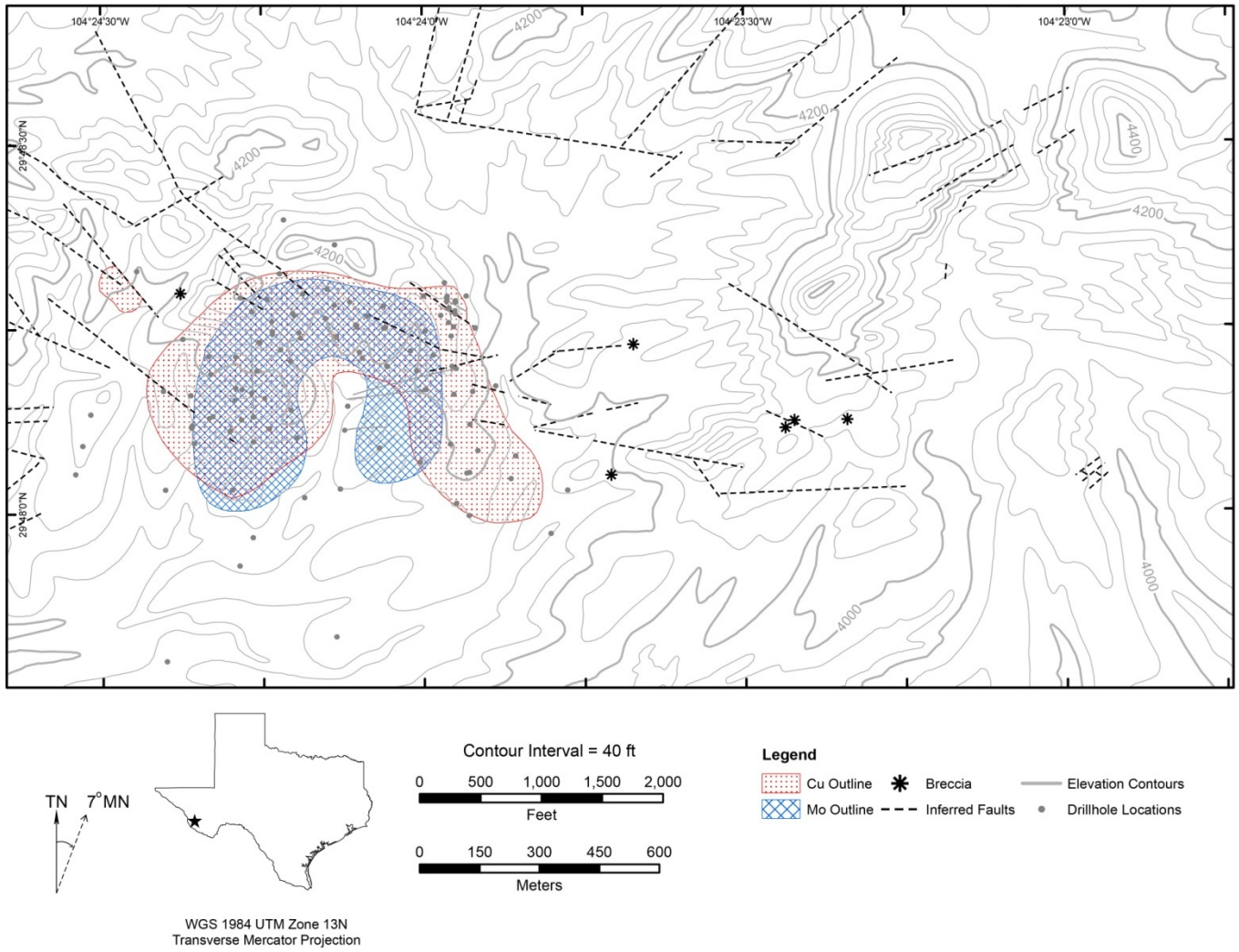

Figure 5.2. Zones of molybdenum and copper concentrations defined by Tosca Resources Corp. and major structures at Red Hills. Figure modified from Tietz (2012).

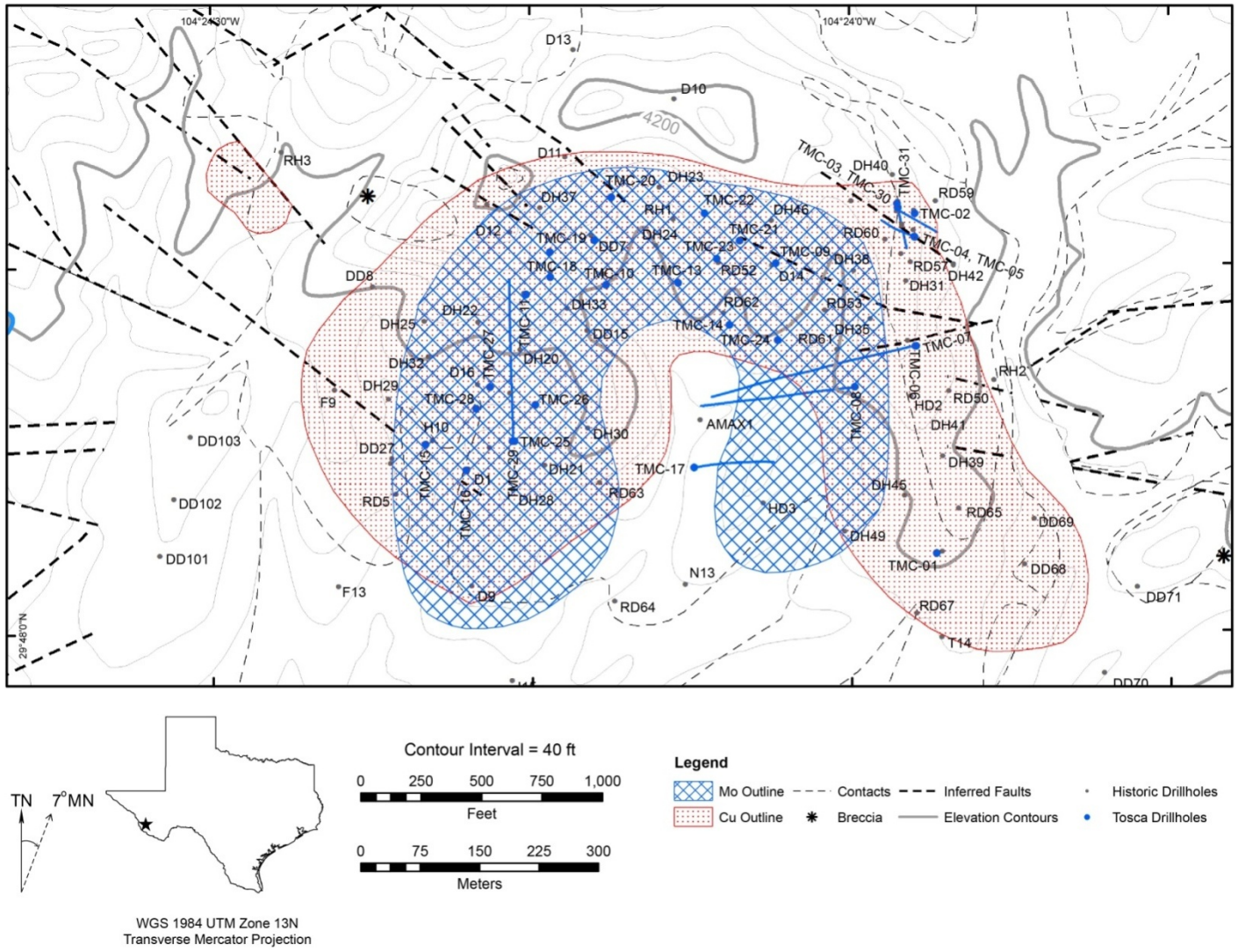

Figure 5.3. Detailed map of Red Hills showing drill hole locations and orientations.

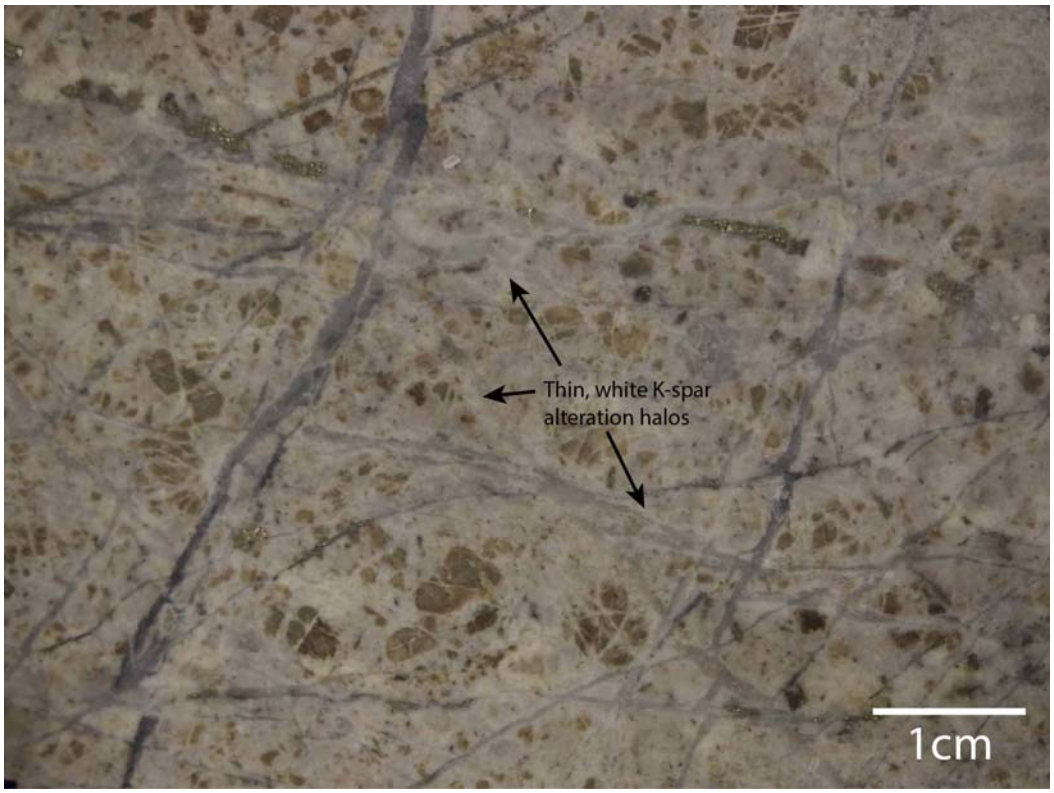

Figure 5.4. Slab of potassically altered QMP overprinted by phyllic alteration in sample TMC25-733. Thin white K-spar alteration halos are widespread around the stockwork veinlets. The K-spar halos have been altered to sericite by pervasive phyllic overprinting. White scale bar represents 1 cm.

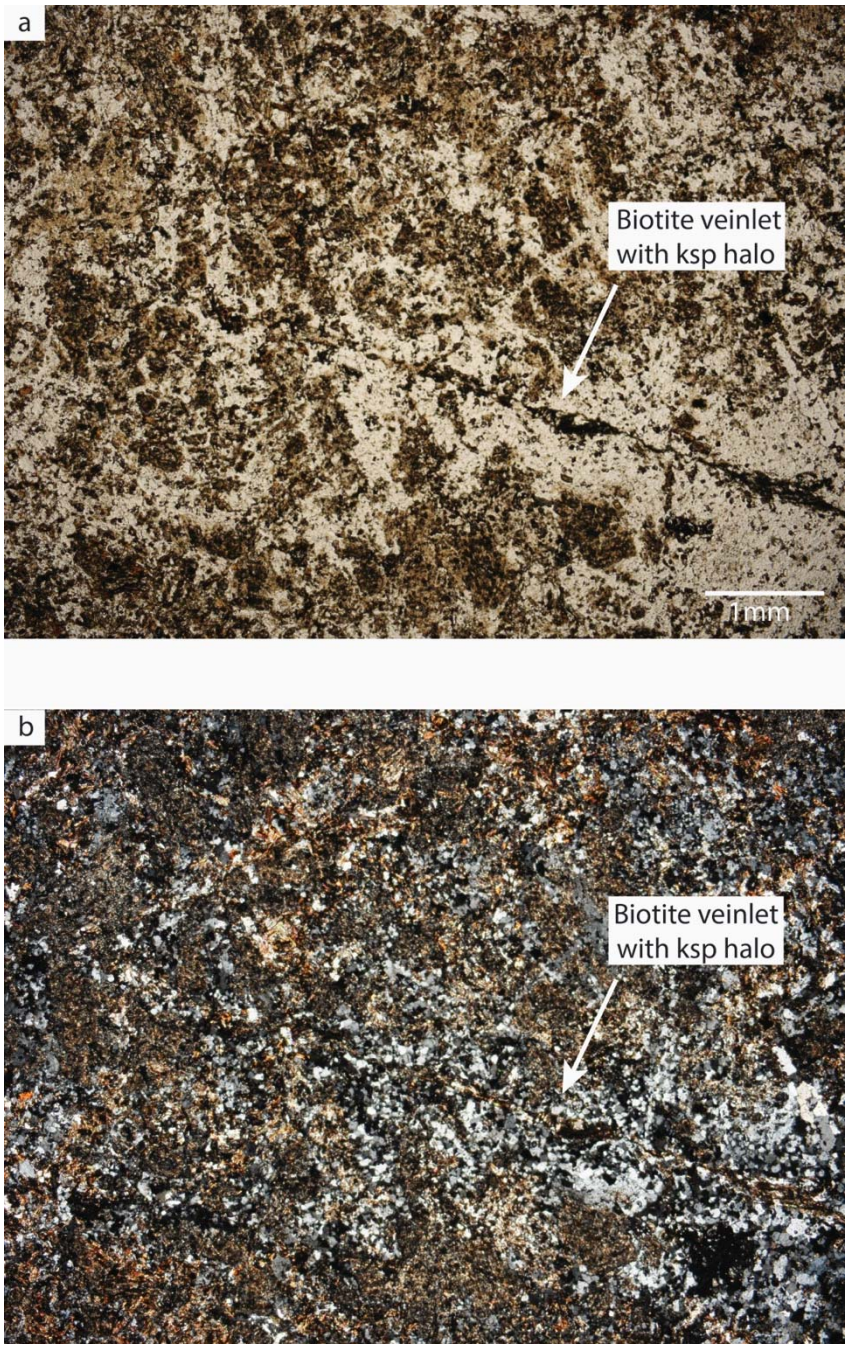

Figure 5.5a. Photomicrograph in plane-polarized light of potassically altered sample TMC12-964 displaying a thin biotite veinlet with a quartz-K-spar alteration halo.

Figure 5.5b. Photomicrograph in cross-polarized light of figure 5.5a displaying pervasive hydrothermal biotization of sample TMC12-964.

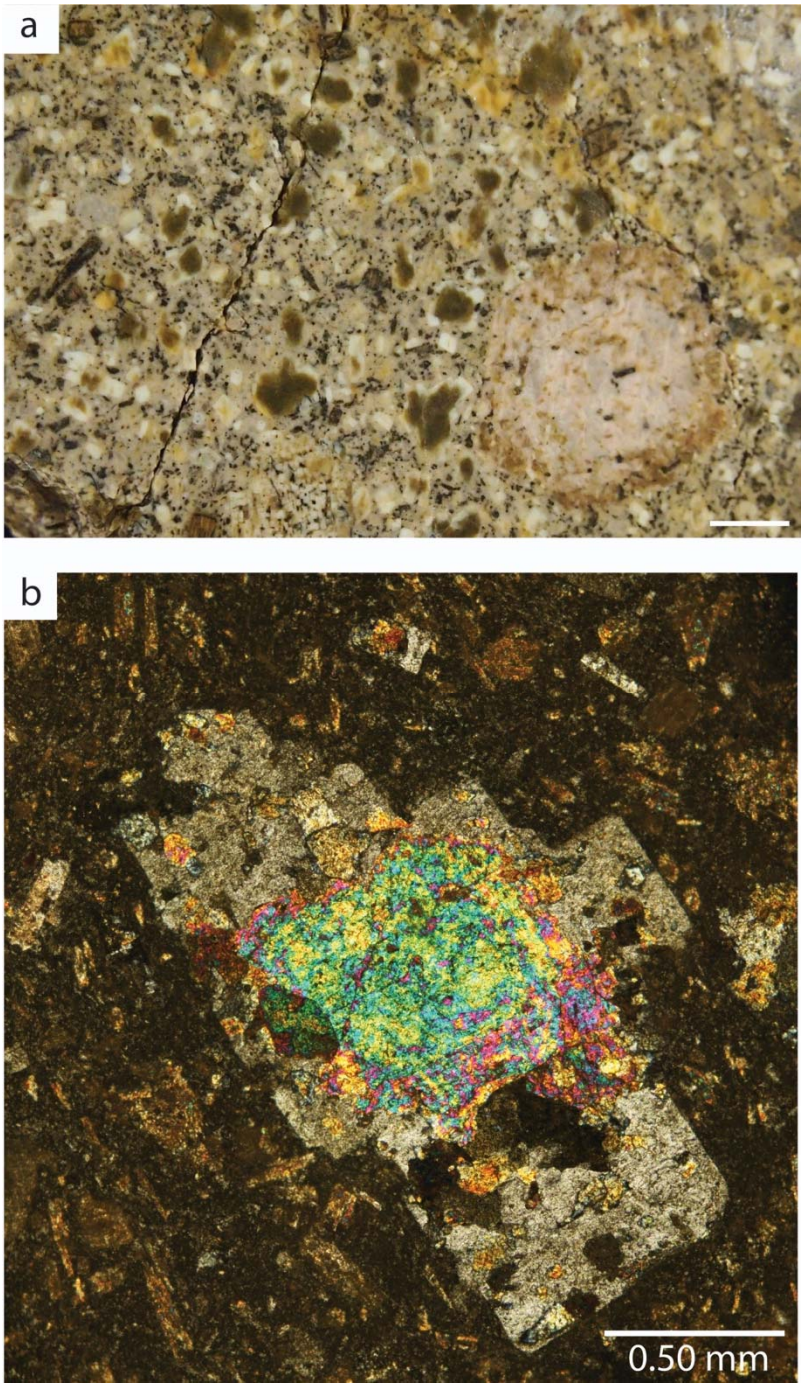

Figure 5.6a. Slab of propylitically altered QMP from sample RH13-21b. Cores of plagioclase phenocrysts have been altered to epidote and biotite inclusions to chlorite. White scale bar represents 1 cm.

Figure 5.6b. Photomicrograph in cross-polarized light of propylitically altered sample RH13-30. Core of plagioclase phenocryst is being replaced by epidote.

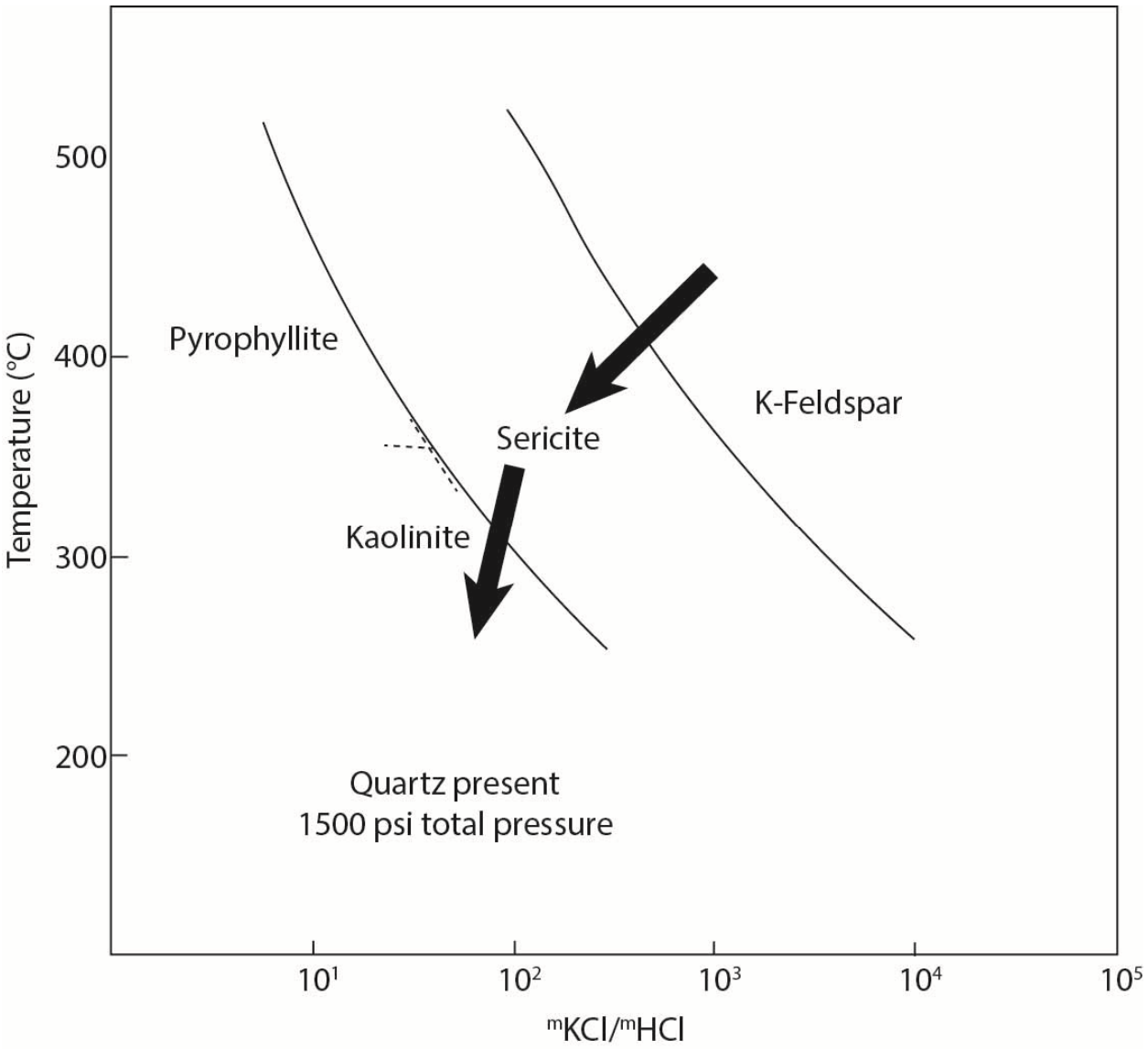

Figure 5.7. Stability diagram of the cooling paths of a hydrothermal solution. Black arrows indicate the path potassic alteration to phyllic alteration to argillic alteration took at the Red Hills. Figure modified from Hemley and Jones (1964).

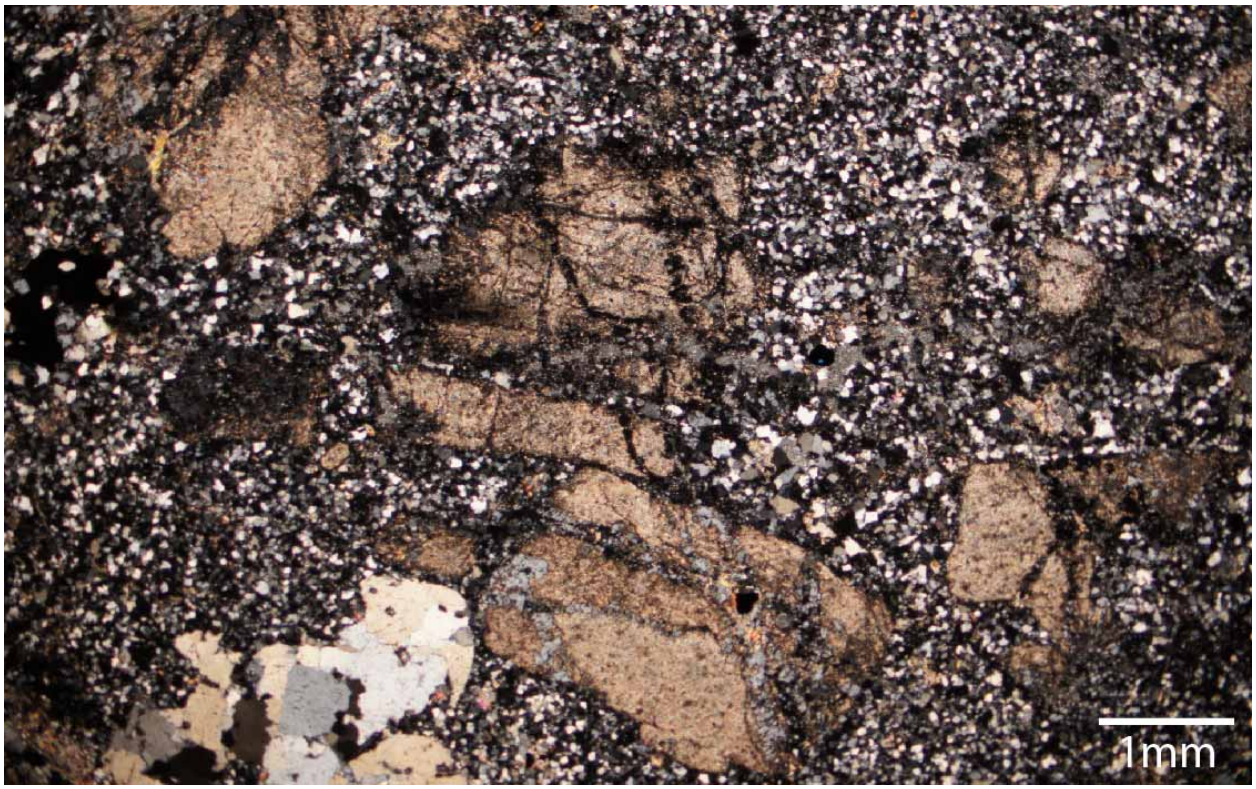

Figure 5.8.Photomicrograph in cross-polarized light from phyllically altered sample TMC26-282. Feldspar are almost completely replaced by sericite encompassed within a fine grained quartz groundmass.

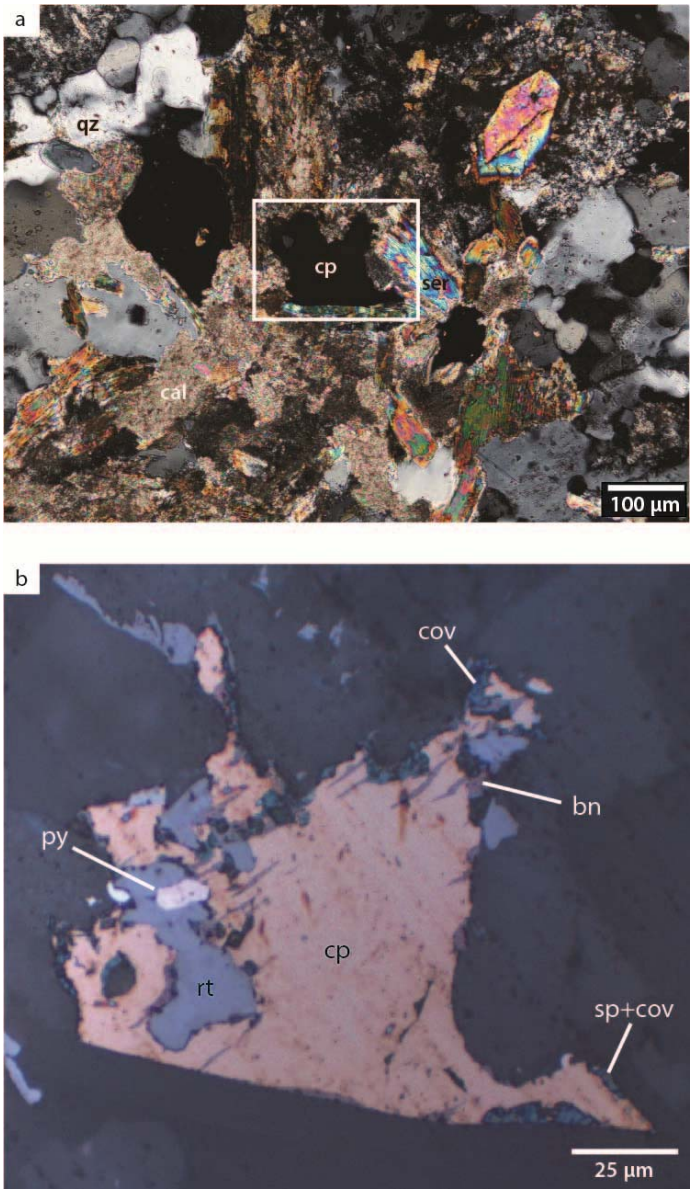

Figure 5.9a. Photomicrograph in cross-polarized light of calcite, phengite, sericite alteration minerals in sample TMC17-1245. White box outlines the area magnified in figure 5.9b. cal = calcite, cp = chalcopyrite, qz = quartz.

Figure 5.9b. Photomicrograph in reflected light in sample TMC17-1245 showing disseminated chalcopyrite grain contains minor bornite exsolution lamellae. Covellite and minor sphalerite is replacing the chalcopyrite along grain boundaries. bn = bornite, cp = chalcopyrite, cov = covellite, py = pyrite, rt = rutile, sp = sphalerite.

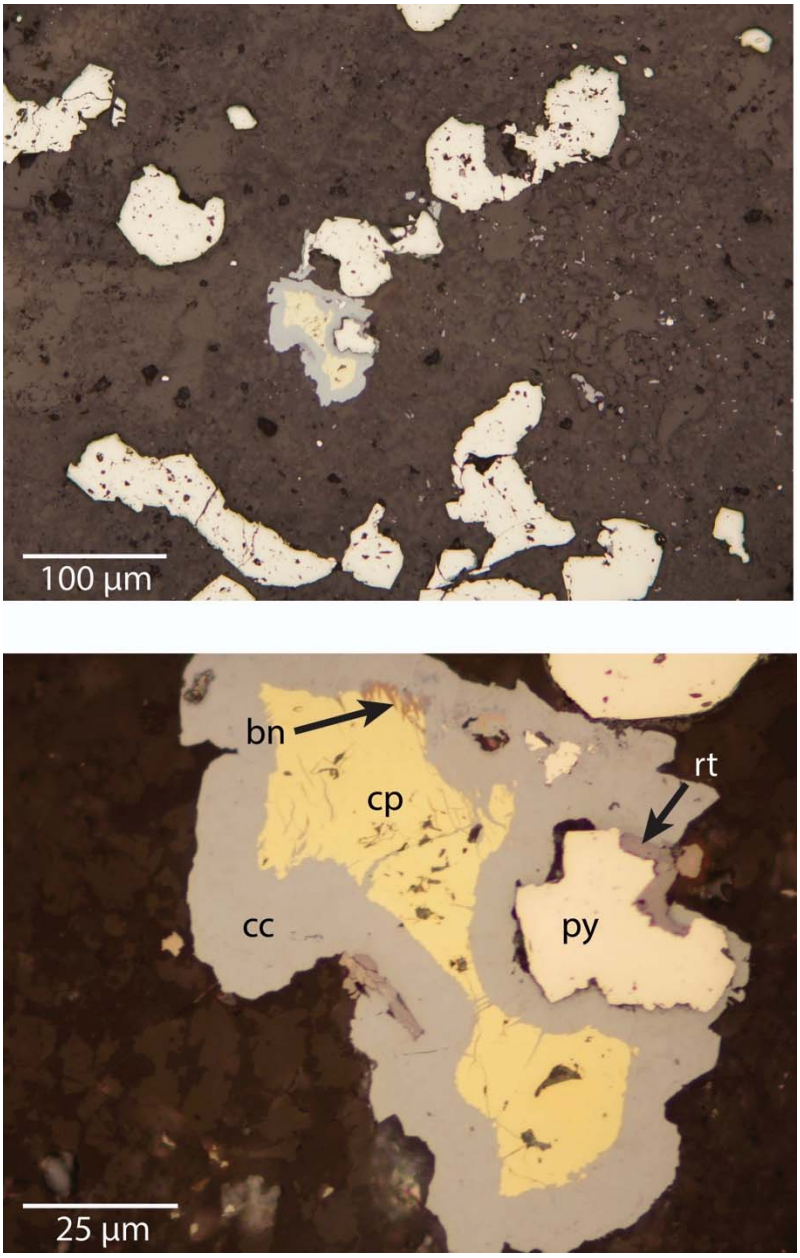

Figure 5.10a. Photomicrograph in reflected light of sample TMC18-187 showing disseminated pyrite and chalcopyrite within the fine-grained groundmass.

Figure 5.10b. Photomicrograph in reflected light of magnified image from figure 5.10a. Chalcopyrite core is bordered by a chalcocite rim and contains bornite lamellae near the chalcopyrite to chalcocite contact as well as in the chalcocite rim. bn = bornite, cc = chalcocite, cp = chalcopyrite, py = pyrite, rt = rutile.

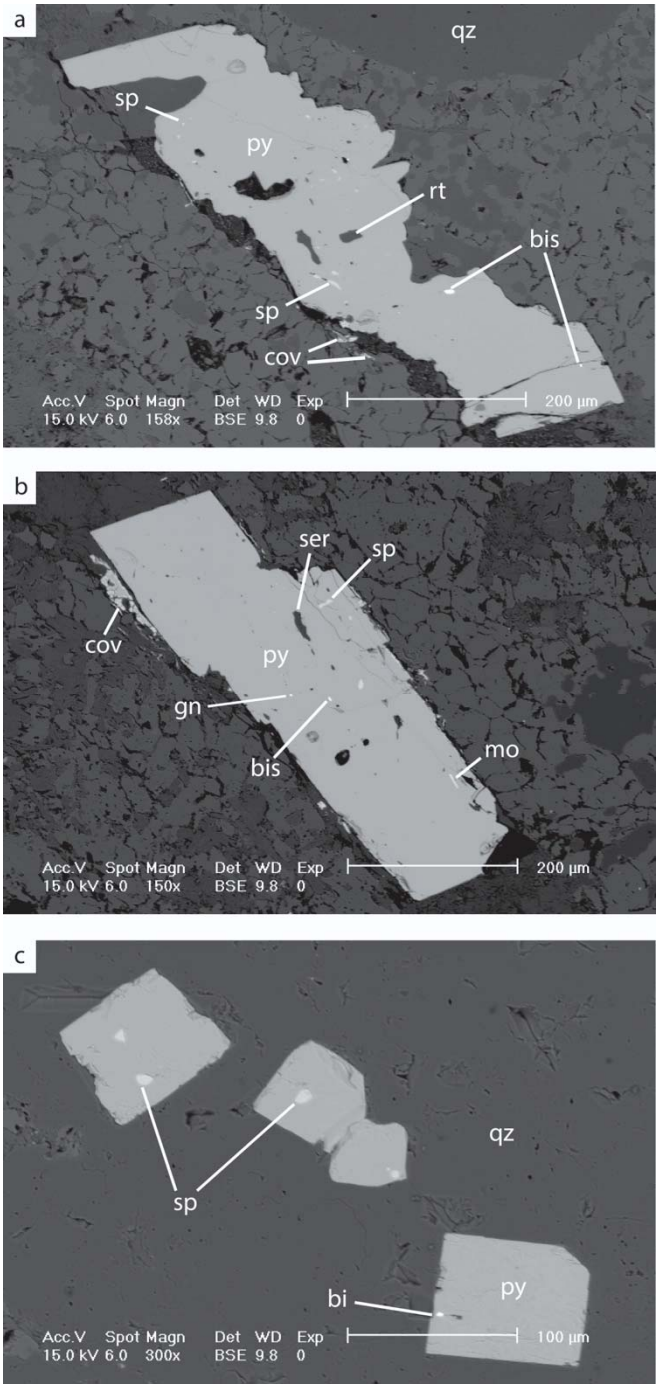

Figure 5.11a-c. Back-scatter electron (BSE) images of anhedral to euhedral disseminated pyrite within the groundmass of phyllically altered sample TMC17-88. Abundant poly-metallic sulfide inclusions are present within euhedral pyrite. bis = bismuthinite, cov = covellite, gn = galena, mo = molybdenite, py = pyrite, qz = quartz, rt = rutile, ser = sericite, sp = sphalerite.

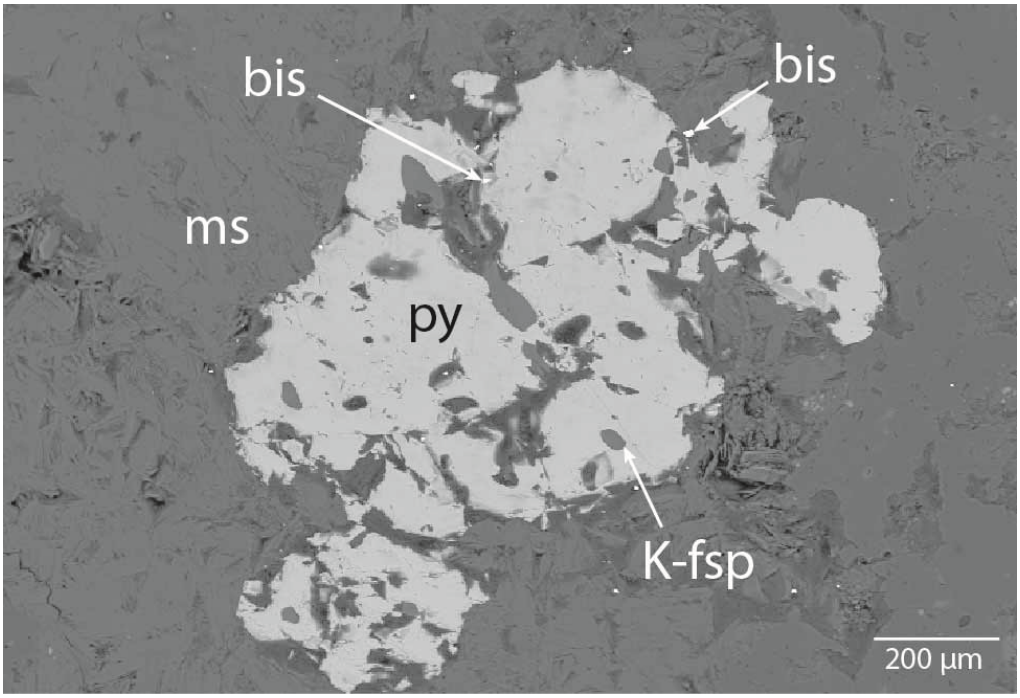

Figure 5.12. Back-scatter electron (BSE) image of an anhedral, disseminated pyrite within aplite crenulate layer of brain rock from sample TMC14-31 displaying bismuthinite micro-inclusions within pyrite. bis = bismuthinite, K-fsp = K-feldspar, ms = muscovite.

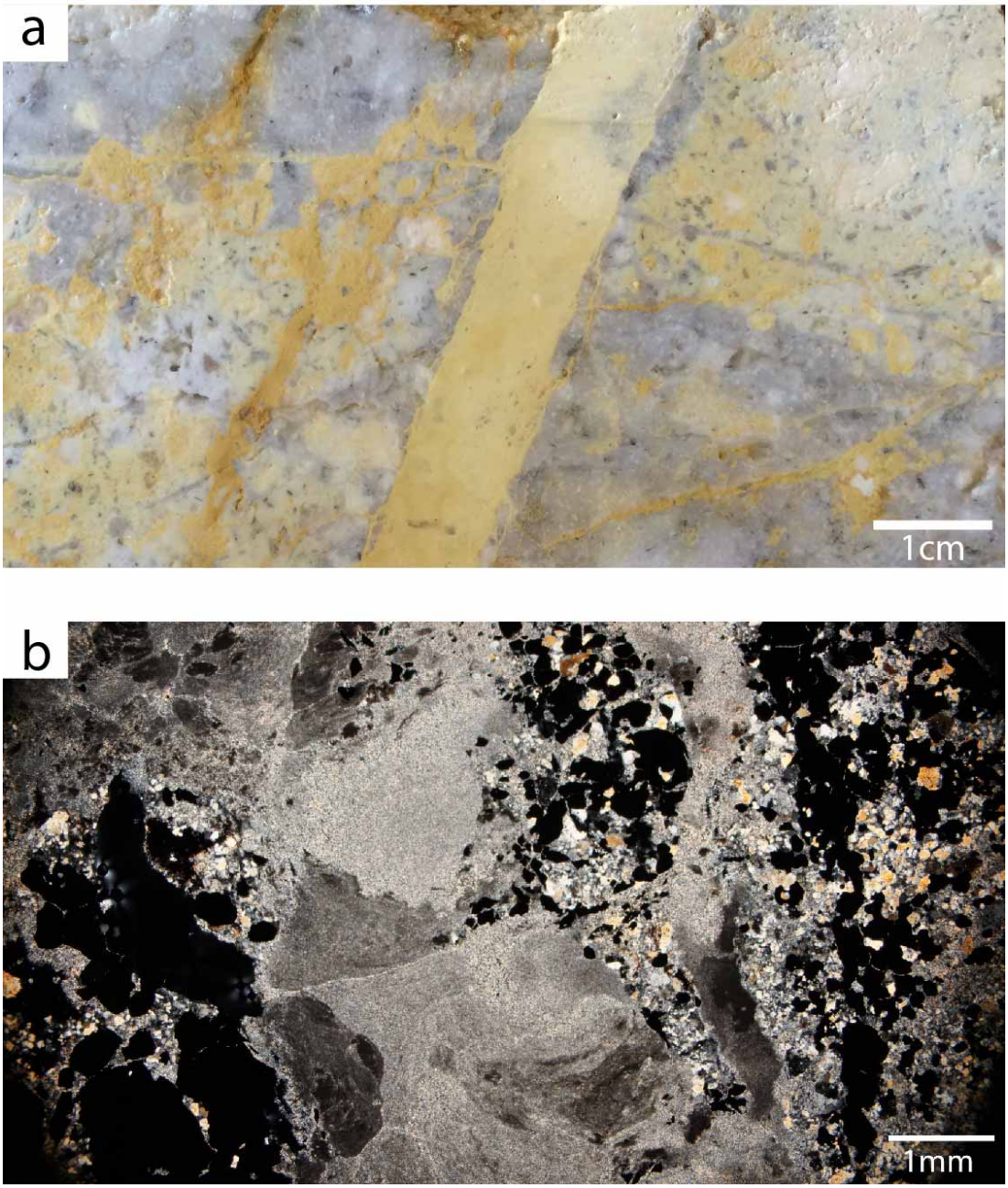

Figure 5.13a. Slab of argillically altered QMP from sample TMC30-87 showing feldspars completely altered to kaolinite and a 1 cm wide supergene alunite vein.

Figure 5.13b. Photomicrograph in cross-polarized light of argillically altered sample TMC15-258 showing massive, fine grained kaolinite.

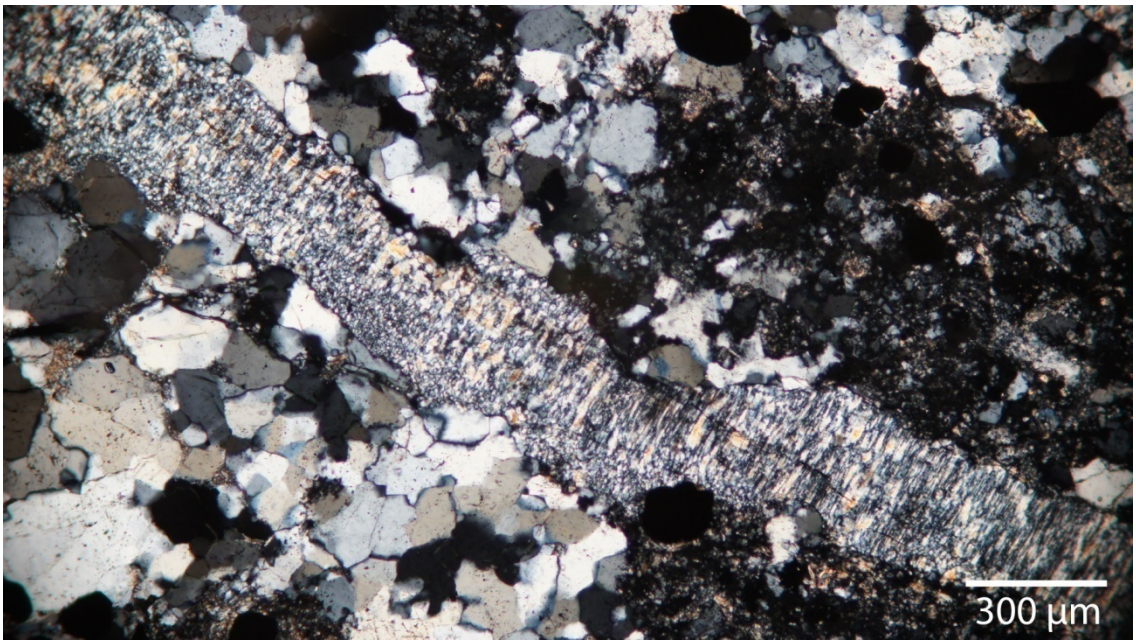

Figure 5.14. Photomicrograph in cross-polarized light displaying coarsely bladed, hypogene alunite vein in sample TMC18-189.

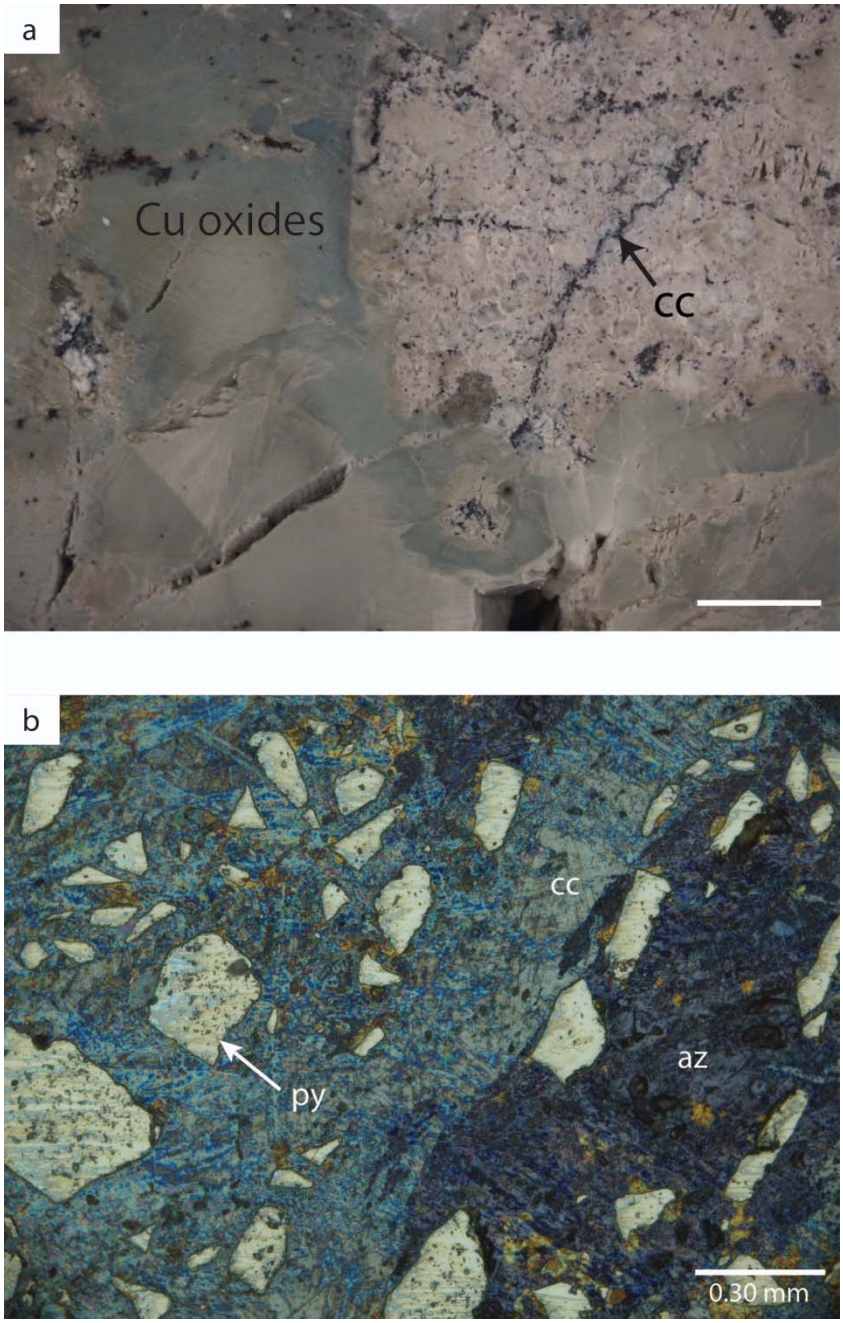

Figure 5.15a. Slab of argillically altered sample TMC3-143 displaying blue copper carbonates and thin chalcocite veinlets. This sample marks the transition from an oxidizing to a reducing environment thus forming the enriched chalcocite blanket beneath the paleowater surface. White scale bar represents 1 cm. cc = chalcocite.

Figure 5.15b. Photomicrograph in reflected-light of chalcocite (left) replacing pyrite and azurite (right) replacing pyrite of sample TMC3-143. py = pyrite, az = azurite.

Figure 5.16 a-c. Slabs of characteristic oxide alteration in the Red Hills leach cap. White scale bar represents 1 cm.

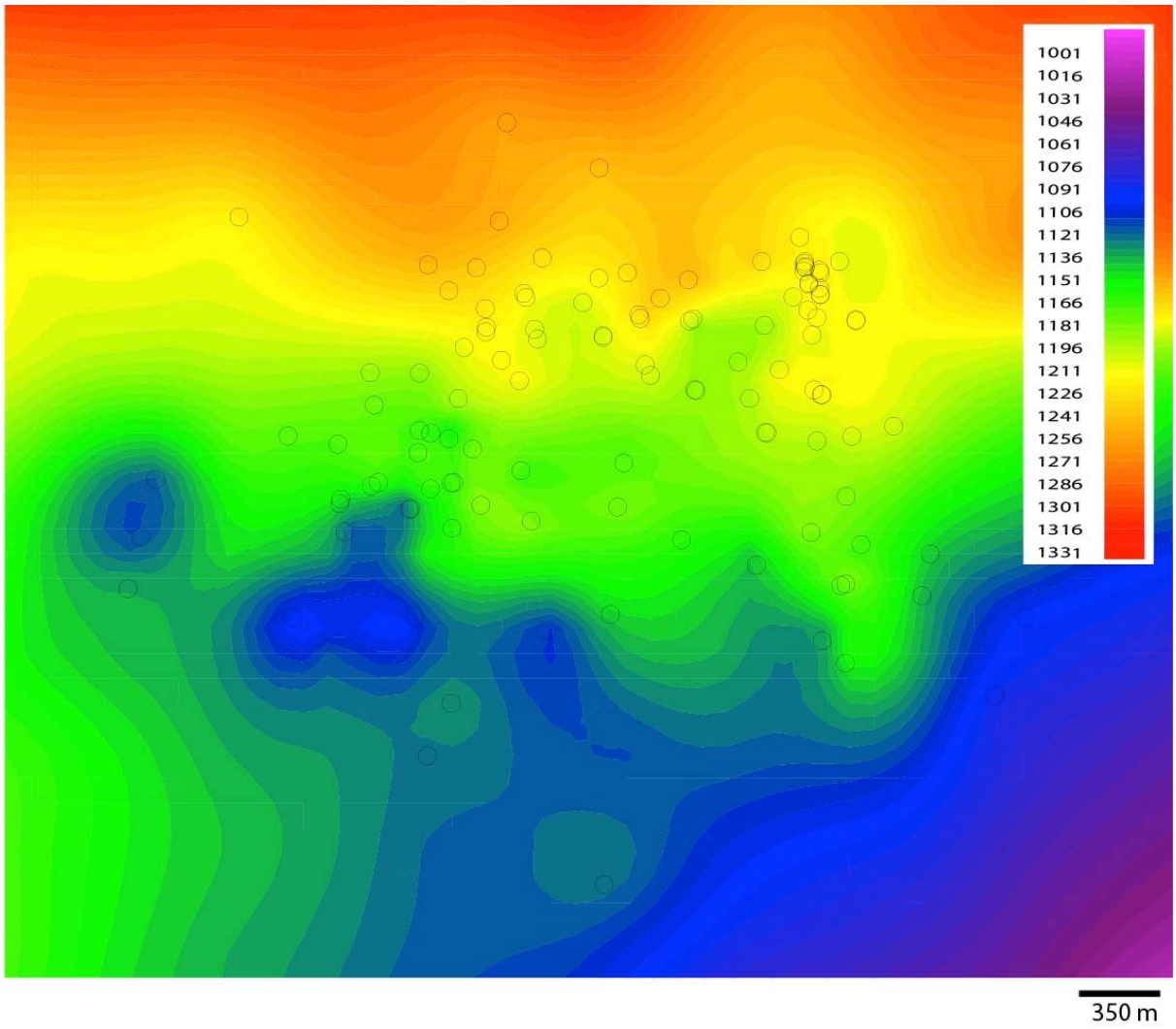

Figure 5.17. Structural map of the base of the oxidized zone, omitting faults, at Red Hills. Black circle outlines represent drill hole locations. Structure contours are 5 m intervals.

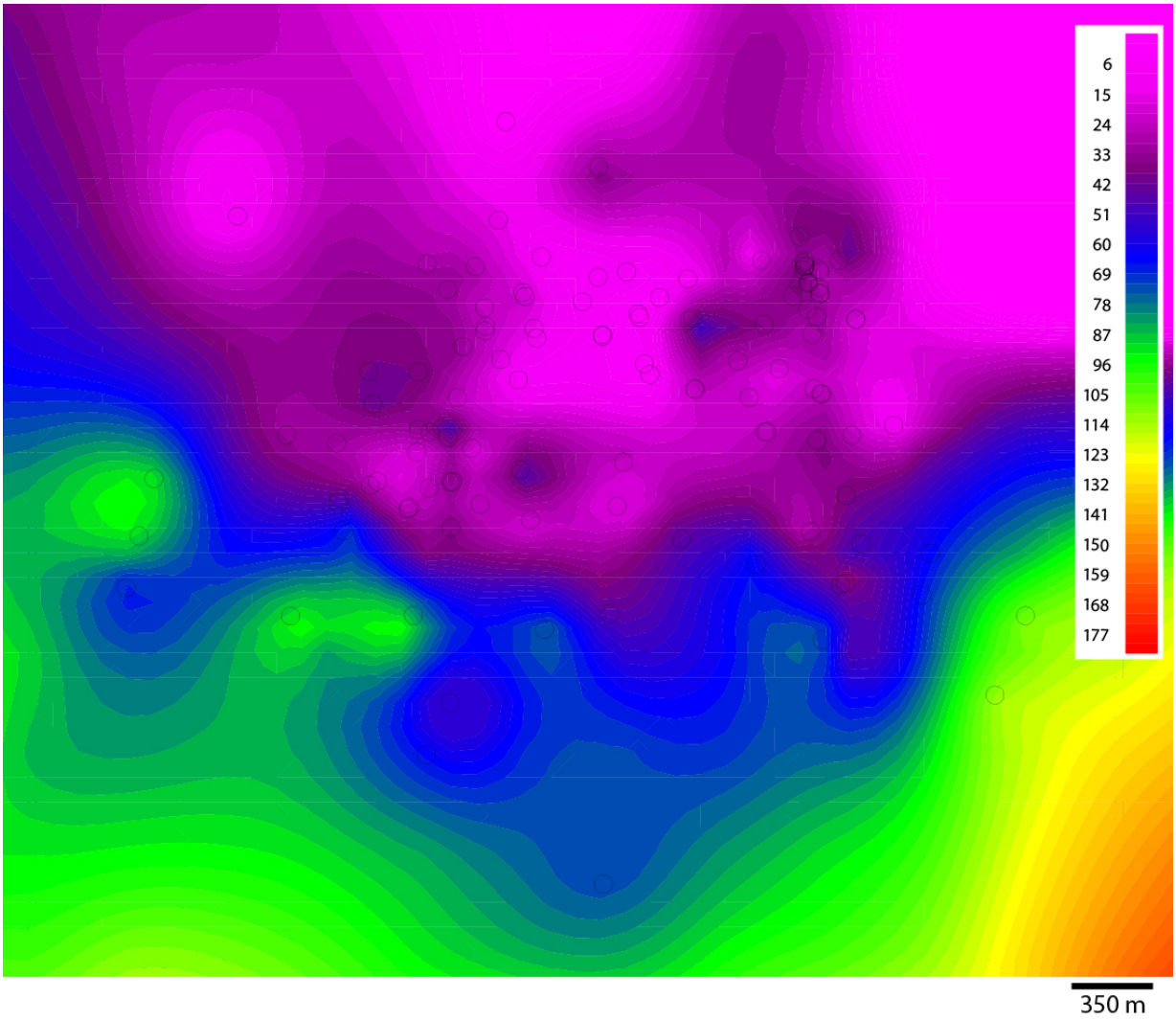

Figure 5.18. Isopach map of net thickness variations within the leach cap at Red Hills. Black circle outlines represent drill hole locations. Legend represents 3 m increments from low to high.

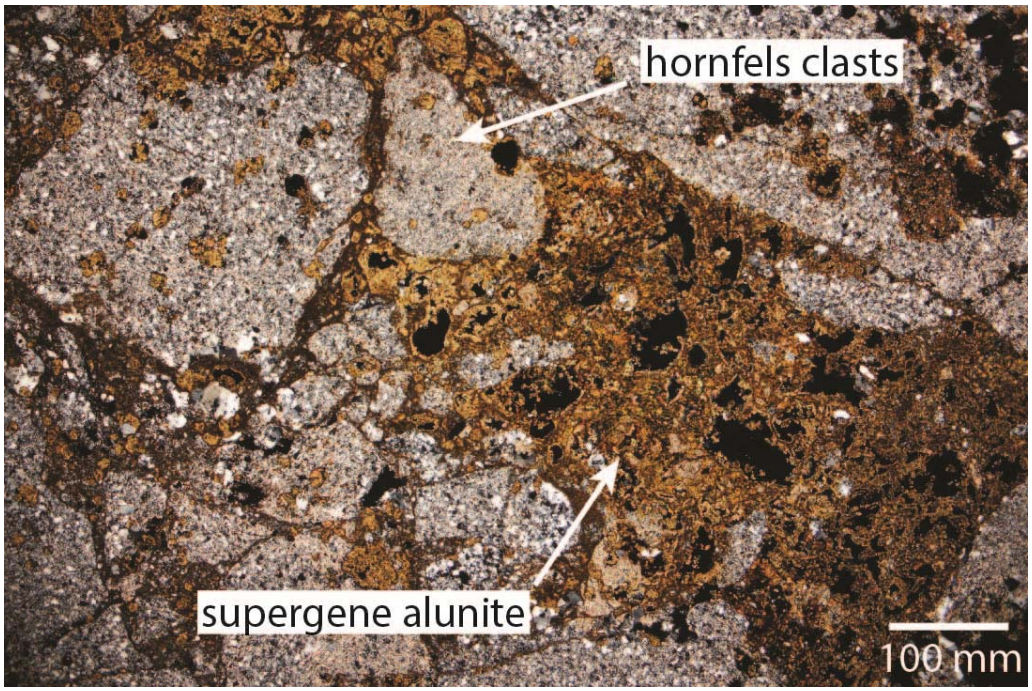

Figure 5.19. Photomicrograph in plane-polarized light of brown, supergene alunite in sample TMC02-18. Alunite cements brecciated hornfels clasts.

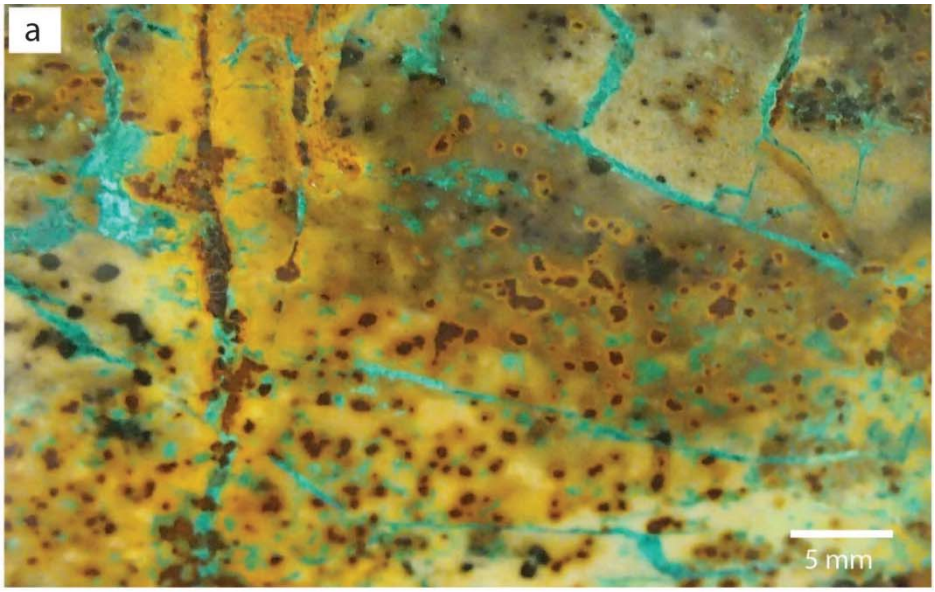

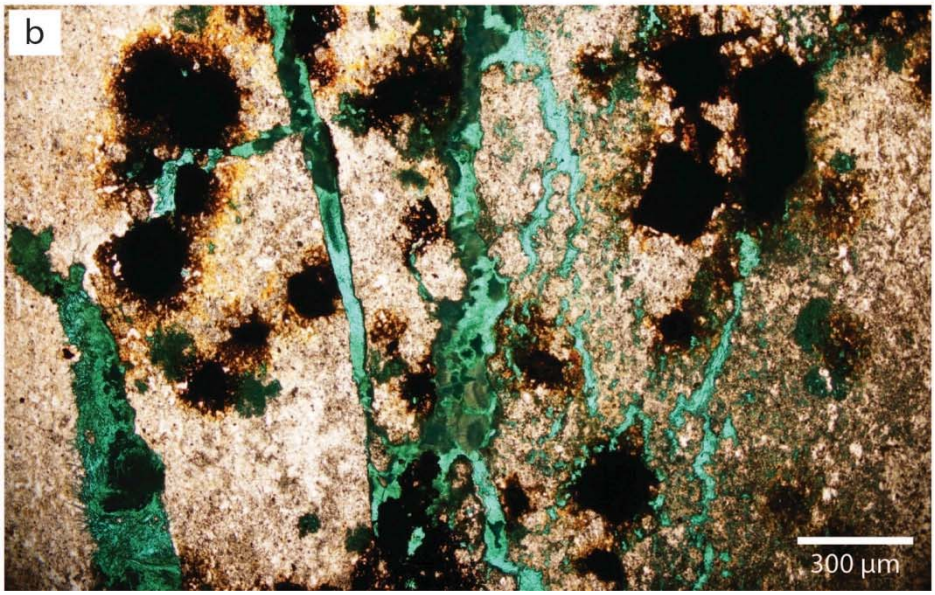

Figure 5.20a. Slab of sample RH13-31. Green-blue chrysocolla along fractures within hornfels.

Figure 5.20b. Photomicrograph in plane-polarized light of sample RH13-31. Green chrysocolla showing radial to fibrous habit within fractures. Dark, circular opaques are goethite partially replaced by hematite.

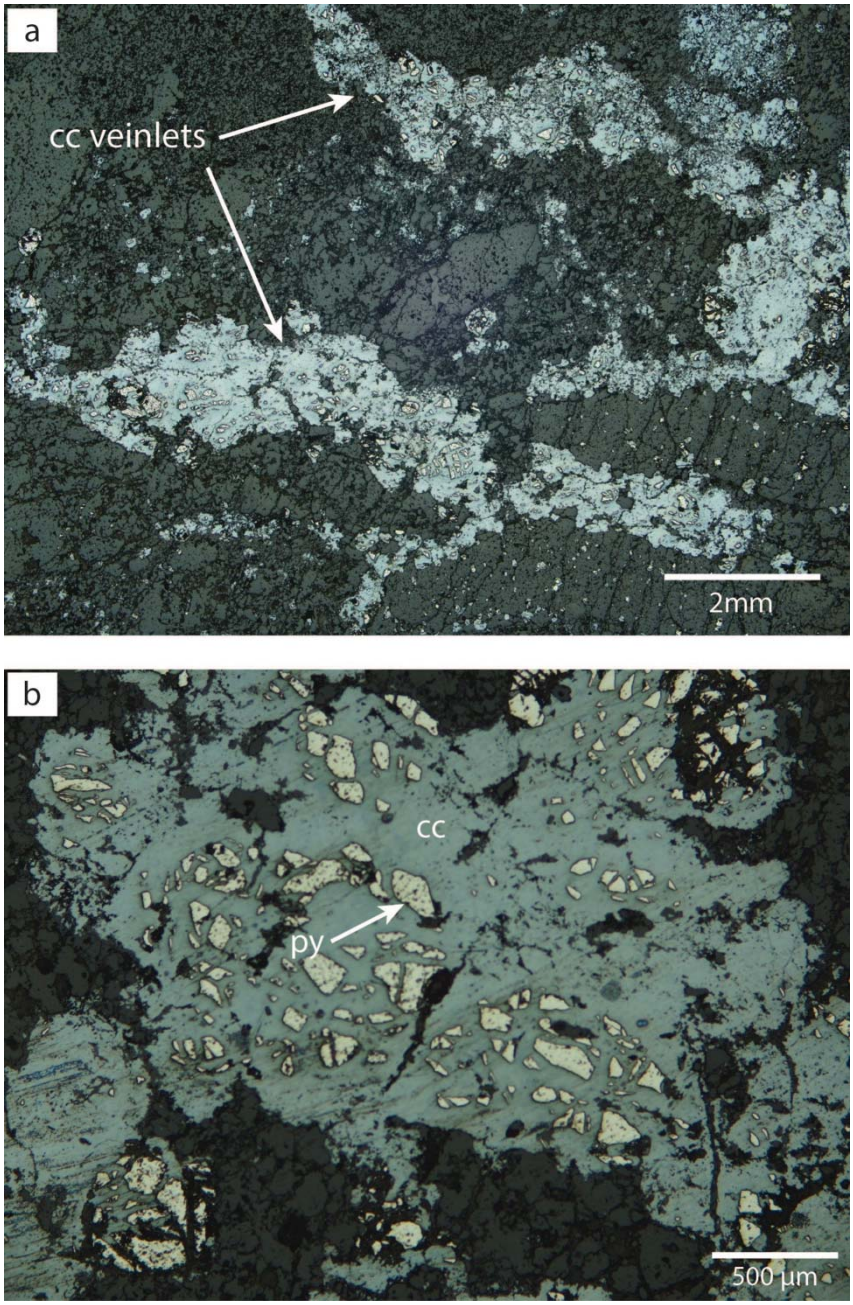

Figure 5.21a. Photomicrograph in reflected-light of chalcocite veinlets in sample TMC-143. cc = chalcocite.

Figure 5.21b. Magnified image of sample TMC-143 in reflected light showing chalcocite replacement of pyrite.

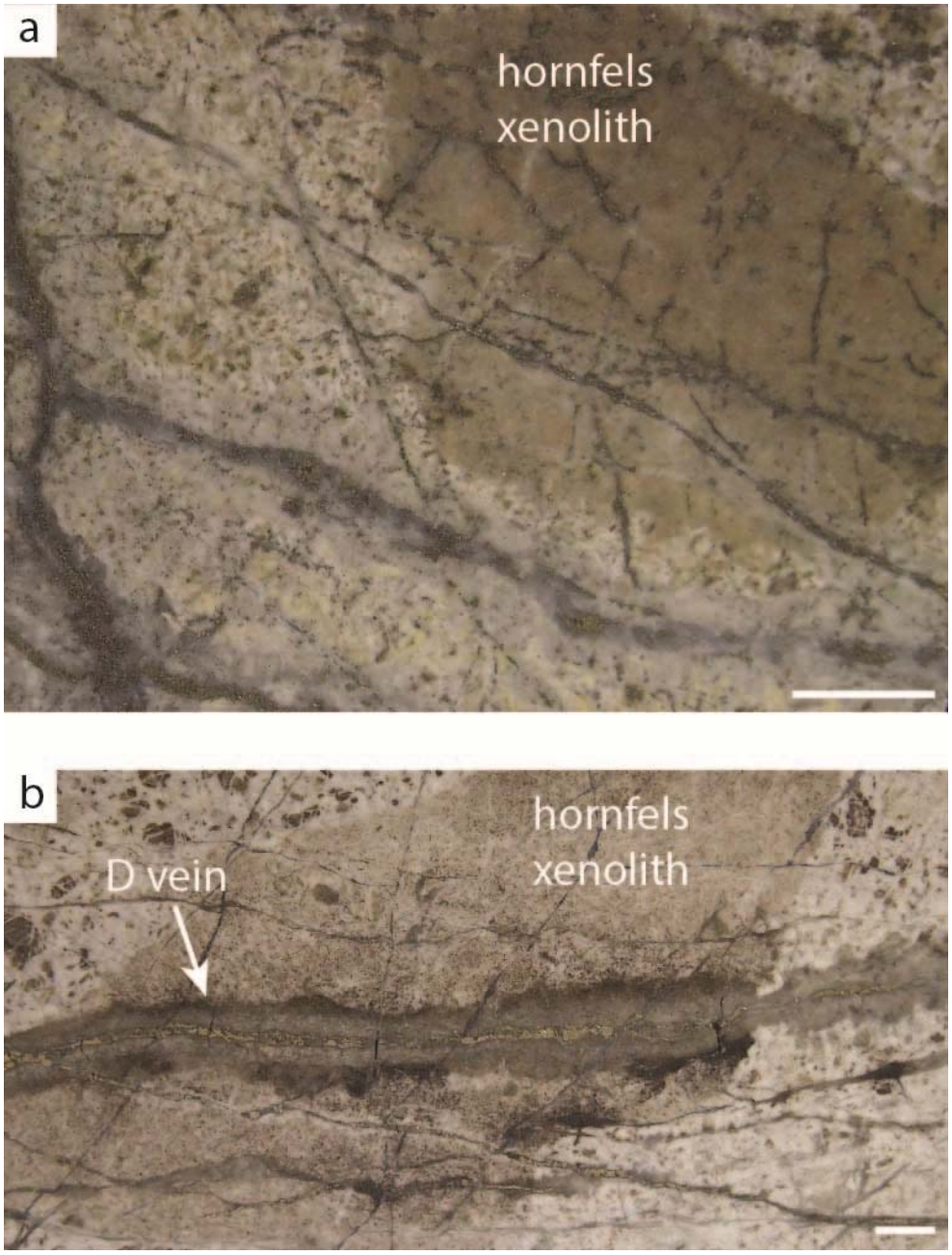

Figure 5.22a. Slab of sample TMC15-336 displaying hornfels xenoliths within quartz-latite porphyry (QLP). White scale bar represents 1 cm.

Figure 5.22b. Slab of sample TMC26-202 displaying differences in alteration character of a D-vein sericite halo between the hornfels and quartz-monzonite porphyry (QMP). White scale bar represents 1 cm.

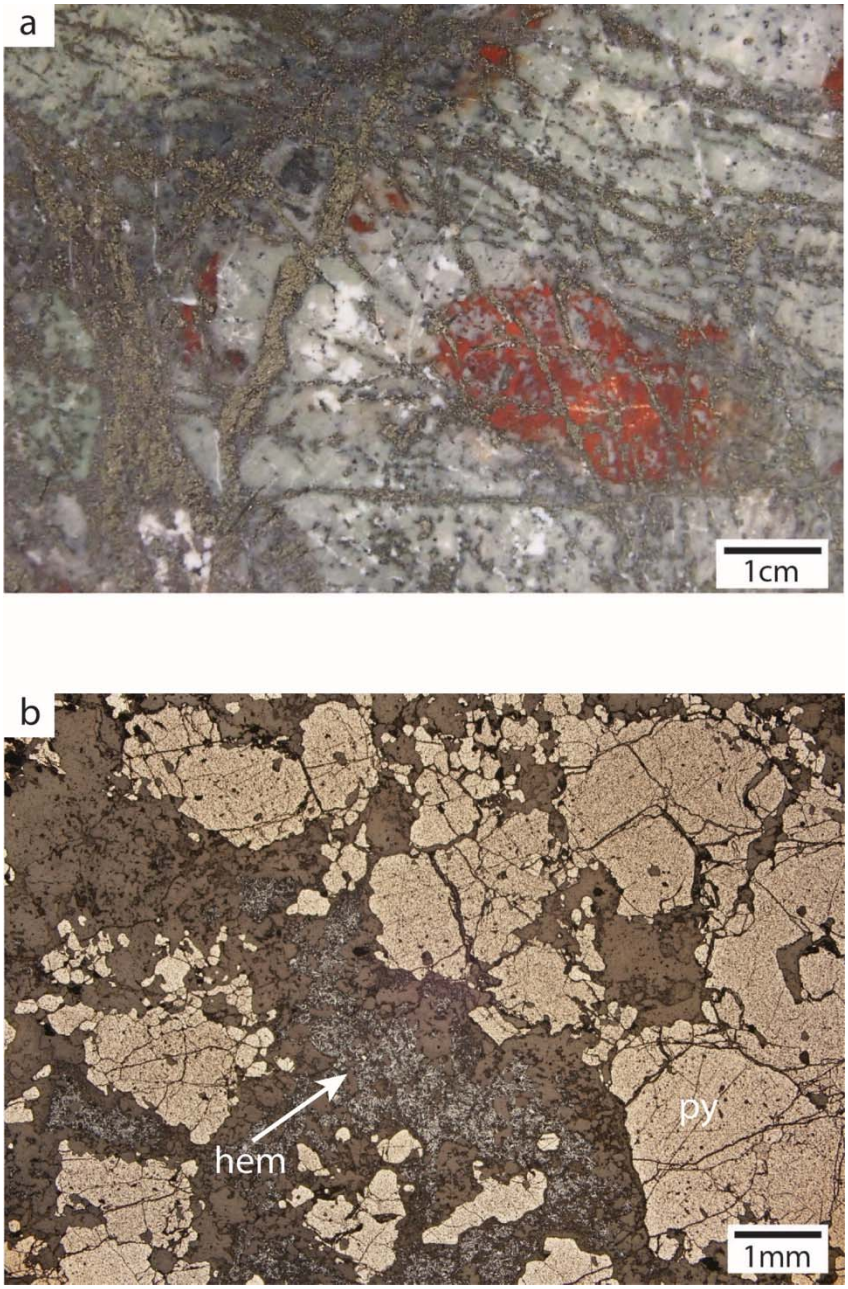

Figure 5.23a. Slab of a highly pyritized hornfels from sample TMC15-258 also displaying large hematite clots.

Figure 5.23b. Photomicrograph in reflected-light of hornfels sample TMC15-258. Massive pyrite is mostly barren but contains abundant, thin microfractures. Fine-grained, bladed hematite is common within the feldspar groundmass.

Chapter 6: Vein Types and SEM-CL Textures in Hydrothermal Quartz

INTRODUCTION

Multiple vein sets generally indicate repeated release of hydrothermal solutions from multiple magma chambers (Proffett, 2003; Sillitoe, 2010). Gustavson and Hunt's (1975) classification scheme of porphyry vein types was generally used to characterize the veins present at the Red Hills. The assignment of vein types was heavily weighted on quartz structure, vein geometry, and cross-cutting relationships with less emphasis on associated sulfides. Similar veining styles occurred with the emplacement of each porphyry intrusion. As mentioned in Chapter 5, the early to late vein sequence at Red Hills is biotite veinlets (only in BP) to A veins to B veins to D veins to hypogene alunite veins (Figure 6.1). Supergene veins of alunite, iron oxides, and copper minerals are superimposed over the hypogene veins.

Scanning electron microscopy cathodoluminescence (SEM-CL) imaging of multi-generational, hydrothermal quartz from separate vein types (Appendix E, Table E-1) was conducted to visualize quartz growth textures to aid in recording changes in the physio-chemical conditions of quartz growth in relation to sulfide deposition as hydrothermal fluids evolved throughout ore genesis. SEM-CL is a near surface phenomenon in which agitated photons are released when an electron beam scans across the surface of a polished thin or thick section (Figure 6.2). These photons emit minor quantities of radiation that is translated into wavelengths within the visible light spectrum. A parabolic mirror guides the light into a photomultiplier tube where a digital CL image is reconstructed. See Appendix B for more detailed description of SEM-CL analytical procedure and image processing.

Intrinsic and extrinsic defects, such as structural defects and impurities respectively, serve as activators or suppressants of CL signals within a solid (Müller et

al., 2003; van den Kerkhof et al., 2004; Götze, 2009; Vasyukova et al., 2013). The solid-state band theory (Figure 6.2) states luminescence will occur when excited electrons travel to lower ground state energies in valence bands, once their transient energies diminish to their original ground state. These electrons must pass through the band gap (space between conduction and valence bands) to return to their ground state energies. The band gap contains abundant traps which represent actual structure defects or impurities. An electron may be caught in this trap until it is able to escape where luminescence will also occur. Currently, definite physical and chemical conditions responsible for variations in CL intensity are poorly known, however, Ti and Al have been suggested to influence high luminescence (Rusk et al., 2008; Leeman et al., 2012; Mercer and Reed, 2013). Nevertheless, this technique reveals a complex paragenesis which is not visible by any other microscopy technique, such as visible or reflected light and secondary electron or back-scattered imaging.

Figure 6.3 shows the most common quartz SEM-CL textures present within the vein quartz at Red Hills. The classification of these textures were heavily influenced by Rusk's (2012) thorough characterization of SEM-CL hydrothermal quartz textures. SEM-CL textures of quartz can be divided into four broad categories: mechanical breakage and dilation, open space quartz growth, dissolution, and recrystallization.

Textures evident by mechanical breakage and dilation are splatter and cobweb (SC) and microbrecciation. Rusk and Reed (2002) used the term *splatter and cobweb* (SC) texture where high density, thin interconnected, transgranular microfractures cut through previous quartz generations in a chaotic fashion. They explain that only porphyry systems exhibit this texture, which is caused by quartz corrosion along microfracture voids into which dark CL quartz precipitates. These fractures typically correspond to trails of secondary fluid inclusions and are strong evidence of repeated fracturing and

fluid fill. Microbrecciation is another mechanical breakage and dilational texture which refers to shards of bright CL intensity quartz engulfed in either dark CL intensity quartz or pyrite.

Embayments and truncations along quartz grain boundaries are common dissolution textures at Red Hills. Dark cores and bright overgrowths (DCBO) in quartz grain is another dissolution texture where moderate CL intensity cores have embayed grain boundaries that are overgrown by bright-luminescent quartz. The dark cores may have originated from a brecciated shard of early quartz that was fractured and dislodged from a vein wall. Pressure drops from unloading by mechanical failure may have caused silica-undersaturated fluids to enter the zone of retrograde solubility (Figure 6.4) that dissolves the bright CL quartz, causing irregular embayments along grain boundaries. Fluid infiltration of lower pressure and temperature silica-saturated fluids typically cement the brecciated quartz grains with euhedral, dark CL intensity quartz. Wavy concentric banding (WCB) is another dissolution feature that contains thin, repeating wavy bands near grain boundary margins on grains that have experienced microbrecciation or grain boundary migration. Successive generations of quartz may nucleate on this embayed core once the hydrothermal fluids exit retrograde solubility and precipitate younger quartz with continuous decrease in CL intensity as the fluids cool.

Open space quartz growth is apparent in veins that contain inward oriented quartz with euhedral growth zones (EGZ). Individual growth zones may vary in CL intensity and may oscillate from bright to moderate to dark luminescence. EGZ quartz may be overgrowths of DCBO quartz, if the appropriate fluid-filled accommodation space is present. Recrystallization of quartz by solid-state processes is evident by mottled to homogenous CL textures where quartz is inherently purified of all intrinsic and extrinsic

defects, suppressing the CL response and leaving previous CL textures untraceable. This texture is prominent near intersections of cross-cutting veins.

EARLY BIOTITE VEINLETS

Early biotite veinlets, Figure 5.5, are locally abundant in BP at thin section scale. These wispy veins are typically a few centimeters long, 0.5 to 1 mm wide, and contain medium-brown biotite and exhibit fine-grained K-feldspar alteration halos indicative of potassic alteration.

A VEINS

A-veins at the Red Hills have been broken into two categories. Early A1 veins are the second oldest veins and contain little to no Mo and Cu. They are assemblages of interlocking granular, milky white quartz, which are typically fine grained (50-200 μm), equant, anhedral, and equigranular. In hand sample, these early A veins are sinuous and typically exhibit pinch and swell structure in randomly oriented stockwork geometry (Figure 6.5 a and c). They are commonly irregular, discontinuous, and segmented. These features indicate the host rock was in a semi-plastic state before the formation of early veins occurred under higher temperature, ductile conditions. The fractures occupied by these veins appear to have been formed before the rock was able to sustain continuous brittle fracture. Later A2 veins appear as radial or concentric fractures, and are more planar compared to their early stockwork A1 counterpart (Figure 6.5a). A-vein quartz consistently displays saccharoidal texture in hand sample with no apparent internal vein structure (due to the absence of parallel fracture walls) that locally have thin, mm-scale, K-feldspar alteration halos. Vein thickness ranges from 0.2 mm to 1.1 cm, whereas thicker, sheeted veins are likely the product of multiple episodes of vein re-opening, quartz recrystallization, and new generations of quartz deposition. A veins are typically

barren but may have local pyrite and minor molybdenite present along the center of the vein or along quartz grain boundaries, respectively.

SEM-CL imaging of A1 and A2 veins reveals two generations of quartz deposition. The first generation quartz in A1 veins (A1 qz1) is anhedral, granular, and has IWGZ CL texture with bright to moderate luminescence. These CL characteristics are not surprising, because early A-vein quartz is considered to form by scavenging silica from the wallrock rather than precipitate in dilational, open fractures like A2-vein quartz (Figure 6.6 and 6.7). Hydrothermal quartz in A2 veins (A2 qz1) contain inward but randomly-oriented, prismatic crystals with EGZ (Figures 6.9 to 6.10). Transgranular microfractures containing non-luminescent quartz post-date A-vein formation. If intense, brittle fracturing is sustained after the development of A veins, microbreccia- or SC-textures can form. Microbrecciated quartz clasts can show multiple episodes of dissolution and reprecipitation of quartz by pressure fluctuations with changing hydrostatic conditions or by episodic variations in temperature where quartz enters the retrograde or prograde solubility zones (Figure 6.11 and Figure 6.4). If A-vein quartz is partially recrystallized, primary defect sites will anneal, suppress the CL response, and show a homogenous to mottled CL texture (Figure 6.7 and 6.12). This texture may form simultaneously with the onset of A2 qz1 deposition.

B VEINS

B veins derive from dilational fractures under more brittle conditions compared to ductile A veins. They typically cut and offset A veins, and tend to be more planar, continuous, and steeply angled (Figure 6.5b). Sinuous B veins are interpreted to be re-opened A veins. Fine grained, equant quartz, similar in morphology to A-vein quartz, typically lines the margins of B veins, which act as a substrate for coarser, pale gray,

vein-filling prismatic, euhedral inward oriented quartz. All B veins display internal asymmetry that is likely due to the irregularities of the substrate quartz on which it nucleate. B veins rarely have K-feldspar alteration halos that are altered to sericite by phyllic overprinting.

The bulk of Mo mineralization in the form of molybdenite is hosted within B veins, which occur along the margins of the vein as "railroad tracks" where they are situated in between grain boundaries of the fine-grained quartz substrate. B vein fragments have been observed in BQMP, thus indicating that magmatic activity was ongoing during quartz-molybdenite mineralization episodes. Sheeted B veins, Figure 6.5b, occur at the brittle-ductile transition, where extreme pressure fluctuations between lithostatic and hydrostatic unloading forces magmatic fluids to flash to form low density vapor and high density brine fluids as seen by vapor-rich and high-salinity multiphase fluid inclusions (Gilmer, 2001; Muntean and Einaudi, 2001). These veins have been interpreted to have formed at shallower depths compared to A veins. Vein centers may be completely closed by quartz crystal faces terminating at the centerline, but vuggy vein centers at Red Hills form locally. Pyrite may occasionally fill the vein center if the vein was re-opened by D-style veining (Figures 6.5 b and c) and late-stage barite may occupy vugs (Figures 6.13 and 6.14). B vein thicknesses range from 0.2 mm to 8.5 mm.

SEM-CL imaging of deep B veins show "substrate" quartz with IWGZ texture with prismatic quartz overgrowths that have thin euhedral growth zones (Figure 6.14 and 6.15). Mo mineralization exists along the vein margins and in between grain boundaries of "substrate" quartz. In CL, sites of Mo deposition emit dark CL intensities that bleed into the bright to moderate CL intensity quartz (Figure 6.16), indicating that molybdenite was precipitated after quartz precipitation. These veins maintained enough porosity to allow Mo to be deposited in these pores. Another scenario of Mo deposition occurs

during microbrecciation, where dark CL quartz and molybdenite comprise the groundmass that cements early bright-CL quartz (Figure 6.17). Occurrences where late shearing has offset the prismatic quartz at micron-scale throws show dark-CL quartz precipitating in the healed damage zone. This dark quartz may either be euhedral or show rhythmic banding, most likely caused by continuous sheering focused along the same fault plane. In scenarios where D-veins have re-opened B-veins, centerline damage zones reveal dissolution surfaces of prior quartz generations that are overgrown by dark CL-intensity, euhedral quartz when pyrite fills the remaining space within the vein (Figure 6.18 and 6.19). Late stage fracturing that produces closely spaced fracture zones may allow access for hydrothermal fluids that cause earlier quartz to recrystallize and exhibit dull, homogenous to mottled CL textures.

Shallow B-veins display considerably different textures compared to deep B-veins (Figures 6.18 to 6.21). Mo deposition occurs along the margins of the vein as “railroad tracks” similar to B veins. Locally, molybdenite grains show zonations (Figure 6.20 c) that may be due to differences in Re concentrations (McCandless et al., 1993). In CL, this vein displays intense microbrecciation where quartz breccia clasts display cyclic quartz dissolution and reprecipitation events of bright to progressively moderate intensity CL, cemented by dark CL quartz. WCB is evident near grain boundaries adjacent to fractures (Figure. 6.23).

Sheeted B veins exhibit all textures listed within Figure 6.3. Vein transects along sheeted B-veins as seen in Figure 6.24 show early quartz grains have a patchy to mottled, bright-luminescent core, overgrown by an intermediate-CL rim at quartz grain boundaries, that may be a product of grain boundary migration as those grains are partially annealed. Repeated brittle fracture has wiped out many CL growth textures, except in the last phase of quartz growth which exhibit euhedral, bright-CL quartz with

EGZ located near the center of the vein. Large secondary fractures cut through the sheeted vein and deposits euhedral, dark-CL quartz. Subsequent fracturing by late tectonic activity may refracture the vein and form microbreccia textures in which shards of earlier quartz generations are engulfed by the sericite matrix.

D VEINS

D-veins are generally characterized as sulfide dominant, pyrite veins with quartz-sericite-pyrite alteration halos that form during the onset of phyllic alteration. At Red Hills, this D-vein description fits the category of D1 veins (Figure 6.25). D2 veins that post-date D1 veins are pyrite veins without alteration halos (Figure 6.25a). Both D1 and D2 veins are planar in geometry, locally vuggy, and cut all vein types. These veins range from 0.5 mm to 1.5 cm in thickness and are continuous for tens of meters. Where quartz is present, it is generally white to clear in color and is typically euhedral which suggests that these veins form by open-space filling.

D-vein quartz displays the most complex CL textures of any vein type. This in part may be due to the complexity of identifying "true" D-vein quartz versus A and B vein quartz that has been re-opened by D-veins. D1 quartz grains may exhibit dark cores and bright overgrowths (DCBO) with a drowned-out CL response caused by recrystallization by the influx and deposition of dark-CL quartz with pyrite parallel to the vein axis (Figure 6.26). Figure 6.27 displays microbrecciation of euhedral quartz with DCBO hosted within a dark CL quartz and pyrite matrix. Edges of the euhedral quartz are dissolved with dark CL overgrowths. Brecciated clasts of this quartz occurs within pyrite as well, indicating mechanical breakage of the vein as it was re-opened before pyrite deposition took place. D2-vein quartz is typically inwardly oriented and euhedral, with oscillating dark-CL growth zones (Figure 6.28).

UNIDIRECTIONAL SOLIDIFICATION TEXTURES

UST quartz was also imaged in CL to ascertain the textural variations within brain rock quartz. UST quartz contain abundant rutile needles, indicating that the magmatic or hydrothermal fluid was saturated with rutile as it precipitated. UST quartz displays a high degree of late-stage fracturing, where euhedral quartz with oscillatory EGZ show intense SC textures of dark CL intensity character (Figure 6.29). Some crenulate quartz layers show multiple generations of dissolution and reprecipitation. Bright euhedral quartz displays resorption surfaces that are overgrown by dark-CL, euhedral quartz, known as BCDO texture. WCB and homogenous to blotchy textures are common in locations which are cut by nearby A veins.

HYPOGENE ALUNITE VEINS

Hypogene alunite veins were studied by x-ray diffraction (XRD), x-ray fluorescence (XRF), and energy dispersive spectroscopy (EDS) in drill core. These veins range from 0.5 mm to 2 cm in thickness and occur in the upper portions of the deposit in near horizontal orientations. In hand sample, these veins are white and consist of microcrystalline, porcelain-like alunite with minor pyrite. The dilational fractures that host hypogene alunite veins post-date all D veins at Red Hills. These veins post-date all major vein styles, including late kaolinite veins associated with argillic alteration (Figure 6.30). Although rare, kaolinite veins contain euhedral, inward oriented quartz growing along the vein margins with fine-grained kaolinite occupying the remaining vein space (Figure 6.31 a, b). In CL, this vein quartz has two distinct generations (Figure 6.32). The first generation is a bright-CL intensity clasts with EGZ. The second generation quartz nucleated on early quartz, but has a dark CL-intensity with no apparent growth zones despite its euhedral character.

VEIN PARAGENESIS

Three possible sequences for mainstage vein development and evolution have been determined for quartz-bearing veins at Red Hills, which is illustrated in Figure 6.32. Sequence 1 displays the formation of barren A1 veins. When fracturing occurs within the semi-plastic to semi-brittle magma, the ingress of silica-rich hydrothermal fluids will interact with the host rock by extracting some silica. Replacement fine-grained hydrothermal quartz will form in these fractures, resulting in the formation of IWGZ textures. The temperature of these fluids is too hot for metal-sulfides to precipitate with this early generation of quartz, as seen in path A to B in Rusk and Reeds quartz solubility diagram (Figure 6.4). If these veins do not sustain further disturbance by a secondary re-opening event, these veins may undergo recrystallization, thus annealing the crystal from primary intrinsic and extrinsic defects, which results in a homogenous to blotchy CL texture. Secondary, dark-CL transgranular microfractures (corresponding to secondary fluid inclusion trails) will be formed by later tectonic activity.

The second sequence represents the formation of A2 and B veins. Quartz from scenario 1 may act as a substrate for the overgrowth of euhedral, inward-oriented quartz formed in more brittle environments where fracturing can react in a dilational manner. As the hydrothermal fluids cool, molybdenum can precipitate from the fluids in quartz grain boundaries where porosity is available. As this occurs, trace elements associated with this fluid will fill in defect sites within quartz, resulting in a different CL quartz character. As these fluids interact with the earlier quartz, a dark-CL quartz bleeds into the early quartz primarily in areas where molybdenite is deposited. Once these veins close, late-tectonic activity may form dark-CL, transgranular microfractures across all quartz generations similar to the waning stages of quartz in scenario 1. Prevalent late stage fracturing that

provided greater accommodation space will be filled with dark-CL, euhedral quartz with EGZ symmetrically pointing toward the interior of the fracture.

The third sequence reflects an environment in which fluctuations from lithostatic to hydrostatic conditions, similar to the throttling cupola mechanism of Cloos (2005). In shallow parts of the system, primary growth textures in quartz from early A and B veins can be completely erased and replaced by obscure dissolution textures. If quartz from stage 2b undergoes minor brittle failure and fluids continue to cool, retrograde solubility will occur dissolving the earlier quartz generations. As these conditions change, quartz can resume precipitation of a dark-CL variety that is coincident with the timing of pyrite deposition by D-style veining. This quartz can either display WCB or EGZ texture, depending on the accommodation space available and the rate at which the fluid is transporting through the vein. If these veins close and tectonic activity ensues, microfractures filled with dark-CL quartz can form. In situations where fracturing is focused along a plane, a thick, dense network of microfractures will form, causing the host quartz crystal to recrystallize along the margins of the concentrated network of fractures.

CONCLUSION AND DISCUSSION

The vein sequence for every igneous phase at Red Hills is as follows: early biotite veinlets are followed by early A1-veins and A2-veins. A-veins are cut by B veins, which are in turn cut by D1 and D2 veins. D veins are cut by kaolinite-quartz veins, which are subsequently cut by hypogene alunite veins. B veins host the majority of the molybdenum in the system and D veins carry minor hypogene copper. Veins are typically re-opened by subsequent fracturing and overgrown by later veining styles (i.e. A veins reopened and filled with D-style veining).

SEM-CL of hydrothermal vein quartz from each vein type reveal unique growth patterns and subsequent deformation textures as well as multiple quartz generations within a single vein. Color CL images using red, green, and blue filters shows silicified wall rock luminesces red and hydrothermal quartz luminesces blue. A1 veins display IWGZ textures with bright to intermediate CL luminescence reflecting precipitation under low and steady crystal growth conditions. A2 and B veins show coarse grained, prismatic quartz that nucleate on A1 substrate quartz. The prismatic quartz shows EGZ that may reflect rapid crystallization. Sites of molybdenite deposition show dark-CL quartz bleeding into the earlier quartz generations as a likely product of trace element interaction and substitution between the hydrothermal fluids and quartz grains. Shallow veins in the deposit typically display evidence of multiple dissolution and reprecipitation textures or dynamic recrystallization textures. D1 veins show DCBO, EGZ, and microbreccia SEM-CL textures which range from bright to intermediate to dark CL luminescence. D2 veins show euhedral, coarse prismatic quartz which emits a dark-CL signature.

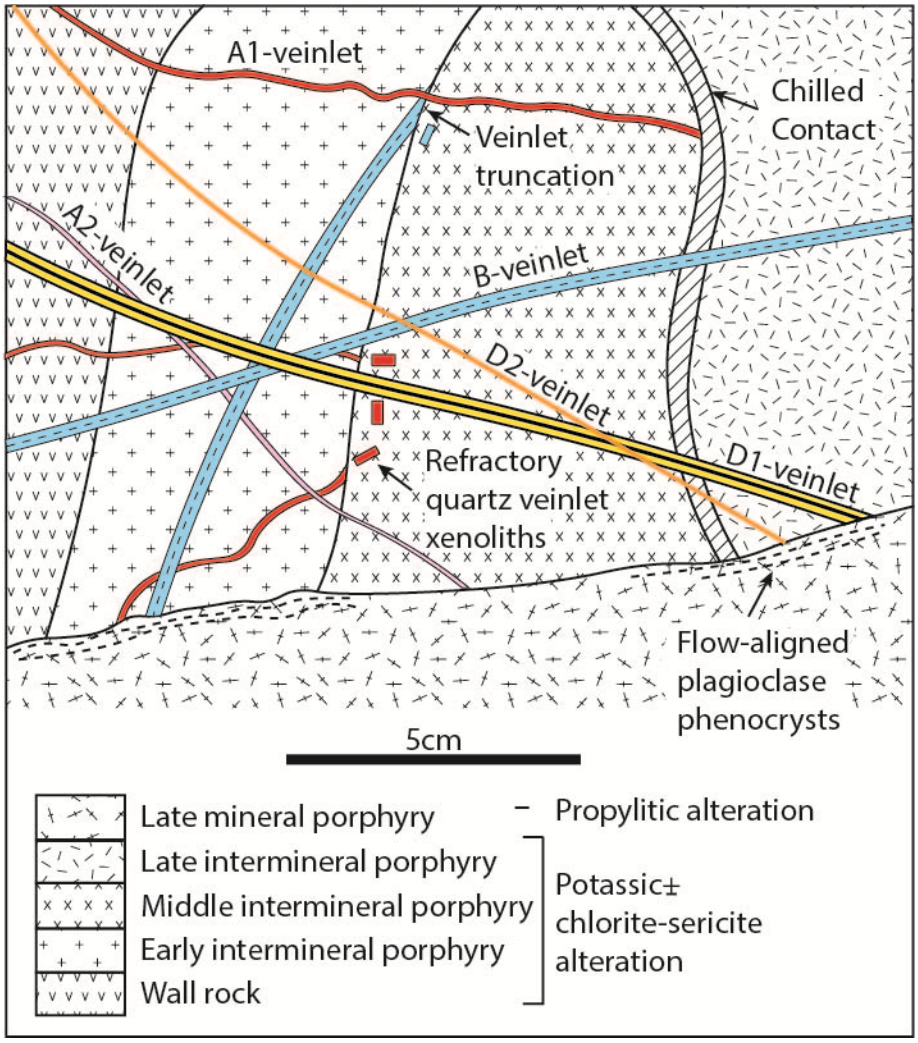

Figure 6.1. Schematic of cross cutting relationships between porphyry phases and vein types typical of porphyry Cu-Mo systems. Figure modified after Sillitoe (2010).

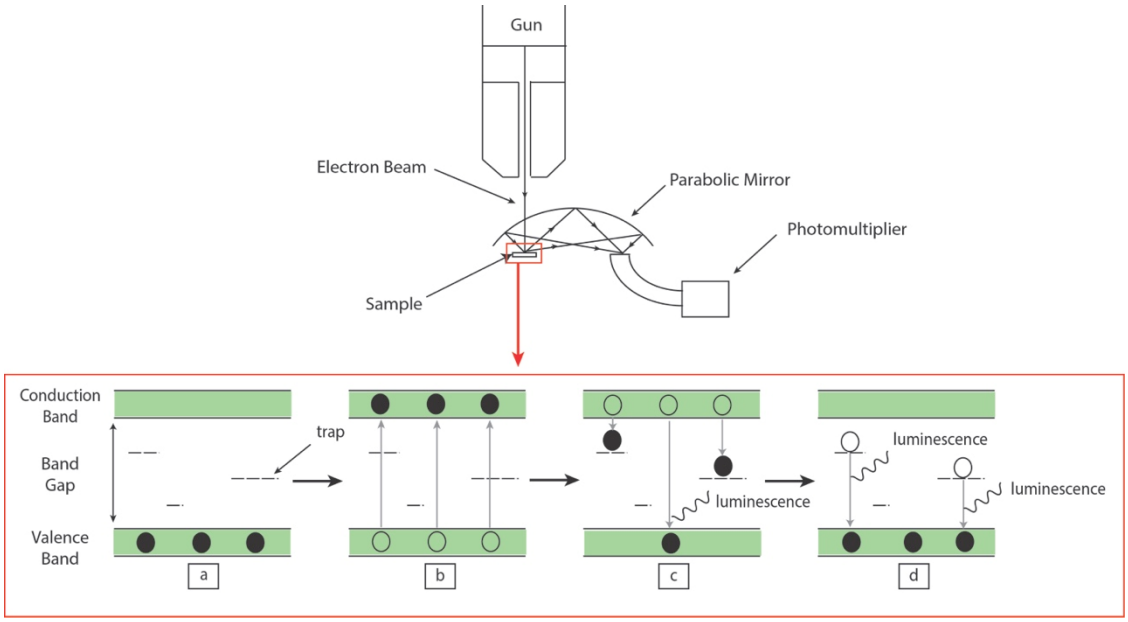

Figure 6.2. Schematic of the solid-state band theory using SEM-CL. Filled circles represent electrons at the location specified in the energy levels at stages a, b, c, and d while unfilled circles represent the prior location of the previous energy stage. a) Unexcited electrons compartmentalized in the valence band at ground state energy, b) electrons excited by electron beam bombardment transition from the valence band to conduction band, c) as the energy diminishes, the electrons will retreat back to the valence band and emit luminescence unless a trap falls within the electron's path, and d) electron's will overcome the barrier trap and return to the valence band causing further luminescence. Figure from Frelinger et al. (2015).

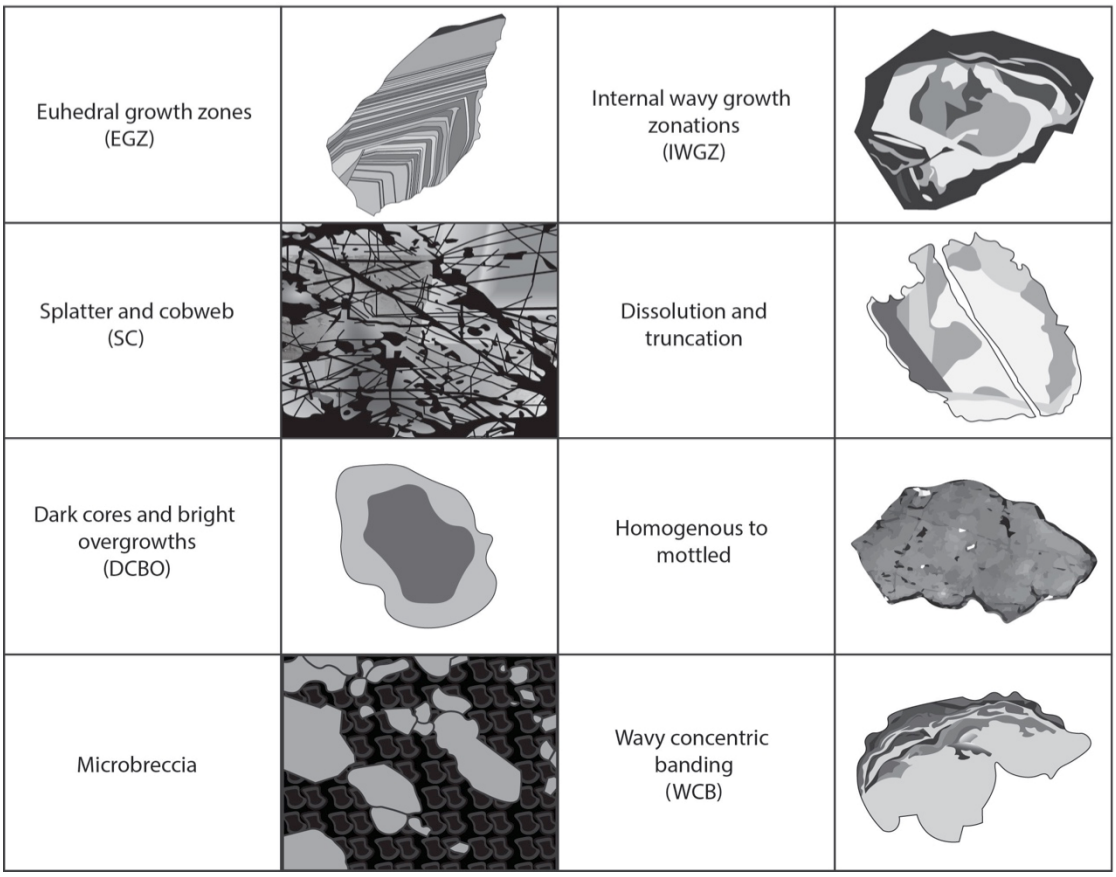

Figure 6.3. Common SEM-CL textures of Red Hills hydrothermal quartz.

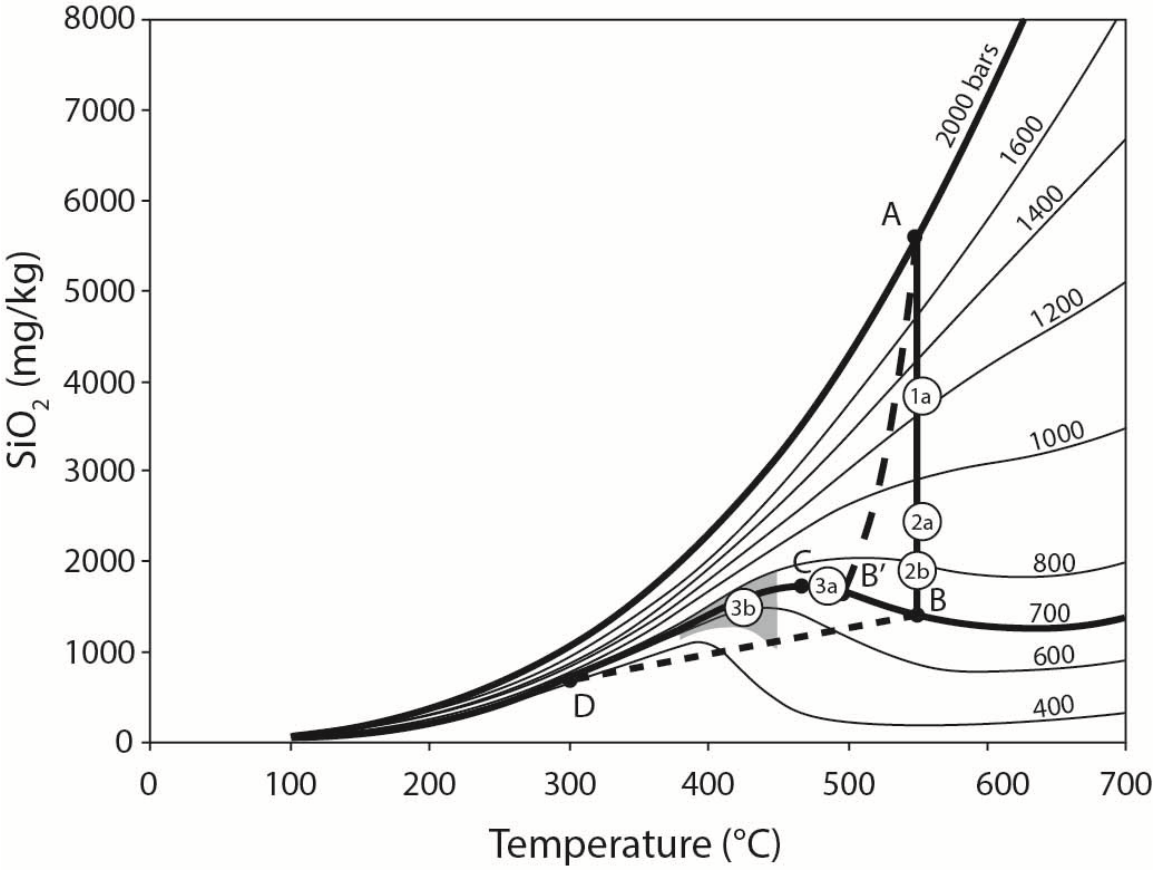

Figure 6.4. Quartz solubility diagram as a function of pressure and temperature from Rusk and Reed (2002). Path A to B represents extreme pressure drop from lithostatic (2000 bar) to hydrostatic (700 bar) unloading in isobaric conditions which is the region quartz 1a to 2c will precipitate quartz. Path B to C represents the conditions of retrograde quartz solubility at 700 bar which 3a broadly fits. As the fluid continues to cool and follow the path below point C at 700 bar, quartz will begin to precipitate once again, stage 3b. Path A to B' is the adiabatic cooling path and B to D is the path of quartz dissolution by fluid cooling. The former is unlikely at Red Hills because the large volume of hot country rock is unlikely to undergo adiabatic cooling. B to D is more likely shallower environments like epithermal environments which is the path where hypogene alunite and kaolinite veins form at Red Hills.

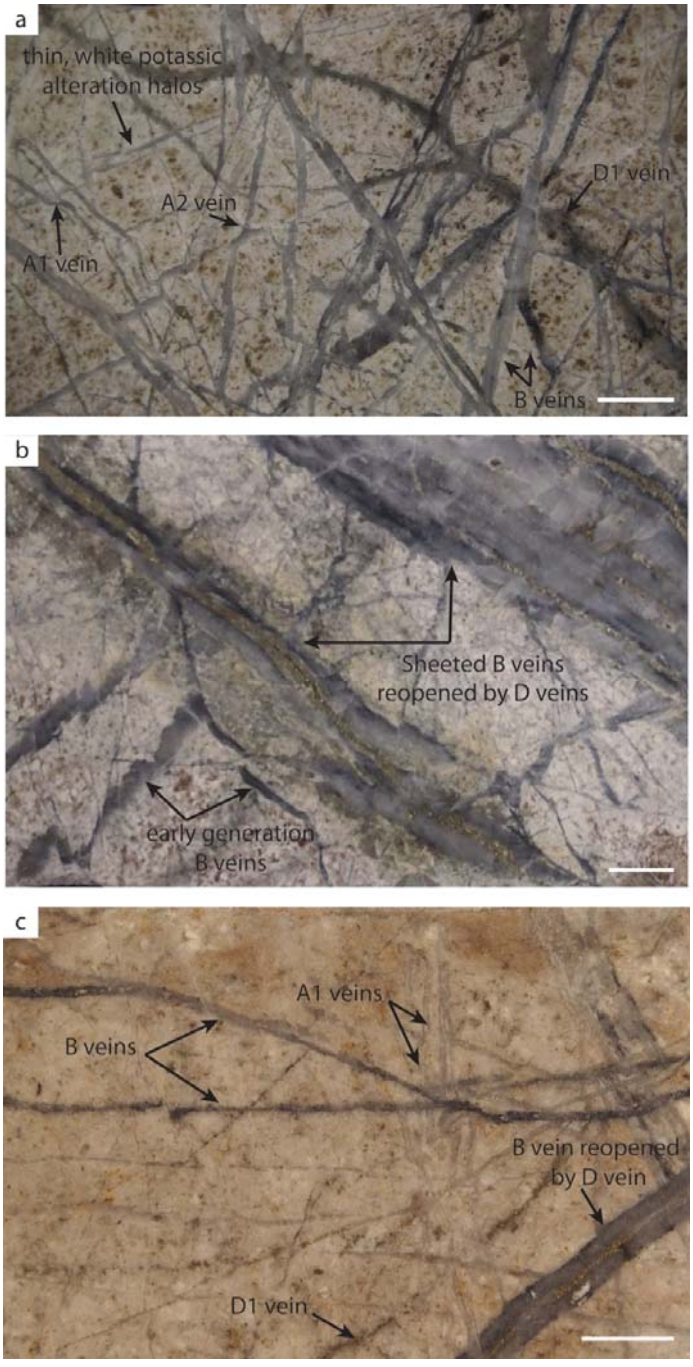
a
thin, white potassic alteration halos
A2 vein
A1 vein
D1 vein
B veins
b
Sheeted B veins reopened by D veins
early generation B veins
c
A1 veins
B veins
B vein reopened by D vein
D1 vein

Figure 6.5a-c.

Figure 6.5a. Stockwork veins from sample TMC25-473. Sinuous A1 veins are cross cut by planar A2 veins. A veins are cut by B veins and then by D1 veins. A and B veins contain mm scale white alteration halos which are interpreted to once have been potassic alteration halos converted to white sericite by pervasive overprinting by phyllic alteration. White scale bar represents 1 cm.

Figure 6.5b. Multiple generations of B veins in phyllically altered BP in sample TMC29-882. Early B veins are cut by later sheeted B veins which have been reopened by D-style veining as evident by pyrite filling the vein center. White scale bar represents 1 cm.

Figure 6.5c. Silicified QLP from sample TMC14-1173. Discontinuous A veins cut by B veins which are reopened by D-style veining. Isolate D veins cut all vein types. White scale bar represents 1 cm.

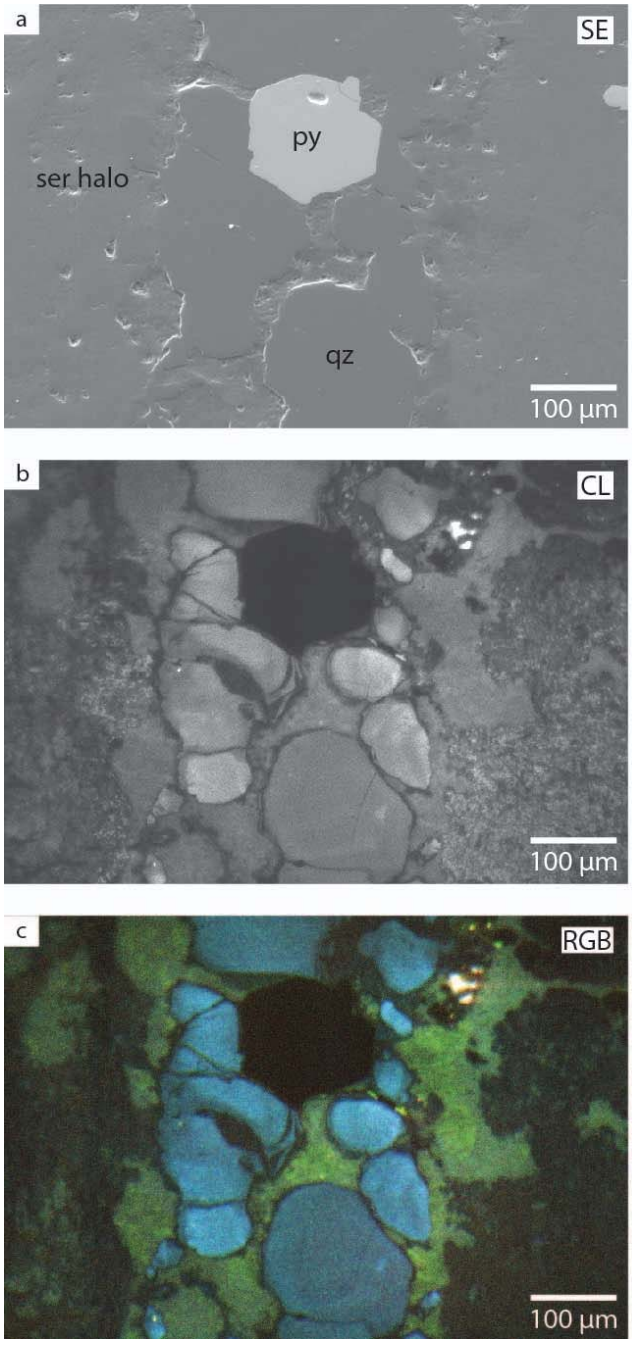

Figure 6.6a-c.

Figure 6.6a. Secondary electron (SE) image of an A1-vein reopened by D-veining from sample RH09. py = pyrite, qz = quartz, ser halo = sericite halo.

Figure 6.6b. Monochromatic CL image of sample RH09. Pyrite lacks luminescence while anhedral, bright CL quartz grains with EGZ have grain boundary interstices flooded with sericite.

Figure 6.6c. Panochromatic (RGB) image of RH09. Hydrothermal quartz luminesces blue while sericite luminesces green. Pyrite lacks luminescence.

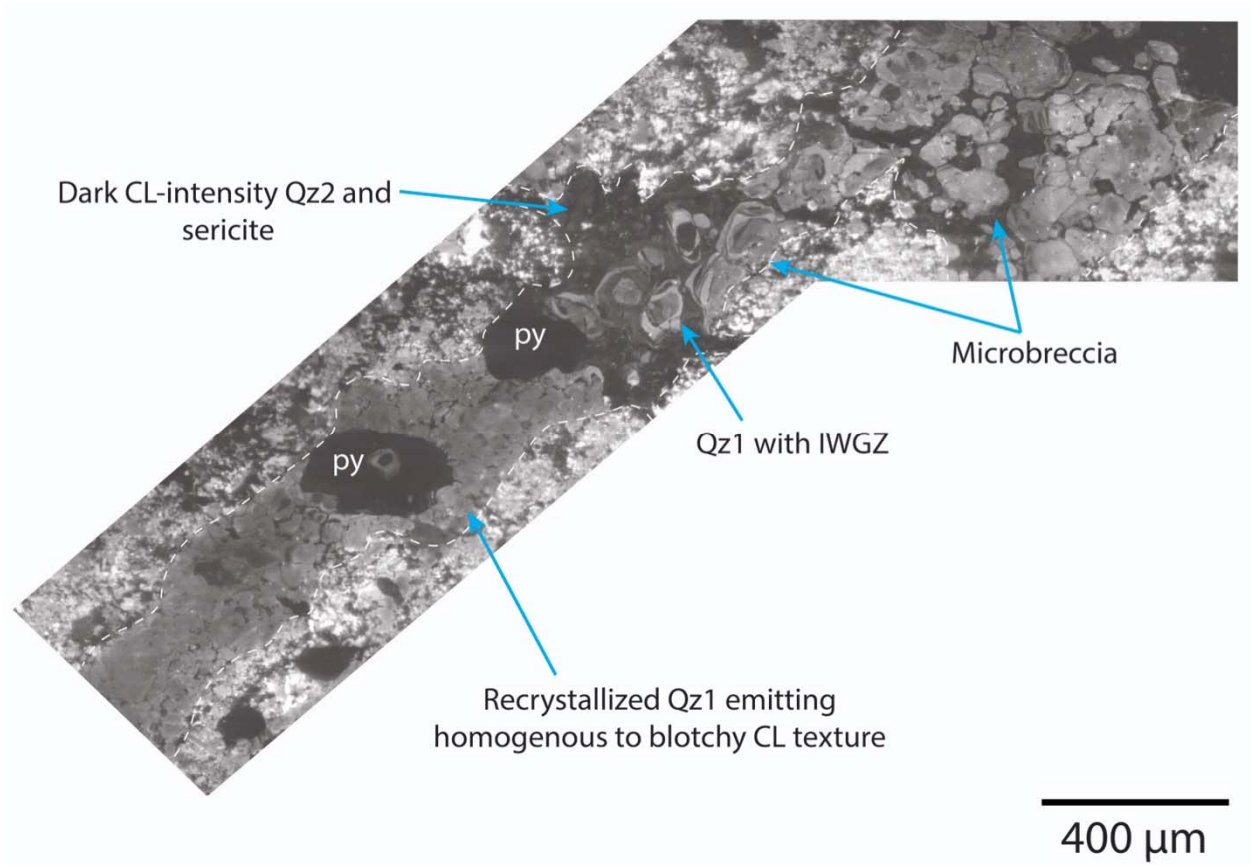

Figure 6.7. CL image of a quartz-pyrite A1-vein in sample RH24. Early quartz (qz1) displays IWGZ where preserved. Recrystallized qz1 in the bottom left shows homogenous to blotchy CL textures. Microbrecciation in the upper portion of the image is evident by dark-CL intensity (qz2) cementing the qz1 clasts. Grain boundaries of the qz1 clasts show WCB near the grain boundaries indicating diffusion followed mechanical breakage caused by microbrecciation.

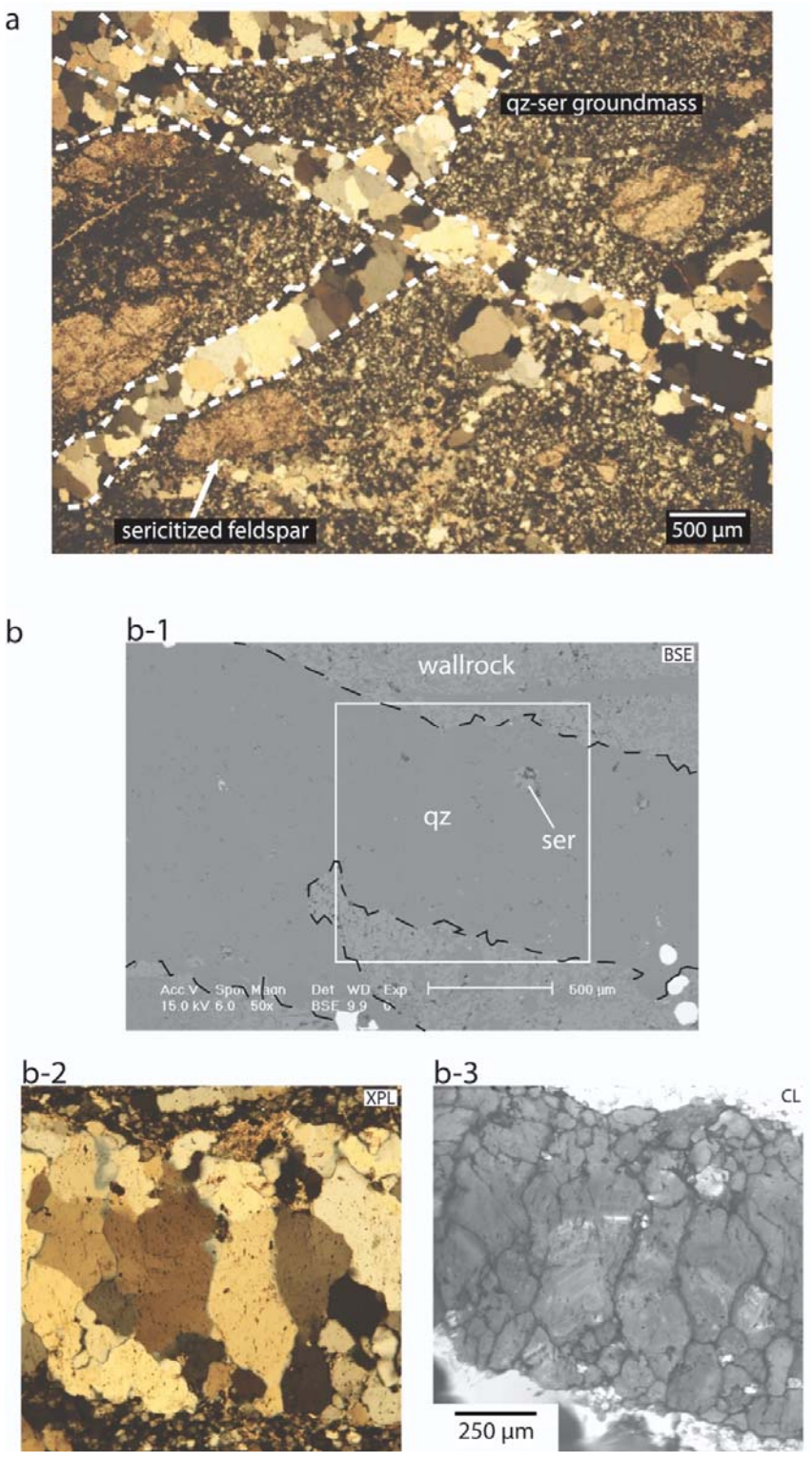
a
qz-ser groundmass
sericitized feldspar
500 µm
b
b-1
wallrock
BSE
qz
ser
500 µm
b-2
XPL
b-3
CL
250 µm

Figure 6.8a-b.

Figure 6.8a. Photomicrograph in cross-polarized light with multiple generations of cross-cutting A2 veins in phyllically altered QLP from sample TMC16-88. Vein margins are outlined in white dashed lines. Qz-ser = quartz-sericite.

Figure 6.8b-1. Back-scattered electron (BSE) image of A2 vein from TMC17-88. White box represents the outline of images 6.7b-2 and 6.7b-3. qz = quartz, ser = sericite.

Figure 6.8b-2. Photomicrograph in cross-polarized light displaying A2 vein quartz from TMC17-88.

Figure 6.8b-3. CL image of A2 vein quartz from TMC17-88. Fine-grained, equant quartz along the vein margin acts as a substrate for the overgrowth of coarse, euhedral, prismatic quartz which EGZ which terminate near the vein edge. These primary CL textures are less defined due to partial recrystallization.

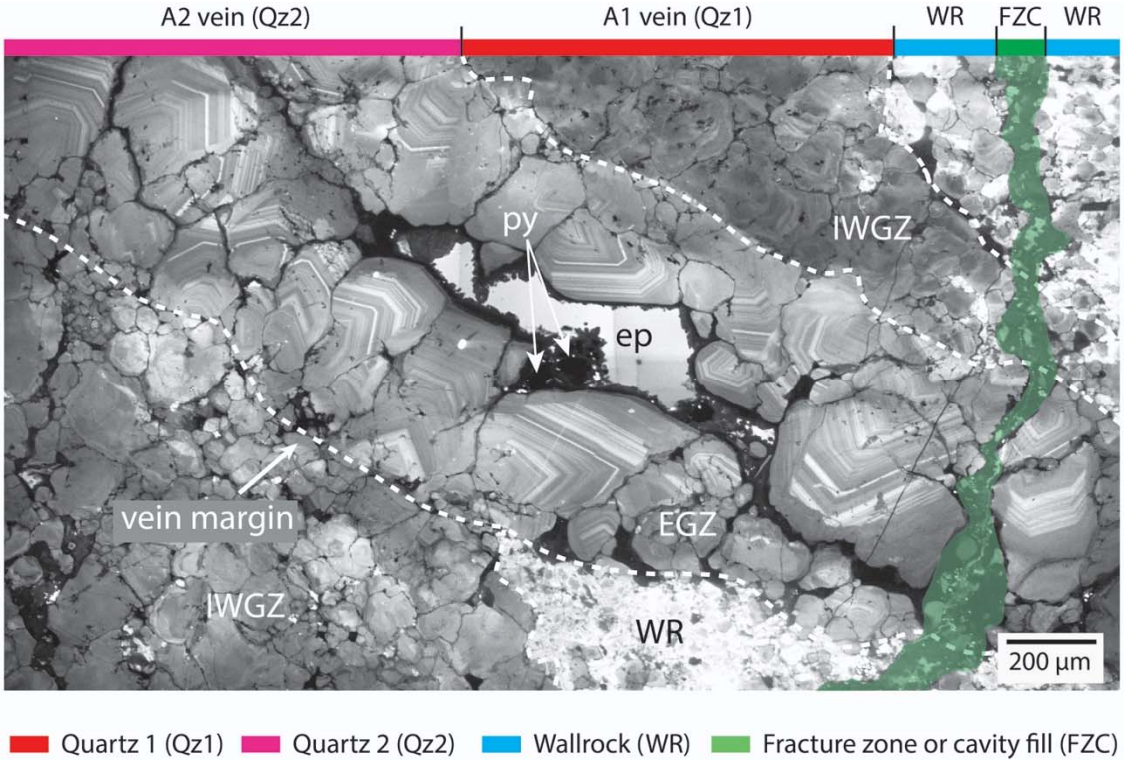

Figure 6.9. A1 quartz (qz1) cut by A2 quartz (qz2) vein in sample TMC25-733. A1 quartz displayed IWGZ texture which is sharply cut by qz2 quartz from A2-veining. Qz2 displays EGZ with oscillating bright and intermediate CL intensities. Dissolution surfaces are also evident in qz2 quartz. Minor pyrite and mo are deposited in the vein center and along quartz gain boundaries. White dashed line outlines the A2 vein margin. A-veins are cut by a sericite-filled fracture. , ep = epoxy , FZC = fracture zone or cavity fill, py = pyrite.

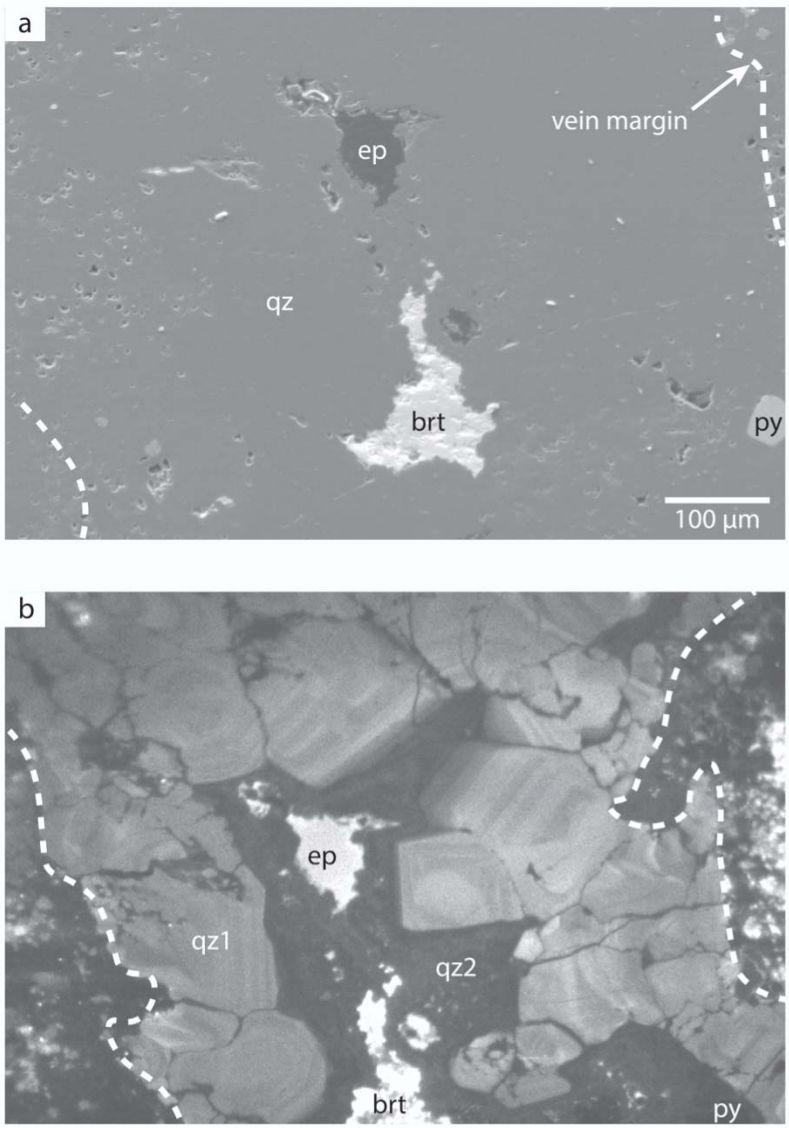

Figure 6.10a. SE image of an A2-quartz vein containing both unfilled vugs and barite filled veins in sample RH09. White dashed line represents the margin of the quartz vein. brt = barite, ep = epoxy, qz = quartz, py = pyrite.

Figure 6.10b. CL image of RH09 A2-vein. Qz1 are euhedral, prismatic, inwardly oriented with bright CL-intensity EGZ. Dark-CL intensity qz2 surrounds qz1. Barite, partially filling the vein center, has high luminescence as does epoxy. White dashed line represents the margin of the quartz vein. qz1 = quartz 1 and qz2 = quartz 2.

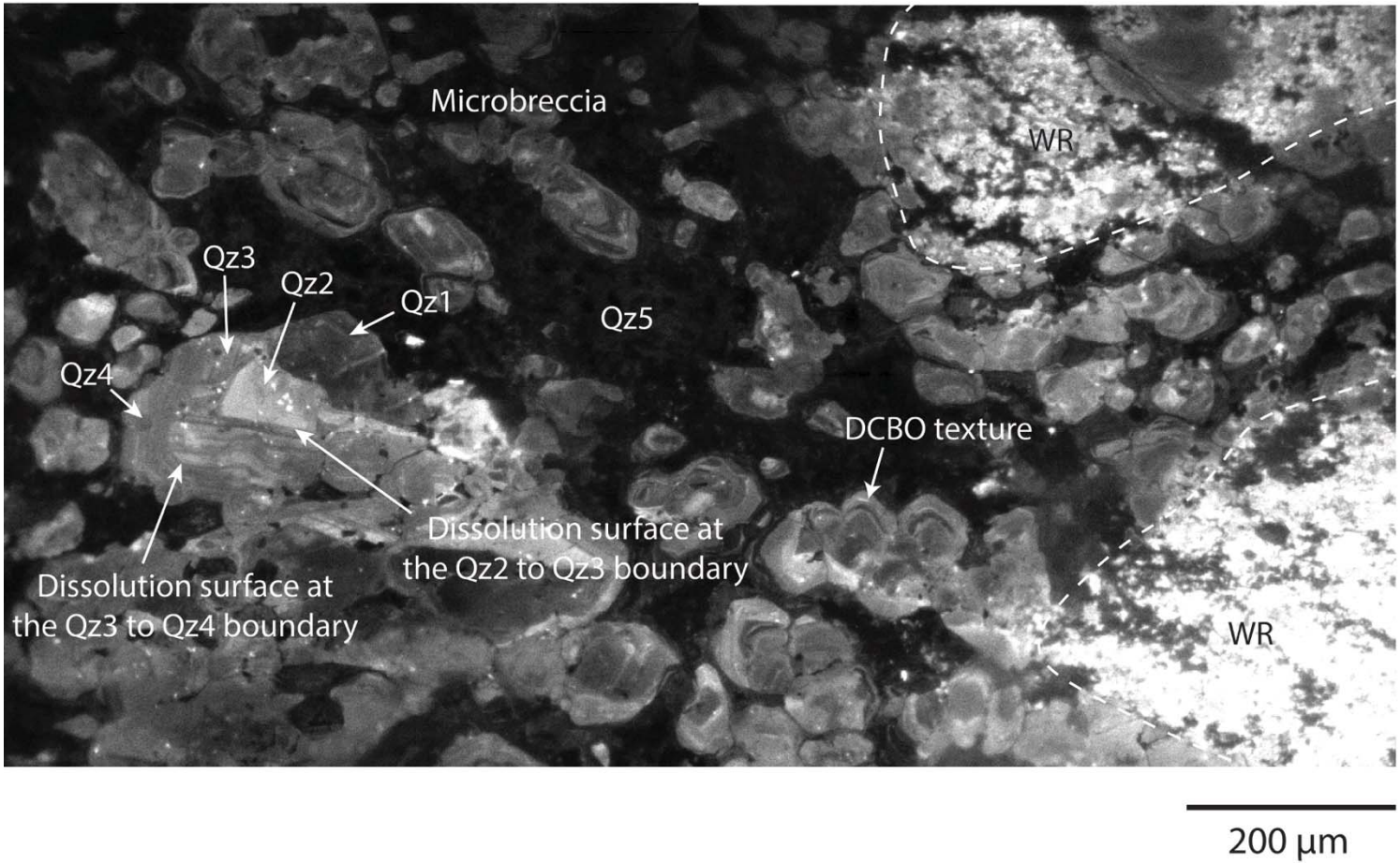

Figure 6.11. CL image displaying intense microbrecciation of sample RH24. Quartz breccia clasts display DCBO, IWGZ, and multiple dissolution-precipitation events. Precipitation following dissolution displays quartz with EGZ. The quartz clasts are surrounded by a flood of a mixture of quartz and sericite.

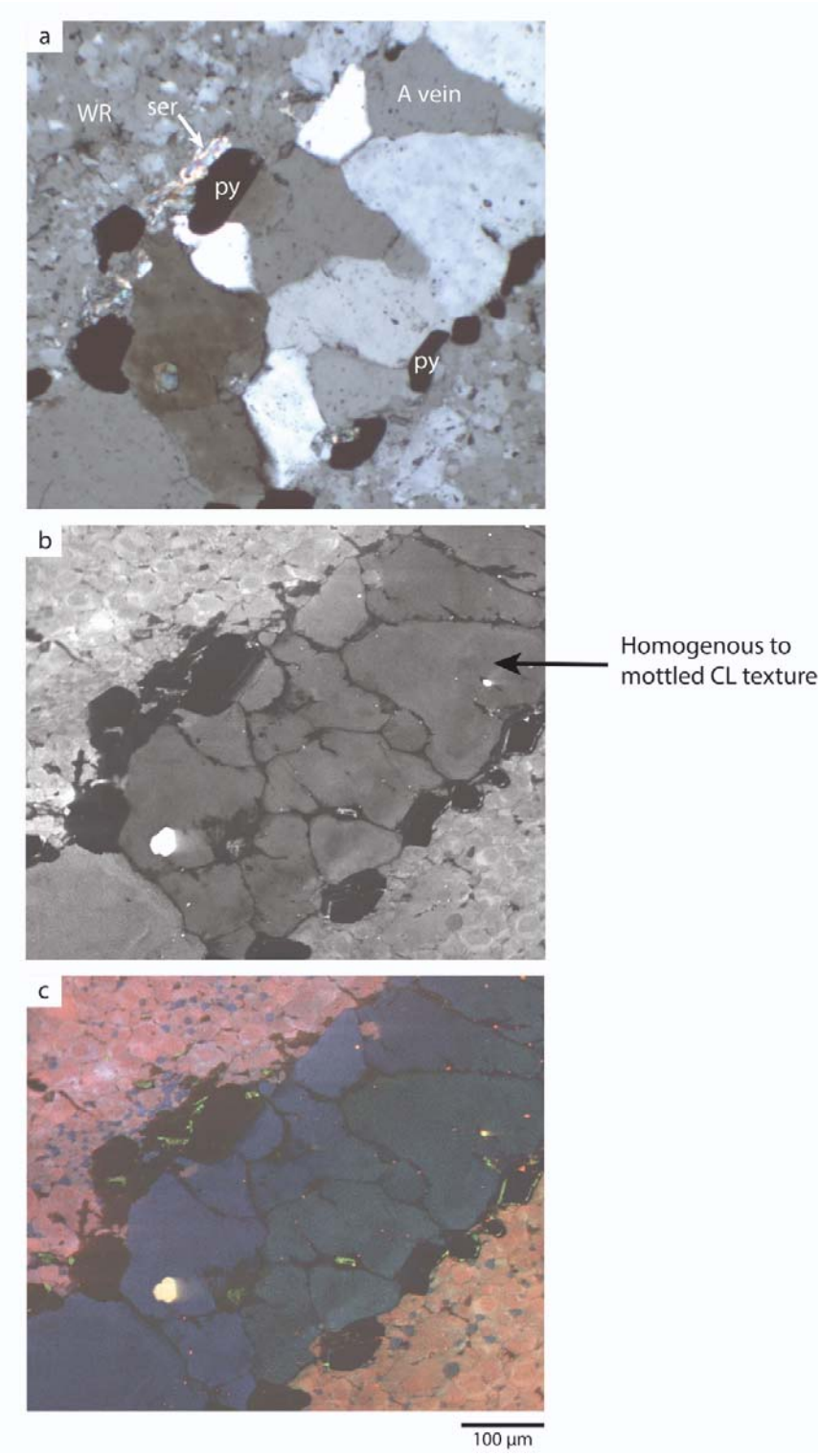

Figure 6.12a-c.

Figure 6.12a. Photomicrograph in cross-polarized light of an A vein in sample TMC14-1173. Pyrite and hydrothermal muscovite borders the margin of the quartz vein. The vein is bounded by silicified wallrock. py = pyrite, ser = sericite, WR = wallrock.

Figure 6.12b. Monochromatic CL image of Figure 6.12a. Quartz has a moderate CL intensity in which primary CL textures have been partially erased by recrystallization, displaying mottled to homogenous CL textures. White luminescent mineral is barite.

Figure 6.12c. Panochromatic CL image of Figure 6.12b. Hydrothermal vein quartz luminesces blue while silicified wallrock luminesces red.

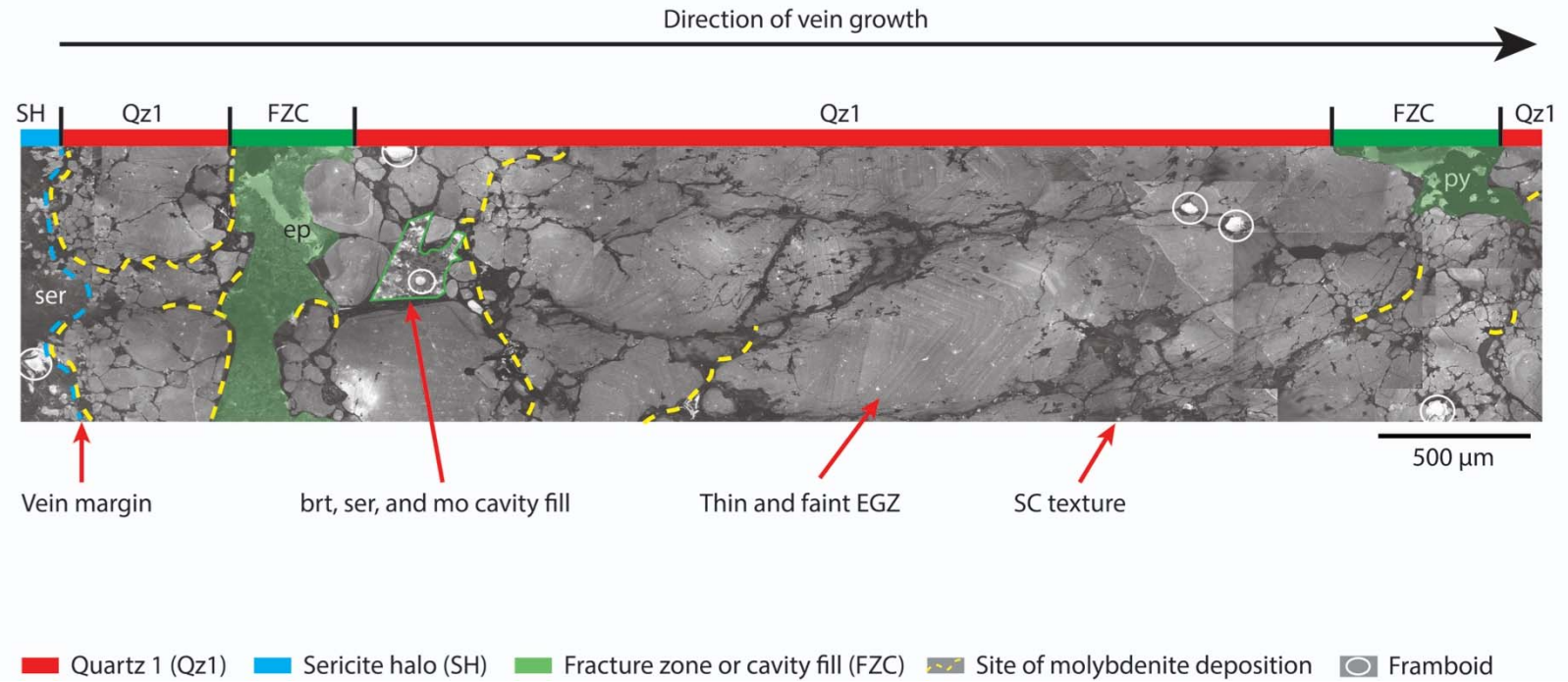

Figure 6.13. CL image of half of a B-vein transect from sample TMC7-1089. Blue dashed line mimics the vein margin. Coarse, inward-oriented, quartz (qz1) displays thin, and faint euhedral growth zones (EGZ) which are cut by dark CL (qz2) transgranular microfractures. Irregular black pits represent opened fluid inclusions on the surface of the quartz grains. Cavities within the veins are filled with barite, sericite, and molybdenite as well as zeolite framboids which have been pervasively silicified. Late stage sericite-filled fractures appear to be the last episode of vein-breakage. Molybdenite (non-luminescent) deposition is highlighted in dashed yellow lines. Mo mineralization is evident between grain boundaries between quartz grain and within cavities.

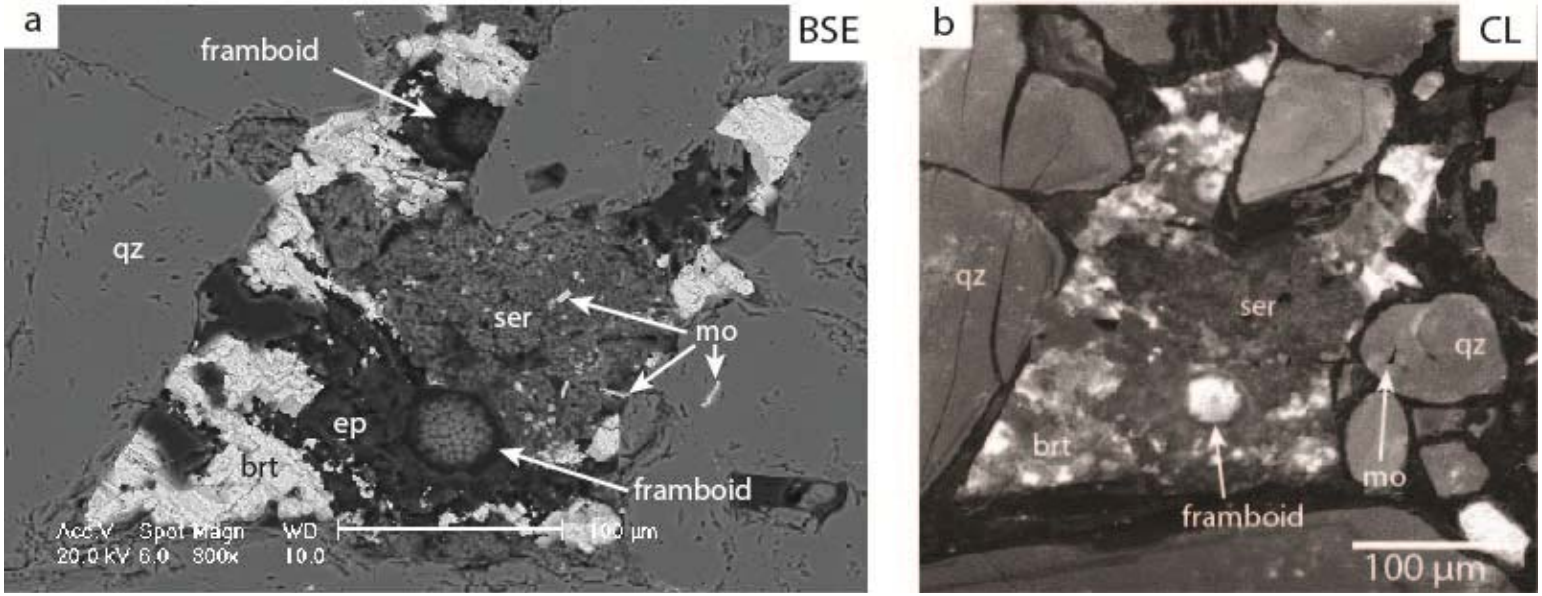

Figure 6.14a. BSE image cavity fill with barite, sericite, molybdenite, and Ca-Na-K zeolite framboid fill in B-vein vugs in sample TMC7-1089. brt = barite, ep = epoxy, mo = molybdenite, qz = quartz, ser = sericite

Figure 6.14b. CL image of Figure 6.14a. Molybdenite grain appears to sit in moderate CL-intensity quartz which shows weak wavy concentric banding.

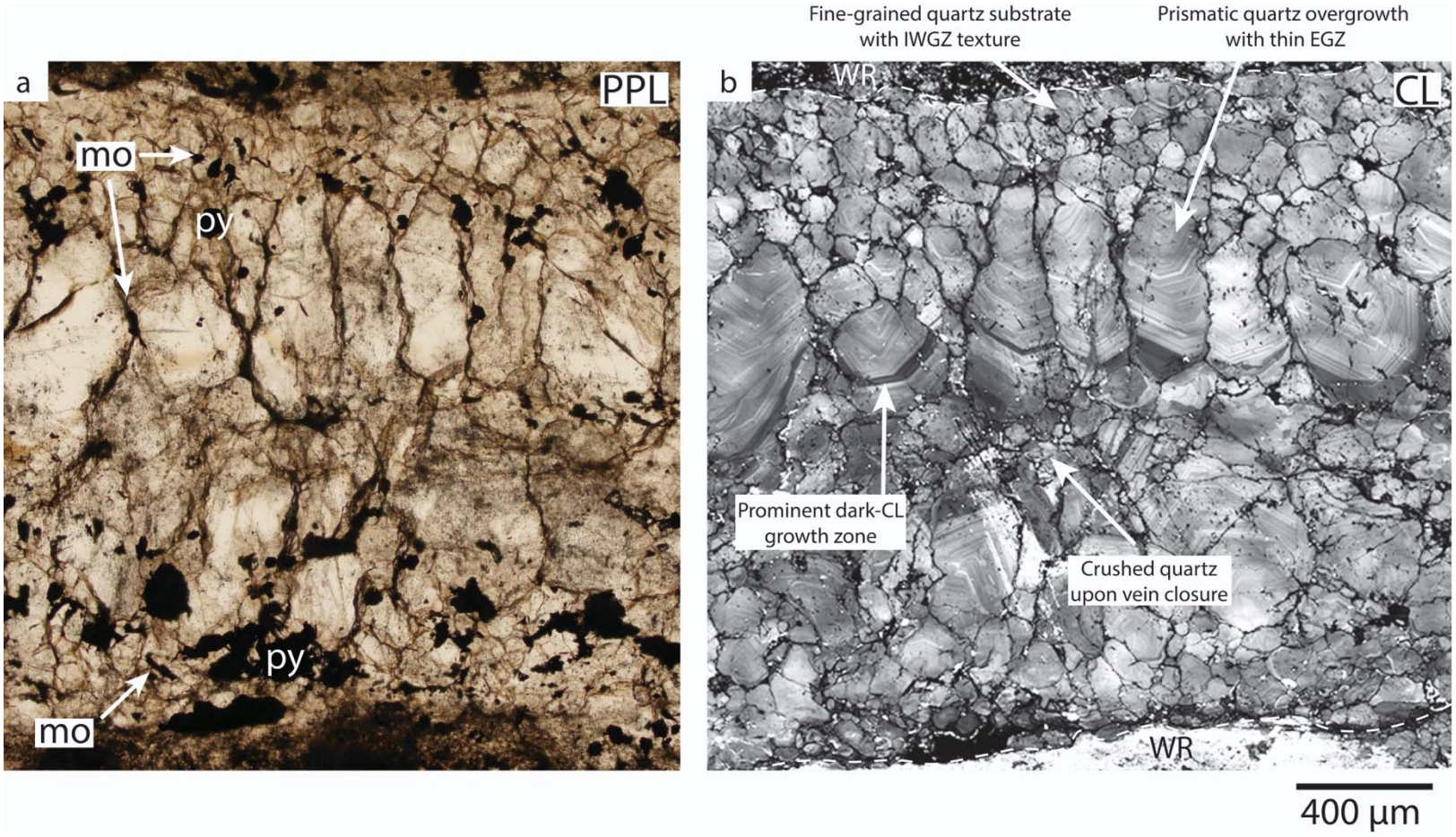

Figure 6.15a-b.

Figure 6.15a. Photomicrograph in plane-polarized light of a B-vein transect in sample TMC12-1075. Molybdenite (mo) deposition, and minor pyrite, is abundant along grain boundaries within the finer-grained substrate quartz along the vein margins. Mo is also, although rarely, found as inclusions in quartz in structural defect sites. mo = molybdenite, py = pyrite

Figure 6.15b. SEM-CL Photomosaic of figure 6.15a. Quartz textures highlighting the asymmetry of B-veins are illuminated by CL which are otherwise absent in transmitted light. Fine-grained, substrate quartz is anhedral with IWGZ and DCBO textures and is overgrown by prismatic, coarse-grained quartz which project towards the interior of the vein. Thin, oscillatory growth zones within the prismatic quartz are punctuated by a large, dark-CL growth band which is continuous among the upper prismatic quartz grains. Finer, anhedral quartz fills the vein center displaying complex CL textures such as IWGZ, dissolution textures, WCB along grain margins, and even homogenous to mottled textures which are most likely a byproduct from the crushing of prismatic quartz during vein closure. Dark-CL, transgranular microfractures cut through all vein quartz. Dashed white line represents the vein margin. WR = wallrock.

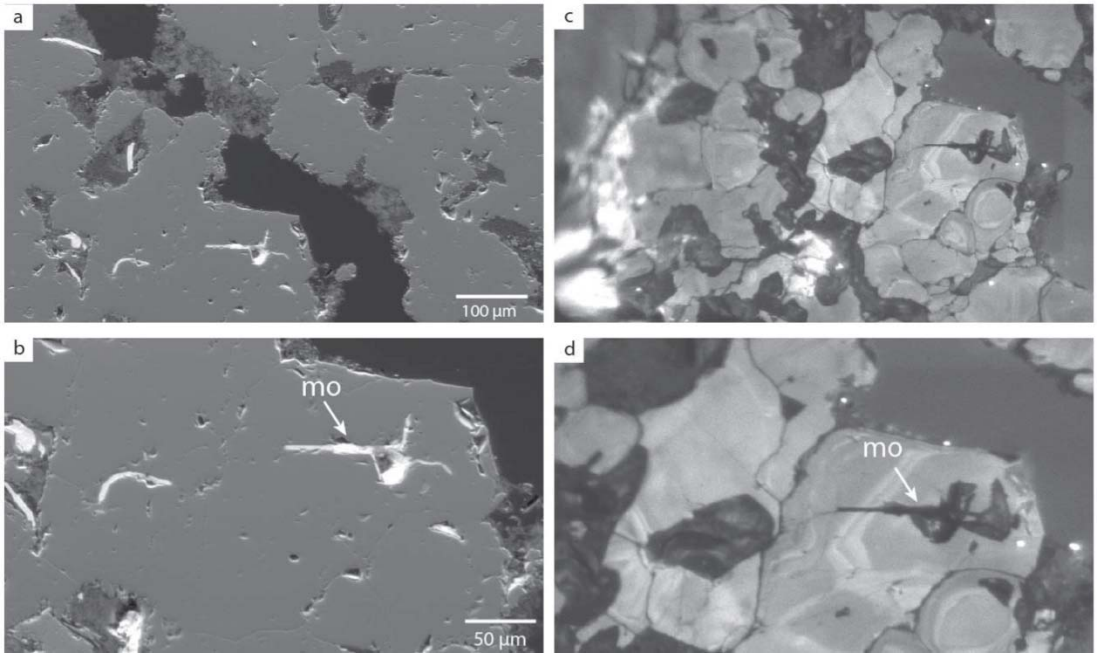

Figure 6.16a. SE image of a quartz-molybdenite vein from sample TMC25-1176.

Figure 6.16b. Magnified SE image of 6.16a. mo = molybdenite

Figure 6.16c. CL image of figure 6.16a. Molybdenite (mo) is deposited along grain boundaries in intergranular fractures in bright-CL intensity quartz with IWGZ and WCB along grain margins. Sites of mo deposition show dark-CL quartz bleeding into the bright-CL quartz while retaining the primary growth textures of the early quartz. This feature may be a product of elemental substitution of Mo or S in the early generation quartz.

Figure 6.16d. Magnified CL image of Figure 6.16c.

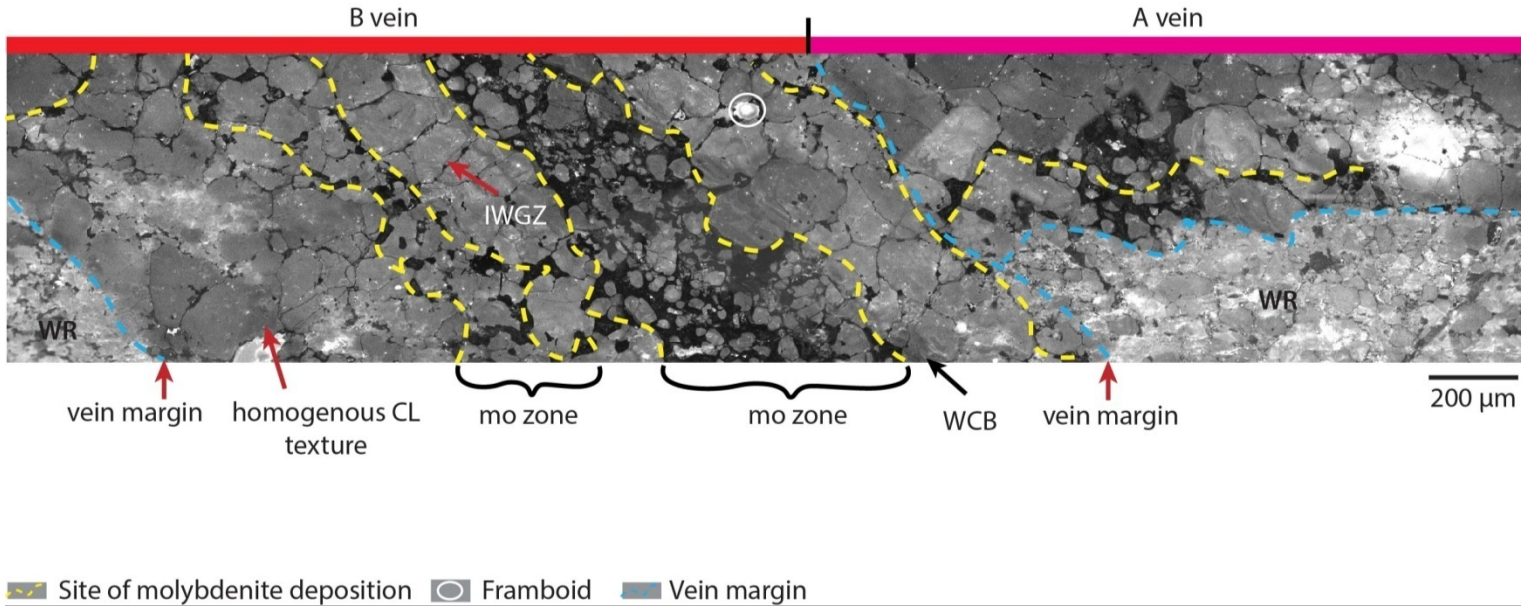

Figure 6.17. Transect of an early sheeted B-vein which cuts through an A vein in sample TMC7-1089. Quartz from both vein types displays homogenous to mottled textures. Multiple Mo deposition events are evident in sheeted B-veins. Mo is either deposited along grain boundaries within a definite quartz layer or within microbrecciated zones. Faint IWGZ primary textures from B-vein quartz is barely visible, but WCB texture is apparent along the grain boundaries in the microbreccia zone where molybdenite (mo) and dark-CL quartz fills make up the breccia matrix. mo = molybdenite, WR = wallrock. Blue dashed lines represent vein boundaries and yellow dashed lines represent lines of Mo deposition.

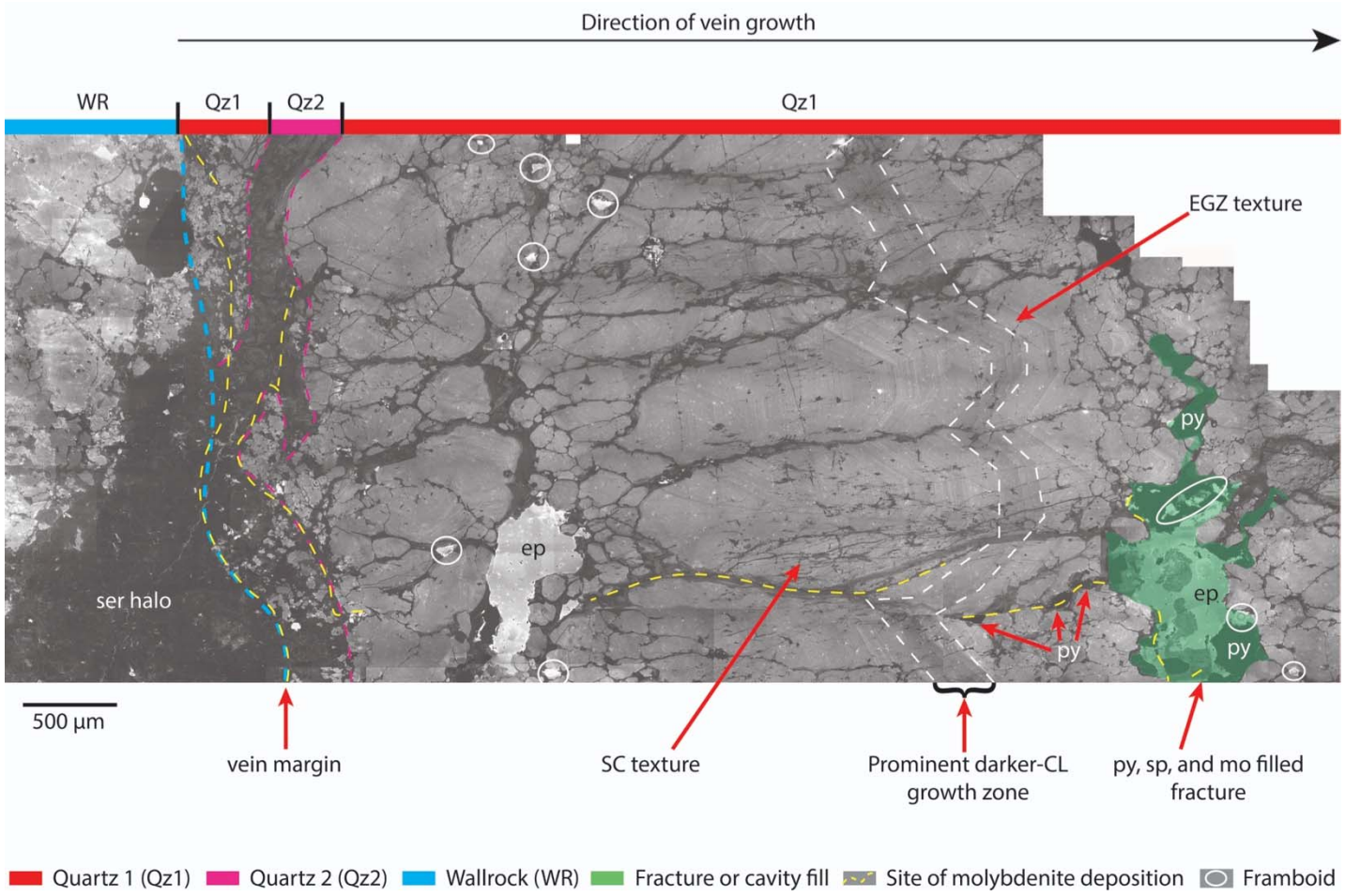
Direction of vein growth
WR
Qz1
Qz2
Qz1
EGZ texture
py
ep
ser halo
ep
py
py
500 µm
vein margin
SC texture
Prominent darker-CL growth zone
py, sp, and mo filled fracture
Quartz 1 (Qz1)
Quartz 2 (Qz2)
Wallrock (WR)
Fracture or cavity fill
Site of molybdenite deposition
Framboid

Figure 6.18.

Figure 6.18. Transect of half of a B vein in sample TMC7-1089. This vein has been reopened by D-style veining as seen by pyrite depositing within the vein center and a sericite halo bordering the vein margins. Euhedral, prismatic quartz (Qz1) projects towards the vein center and are cut by abundant secondary, dark-CL fractures. Vugs within the D-vein have been filled with pyrite, zeolite framboids, and sericite. In areas of focused fracturing displays SC textures which abundant dark pits representing secondary fluid inclusion trails. A prominent dark-CL growth zone also found in TMC12-1075 is also found in this B-vein. Dark-CL, euhedral quartz along the left side of the B-vein is deposited along an open space fracture caused by D-style fracturing. Osillatory dark-CL intensity EGZ in second generation quartz (Qz2) is randomly oriented but projects inward.

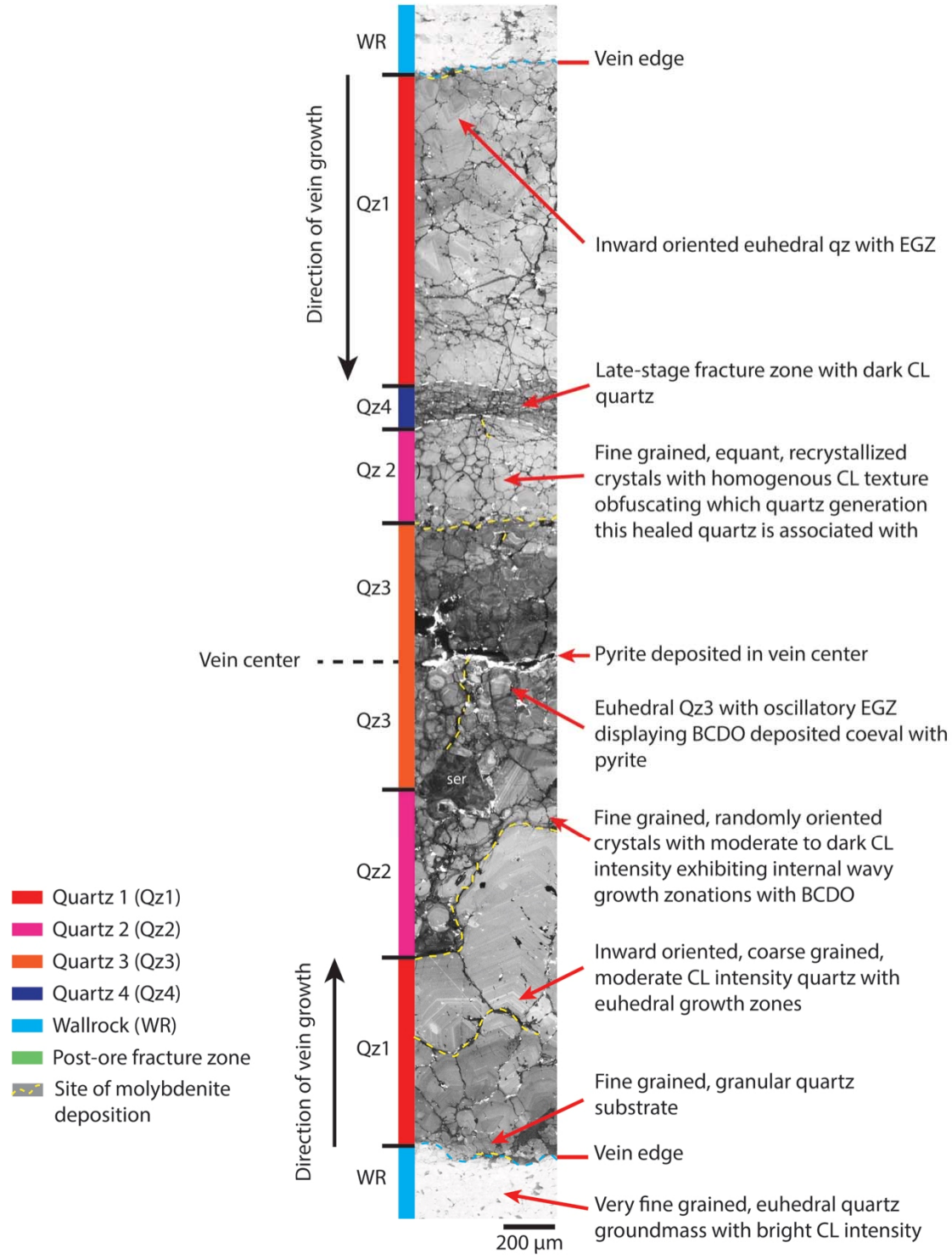
WR
Vein edge
Direction of vein growth
Qz1
Inward oriented euhedral qz with EGZ
Late-stage fracture zone with dark CL quartz
Qz4
Qz 2
Fine grained, equant, recrystallized crystals with homogenous CL texture obfuscating which quartz generation this healed quartz is associated with
Qz3
Vein center
Pyrite deposited in vein center
Qz3
Euhedral Qz3 with oscillatory EGZ displaying BCDO deposited coeval with pyrite
ser
Fine grained, randomly oriented crystals with moderate to dark CL intensity exhibiting internal wavy growth zonations with BCDO
Qz2
Inward oriented, coarse grained, moderate CL intensity quartz with euhedral growth zones
Direction of vein growth
Qz1
Fine grained, granular quartz substrate
Vein edge
WR
Very fine grained, euhedral quartz groundmass with bright CL intensity
200 µm
Quartz 1 (Qz1)
Quartz 2 (Qz2)
Quartz 3 (Qz3)
Quartz 4 (Qz4)
Wallrock (WR)
Post-ore fracture zone
Site of molybdenite deposition

Figure 6.19.

Figure 6.19. SEM-CL image of a B vein transect in sample TMC14-1173, which has been reopened by D-style veining. Five quartz generations are observed along the vein transect. The timing between Qz3 and Qz4 is unclear, and may therefore be interchangeable.

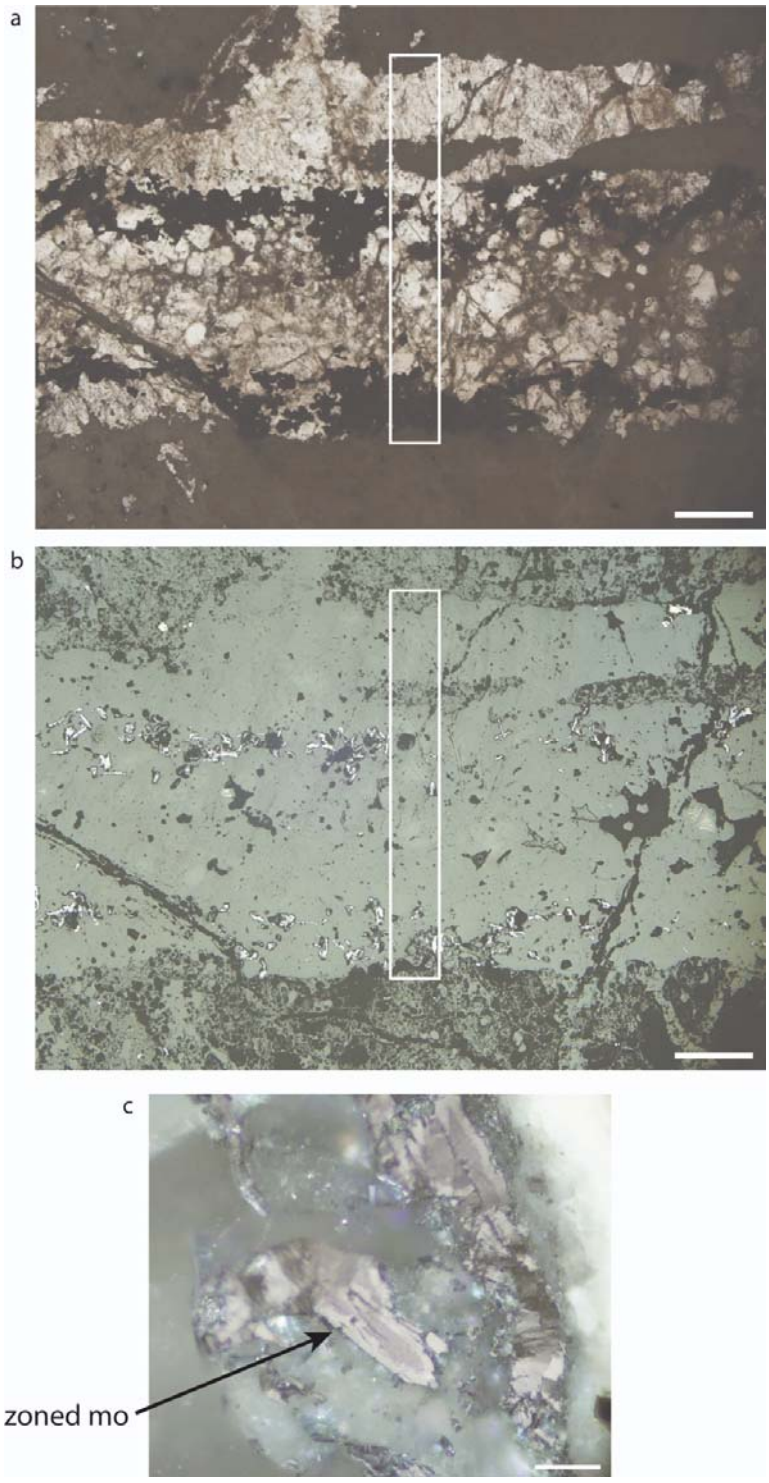

Figure 6.20a-c.

Figure 6.20a. Photomicrograph in plane-polarized light of thick section TMC14-380 showing transects of an A vein up the upper portion of the image cut by B-style veining. White box represents the area where a SEM-CL image transect was taken. White scale bar represents 1 mm.

Figure 6.20b. Photomicrograph in reflected light as the same area in figure 6.20a. Molybdenite is deposited along the vein margins of the B vein. White box represents the area where a SEM-CL image transect was taken. White scale bar represents 1 mm.

Figure 6.20c. Photomicrograph in reflected light of molybdenite (mo) in B-veins. Compositional zoning is apparent in molybdenite in shallow B-vein samples. White scale bar represents 50 μm.

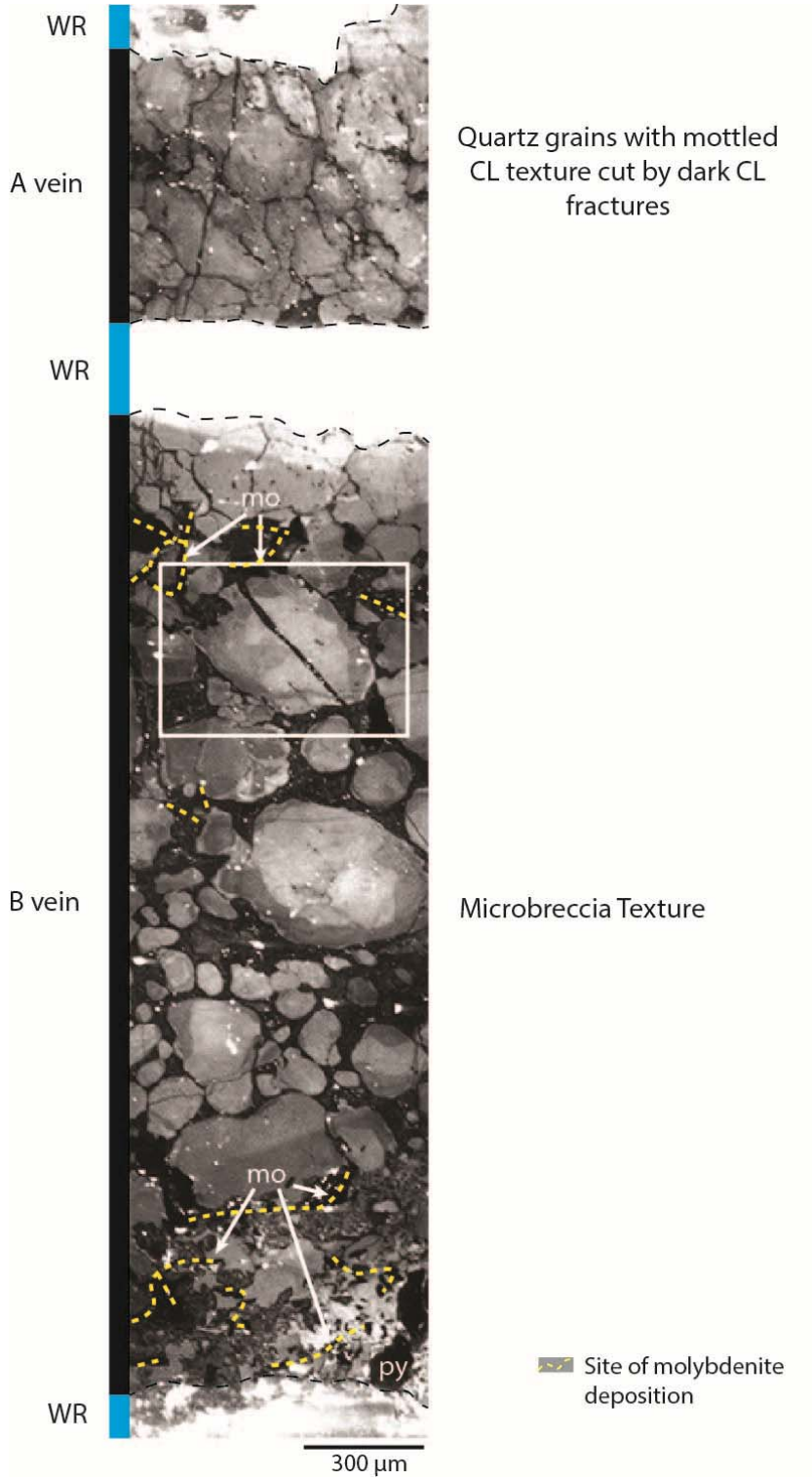
WR
A vein
Quartz grains with mottled CL texture cut by dark CL fractures
WR
mo
B vein
Microbreccia Texture
mo
py
WR
Site of molybdenite deposition
300 µm

Figure 6.21.

Figure 6.21. SEM-CL transects of A and B veins in sample TMC14-380. The A vein at the top of the image is cut by the lower B vein. A-vein quartz displays mottled to homogenous textures cut by dark-CL microfractures. B-vein quartz has been intensely brecciated. Multiple dissolution-precipitation episodes are evident within the quartz clasts which are cemented by dark-CL quartz and sericite. The white-box outline represents the magnified area which is explained in more detail in figure 6.21. Dashed black lines represent vein margins. WR = wallrock.

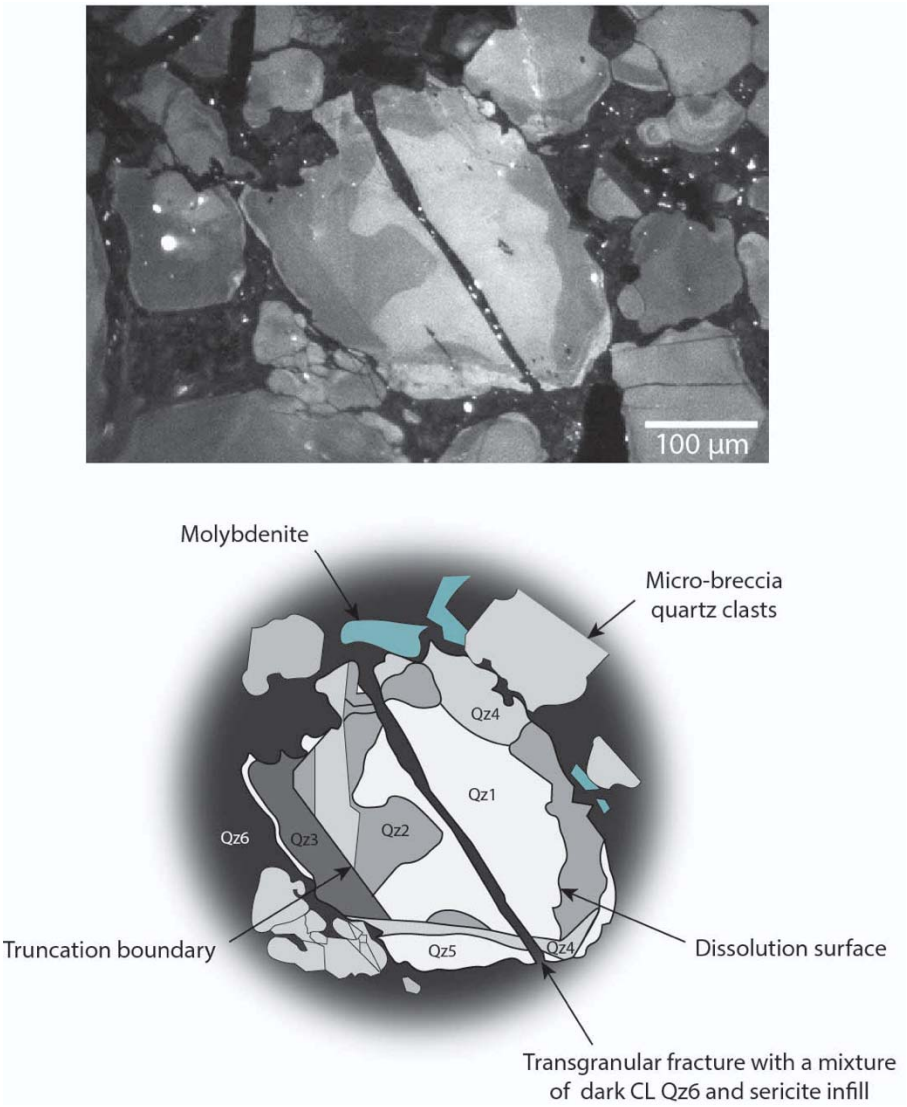

Figure 6.22. Magnified SEM-CL image of the highlighted area in Figure 6.21. Six generations of quartz have been identified in this vein-type which is largely based on dissolution-precipitation textures. CL-intensities vary with each quartz generations.

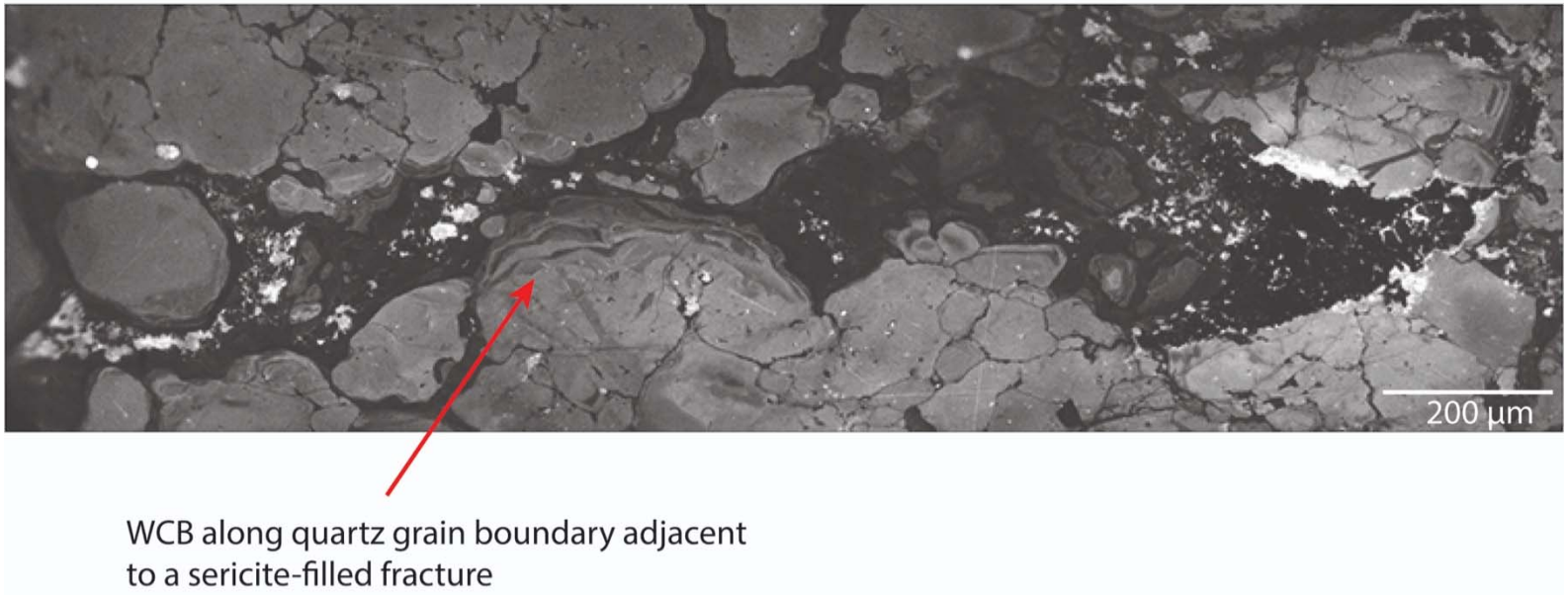

Figure 6.23. SEM-CL image of vein quartz in surface sample RH07 highlighting WCB textures are most prominent along grain boundaries adjacent to fracture zones.

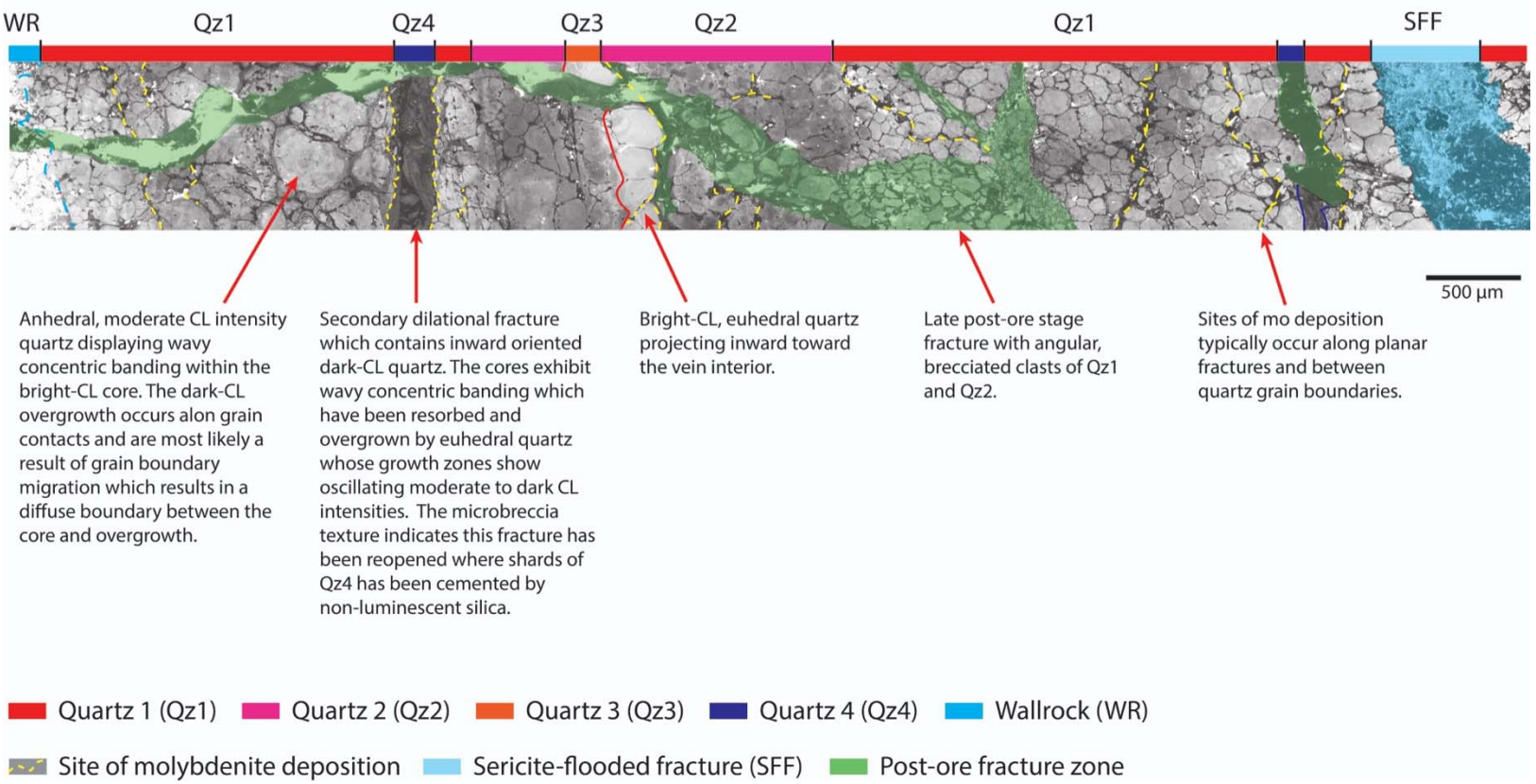

Figure 6.24. SEM-CL image of a sheeted B vein transect in sample TMC14-31b. Four quartz generations associated their own episode of molybdenite mineralization have been observed. A shallow late-stage fracturing event has formed brecciated clasts of all distinct quartz generations with sericite infill between the interstices of the breccia clasts.

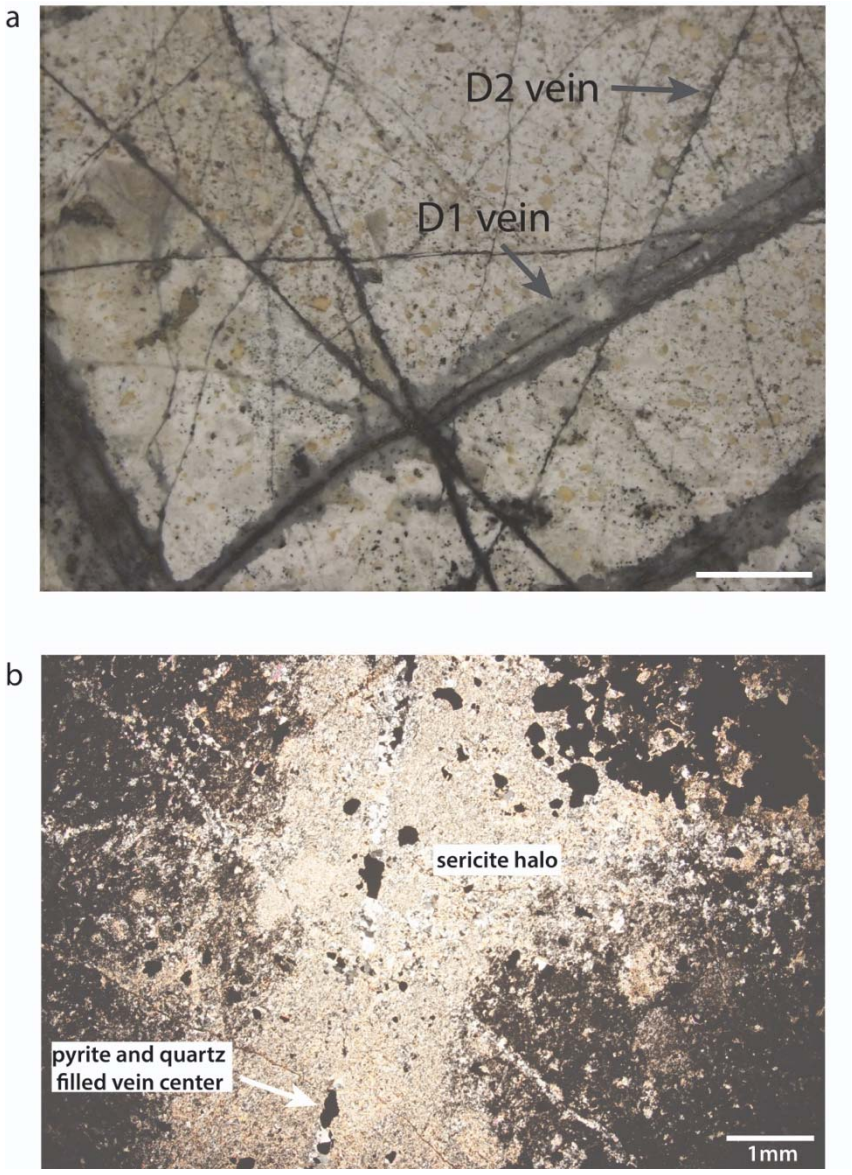

Figure 6.25a. Slab of intersecting D-style veins in hand sample TMC01-114. White scale bar represents 1 cm.

Figure 6.25b. Photomicrograph in cross-polarized light of sample TMC01-114 displaying the prominent sericite, with minor pyrite and quartz, halo of D1 veins with pyrite and minor quartz vein fill.

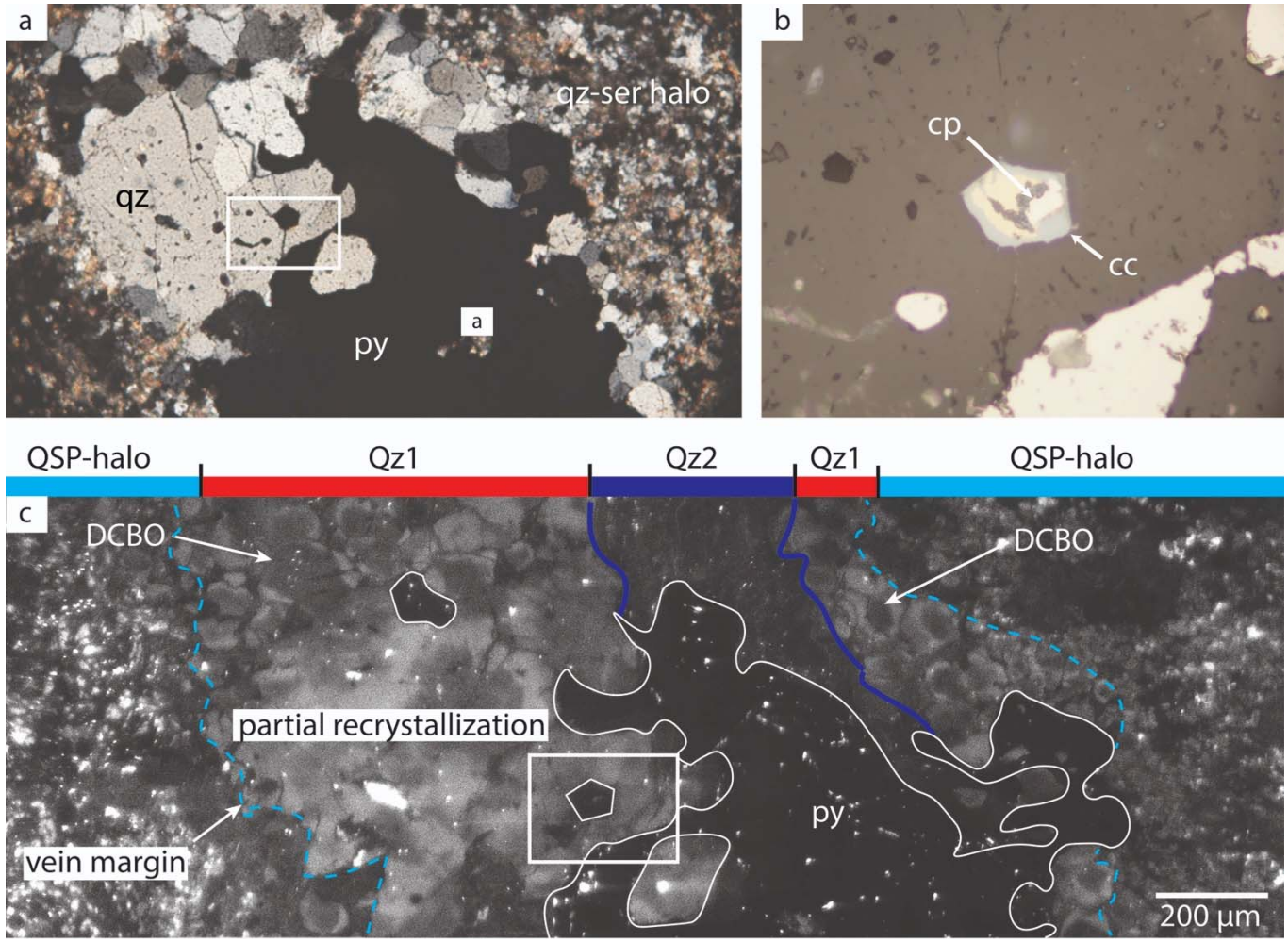

Figure 6.26a-c.

Figure 6.26a. Photomicrograph in cross-polarized light of a D1 vein from sample TMC18-187. py = pyrite, qz = quartz, qz-ser halo = quartz-sericite halo. White box outline represents the magnified reflected light image in figure 6.25b and the same outlined area in figure 6.25c.

Figure 6.26b. Photomicrograph in reflected light in sample TMC18-187 of an isolated chalcopyrite grain with a chalcocite replacement rim within D vein quartz. cc = chalcocite, cp = chalcopyrite.

Figure 6.26c. SEM CL image transect of figure 6.26a. Two distinct quartz generations have been identified in this vein type. Anhedral quartz 1 (Qz1) displays DCBO textures while quartz 2 (Qz2) associated with pyrite deposition has a dark-CL intensity with indiscernible CL textures.

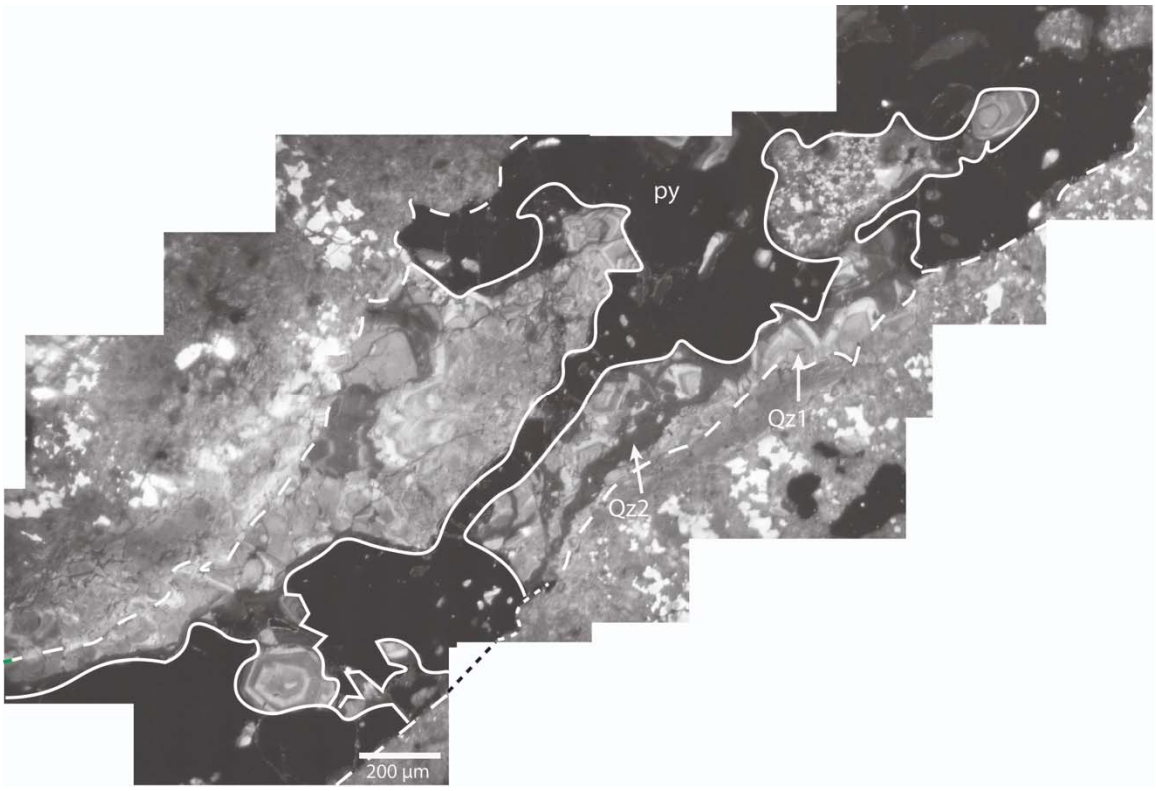

Figure 6.27. SEM-CL image of a D2 vein transect from sample TMC25-136. Oscillatory bright to moderate CL intensity quartz 1 (Qz1) displays EGZ textures where some prismatic quartz located left to the pyrite vein center shows irregular embayments on the edges of the grain followed by the overgrowth of dark-CL quartz. Qz1 has been brecciated before the precipitation of late-stage pyrite as seen by clasts of Qz1 within pyrite. Dark-CL quartz 2 (Qz2) and pyrite cements the Qz1 breccia clasts.

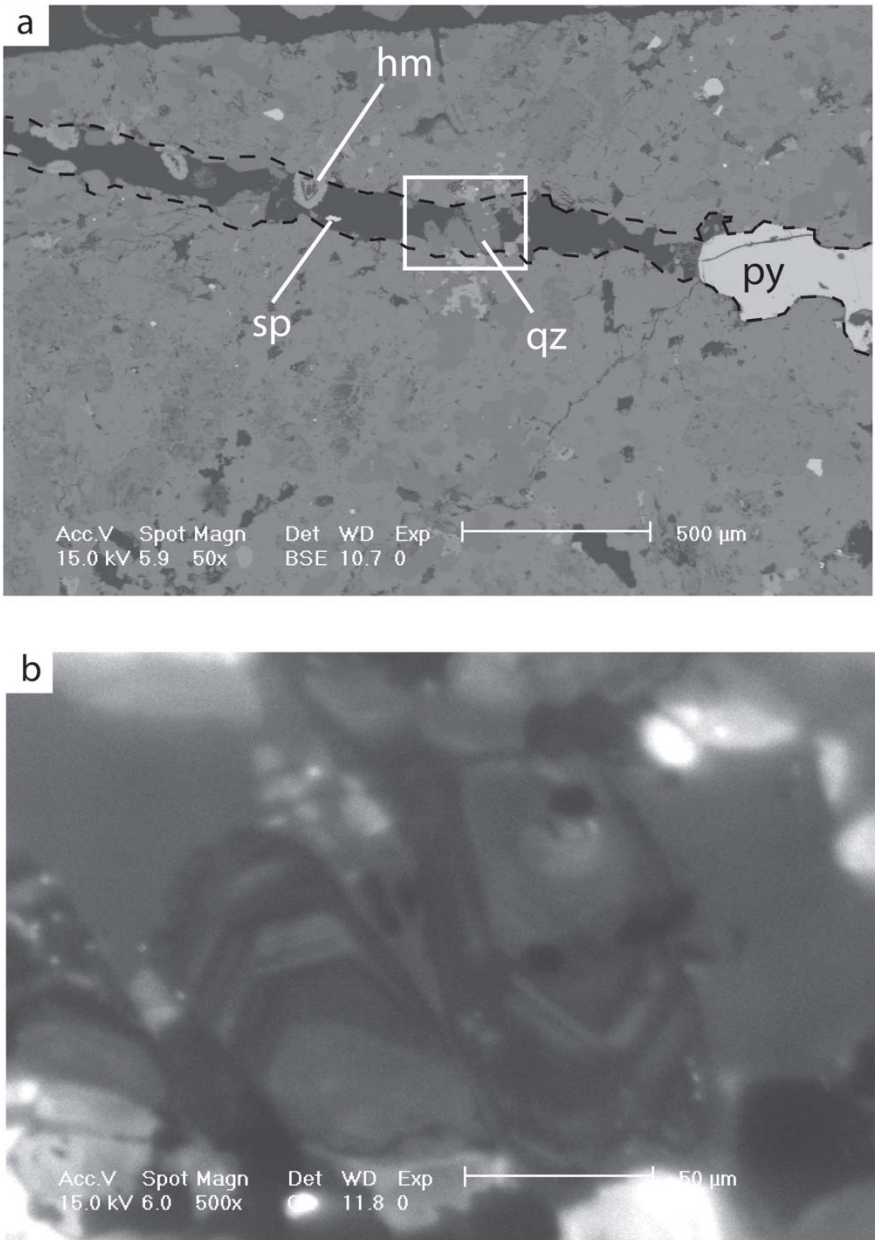

Figure 6.28a. BSE image of a D2 vein from sample TMC25-1176. Euhedral quartz and hematite grow into the open space fracture which is partially filled with pyrite. Disseminated sphalerite grains are also found within the vein. White outline represent the SEM-CL imaging area. hm = hematite, py = pyrite, qz = quartz, sp = sphalerite.

Figure 6.28b. SEM-CL image of D2 vein quartz from sample TMC25-1176. D2 vein quartz displays oscillatory dark-CL intensity EGZ.

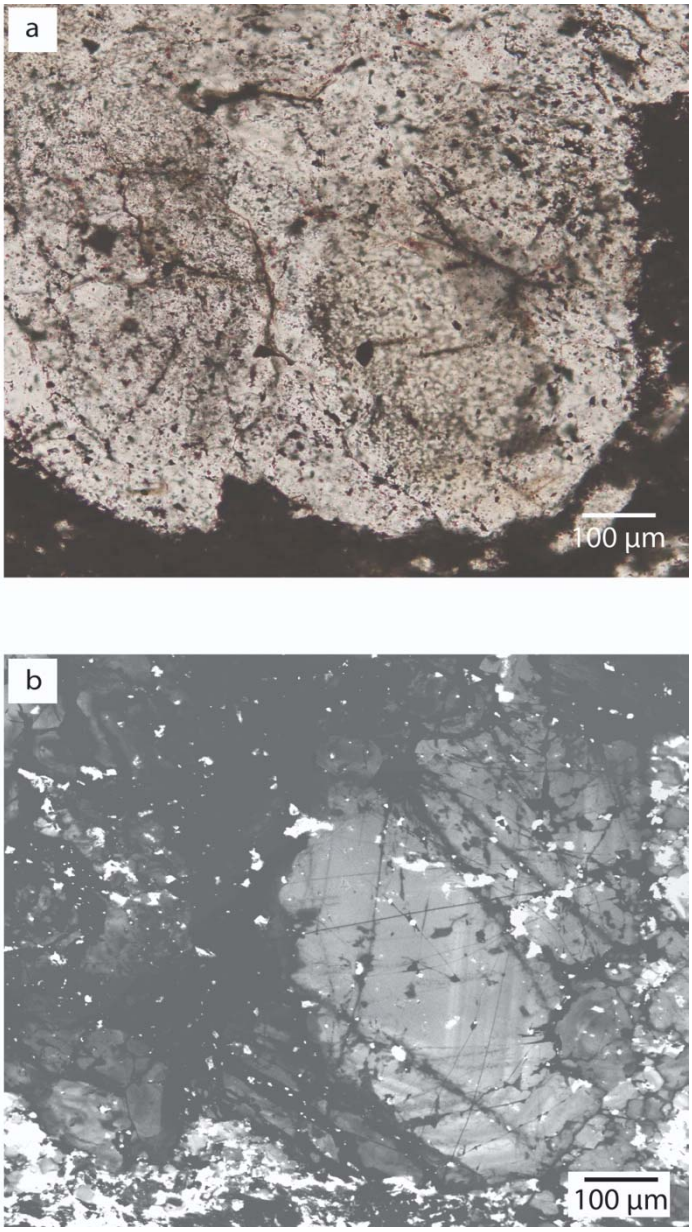

Figure 6.29a. Photomicrograph in plane-polarized light of "brain rock" quartz in thick section TMC14-31b.

Figure 6.29b. SEM-CL image of Figure 6.29a. UST quartz shows bright-CL intensity quartz with EGZ which has been affected by intense late-stage fracturing and microbrecciation. Dark-CL quartz flooding around the bright-CL quartz contains abundant concentrations of fluid inclusions. SC textures and black fluid inclusions pits correspond in CL intensity to the dark-CL quartz cement.

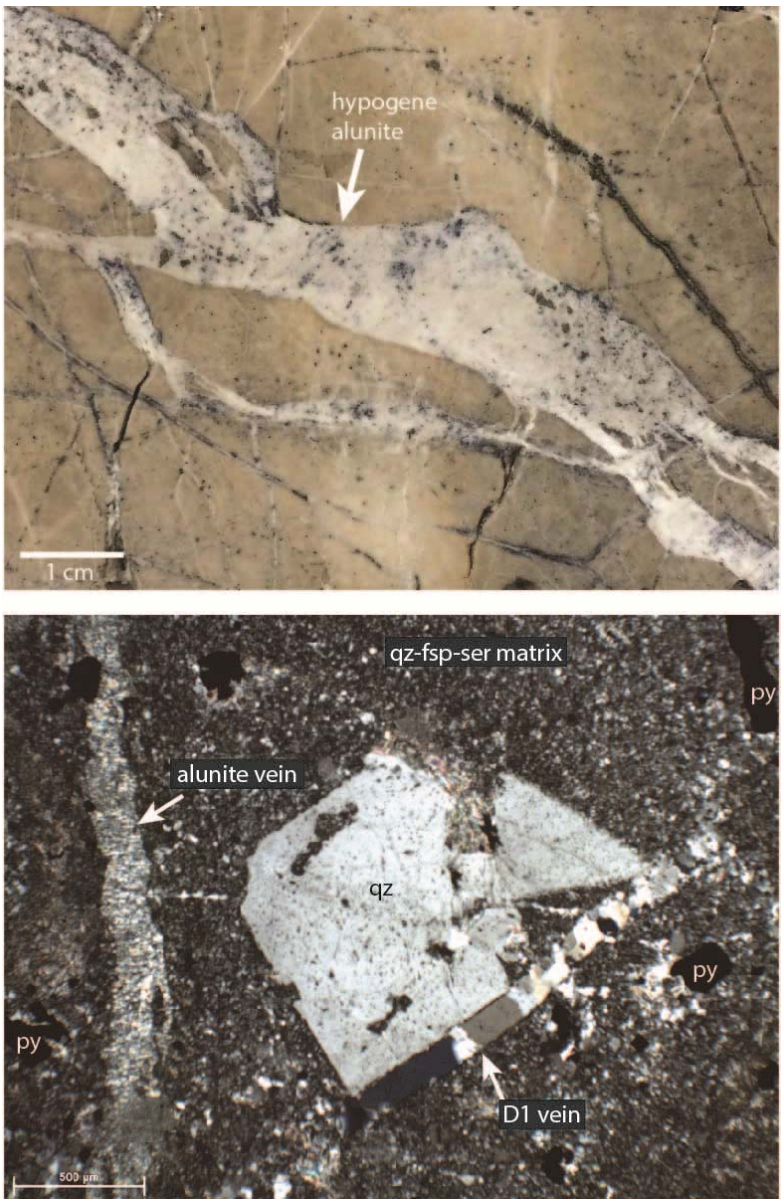

Figure 6.30a. Slab of TMC20-24 showing hypogene alunite vein within pyritic hornfels.

Figure 6.30b. Photomicrograph in cross-polarized light displaying cross cutting veins in argillically altered sample TMC25-136. A hypogene alunite vein in the left part of the image which cuts the oblique D1 vein. A euhedral, sector zoned quartz grain (confirmed by EDS) sits within the quartz-feldspar groundmass. fsp = feldspar, py = pyrite, qz = quartz, ser = sericite.

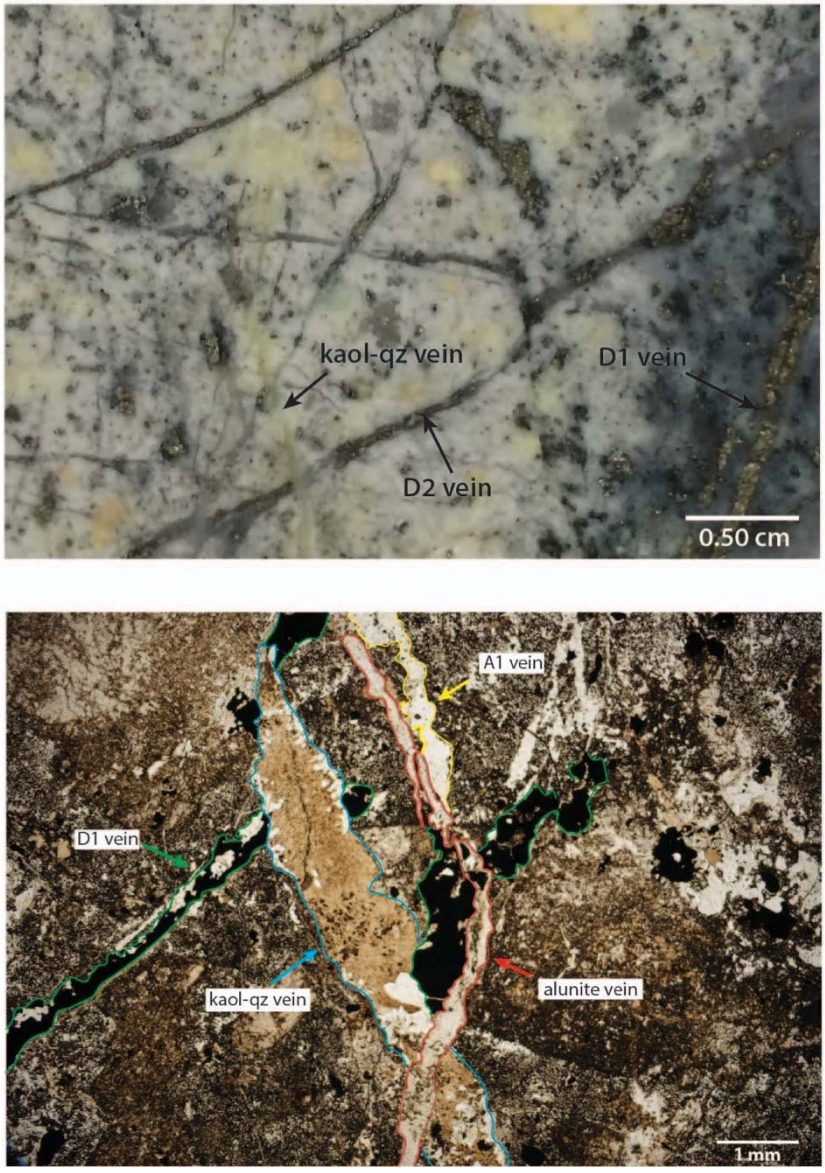

Figure 6.31a. Slab of sample TMC25-136. Kaolinite-quartz (kaol-qz) vein cuts D2 vein, which cuts D1 vein.

Figure 6.31b. Photomicrograph in cross-polarized light of sample TMC25-136. Euhedral quartz borders a D1 vein within a quartz-feldspar-sericite groundmass. To the left of the image is a hypogene alunite veins displaying the characteristic bladed habit. py = pyrite, qz = quartz, qz-fsp-ser matrix = quartz-feldspar-sericite matrix.

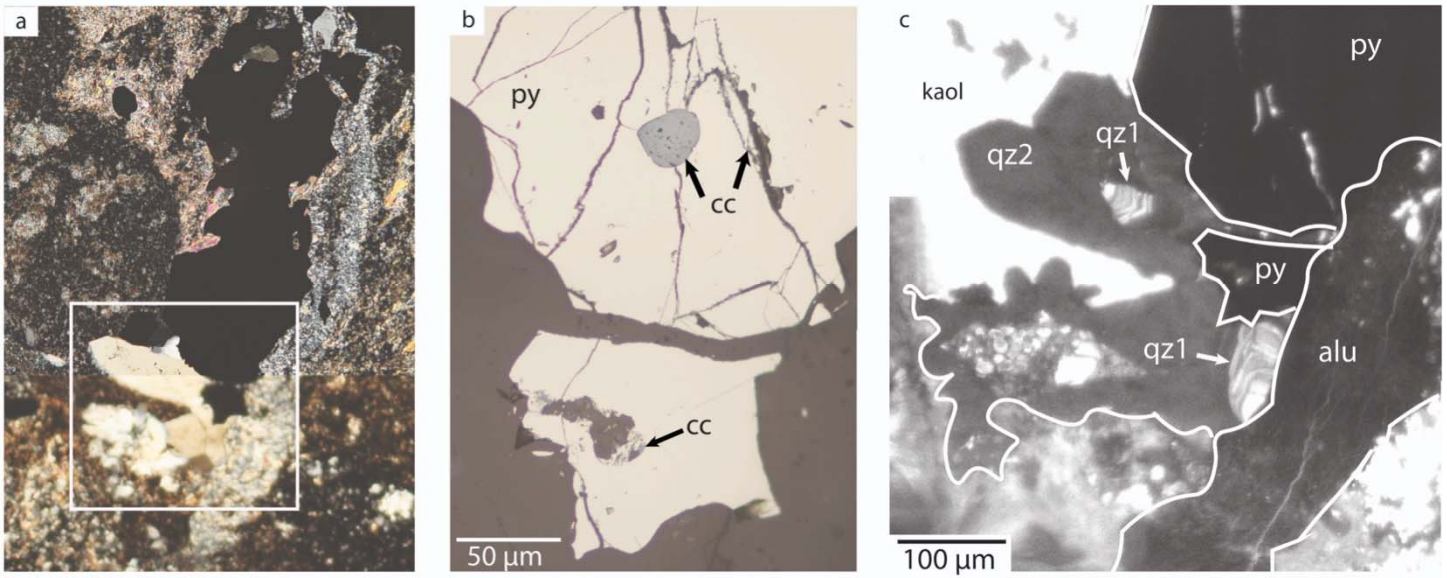

Figure 6.32a. Photomicrograph in cross-polarized light of sample TMC25-136. Pyrite vein is cut by a kaol-quartz vein which is cut by a late-stage alunite vein. White outline box represents magnified reflected light and SEM-CL images in figures 6.30b and 6.30c, respectively.

Figure 6.32b. Photomicrograph in reflected light of D-vein pyrite with chalcocite inclusions which also coats pyrite fractures. py = pyrite, cc = chalcocite

Figure 6.32c. SEM-CL image of the highlighted area in Figure 6.32a. Euhedral, inward oriented quartz 1 (Qz1) associated with kaolinite-quartz, dilational vein shows two generations of quartz. Bright CL-quartz with EGZ are the cores for dark-CL quartz 2 (Qz2) to nucleate from and form euhedral quartz. Qz2, however, shows no obvious CL textures, which may be an artifact, produced by low image resolution. alu = alunite, kaol = kaolinite, py = pyrite, qz = quartz.

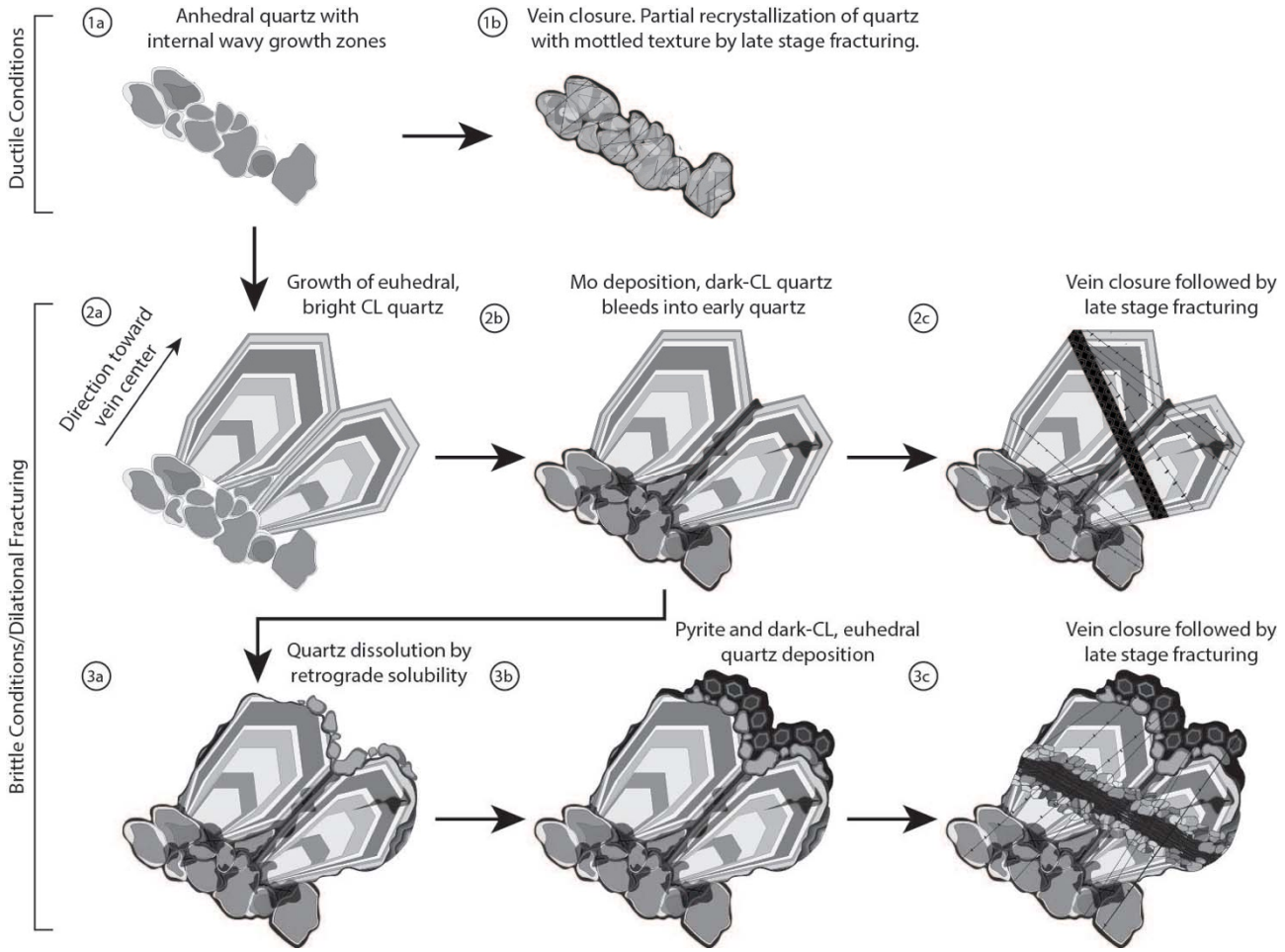

Figure 6.33. Sequence of vein formation at the Red Hills.

1a) Formation of early A1, replacement veins by fine grained, anhedral quartz exhibiting bright to moderate CL intensity dominated by IWGZ texture.

1b) Recrystallization of A1 veins causing slight purification of intrinsic and extrinsic defects within early quartz. Mottled to homogenous CL texture will form as a result and thin, dark-CL intensity transgranular, healed microfractures corresponding to secondary fluid inclusion trails will form post-vein formation.

2a) Initial formation of A2 to B veins by coarse, prismatic, bright to moderate CL quartz with characteristic EGZ texture growing toward the vein interior, indicative of a dilational fracturing environment, overgrowing 1a quartz substrate.

2b) Deposition of molybdenite $\pm$ pyrite preferentially in between quartz grain boundaries in 1a substrate quartz and intergranular fractures in 2a quartz. Dark-CL intensity quartz bleeds into the early quartz in locations of Mo deposition, while retaining primary textures of the early quartz.

2c) Late-stage fracturing forms thin healed, dark-CL intensity microfractures or large, planar dark-CL euhedral quartz inward from the fracture margin. These late, fractures typically forms micro-offsets of early quartz generations and are typically barren.

3a) Dissolution of 2b quartz if veins remain open or contain abundant vugs. Anhedral quartz with IWGZ will form if the vein is damaged by brittle fracturing, dislodging quartz clasts from the parent grain causing them to be more susceptible to recrystallization and dissolution upon retrograde solubility by the ingress of cooler fluids flowing through the vein.

3b) Deposition of euhedral, dark-CL intensity quartz with oscillatory EGZ near similar timing of pyrite deposition once retrograde solubility is bypassed.

3c) Intense late stage microfracturing causes partial recrystallization of quartz shards from 3a which formed along the margins of a zone of high density microfractures. Thin,

dark-CL intensity microfractures cut through all quartz generations forming trails of secondary fluids inclusions and SC texture if the elevated intensities of post-depositional fracturing occur by late tectonic activity.

Table 6.1. SEM-CL textures of hydrothermal quartz based on vein type.

Vein Type		Mineral	Morphology	CL Intensity	CL Textures
Early to Late					
D	D2	Qz1	Euhedral	Moderate – High	EGZ, Dissolution, SC, BCDO, IWGZ
		Pyrite±po±cp±cc ±sp	Anhedral	NA	
	D1	Qz1	Anhedral	Bright	IWGZ, BCDO
		Qz2	Anhedral	Low	IWGQ
		Pyrite±po±cp±cc	Anhedral	NA	
		Sericite	Euhedral	NA	
B		Qz1	Subhedral	Moderate	IWGZ
		Mo	Euhedral	NA	
		Qz2	Euhedral	Moderate - High	EGZ, Dissolution
		Qz3	Subhedral	Moderate -Low	IWGZ, EGZ, Dissolution, SC
		Py	Anhedral	NA	
		Qz4	Euhedral	Low	EGZ
A	A2	Qz1	Anhedral	High - Moderate	IWGZ, BCDO
		Qz2	Euhedral	High -Moderate	EGZ, TB, Dissolution
		Qz3	Curvilinear – Secondary Growth	Moderate – Low	WCB, SC, DCBO
	A1	Qz1	Subhedral	Moderate	WCB, homogenous to mottled
		Qz2	Euhedral	Low	SC

Chapter 7: Conclusions and Discussion

The Red Hills deposit is the easternmost Laramide-aged porphyry Mo-Cu deposit in southwestern North America (Figure 7.1), which developed from multiple episodes of magmatic and hydrothermal activity. It broadly falls into the category of the less intensely mineralized arc-related, low fluorine calc-alkaline differentiate. These deposits have lower initial molybdenum concentrations due to higher Ti and Fe concentrations and less K, Rb, and F, the ingredients that enhance molybdenum concentrations as seen in Climax-type porphyry Mo deposits (Westra and Keith, 1981; Taylor et al., 2010).

The availability of new core has confirmed that the Red Hills deposit is a result of multiple magmatic intrusions of porphyritic character intruding into the overlying sedimentary Permian and Cretaceous wallrock by probable passage of reactivated, Texas lineament basement structures when the Farallon plate was shallowly subducting (~20°) under the North American plate during the Laramide orogeny. From oldest to youngest, these phases are the biotite porphyry (BP), the biotite quartz monzonite porphyry (BQMP), the quartz monzonite porphyry (QMP), the quartz latite porphyry (QLP), and the granodiorite porphyry (GP) with microgranular mafic enclaves. These phases exist as a series of dikes and sills from which the whole system appears structurally intact, upright, and is likely sourced from a larger magmatic system at depth.

Whole-rock geochemical data on Red Hills intrusions suggest that Red Hills has a high-K, calc-alkaline to alkali-calcic magma series affinity. On Westra and Keith's (1981) map of the spatial distribution of stockwork molybdenite deposit magmatism from 80 to 60 Ma, the Red Hills is an obvious outlier, extending further east than any stockwork molybdenum deposit in south-western North America (Figure 7.2). Whole rock geochemistry suggests that all igneous phases at Red Hills are relatively undifferentiated

and are sourced from primary melt. Based on low Nb/Rb and Nb/Sr values, Red Hills plots within the arc-related porphyry Mo deposit model (Westra and Keith's, 1981 calc-alkaline to high K calc-alkaline stockwork Mo deposit equivalent) (Figure 7.3). In order to fall into the category of Westra and Keith's (1981) low fluorine, high K calc-alkaline-type Mo deposit, magmatism at Red Hills would have formed on the order of 250 km trench-ward from Gilmer's (2001) alkali-calcic-dominant interpretation, approximately 825 km from the trench assuming a 20° subduction angle dip.

Rare-earth-element (REE) patterns of sampled Shafter dikes mimic the Red Hills signature, suggesting that the Shafter intrusions may be cogenetic with and sourced from the same magma system as the Red Hills. This relationship provides support for the Shafter mineralization model of the Head (2002) involving Laramide magmatism at depth.

New U-Pb zircon ages have revealed older and younger crystallization ages (BQMP: 66.08 ± 0.31 Ma and MP: 62.54 ± 0.49 Ma) of the Red Hills stock compared to the 61.6 ± 0.3 Ma sericite ^{40}Ar-^{39}Ar date and 64.1 ± 0.2 Ma U-Pb zircon date of Gilmer (2001). This suggests magmatism at Red Hills spanned at least 6 M.y., but the duration of hydrothermal activity is currently unknown. The single mineralization age by Gilmer (2001) from Re-Os analyses of molybdenite is 60.2 ± 0.3 Ma, significantly younger than the crystallization ages of the porphyritic stock. Future work should analyze a greater number of samples to obtain better temporal resolution between the mineralization and crystallization ages of the deposit.

The paragenesis of Laramide magmatism, stockwork veining, and vein-fill is summarized in Figure 7.5. Stockwork fracturing, induced by fluid overpressure from exsolved magmatic fluids against the surrounding wall rock, occurred when the tensile strength of the wallrock was overcome. The ingress of metal-rich fluids into the fractures

and eventual sealing by mineral precipitation caused episodic pressure buildup leading to cycles of multigeneration, crosscutting stockwork veins of differing mineralogies. The circulation of meteoric fluids was induced by the thermal gradients derived from the heat emitted from the magmatic stock and hydrothermal fluids.

Hypogene vein styles for each intrusive phase is expressed as barren quartz stockwork A veins (separated into A1 and A2 based on vein geometry and style of quartz deposition as the system progressed from ductile to increasingly brittle conditions) followed by B, Mo-bearing veins in the form of molybdenite followed by pyritic, Cu-bearing, D veins (separated into D1 and D2 veins) and ending with hypogene kaolinite-alunite veins. A and B veins are interpreted to be coincident with potassic alteration as seen by thin mm K-feldspar vein selvages or as thin biotite veinlets in the BP. Pervasive phyllic alteration has destroyed much of the evidence of potassic alteration, and is coincident with the formation of pyritic D vein with sericite alteration halos. Copper minerals in D-veins occur as inclusions within pyrite commonly in the form of chalcopyrite, but also covellite, bornite, and chalcocite. Westra and Keith's (1981) model indicates that pyrite halos are weakly developed in arc-related porphyry Mo deposits due to limited H_2S fractionation into the vapor phase by the lack of boiling. Red Hills, however, has a prominent pyritic halo associated with phyllic alteration which, along with comparably greater copper enrichment, further calls into question whether Red Hills is either a high K calc-alkaline stockwork Mo deposit substantially enriched in Cu or a porphyry Cu deposit substantially enriched in Mo.

Intermediate argillic alteration is exposed on the surface at Red Hills and extends no more than 60 m (~200 ft) below the surface. Propylitic alteration extends approximately 500 m (1640 ft) east of the western, mineralized part at Red Hills and is defined by chlorite, epidote, and calcite alteration minerals. Hornfels and skarn

occurrences exist near contact aureoles of the magmatic stock. The skarns are primarily composed of grossular-andradite-garnet, and are weakly mineralized in Pb, Zn, and minor Ag. The supergene zone is characterized as a hematite-goethite-jarosite leached cap with supergene alunite veins that overlie a thin chalcocite enrichment blanket that is best developed in pyritic hornfels.

In order to assess the accuracy of categorized hypogene and supergene alunite veins, S isotope studies should be conducted in future studies. Hypogene alunite should display appreciable ^{34}S enrichment relative to associated sulfides, such as pyrite, whereas supergene alunite should have nearly identical composition to the parental sulfide (Field, 1966).

Scanning electron microscopy- cathodoluminescence (SEM-CL) imaging of hydrothermal quartz from A, B, and D veins reveals three separate possible sequences of quartz and/or sulfide deposition as a vein evolved. This sequence involves early, metal-barren quartz veins progressing into molybdenum-rich veins and terminating with copper-bearing pyrite veins. Early A1 veins have sinuous vein geometries filled with granular quartz, which display wavy growth zones to mottled and/or homogenous CL textures, which are interpreted to be a product from a ductile environment. Late A2 veins are more planar, and contain highly luminescent euhedral, inward-oriented hydrothermal quartz showing oscillatory, euhedral growth zone CL textures typically overgrowing A1 quartz. A2 veins are evidence that the hydrothermal system has progressed into a more brittle environment. Deep B vein-quartz is similar in character as A2 vein-quartz, with the exception that dark-CL quartz pools into the bright CL quartz at sites of molybdenite deposition, suggesting sulfides suppress CL luminescence. Assuming molybdenite deposition is due to cooling of the hydrothermal fluids, the fluids would enter the zone of retrograde solubility of quartz, which is supported by the partially dissolved and embayed

grain boundaries of B-vein quartz. Shallow B veins display greater complexity compared to deeper veins, based on repeated dissolution and re-precipitation quartz CL textures revealing at most five separate quartz generations. Microbrecciation is common where cyclic dissolution textures appear. These textures appear to be products of pressure fluctuations during hydrostatic loading and unloading as veins are commonly sealed and later re-opened by recurring tectonic activity. Late stage D vein-quartz is typically characterized as dark-CL quartz with rhythmic bands or as euhedral quartz with oscillatory growth zones. Stockwork veining and vein fill at Red Hills commonly displays multiple quartz generations with younger veins superimposed on older veins (i.e. B or D vein quartz overgrown on A vein quartz), a common feature documented in many porphyry Cu deposits (Penniston-Dorland, 2001; Rusk and Reed, 2002; Rusk et al., 2008; Müller et al., 2010; Landtwing and Pettke, 2005; Rusk, 2012).

The sequence of Mo mineralization preceding Cu mineralization from low fluorine fluids at Red Hills has similarities to the Westra and Keith's (1981) and Taylor et al.'s (2010) calc-alkaline to high K calc-alkaline, volcanic arc-related stockwork molybdenum deposit model, but a disparity exists between the hydrothermal fluid characteristics and depth of emplacement. Arc-related porphyry Mo deposits form at deeper levels, 4 - 5 km (Linnen and Williams-Jones, 1990), compared to the 2 – 3 km depth estimated at Red Hills (Gilmer, 2001). Hydrothermal fluids from the arc-related porphyry model (Taylor et al., 2010) are typically vapor dominant, with low to moderate salinities (< 16 wt. % NaCl equiv) at moderate temperatures (250-400°C) with CO_2-bearing inclusions, indicating that the hydrothermal fluids did not boil. This contradicts Gilmer's (2001) observation of boiling assemblages in the quartz monzonite porphyry (samples RH06, RH07, RH09, and RH24) with exceptionally higher salinity inclusions that are more similar to classic porphyry Cu deposits (Sillitoe, 2010; Bodnar, 1995;

Beane and Bodnar, 1995). Fluid inclusions in vein quartz ranged from 33 to 47 wt. % NaCl equiv. in the phyllic alteration zone with an average 400°C homogenization temperature.

Minor additional fluid inclusion petrography of deep quartz-molybdenite B veins at Red Hills revealed the majority of primary fluid inclusion assemblages were a mixture of vapor-rich inclusions, intermediate density inclusions with chalcopyrite daughter crystals with an average 35% vapor bubble, and brine inclusions with halite, sylvite, anhydrite, hematite, and chalcopyrite daughter salts. Rusk et al. (2008), however, documented low salinity fluid inclusion assemblages in late-stage quartz-molybdenum veins that they interpreted to form by pressure-release rather than cooler fluid temperatures at the Butte porphyry Cu-Mo deposit in Montana. This calls into question the drivers of molybdenum and copper precipitation at Red Hills.

According to Candela and Holland (1984), molybdenum strongly partitions into an aqueous phase from an evolving and crystallizing magma chamber, and reach their maximum ore-fluid concentrations in the late stages of vapor saturation. Candela and Holland (1984) reported that the partition coefficient of molybdenum is independent of soft chloride complexes, and that hard hydroxyl complexes are the dominant ligands for molybdenum transport. During crystallization, molybdenum acts as an incompatible element throughout, whereas copper behaves as a compatible element until water saturation of the melt occurs and copper enters the fluid phase. This difference in behavior suggests early fluid unmixing or vapor evolution of highly acidic solutions is an efficient method to scavenge copper for porphyry Cu deposits (Keppler and Wyllie, 1991). Molybdenum enrichment, however, occurs during late vapor saturation from low acidic solutions in which molybdenum concentrations in hydroxyl stable conditions can occur at the carapace of the magma chamber by second boiling of exsolving magmatic

fluids while most of the copper will be lost to crystalline phases (Keppler and Wyllie, 1991; Burnham, 1997). Due to the existence of multi-phase brine inclusions, chlorine must have been the dominant halogen in the hydrothermal fluids for copper transport, especially in the phyllic alteration zone at Red Hills, similar to porphyry Cu deposits (Rusk et al., 2008).

Ulrich and Mavrogenes (2008) indicated that molybdenum solubility is temperature dependent, with greater solubility at higher temperatures. In contrast, Candela (1992) emphasized that the compatibility of molybdenum between crystal and melt is dependent on the oxygen fugacity of the magma, with molybdenum acting more incompatibly under oxidizing conditions. Smith et al. (1980) reported that molybdenite precipitates in response to cooling and a decrease in pH. Stockwork fracturing of the host rock can be an expedient mechanism for instantaneous pressure release and temperature drop for molybdenite deposition to occur. Decreasing fO_2 or fH_2O by an increase in fS_2 may also be mechanism for molybdenite precipitation (Rempel et al., 2006). At high temperatures, the partitioning of molybdenum into an aqueous solution is independent of CO_2, F, Cl, and S, content but can be transported in the vapor phase as hydroxide and oxymolybdate species (Rempel et al., 2006; Westra and Keith, 1981).

Based on the appropriate oxidized magma composition, thin potassic alteration halos, existence of L-V dominant and intermediate-density fluid inclusions in deep quartz-molybdenite veins at Red Hills, and SEM-CL textures of hydrothermal quartz in B veins, evidence supports that molybdenite was largely transported from a reduced, acidic aqueous solution by hydroxyl complexes similar to Seo et al.'s (2012) findings at Bingham Canyon. Mechanisms for early molybdenite precipitation could be due to a change in the physio-chemical conditions by decreases in pH, temperature, fO_2, or fH_2O, by an increase in fS_2, repeated episodes of fracturing, fluid ascent, and fracture sealing

by mineral precipitation forming crosscutting stockwork veins of varying mineralogies. Late copper deposition likely occurred when the hydrothermal fluids reached the boiling horizon where brine-vapor unmixing in combination with the slower rate of decompression relative to fluid cooling as suggested by Rusk et al. (2008). Greater efficiency of copper transportation and deposition by the availability of chloride complexes from increasingly acidic, reduced fluid compared to earlier Mo-rich fluids could be achieved to produce pyrite veins with sericitic alteration which pervasively overprints the deposit.

Future work should try to delineate what mechanism was the dominant driver of molybdenite concentration at Red Hills. Due to the shallow level of emplacement at Red Hills, perhaps meteoric water played a greater role as an effective means of molybdenite precipitation at the top and peripheries of the deposit during the waning stages of the hydrothermal system. Future work include conduct oxygen stable isotope studies on the various quartz veins to constrain this relationship.

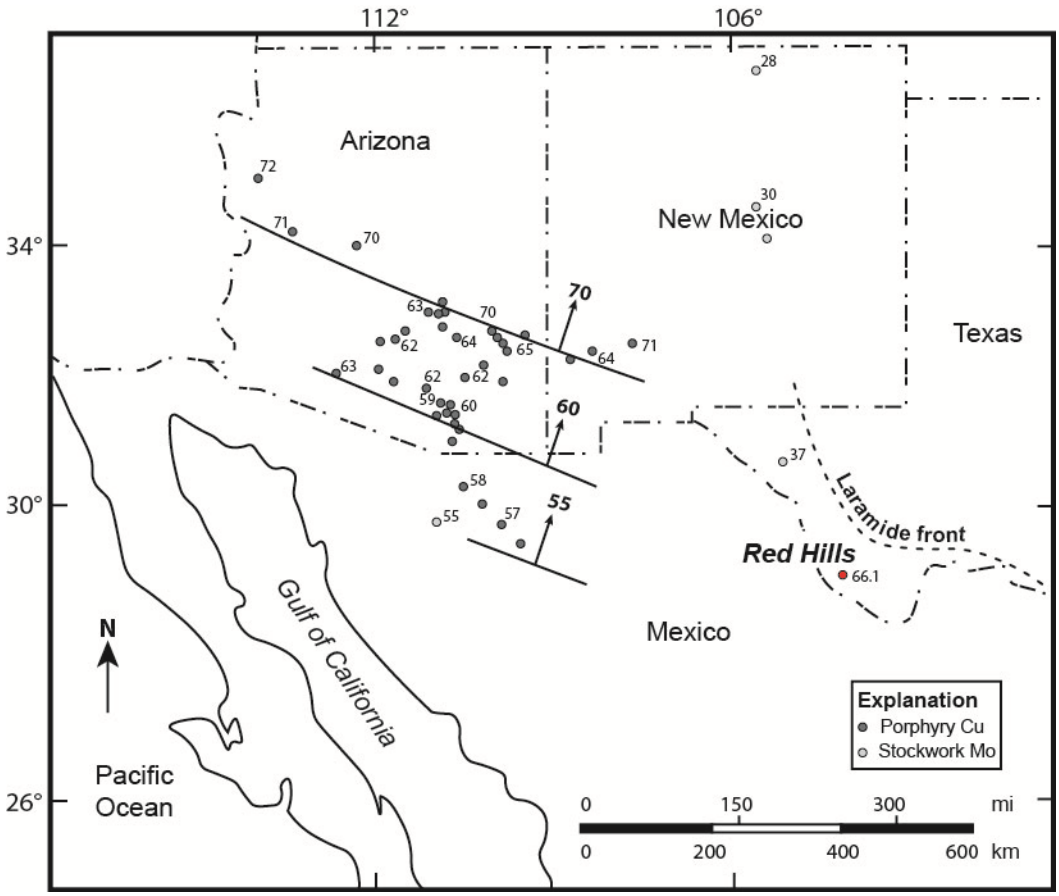

Figure 7.1. Distribution of porphyry Cu and stockwork Mo deposits in southwestern North America. Dark gray dots represent porphyry Cu deposits and light gray dots represent stockwork Mo deposits. Modified after Titley (1993). Laramide front after Muehlberger (1980).

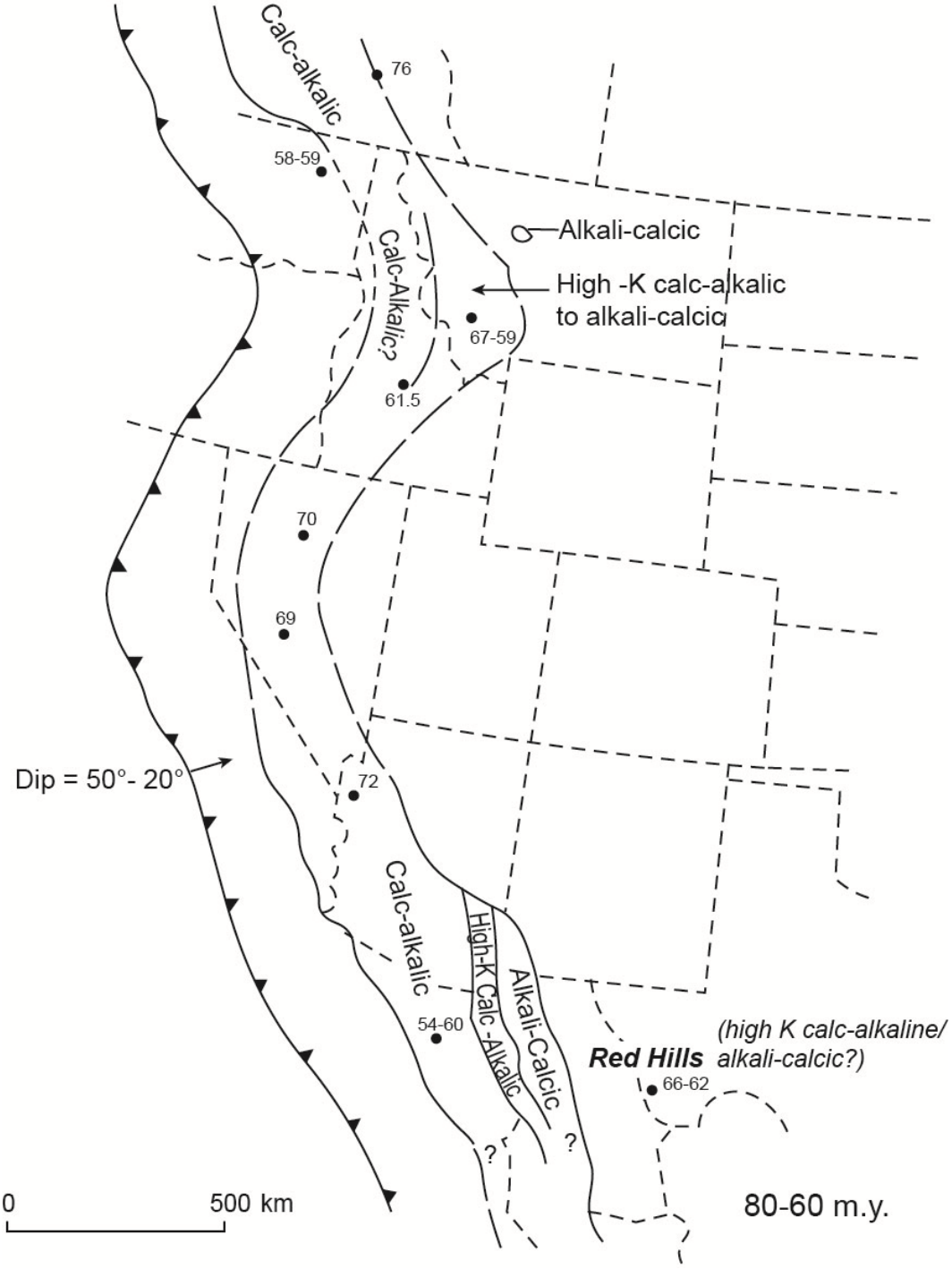

Figure 7.2. Spatial distribution of magmatism and stockwork molybdenum deposits in western United States from 80-60 Ma. Modified after Westra and Keith (1981).

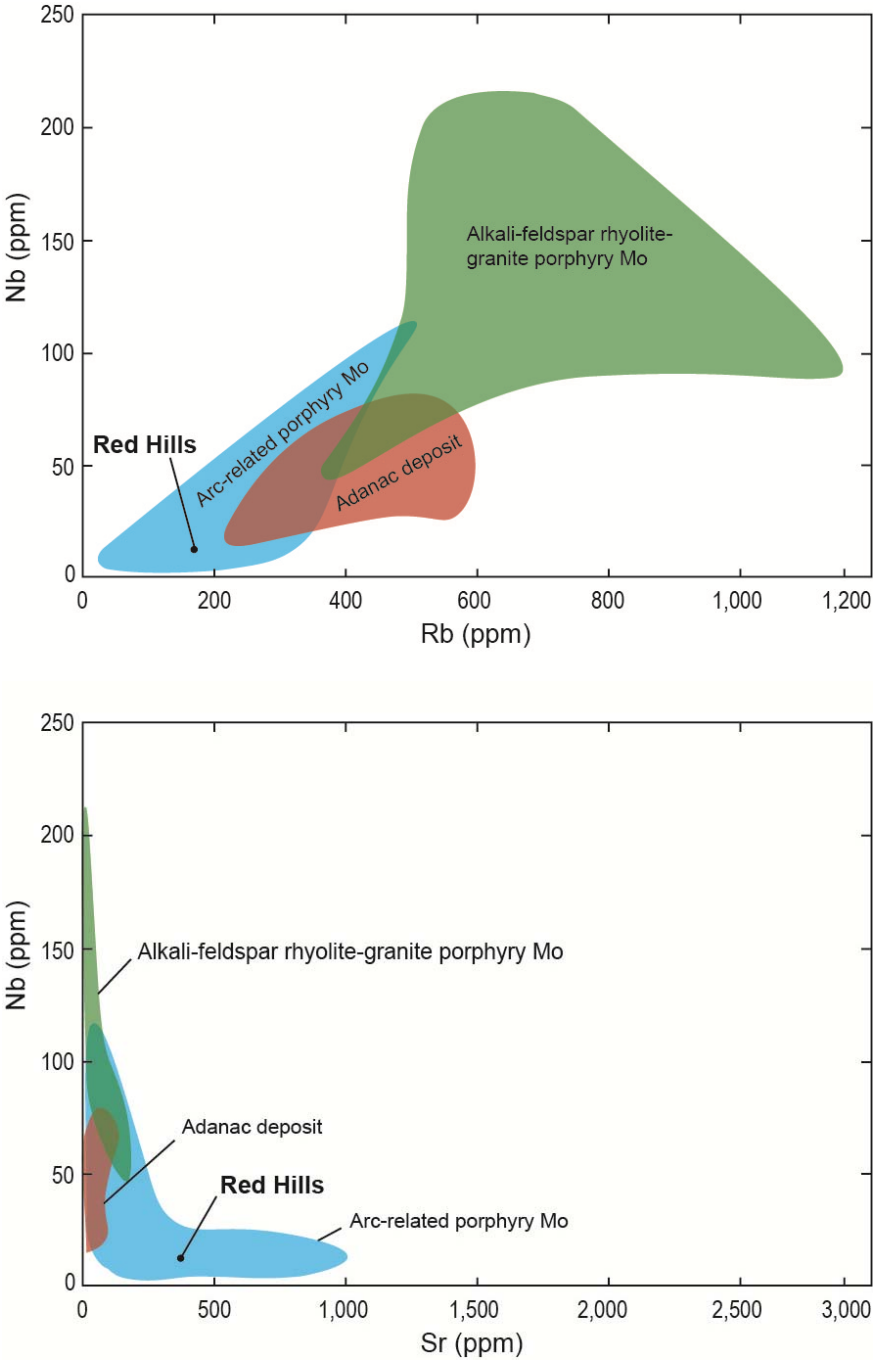

Figure 7.3. Nb/Rb and Nb/Sr diagrams of unaltered to weakly altered intrusions associated with arc-related porphyry Mo deposits. Modified after Taylor et al. (2010).

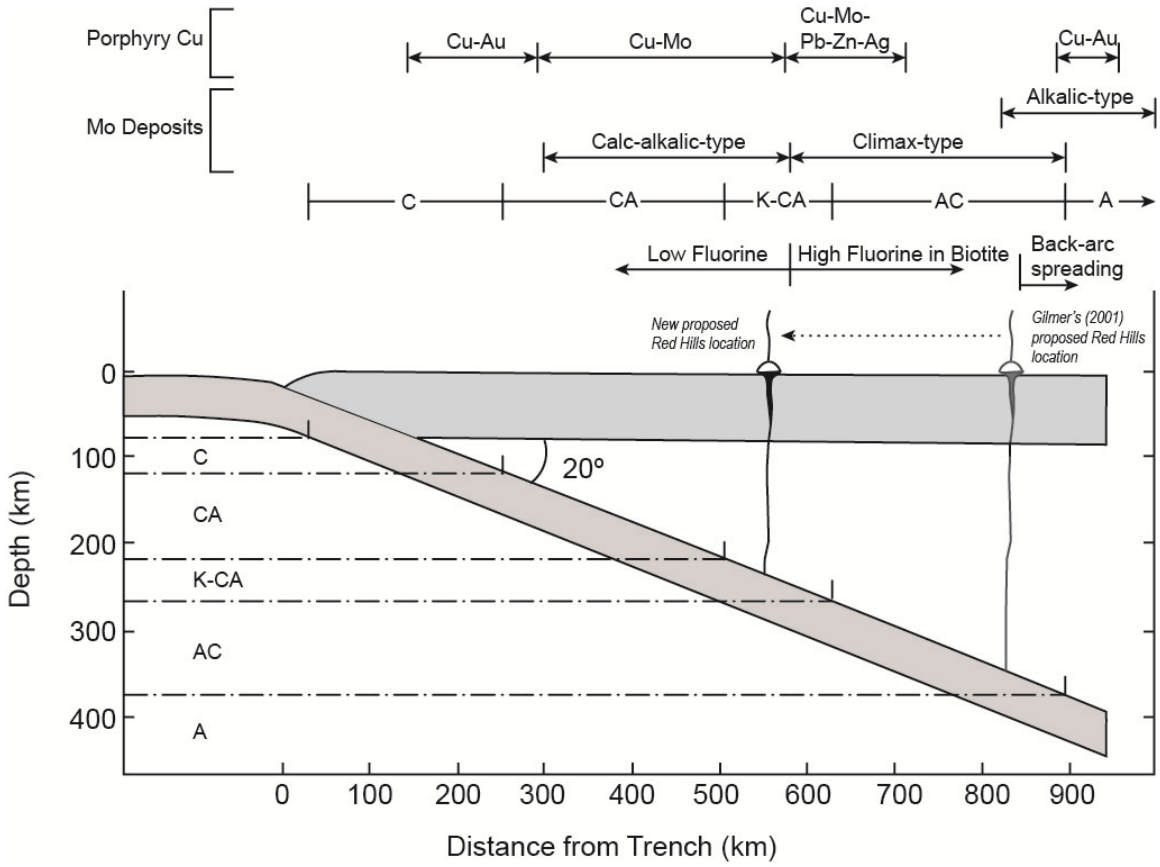

Figure 7.4. Schematic of magma chemistries at 20° dip subduction angle at approximately 65 Ma for porphyry Cu and stockwork molybdenum deposits. Modified after (Westra and Keith, 1981). Red Hills former location from Gilmer (2001). Magma series abbreviations, C: calcic, CA: calc-alkaline, K-CA: high K calc-alkaline, AC: alkali-calcic, A: alkalic.

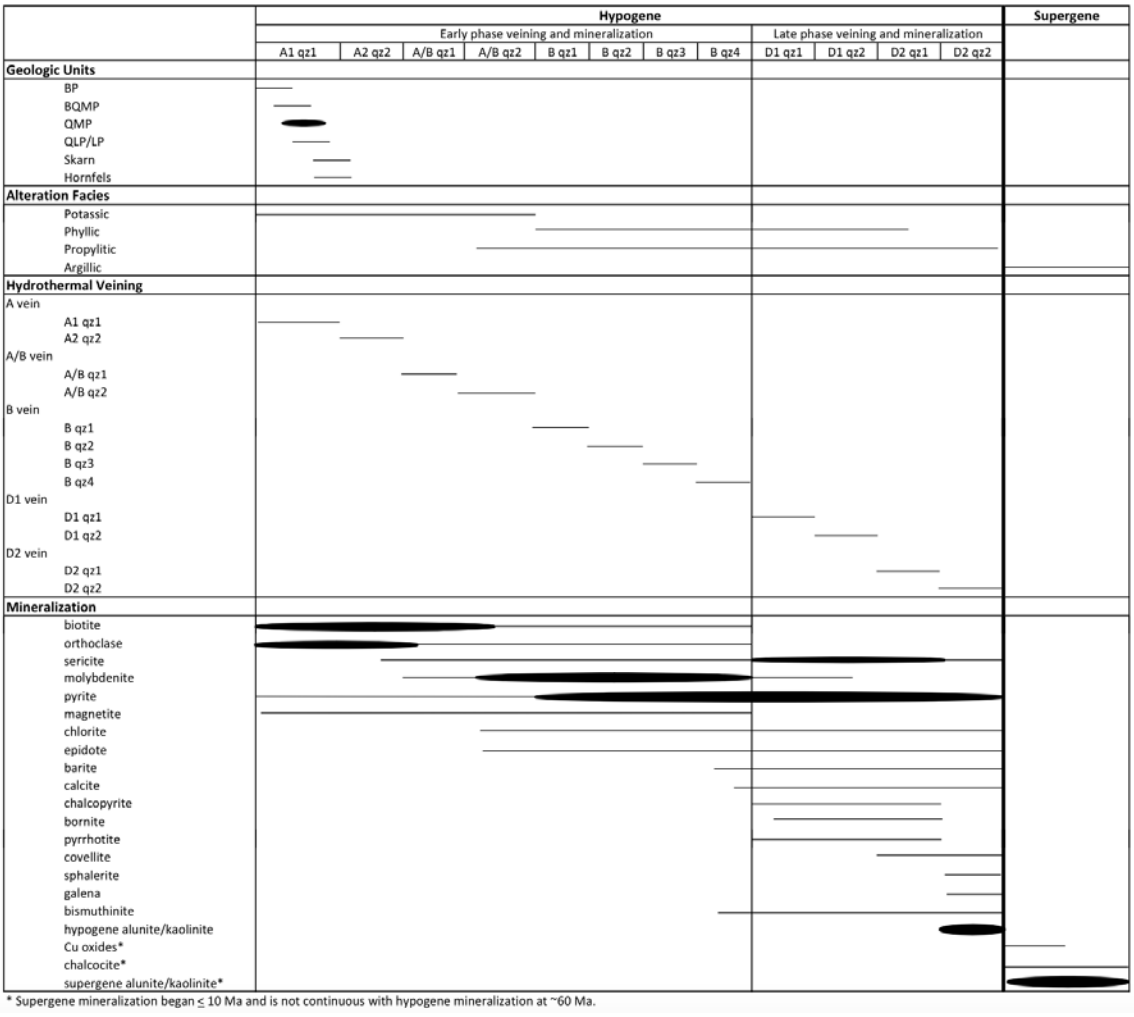

Figure 7.5. Paragenesis of intrusive phases, stockwork veining, and vein-fill of the Red Hills deposit. Thicker lines represent greater abundance.

Appendix A: Sample Locations and Descriptions

Coordinate System: WGS 1984 UTM Zone 13N, Transverse Mercator Projection.

Table A-1: Survey Information for Drill Hole Collar Locations

Hole ID	Longitude	Latitude	z	Max Depth	Hole Path	Azimuth	Dip	Company	Date	Type
AMAX1	104° 24' 7.160" W	29° 48' 8.705" N	3917	2912	Linear	0	-90	AMAX	1967	core
D1	104° 24' 18.06" W	29° 48' 6.739" N	3894	1007.5	Linear	0	-90	Duval	1971	rotary/core
D10	104° 24' 8.316" W	29° 48' 21.831" N	4199	507	Linear	0	-90	Duval	1971	core
D11	104° 24' 13.45" W	29° 48' 19.493" N	4161	500	Linear	0	-90	Duval	1971	core
D12	104° 24' 17.11" W	29° 48' 17.561" N	4184	605	Linear	0	-90	Duval	1971	core
D13	104° 24' 13.04" W	29° 48' 23.870" N	4120	500	Linear	0	-90	Duval	1971	core
D14	104° 24' 3.750" W	29° 48' 15.008" N	4077	1685	Linear	0	-90	Duval	1971	core
D16	104° 24' 17.60" W	29° 48' 10.197" N	3930.05	646	Linear	0	-90	Duval	1971	core
D9	104° 24' 17.92" W	29° 48' 1.939" N	3906	1162	Linear	0	-90	Duval	1971	core
DD101	104° 24' 32.56" W	29° 48' 3.221"N	3944	730	Linear	0	-90	ASARCO	1955	core
DD102	104° 24' 31.90" W	29° 48' 5.528" N	3956	300	Linear	0	-90	ASARCO	1955	core
DD103	104° 24' 31.12" W	29° 48' 8.086" N	3973	300	Linear	0	-90	ASARCO	1955	core
DD15	104° 24' 12.46" W	29° 48' 12.387" N	4007	926	Linear	0	-90	Duval	1971	core
DD27	104° 24' 21.65" W	29° 48' 7.160" N	3921	220	Linear	0	-90	Duval	1971	core
DD6	104° 24' 16.09" W	29° 48' 9.825"N	3927	650	Linear	0	-90	Duval	1971	core
DD68	104° 23' 51.94" W	29° 48' 2.739" N	3953	358	Linear	0	-90	Duval	1983	core
DD69	104° 23' 51.49" W	29° 48' 4.590"N	3958	266	Linear	0	-90	Duval	1983	core
DD7	104° 24' 12.23" W	29° 48' 16.261" N	4058	2106	Linear	0	-90	Duval	1971	core
DD70	104° 23' 48.22" W	29° 47' 58.260" N	3941	370	Linear	0	-90	Duval	1983	core
DD71	104° 23' 46.65" W	29° 48' 1.782" N	3955	358	Linear	0	-90	Duval	1983	core
DD8	104° 24' 22.51" W	29° 48' 14.202" N	4001	869	Linear	0	-90	Duval	1971	core
DH17	104° 24' 8.187" W	29° 48' 14.366" N	3975.19	700	Linear	0	-90	Duval	1971	core
DH18	104° 24' 17.06" W	29° 48' 7.603" N	3922	390	Linear	0	-90	Duval	1971	core
DH19	104° 24' 14.15" W	29° 48' 14.777" N	4079	366	Linear	0	-90	Duval	1971	core

Hole ID	Longitude	Latitude	z	Max Depth	Hole Path	Azimuth	Dip	Company	Date	Type
DH20	104° 24' 15.60" W	29° 48' 11.606" N	4000	358	Linear	0	-90	Duval	1971	core
DH21	104° 24' 14.47" W	29° 48' 6.865" N	3968	489	Linear	0	-90	Duval	1971	core
DH22	104° 24' 17.57" W	29° 48' 12.746" N	4017	636	Linear	0	-90	Duval	1971	core
DH23	104° 24' 9.023" W	29° 48' 18.234" N	4044	509	Linear	0	-90	Duval	1971	core
DH24	104° 24' 9.204" W	29° 48' 15.848" N	3972	376	Linear	0	-90	Duval	1971	core
DH25	104° 24' 20.09" W	29° 48' 12.783" N	4029	429	Linear	0	-90	Duval	1971	core
DH26	104° 24' 11.67" W	29° 48' 14.674" N	4000	359	Linear	0	-90	Duval	1971	core
DH27A	104° 24' 21.70" W	29° 48' 6.960" N	3919	455	Linear	0	-90	Duval	1971	core
DH28	104° 24' 15.95" W	29° 48' 5.844" N	3922	436	Linear	0	-90	Duval	1971	core
DH29	104° 24' 21.79" W	29° 48' 9.612" N	3928	413	Linear	0	-90	Duval	1971	core
DH30	104° 24' 12.43" W	29° 48' 8.384" N	3979	388	Linear	0	-90	Duval	1972	core
DH31	104° 23' 57.46" W	29° 48' 14.353" N	4085	481	Linear	0	-90	Duval	1972	core
DH32	104° 24' 19.91" W	29° 48' 11.343" N	3999	483	Linear	0	-90	Duval	1972	core
DH33	104° 24' 13.37" W	29° 48' 13.302" N	4042	368	Linear	0	-90	Duval	1972	core
DH34	104° 24' 16.06" W	29° 48' 16.414" N	4154	385	Linear	0	-90	Duval	1972	core
DH35	104° 23' 57.39" W	29° 48' 11.918" N	4069.9	322	Linear	0	-90	Duval	1972	core
DH36	104° 23' 57.64" W	29° 48' 16.661" N	4107	302	Linear	0	-90	Duval	1972	core
DH37	104° 24' 14.63" W	29° 48' 17.423" N	4157	322	Linear	0	-90	Duval	1972	core
DH38	104° 23' 59.92" W	29° 48' 14.786" N	4014	315	Linear	0	-90	Duval	1972	core
DH39	104° 23' 55.76" W	29° 48' 7.163" N	4008	332	Linear	0	-90	Duval	1972	core
DH40	104° 23' 58.07" W	29° 48' 18.705" N	4119	315	Linear	0	-90	Duval	1972	core
DH41	104° 23' 57.25" W	29° 48' 9.641" N	4040	258	Linear	0	-90	Duval	1972	core
DH42	104° 23' 55.21" W	29° 48' 15.025" N	4037	41	Linear	0	-90	Duval	1972	core
DH42A	104° 23' 55.21" W	29° 48' 14.975" N	4036	280	Linear	0	-90	Duval	1972	core
DH43	104° 23' 56.04" W	29° 48' 17.617" N	4061	345.5	Linear	0	-90	Duval	1972	core
DH44	104° 24' 0.026" W	29° 48' 17.636" N	4080	171	Linear	0	-90	Duval	1972	core

Hole ID	Longitude	Latitude	z	Max Depth	Hole Path	Azimuth	Dip	Company	Date	Type
DH45	104° 23' 57.57" W	29° 48' 5.564" N	3970	190	Linear	0	-90	Duval	1972	core
DH46	104° 24' 3.790" W	29° 48' 16.840" N	4123	20	Linear	0	-90	Duval	1972	core
DH46A	104° 24' 3.768" W	29° 48' 16.841" N	4123	185	Linear	0	-90	Duval	1972	core
DH47	104° 23' 57.82" W	29° 48' 17.607" N	4113.02	205	Linear	0	-90	Duval	1972	core
DH48	104° 23' 57.69" W	29° 48' 15.460" N	4092	272	Linear	0	-90	Duval	1972	core
DH49	104° 24' 0.389 W	29° 48' 4.123" N	3952	310	Linear	0	-90	Duval	1972	core
F13	104° 24' 24.18" W	29° 48' 1.935" N	3881	726	Linear	0	-90	ASARCO	1955	core
F20	104° 24' 24.08" W	29° 47' 47.974" N	3911	740	Linear	0	-90	ASARCO	1955	core
F9	104° 24' 24.33" W	29° 48' 9.986" N	3947	630	Linear	0	-90	ASARCO	1955	core
H10	104° 24' 19.73" W	29° 48' 7.902" N	3900	586	Linear	0	-90	ASARCO	1955	core
HD2	104° 23' 59.82" W	29° 48' 10.007" N	4010	701	Linear	0	-90	Duval	1971	rotary/core
HD3	104° 24' 4.219" W	29° 48' 5.271" N	3967	1744	Linear	0	-90	Duval	1971	rotary/core
HD4	104° 24' 15.41" W	29° 48' 13.907" N	4085.47	500	Linear	0	-90	Duval	1971	rotary
I16	104° 24' 17.28" W	29° 47' 55.741" N	3876	693	Linear	0	-90	ASARCO	1955	core
J15	104° 24' 16.04" W	29° 47' 58.051" N	3866	258	Linear	0	-90	ASARCO	1955	core
N13	104° 24' 7.888" W	29° 48' 1.967" N	3902	454	Linear	0	-90	ASARCO	1955	core
N19	104° 24' 8.274" W	29° 47' 49.950" N	3928	488	Linear	0	-90	ASARCO	1955	core
RD5	104° 24' 21.46" W	29° 48' 5.711" N	3909	400	Linear	0	-90	Duval	1971	rotary
RD50	104° 23' 55.47" W	29° 48' 9.846" N	4031	165	Linear	0	-90	Duval	1973	rotary
RD51	104° 23' 59.14" W	29° 48' 12.815" N	4035	325	Linear	0	-90	Duval	1973	rotary
RD52	104° 24' 6.268" W	29° 48' 15.134" N	4042	155	Linear	0	-90	Duval	1973	rotary
RD53	104° 24' 1.278" W	29° 48' 13.175" N	3979	190	Linear	0	-90	Duval	1973	rotary
RD54	104° 24' 3.435" W	29° 48' 11.909" N	3976	180	Linear	0	-90	Duval	1973	rotary
RD55	104° 23' 57.64" W	29° 48' 16.612" N	4107	205	Linear	0	-90	Duval	1973	rotary
RD56	104° 23' 57.89" W	29° 48' 17.197" N	4110	200	Linear	0	-90	Duval	1973	rotary
RD57	104° 23' 57.24" W	29° 48' 15.121" N	4085	200	Linear	0	-90	Duval	1973	rotary

Hole ID	Longitude	Latitude	z	Max Depth	Hole Path	Azimuth	Dip	Company	Date	Type
RD58	104° 23' 57.10" W	29° 48' 16.427" N	4095	200	Linear	0	-90	Duval	1973	rotary
RD59	104° 23' 57.08" W	29° 48' 17.229" N	4097	280	Linear	0	-90	Duval	1973	rotary
RD60	104° 23' 58.44" W	29° 48' 16.054" N	4085	200	Linear	0	-90	Duval	1973	rotary
RD61	104° 24' 0.703" W	29° 48' 11.553" N	3985	220	Linear	0	-90	Duval	1973	rotary
RD62	104° 24' 6.037" W	29° 48' 13.071" N	3971	155	Linear	0	-90	Duval	1973	rotary
RD63	104° 24' 11.89" W	29° 48' 6.147" N	3948	200	Linear	0	-90	Duval	1973	rotary
RD64	104° 24' 11.20" W	29° 48' 1.289" N	3888	255	Linear	0	-90	Duval	1973	rotary
RD65	104° 23' 55.03" W	29° 48' 5.026" N	4004	280	Linear	0	-90	Duval	1973	rotary
RD66	104° 23' 55.82" W	29° 48' 3.266" N	3993	200	Linear	0	-90	Duval	1973	rotary
RD67	104° 23' 57.02" W	29° 48' 0.750" N	3950	255	Linear	0	-90	Duval	1973	rotary
RH1	104° 24' 8.374" W	29° 48' 16.922" N	4016	1045	Linear	0	-90	PD	1965	core
RH2	104° 23' 53.34" W	29° 48' 10.284" N	3974	648	Linear	0	-90	PD	1965	core
RH3	104° 24' 26.77" W	29° 48' 19.738" N	4007	488	Linear	0	-90	PD	1965	core
SD141	104° 19' 44.38" W	29° 47' 31.722" N	4,135	914	Linear	0	-90	Gold Fields		
SD142	104° 19' 29.64" W	29° 47' 48.773" N	4,165	755	Linear	0	-90	Gold Fields		
SD146	104° 19' 41.74" W	29° 47' 46.447" N	4,132	527	Linear	0	-90	Gold Fields		
SD147	104° 19' 33.15" W	29° 47' 33.537" N	4,202	722	Linear	0	-90	Gold Fields		
SD149	104° 19' 26.51" W	29° 47' 48.697" N	4,179	542	Linear	0	-90	Gold Fields		
SD151	104° 19' 28.20" W	29° 47' 42.901" N	4,194	636	Linear	0	-90	Gold Fields		
SD152	104° 19' 24.60" W	29° 47' 48.420" N	4,192	592	Linear	0	-90	Gold Fields		
SD154	104° 19' 29.95" W	29° 47' 44.327" N	4,181	562	Linear	0	-90	Gold Fields		
SD155	104° 19' 33.21" W	29° 47' 43.601" N	4,173	867	Linear	0	-90	Gold Fields		
SD158	104° 19' 30.44" W	29° 47' 43.893" N	4,181	951	Linear	0	-90	Gold Fields		
SD159	104° 19' 30.39" W	29° 47' 32.998" N	4,219	678	Linear	0	-90	Gold Fields		
SD163	104° 19' 31.51" W	29° 47' 46.345" N	4,167	778	Linear	0	-90	Gold Fields		
SD164	104° 19' 25.34" W	29° 47' 53.455" N	4,178	580	Linear	0	-90	Gold Fields		

Hole ID	Longitude	Latitude	z	Max Depth	Hole Path	Azimuth	Dip	Company	Date	Type
SD168	104° 19' 28.13" W	29° 47' 54.480" N	4,190	688	Linear	0	-90	Gold Fields		
SD169	104° 19' 26.01" W	29° 48' 5.999" N	4,241	549	Linear	0	-90	Gold Fields		
SD171	104° 19' 31.84" W	29° 47' 52.637" N	4,177	828	Linear	0	-90	Gold Fields		
SD172	104° 19' 25.23" W	29° 48' 3.825" N	4,181	447	Linear	0	-90	Gold Fields		
SD177	104° 19' 35.78" W	29° 47' 42.623" N	4,170	898	Linear	0	-90	Gold Fields		
SD181	104° 19' 38.47" W	29° 47' 42.746" N	4,155	693	Linear	0	-90	Gold Fields		
SD186	104° 19' 29.33" W	29° 47' 45.869" N	4,174	714	Linear	0	-90	Gold Fields		
SD189	104° 19' 30.06" W	29° 48' 12.319" N	4,182	320	Linear	0	-90	Gold Fields		
SD194	104° 19' 41.72" W	29° 47' 41.901" N	4,114	466	Linear	0	-90	Gold Fields		
SD198	104° 19' 48.01" W	29° 47' 34.652" N	4,076	451	Linear	0	-90	Gold Fields		
SD202	104° 19' 51.32" W	29° 47' 34.580" N	4,081	502	Linear	0	-90	Gold Fields		
SD207	104° 19' 45.51" W	29° 47' 33.629" N	4,123	636	Linear	0	-90	Gold Fields		
SD208	104° 19' 28.35" W	29° 48' 3.455" N	4,210	551	Linear	0	-90	Gold Fields		
SD212	104° 19' 45.02" W	29° 47' 42.016" N	4,100	487	Linear	0	-90	Gold Fields		
SD217	104° 19' 30.79" W	29° 47' 51.027" N	4,169	823	Linear	0	-90	Gold Fields		
SD222	104° 19' 17.98" W	29° 47' 50.456" N	4,211	525	Linear	0	-90	Gold Fields		
SD224	104° 19' 27.37" W	29° 47' 51.227" N	4,174	668	Linear	0	-90	Gold Fields		
SD236	104° 19' 12.18" W	29° 47' 49.446" N	4,229	402	Linear	0	-90	Gold Fields		
SD240	104° 19' 6.328" W	29° 47' 47.860" N	4,266	303	Linear	0	-90	Gold Fields		
SD242	104° 19' 31.00" W	29° 47' 57.219" N	4,192	508	Linear	0	-90	Gold Fields		
SD244	104° 19' 34.48" W	29° 48' 4.081" N	4,161	570	Linear	0	-90	Gold Fields		
SD245	104° 19' 36.43" W	29° 47' 53.453" N	4,176	538	Linear	0	-90	Gold Fields		
SD248	104° 19' 6.647" W	29° 48' 9.505" N	4,155	233	Linear	0	-90	Gold Fields		
SD249	104° 19' 3.287" W	29° 48' 9.289" N	4,158	223	Linear	0	-90	Gold Fields		
SD251	104° 19' 9.478" W	29° 48' 9.064" N	4,179	335	Linear	0	-90	Gold Fields		
SD255	104° 19' 26.12" W	29° 47' 57.204" N	4,217	690	Linear	0	-90	Gold Fields		

Hole ID	Longitude	Latitude	z	Max Depth	Hole Path	Azimuth	Dip	Company	Date	Type
SD258	104° 19' 34.66" W	29° 47' 58.347" N	4,187	549	Linear	0	-90	Gold Fields		
SD267	104° 19' 38.49" W	29° 47' 52.106" N	4,158	564	Linear	0	-90	Gold Fields		
SD268	104° 19' 37.26" W	29° 47' 56.755" N	4,202	604	Linear	0	-90	Gold Fields		
SD269	104° 19' 36.60" W	29° 48' 1.665" N	4,149	593	Linear	0	-90	Gold Fields		
SD270	104° 19' 51.42" W	29° 47' 41.405" N	4,120	145	Linear	0	-90	Gold Fields		
SD294	104° 19' 42.91" W	29° 48' 6.451" N	4,137	688	Linear	0	-90	Gold Fields		
SD296	104° 19' 39.54" W	29° 48' 5.315" N	4,128	551	Linear	0	-90	Gold Fields		
SD297	104° 19' 47.58" W	29° 48' 5.524" N	4,122	737	Linear	0	-90	Gold Fields		
SD298	104° 20' 36.18" W	29° 46' 46.706" N	4,010	1772	Linear	0	-90	Gold Fields		
SD299	104° 20' 16.43" W	29° 45' 53.516" N	3,980	1472	Linear	0	-90	Gold Fields		
SD300	104° 19' 55.53" W	29° 47' 54.837" N	4,128	846	Linear	0	-90	Gold Fields		
SD301	104° 20' 29.74" W	29° 46' 23.892" N	3,870	1554	Linear	0	-90	Gold Fields		
SD302	104° 20' 18.09" W	29° 47' 6.792" N	3,870	1554	Linear	0	-90	Gold Fields		
SD304	104° 19' 55.37" W	29° 47' 37.810" N	3,964	1036	Linear	0	-90	Gold Fields		
SD305	104° 19' 57.59" W	29° 47' 39.733" N	4,086	673	Linear	0	-90	Gold Fields		
SD307	104° 19' 57.20" W	29° 45' 41.207" N	4,114	743	Linear	0	-90	Gold Fields		
SD308	104° 20' 29.52" W	29° 46' 24.961" N	4,046	972	Linear	0	-90	Gold Fields		
SD310	104° 19' 47.73" W	29° 46' 6.447" N	3,846	1492	Linear	0	-90	Gold Fields		
SD311	104° 19' 35.73" W	29° 46' 53.435" N	4,050	433	Linear	0	-90	Gold Fields		
SD312	104° 19' 38.91" W	29° 46' 53.055" N	4,150	557	Linear	0	-90	Gold Fields		
SD313	104° 19' 33.85" W	29° 46' 29.059" N	4,130	850	Linear	0	-90	Gold Fields		
SD314	104° 19' 42.21" W	29° 46' 52.081" N	4,110	456	Linear	0	-90	Gold Fields		
SD315	104° 19' 40.81" W	29° 46' 5.817" N	4,180	367	Linear	0	-90	Gold Fields		
SD316	104° 19' 38.06" W	29° 46' 27.198" N	4,080	355	Linear	0	-90	Gold Fields		
SD317	104° 19' 41.34" W	29° 46' 29.691" N	4,080	546	Linear	0	-90	Gold Fields		
SD318	104° 19' 44.74" W	29° 46' 30.005" N	4,080	740	Linear	0	-90	Gold Fields		

Hole ID	Longitude	Latitude	z	Max Depth	Hole Path	Azimuth	Dip	Company	Date	Type
SD319	104° 19' 48.15" W	29° 46' 29.825" N	4,060	880	Linear	0	-90	Gold Fields		
SD320	104° 19' 46.35" W	29° 45' 35.239" N	4,100	763	Linear	0	-90	Gold Fields		
SD321	104° 20' 11.87" W	29° 45' 39.428" N	4,040	1509	Linear	0	-90	Gold Fields		
SD322	104° 20' 5.985 W	29° 45' 19.886" N	3,995	1328	Linear	0	-90	Gold Fields		
SD323	104° 20' 18.84" W	29° 45' 15.295" N	3,970	1732	Linear	0	-90	Gold Fields		
SD324	104° 20' 26.52" W	29° 44' 45.519" N	4,015	974	Linear	0	-90	Gold Fields		
SD325	104° 20' 0.696" W	29° 43' 47.048" N	3,935	1133	Linear	0	-90	Gold Fields		
SD326	104° 19' 53.88" W	29° 43' 30.571" N	3,980	960	Linear	0	-90	Gold Fields		
SD327	104° 20' 35.23" W	29° 44' 16.540" N	3,900	720	Linear	0	-90	Gold Fields		
SD328	104° 20' 24.83" W	29° 45' 19.089" N	4,050	2100	Linear	0	-90	Gold Fields		
T14	104° 23' 55.86" W	29° 47' 59.756" N	3951	687	Linear	0	-90	ASARCO	1955	core
TMC-01	104° 23' 56.07" W	29° 48' 3.206" N	3994.34	220	Linear	0	-90	Tosca	2011	core
TMC-02	104° 23' 57.04" W	29° 48' 17.113" N	4096.32	249	Linear	0	-90	Tosca	2011	core
TMC-03	104° 23' 57.86" W	29° 48' 17.518" N	4112.63	248	Curved	167	-60	Tosca	2011	core
TMC-04	104° 23' 57.04" W	29° 48' 16.144" N	4092.34	299	Curved	290	-70	Tosca	2011	core
TMC-05	104° 23' 57.07" W	29° 48' 16.156" N	4092.58	248	Curved	294	-50	Tosca	2011	core
TMC-06	104° 23' 56.99" W	29° 48' 11.699" N	4067.02	229	Linear	0	-90	Tosca	2011	core
TMC-07	104° 23' 57.02" W	29° 48' 11.698" N	4067.02	1491	Curved	263	-57	Tosca	2011	core
TMC-08	104° 23' 59.89" W	29° 48' 10.026" N	4009.21	1400	Curved	266	-59	Tosca	2011	core
TMC-09	104° 24' 3.575" W	29° 48' 15.094" N	4077.22	269	Linear	0	-90	Tosca	2011	core
TMC-10	104° 24' 12.10" W	29° 48' 16.083" N	4059.24	220	Linear	0	-90	Tosca	2011	core
TMC-11	104° 24' 15.31" W	29° 48' 13.879" N	4085.13	349	Linear	0	-90	Tosca	2011	core
TMC-12	104° 24' 11.55" W	29° 48' 14.241" N	3988.36	1129	Linear	0	-90	Tosca	2011	core
TMC-13	104° 24' 8.162" W	29° 48' 14.309" N	3975.67	189	Linear	0	-90	Tosca	2011	core
TMC-14	104° 24' 5.770" W	29° 48' 12.597" N	3962.46	1200	Linear	0	-90	Tosca	2011	core
TMC-15	104° 24' 20.07" W	29° 48' 7.750" N	3899.42	350	Linear	0	-90	Tosca	2011	core

Hole ID	Longitude	Latitude	z	Max Depth	Hole Path	Azimuth	Dip	Company	Date	Type
TMC-16	104° 24' 18.16" W	29° 48' 6.676" N	3893.9	300	Linear	0	-90	Tosca	2011	core
TMC-17	104° 24' 7.464 W	29° 48' 6.748" N	3917.22	1249	Curved	90	-75	Tosca	2011	core
TMC-18	104° 24' 14.16" W	29° 48' 14.572" N	4077.29	1199	Linear	0	-90	Tosca	2011	core
TMC-19	104° 24' 14.19" W	29° 48' 15.595" N	4078.81	275	Curved	24.8	-89.6	Tosca	2011	core
TMC-20	104° 24' 11.27" W	29° 48' 17.840" N	4056.53	249	Curved	143.9	-89.2	Tosca	2011	core
TMC-21	104° 24' 5.262" W	29° 48' 16.026" N	4073.45	249	Curved	133.1	-89.8	Tosca	2011	core
TMC-22	104° 24' 6.920" W	29° 48' 17.156" N	4059.37	249	Curved	351.3	-88.9	Tosca	2011	core
TMC-23	104° 24' 6.356" W	29° 48' 15.295" N	4043.2	249	Curved	255.3	-89.3	Tosca	2011	core
TMC-24	104° 24' 3.499" W	29° 48' 11.956" N	3976.42	199	Curved	211.7	-89.3	Tosca	2011	core
TMC-25	104° 24' 15.99" W	29° 48' 7.865" N	3938.88	1189	Curved	279.9	-89.9	Tosca	2011	core
TMC-26	104° 24' 14.89" W	29° 48' 9.358" N	3926.7	347	Curved	242.7	-89.7	Tosca	2011	core
TMC-27	104° 24' 17.03" W	29° 48' 10.081" N	3929.33	349	Curved	11.9	-89.2	Tosca	2011	core
TMC-28	104° 24' 17.68" W	29° 48' 9.214" N	3909.51	399	Curved	355.3	-89.9	Tosca	2011	core
TMC-29	104° 24' 15.88" W	29° 48' 7.870" N	3938.74	998	Curved	0.7	-48.6	Tosca	2011	core
TMC-30	104° 23' 57.84" W	29° 48' 17.350" N	4111.65	253	Curved	170	-50.3	Tosca	2011	core
TMC-31	104° 23' 57.81" W	29° 48' 17.351" N	4111.58	451	Curved	121.1	-66.4	Tosca	2011	core

Table A-2: Field Sample Locations and Description

Field Sample	Latitude	Longitude	Elevation (ft)	Unit	Alteration
RH08	29° 48' 21" N	104° 24' 05" W	4240	QMP	Phyllic
RH09	29° 48' 10" N	104° 24' 11" W	3990	QMP	Phyllic
RH24	29° 48' 17" N	104° 24' 01" W	4120	QMP	Phyllic
RH13-01	29° 48' 16.622" N	104° 23' 55.254" W	4127	RM	Unaltered
RH13-02	29° 48' 38.289" N	104° 23' 13.979" W	4219	QMP	Propylitic
RH13-03	29° 48' 43.221" N	104° 23' 19.940" W	4255	LP	Oxide
RH13-04	29° 48' 28.354" N	104° 23' 24.775" W	4291	QMP	Unaltered
RH13-05	29° 48' 33.390" N	104° 23' 26.336" W	4124	BQMP	Propylitic
RH13-06	29° 48' 30.469" N	104° 23' 27.270" W	4177	QMP	Propylitic
RH13-07	29° 48' 30.563" N	104° 23' 27.634" W	4206	QMP	Propylitic
RH13-08	29° 48' 28.320" N	104° 23' 29.023" W	4154	QL	Argillic
RH13-09	29° 48' 30.995" N	104° 23' 40.723" W	4160	QMP	Propylitic
RH13-10	29° 48' 31.960" N	104° 23' 47.412" W	4131	QMP	Propylitic
RH13-11	29° 48' 19.075" N	104° 23' 42.598" W	4098	RM	Unaltered
RH13-12	29° 48' 16.069" N	104° 23' 43.009" W	4108	QMP	Silicified
RH13-13	29° 48' 15.263" N	104° 23' 44.395" W	4058	QL	Silicified
RH13-14	29° 48' 15.108" N	104° 23' 45.633" W	4062	RM	Leach Cap
RH13-15	29° 48' 12.537" N	104° 23' 49.370" W	4042	Hornfels	Argillic/Phyllic
RH13-16	29° 48' 2.788" N	104° 23' 44.506" W	4042	Hornfels	Silicified
RH13-17	29° 48' 3.631" N	104° 23' 41.939" W	4003	Hornfels	Leach Cap
RH13-18	29° 48' 7.252" N	104° 23' 30.491" W	4006	QMP	Unaltered to weakly Propylitic
RH13-19	29° 48' 6.446" N	104° 23' 24.155" W	4016	RM	Brecciated
RH13-20	29° 48' 7.483" N	104° 23' 20.566" W	4098	QMP	Silicified
RH13-21a and b	29° 48' 14.038" N	104° 23' 10.418" W	4147	QMP/ME	Unaltered
RH13-22	29° 48' 20.011" N	104° 23' 11.073" W	4108	QL	Argillic/Propylitic
RH13-23	29° 48' 11.079" N	104° 23' 58.999" W	4108	QL?	Argillic
RH13-24	29° 48' 9.225" N	104° 24' 2.214""W	4154	QMP	Phyllic
RH13-25	29° 48' 11.400" N	104° 24' 3.982""W	3990	QMP	Silicification/Leach Cap/sericite
RH13-26	29° 48' 6.284" N	104° 24' 6.970""W	3940	QMP	Argillic
RH13-27	29° 48' 6.021" N	104° 24' 18.277" W	3957	Hornfels	Leach Cap
RH13-28	29° 48' 14.122" N	104° 24' 28.080" W	3924	Skarn	Skarn
RH13-29a	29° 48' 17.398" N	104° 24' 27.252" W	3898	Hornfels	Supergene: Cu oxides
RH13-29b	29° 48' 17.394" N	104° 24' 27.259" W	3953	Hornfels	Supergene: Cu oxides
RH13-30	29° 48' 19.731" N	104° 24' 26.835" W	3996	LP	Weakly altered
RH13-31	29° 48' 18.00" N	104° 24' 28.94" W	3996	Hornfels	Supgergene: Cu oxides
RHS-105	29° 48' 10.00" N	104° 23' 06.00" W	1224	QLP	Unaltered

Table A-3: Thin Section Descriptions

Thin Section Sample	Lithology	Alteration 1	Alteration 2	Thin Section Type
RH08	QMP	Phyllic		Thin
RH09	QMP	Phyllic		Thin
RH24	QMP	Phyllic		Thin
RH13-10	QMP	Propylitic		Thin
RH13-11	RM	Unaltered		Thin
RH13-12	QMP	Silicified		Thin
RH13-18	QMP	Propylitic		Thin
RH13-20	QMP	Silicified	Brecciated	Thin
RH13-21a	QMP	Unaltered	Propylitic	Thin
RH13-21b	ME	Unaltered		Thin
RH13-27	RM	Hornfel		Thin
RH13-28	RM	Skarn		Thin
RH13-29a	RM	Hornfel	Cu oxides	Thin
RH13-29b	RM	Hornfel	Cu oxides	Thin
RH13-30	LP	Unaltered		Thin
RH13-31	RM	Hornfel	Cu oxide	Thin
TMC01-20	RM	Hornfel	Leach Cap	Thin
TMC01-114	QMP	Phyllic		Thin
TMC02-18	RM	Hornfel	Leach Cap	Thin
TMC3-143	LP	Supergene		Thin
TMC7-1089 P	LP	Phyllic		Thin
TMC7-1089-CL-A	LP	Phyllic		Thick
TMC12-964	Contact: BQMP and BP	Phyllic		Thin
TMC12-1071 P	BP	Phyllic		Thin
TMC12-1075-CL-A	BP	Silicified		Thick
TMC12-1075-spectrum	BP	Silicified		Thin
TMC14-31b-CL-A	LP	UST		Thick
TMC14-380-CL-A	QMP	Phyllic	Potassic	Thick
TMC14-1173 P	QMP	Phyllic		Thin
TMC14-1173-CL-A	QMP	Phyllic		Thick
TMC15-188	QMP	Phyllic		Thin
TMC15-258P	RM	Leach Cap	Pyritic	Thin
TMC15-347	RM	Hornfel	Pyritic	Thin
TMC17-88	QLP	Phyllic	Argillic	Thin
TMC17-1245	BQMP	Phyllic	Silicified	Thin
TMC18-187	LP	Phyllic		Thin

Thin Section Sample	Lithology	Alteration 1	Alteration 2	Thin Section Type
TMC18-189 P	LPbx	Phyllic	Fault Breccia	Thin
TMC19-32A P	QLP	Argillic	Leach Cap	Thin
TMC19-32-CL-A	QLP	Argillic	Leach Cap	Thick
TMC22-109	BQMP	Phyllic		Thin
TMC25-136	QMP	Phyllic	Argillic	Thin
TMC25-733	QMP	Phyllic	Potassic	Thin
TMC25-1176	LP	Phyllic	Argillic	Thin
TMC26-282 P	Contact: BQMP and BP	Phyllic		Thin
TMC27-192	RM?	Metasediment	Silicified	Thin
TMC29-882 P	BP	Phyllic	Potassic?	Thin

Appendix B: Analytical Methods and Procedures

U-Pb Procedures

Rock samples were crushed to mineral size under clean conditions using a jaw crusher and disc pulverizer, and minerals were separated using a Wilfley table, disposable sieves, heavy liquids and a Frantz magnetic separator at The University of Texas at Austin. Inclusion-free whole zircons hand-picked under an optical microscope were measured parallel to the c- and a-axes and mounted on epoxy pucks parallel to the c-axis. Unpolished individual grains were split-streamed to ~17 μm depths at 30-40 μm spot sizes for simultaneous U-Pb and trace element concentrations in the manner of Kylander-Clark et al. (2013) at the University of Texas at Austin. Samples were analyzed on two ThermoScientific Element2 magnetic sector inductively-coupled-plasma mass spectrometers (ICP-MS) with a Photon Machines Analyte G.2 Excimer laser. A large-volume Helex cell achieves <0.3s washout times, critical for high-resolution depth profiles (Smye and Stockli, 2014). Primary standard bracketing controlled for downhole fractionation, and secondary standards served as an independent verification of ages. Laser power and attenuation settings include 4 mJ power setting, 190 nm laser wavelength, 1.48 J/cm^2 fluence, and a 10 Hz repetition rate. Raw U-Pb and trace element data were reduced in Iolite using VizualAgeDRS and TraceElementIS, respectively, and exported in whole grain packages as well as 2-second depth intervals (Ludwig, 2003; Paton et al, 2011; Petrus and Kamber, 2012). Results are reported in Table 1 with 2σ errors. Linear regressions were performed using the procedure of Davis (1982). The goodness of fit of a regressed line is represented as a probability of fit, where 10% or better is considered acceptable and corresponds to a Mean Square of Weighted Deviates (MSWD) of 2 or less.

Energy Dispersive Spectrography

Thin (~30 μm thickness) and thick (~100 μm) sections with 2.5 x 5 cm dimensions were coated with a 15 to 25 nm thick carbon coat which was measured by observing color changes to light red or blue on a brass plate. EDS was performed using a Philips FEI XL 30 Environmental SEM microscope at The University of Texas at Austin. Experimental conditions utilized were 15kV accelerating voltage, 15nA on brass sample current, 0 (~500nm) probe diameter, 15 second dwell time, 10mm working distances at 50 to 200x magnifications. EDS was utilized for point data in which peak searches were performed before each session. Areas of interest were identified by backscatter electron imaging. Specific mineral were targeted as point data with the electron beam and elements peaks recorded. Mineral identifications were based on the elements identified within the spectra and other observable mineral characteristics, such as morphology and cleavage.

Scanned Electron Microscopy Cathodoluminescence

Thin (~30 μm thickness) and thick (~100 μm) sections with 2.5 x 5 cm dimensions were coated with a 15 to 25 nm thick carbon coat which was measured by observing color changes to light red or blue on a brass plate. Samples were either cut parallel or perpendicular to the vein axis. Thin and thick sections were scanned and mapped for regions of interest. Selected regions contained crystals that were of local importance based on vein type, cross-cutting relationships, and relation to any sulfide present or absent. Clean, elongate crystals with workable fluid inclusions were ideal selections for follow up trace element work. CL scans were completed at the University of Texas at Austin using a Phillips FEI XL 30 Environmental SEM microscope with a

Gatan cathodoluminescence detector attachment. Working conditions for the ESEM based on high vacuum (10^{-6} torr chamber pressure) or low vacuum (0.1-1.0 torr chamber pressure) setting are described in Table B-1. Photomultiplier tube voltages (PMT volts) generally decreased by -20V by each increasing increment of the listed accelerating voltages in Table B-1. 12kV and 15kV accelerating voltages produced the highest resolution images in SEM-CL. 5-6 beam spot size (~500nm) probe diameter, 12 to 13 mm working distance (approximately 1-2mm away from the CL detector), and slow scan speeds with 15s dwell times were the operating conditions used.

Prior to CL imaging, the area of interest in the sample needed to be focused in secondary electron (SE) mode at magnifications at least three times higher than CL image magnification used to acquire images. Most images were taken at 150X magnification. Color SEM-CL imaging requires the electron beam to scan over the same area three times using different color filters: red, green, and blue. The PMT voltage was increased with the red and green optical filters in order to generate adequate CL emissions. An increase of -150 V to -200 V was used for the green filter and the red filter requires an increase of -200 V to -300 V. A "true-color" image is reconstructed from the separate RGB channels via an image processing program.

The field of view on individual scan is restricted to areas approximately 800 x 600 μm dimensions. This limitation required multiple scans of a single area within a single sample. In order to merge multiple photos via Photoshop CC, a 40% overlap between adjacent photos was required to easily merge the photos correctly. Panochromatic SEM-CL images were taken with a 712 x 484 pixel resolution.

Table B-1: Ideal photomultiplier tube voltages for SEM-CL imaging

Mode	Accelerating Voltage (kV)	PMT Voltage (V)
High Vacuum	7.5	-650 to -655
	12	-600 to -605
	15	-570 to -580
	20	-535 to -545
	30	-510 to -515
Low Vacuum	12	-605 to -610
	15	-550 to -560
	20	-530 to -540
	30	-530 to -540

Image Processing

Photo mosaics from individual SEM-CL images were constructed using the image processing program Adobe® Photoshop CC. SEM-CL photos of an area were stitched using the "Photomerge" function to autonomously align a series of images (~200 images for large scan areas) while selecting the "Reposition" and "Auto-Blend" option to produce a seamless, single mosaic. Contrast and brightness levels were adjusted afterward to improve the visibility of CL textures.

Color CL images using the RGB filters required merging all three images within a single file, while assigning the appropriate color channel to produce a "true-color" SEM-CL image.

Appendix C: Whole Rock Geochemistry*

* Analyses were completed by ACME Labs by ICP-MS. Samples were crushed on 10 mesh and pulverized before analyses were completed.

Table C-1: Oxide and Trace Element Detection Limits

Oxide	Detection Limit		Trace Element	Detection Limit		Trace Element	Detection Limit
SiO_2	0.01%		Ba	1 ppm		Sr	0.5 ppm
Al_2O_3	0.01%		Be	1 ppm		Ta	0.1 ppm
CaO	0.01%		Ce	0.1 ppm		Tb	0.01 ppm
Cr_2O_3	0.002%		Co	0.2 ppm		Th	0.2 ppm
Fe_2O_3	0.04%		Cs	0.1 ppm		Tm	0.01 ppm
K_2O	0.01%		Dy	0.05 ppm		U	0.1 ppm
MgO	0.01%		Er	0.03 ppm		Ag	0.1 ppm
MnO	0.01%		Eu	0.02 ppm		As	0.5 ppm
Na_2O	0.01%		Ga	0.5 ppm		Au	0.5 ppb
P_2O_5	0.01%		Gd	0.05 ppm		Bi	0.1 ppm
TiO_2	0.01%		Hf	0.1 ppm		Cd	0.1 ppm
LOI	0.10%		Ho	0.02 ppm		Cu	0.1 ppm
Sum	0.01%		La	0.1 ppm		Hg	0.01 ppm
			Lu	0.01 ppm		Mo	0.1 ppm
			Nb	0.1 ppm		Ni	0.1 ppm
			Nd	0.3 ppm		Pb	0.1 ppm
			Pr	0.02 ppm		Sb	0.1 ppm
			Rb	0.1 ppm		Se	0.5 ppm
			Sc	1 ppm		Tl	0.1 ppm
			Sm	0.05 ppm		Zn	1 ppm
			Sn	1 ppm			

Table C-2: Summary of Red Hills Whole Rock Geochemistry

Oxides (%)	**RH13-21a**	**RH13-21b**	**TMC12-965**	**TMC12-965**	**TMC14-31b**	**TMC14-380**	**SH12-4**	**SD-253**
SiO2	65.03	51.63	58.62	64.98	82.57	69.84	43.78	41.52
Al2O3	15.37	16.47	16.01	15.30	7.46	15.71	16.52	13.34
Fe2O3	4.27	8.05	4.70	4.44	2.01	1.37	8.07	8.9
MgO	1.35	2.21	3.20	1.06	0.12	0.14	2.78	9.21
CaO	3.02	5.76	1.03	0.93	0.03	0.12	11.12	13.08
Na2O	3.78	4.37	0.49	1.74	0.16	0.30	3.06	1.59
K2O	4.12	2.59	8.79	5.56	3.80	7.13	2.43	2.04
TiO2	0.48	1.09	0.96	0.40	0.24	0.47	1.37	1.74
P2O5	0.25	0.51	0.35	0.20	0.06	0.24	0.49	0.67
MnO	0.12	0.25	0.09	0.06	<0.01	<0.01	0.26	0.15
Cr2O3	<0.002	<0.002	0.011	<0.002	0.002	<0.002	<0.002	0.071
Ni (ppm)	<20	<20	<20	<20	<20	<20	<20	177
Sc (ppm)	5	12	15	5	2	2	18	29
LOI	1.9	6.8	5.4	5.1	3.3	4.3	9.8	6.9
Sum	99.70	99.71	99.66	99.73	99.75	99.64	99.71	99.2
REE elements (ppm)								
Ba	1033	738	1658	1294	1043	1324	595	4616
Be	5	8	3	<1	<1	<1	<1	<1
Co	5.6	15.9	11.7	7.3	4.0	17.5	18.5	52.0
Cs	5.4	4.4	8.5	8.6	1.6	3.8	2.7	209.6
Ga	17.7	23.1	23.3	17.4	7.9	18.6	17.9	16.8
Hf	5.1	5.6	4.7	4.3	2.8	4.5	3.3	3.8
Nb	11.0	12.4	14.1	11.5	8.2	14.7	9.5	23.6

REE elements (ppm)								
Rb	159.8	125.3	291.8	176.7	78.1	148.3	62.6	63.1
Sn	1	2	1	1	1	<1	<1	<1
Sr	587.8	438.6	247.2	217.0	134.1	634.6	735.6	835.5
Ta	0.7	0.7	0.7	0.8	0.7	0.9	0.5	1.3
Th	9.4	6.7	6.3	7.9	5.5	8.8	3.4	4.9
U	4.0	3.9	3.1	3.0	2.3	2.4	0.9	1.8
V	52	121	137	50	27	46	192	275
W	1.2	3.1	6.8	6.7	13.8	20.5	<0.5	<0.5
Zr	168.7	236.7	206.4	164.5	107.0	183.6	142.3	135.6
Y	16.6	29.3	18.7	15.7	8.1	5.0	27.9	21.9
La	27.4	38.3	37.1	26.8	23.5	23.3	22.8	32.0
Ce	52.1	79.2	61.4	49.1	37.1	40.1	46.4	64.1
Pr	5.67	9.22	6.97	5.07	3.73	4.14	6.32	8.08
Nd	23.0	35.8	28.3	19.6	13.0	16.5	29.0	34.1
Sm	4.03	6.98	4.94	3.19	2.16	3.80	6.44	7.53
Eu	1.13	2.15	1.39	0.97	0.52	1.11	2.00	2.25
Gd	3.64	6.67	4.37	3.16	1.46	2.73	6.16	6.87
Tb	0.52	0.99	0.65	0.46	0.22	0.39	0.87	0.94
Dy	3.18	5.69	3.42	2.90	1.10	1.75	5.31	5.03
Ho	0.67	1.18	0.77	0.57	0.32	0.28	1.09	0.86
Er	1.83	3.78	2.21	1.71	0.81	0.56	3.07	2.19
Tm	0.33	0.54	0.32	0.26	0.13	0.10	0.45	0.30
Yb	2.11	3.66	2.15	2.01	0.93	0.70	2.88	1.84
Lu	0.36	0.53	0.34	0.29	0.13	0.13	0.45	0.22
TOT/C (%)	0.19	1.15	0.68	0.44	0.03	0.05	2.72	0.75
TOT/S (%)	<0.02	<0.02	0.98	1.92	1.40	1.09	<0.02	0.33

Metals (ppm)								
Mo	1.0	1.1	26.8	25.5	115.6	198.8	0.8	0.9
Cu	2.7	3.1	10.8	11.6	105.5	15.6	35.2	68.7
Pb	2.7	5.6	2.5	2.2	0.7	1.3	5.2	5.2
Zn	43	115	50	18	5	19	93	148
Ni	2.3	2.6	10.4	3.1	4.4	3.3	1.9	178.0
As	<0.5	<0.5	0.8	0.8	0.5	6.0	<0.5	0.9
Cd	<0.1	<0.1	<0.1	<0.1	0.2	0.1	0.3	0.3
Sb	<0.1	<0.1	0.4	0.3	<0.1	0.2	<0.1	<0.1
Bi	<0.1	<0.1	0.2	0.2	<0.1	0.1	<0.1	<0.1
Ag	<0.1	<0.1	<0.1	<0.1	<0.1	<0.1	<0.1	<0.1
Au (ppb)	<0.5	0.8	<0.5	<0.5	<0.5	<0.5	0.5	<0.5
Hg	<0.01	<0.01	<0.01	<0.01	0.01	<0.01	<0.01	0.03
Tl	<0.1	0.1	0.6	0.2	<0.1	0.3	<0.1	1.1
Se	<0.5	<0.5	<0.5	<0.5	<0.5	<0.5	<0.5	<0.5

Appendix D: U-Pb Samples

Table D-1. Summary of U-Pb zircon results from samples RHS-105 and TMC17-1245.

								207/235		206/238		207/206		Best age		
Grain #	[U] ppm	U/Th	207/235	2σ error	206/238	2σ error	RHO	Age (Ma)	2σ error	Age (Ma)	2σ error	Age (Ma)	2σ error	(Ma)	2σ error	% Discordance*
RHS_105_1	265.1	1.55	0.06670	0.00160	0.00995	0.00013	0.19270	65.5	1.5	63.9	0.8	180	26	63.9	0.8	2.5
RHS_105_2	289.7	1.43	0.06400	0.00140	0.00968	0.00010	0.21581	62.9	1.3	62.1	0.7	153	27	62.1	0.7	1.3
RHS_105_3	248	1.90	0.06430	0.00160	0.00979	0.00012	0.02783	63.3	1.5	62.8	0.8	178	27	62.8	0.8	0.8
RHS_105_4	318	1.37	0.06680	0.00140	0.00993	0.00013	0.09616	65.6	1.3	63.7	0.8	195	26	63.7	0.8	2.9
RHS_105_5	428	1.38	0.06590	0.00140	0.00996	0.00012	0.07004	64.8	1.3	63.9	0.8	169	27	63.9	0.8	1.4
RHS_105_6	302	1.89	0.06710	0.00150	0.00983	0.00015	0.19355	65.9	1.4	63.0	0.9	202	26	63.0	0.9	4.3
RHS_105_7	269	1.85	0.06790	0.00150	0.00992	0.00012	0.00441	66.7	1.5	63.6	0.8	190	26	63.6	0.8	4.6
RHS_105_8	164.7	1.68	0.06990	0.00170	0.00997	0.00014	0.05548	68.6	1.6	63.9	0.9	225	29	63.9	0.9	6.8
RHS_105_9	270	2.00	0.06560	0.00150	0.00993	0.00012	0.00640	64.5	1.4	63.7	0.8	186	32	63.7	0.8	1.2
RHS_105_10	223	1.81	0.06660	0.00170	0.00996	0.00013	0.13650	65.5	1.6	63.9	0.8	209	34	63.9	0.8	2.5
RHS_105_11	290	1.81	0.06630	0.00140	0.00983	0.00012	0.14936	65.1	1.3	63.0	0.8	187	26	63.0	0.8	3.2
RHS_105_12	256	1.72	0.06500	0.00170	0.00972	0.00014	0.02384	64.0	1.6	62.3	0.9	219	37	62.3	0.9	2.6
RHS_105_13	228	1.77	0.06670	0.00170	0.01012	0.00014	0.03179	65.6	1.6	64.9	0.9	176	38	64.9	0.9	1.1
RHS_105_14	301	1.87	0.06200	0.00120	0.00935	0.00010	0.11416	61.0	1.2	60.0	0.6	156	24	60.0	0.6	1.6
RHS_105_15	411	1.44	0.06600	0.00180	0.00995	0.00013	0.12682	64.9	1.8	63.8	0.8	163	30	63.8	0.8	1.7
RHS_105_16	242.4	1.49	0.07000	0.00310	0.00977	0.00022	0.00280	68.6	2.9	62.7	1.4	334	71	62.7	1.4	8.6
RHS_105_17	355.9	1.86	0.06350	0.00150	0.00952	0.00012	0.10754	62.5	1.4	61.1	0.8	177	21	61.1	0.8	2.3
RHS_105_18	343	1.86	0.06360	0.00170	0.00957	0.00015	0.05033	62.6	1.6	61.4	0.9	136	35	61.4	0.9	1.9
RHS_105_19	395	1.28	0.06450	0.00150	0.00985	0.00012	0.15341	63.6	1.4	63.2	0.8	139	25	63.2	0.8	0.6
RHS_105_20	438	1.70	0.06180	0.00200	0.00943	0.00016	0.08250	60.8	1.9	60.5	1.0	152	41	60.5	1.0	0.5
RHS_105_21	389	2.32	0.06550	0.00330	0.00969	0.00028	0.32681	64.4	3.2	62.2	1.8	220	75	62.2	1.8	3.4
RHS_105_22	272	1.88	0.06430	0.00150	0.00965	0.00012	0.19042	63.2	1.4	61.9	0.8	187	31	61.9	0.8	2.1
RHS_105_23	250	1.83	0.06480	0.00140	0.00984	0.00012	0.01745	63.7	1.4	63.1	0.7	147	26	63.1	0.7	0.9
RHS_105_24	366.3	1.94	0.06310	0.00110	0.00952	0.00012	0.40275	62.1	1.1	61.1	0.8	136	29	61.1	0.8	1.6
RHS_105_25	284	2.17	0.06250	0.00160	0.00951	0.00012	0.21495	61.6	1.5	61.0	0.7	157	25	61.0	0.7	1.0
RHS_105_26	234	1.86	0.06310	0.00150	0.00979	0.00014	0.01437	62.1	1.4	62.8	0.9	163	36	62.8	0.9	1.1
RHS_105_27	224.1	1.54	0.05640	0.00230	0.00854	0.00014	0.21921	55.7	2.2	54.8	0.9	210	41	54.8	0.9	1.6
RHS_105_28	239	1.86	0.06620	0.00160	0.00985	0.00013	0.09981	65.3	1.6	63.2	0.8	175	30	63.2	0.8	3.2

								207/235		206/238		207/206		Best age		
Grain #	[U] ppm	U/Th	207/235	2σ error	206/238	2σ error	RHO	Age (Ma)	2σ error	Age (Ma)	2σ error	Age (Ma)	2σ error	(Ma)	2σ error	% Discordance*
TMC17_2	310.8	1.08	0.06780	0.00130	0.01031	0.00012	0.27156	66.6	1.3	66.1	0.8	159	24	66.1	0.8	0.7
TMC17_4	321	1.28	0.06570	0.00130	0.01015	0.00014	0.00408	64.6	1.2	65.1	0.9	145	25	65.1	0.9	0.8
TMC17_5	432	1.31	0.06830	0.00180	0.01025	0.00016	0.07076	67.1	1.7	65.8	1.0	192	35	65.8	1.0	1.9
TMC17_6	206.4	1.61	0.06900	0.00220	0.01043	0.00014	0.19244	67.7	2.1	66.9	0.9	211	37	66.9	0.9	1.2
TMC17_7	391	1.07	0.06680	0.00120	0.01013	0.00013	0.16954	65.6	1.2	65.0	0.9	165	26	65.0	0.9	0.9
TMC17_8	210	1.39	0.07020	0.00200	0.01046	0.00014	0.15966	68.9	1.9	67.1	0.9	262	44	67.1	0.9	2.6
TMC17_9	272	1.49	0.07040	0.00190	0.01046	0.00015	0.57040	69.0	1.8	67.1	1.0	159	25	67.1	1.0	2.8
TMC17_10	1508	0.55	0.07090	0.00150	0.01013	0.00010	0.27072	69.6	1.4	65.0	0.6	247	34	65.0	0.6	6.7
TMC17_11	356	1.17	0.06660	0.00160	0.01020	0.00016	0.18394	65.4	1.5	65.4	1.0	170	33	65.4	1.0	0.0
TMC17_12	385	1.30	t	0.00140	0.01026	0.00012	0.18031	67.1	1.3	65.8	0.8	173	24	65.8	0.8	2.0
TMC17_13	368	1.53	0.06750	0.00310	0.01015	0.00018	0.09612	66.3	3.0	65.1	1.2	250	100	65.1	1.2	1.8
TMC17_14	456	1.48	0.06870	0.00130	0.01053	0.00011	0.16904	67.6	1.3	67.5	0.7	146	24	67.5	0.7	0.1
TMC17_15	303.3	1.21	0.06940	0.00150	0.01023	0.00013	0.22956	68.1	1.4	65.6	0.9	190	22	65.6	0.9	3.7
TMC17_16	362	1.23	0.06770	0.00140	0.01020	0.00011	0.03883	66.5	1.3	65.4	0.7	179	25	65.4	0.7	1.6
TMC17_17	529	1.10	0.06900	0.00140	0.01022	0.00011	0.14798	67.7	1.3	65.5	0.7	153	22	65.5	0.7	3.2
TMC17_18	567	1.00	0.06940	0.00120	0.01049	0.00009	0.06510	68.1	1.2	67.3	0.6	123	20	67.3	0.6	1.2
TMC17_19	412	1.35	0.06860	0.00160	0.01036	0.00014	0.34897	67.5	1.5	66.5	0.9	135	24	66.5	0.9	1.5
TMC17_20	436.2	1.10	0.06850	0.00140	0.01025	0.00010	0.13500	67.3	1.3	65.7	0.7	202	25	65.7	0.7	2.3
TMC17_21	359	1.16	0.07000	0.00110	0.01038	0.00011	0.07106	68.7	1.0	66.6	0.7	162	23	66.6	0.7	3.1
TMC17_22	350.5	1.52	0.06810	0.00240	0.01034	0.00022	0.21600	66.8	2.3	66.3	1.4	202	46	66.3	1.4	0.7
TMC17_23	338	1.33	0.07060	0.00170	0.01059	0.00015	0.03890	69.5	1.5	67.9	1.0	177	30	67.9	1.0	2.3
TMC17_24	270.3	1.34	0.06800	0.00150	0.01018	0.00013	0.06965	66.7	1.5	65.3	0.8	196	28	65.3	0.8	2.1
TMC17_25	332.1	1.73	0.06750	0.00160	0.01025	0.00016	0.37102	66.3	1.5	65.8	1.0	133	25	65.8	1.0	0.8
TMC17_26	236.7	1.50	0.06910	0.00160	0.01036	0.00014	0.30759	68.1	1.4	66.5	0.9	148	22	66.5	0.9	2.4
TMC17_27	333	1.16	0.06880	0.00130	0.01034	0.00010	0.15931	67.5	1.3	66.3	0.6	154	24	66.3	0.6	1.7
TMC17_28	599	0.68	0.07080	0.00190	0.01020	0.00011	0.36462	69.5	1.8	65.4	0.7	227	52	65.4	0.7	5.9

Appendix E: Scanned Luminescence Samples

CL textural observations were conducted on two or more regions of interest identified for each thin or thick section. Regions of interest typically contained one to three individual quartz crystals ranging in size from 0.25 mm to 5 mm. Single images were compiled in to a views of single or multiple quartz crystals. Vein transects were conducted along veins that ranged from 0.5 cm to 2 cm across the width of a vein. Data presented here is a summary of the features identified over the selected regions of interest.

Table E-1: Summary of Sample Scanned Luminescence Characteristics and Textures

Sample	Vein Type	Mineral	Halo	Morphology	CL Intensity	EGZ	IWGZ	SC	BCDO	DCBO	WCB	Mottled/Partially Recrystallized	Secondary Microfractures	Truncation Boundary	Dissolution Front	Microbreccia	Homogenous	Pinch outs	Gangue Minerals	Opaque minerals	Site
RH08	B	qz1	none	subhedral	bright to moderate	X	X	X				X	X			X			ser	py	1
		qz2	none	NA	dark																1
	A1	qz1	none	sub	bright to moderate						X	X				X	X		ser	py	2
		qz2	none	NA	dark																2
	B	qz1	none	subhedral	bright to dark				X					X							3
		qz2	none	subhedral	moderate to dark	X					X				X	X			ser		3
	A2	qz1	none	equant	bright to dark		X												ser, alu?	py	4
RH09b	A1	qz1	none	euhedral	bright to moderate	X	X													py	1
	A2	qz1	none	euhedral	bright to moderate	X							X								2
		qz2	none	euhedral	dark						X				X				ser, bar	py	2
	A2	qz1	none	subhedral	bright to moderate						X	X	X							py	3
RH24	A2	qz1	none	subhedral	moderate to light	X	X					X								py	1
		qz2	none	euhedral	dark to bright	X															1
		qz3	none	NA	moderate								X						framboid, ser	cp	1
	A1	qz1	none	anhedral	dark to bright		X			X										py	2
		qz2	none	anhedral	moderate																2
		qz3	none	anhedral	dark								X								2
	A1	qz1	none	anhedral	dark					X				X	X		X				3

Sample	Vein Type	Mineral	Halo	Morphology	CL Intensity	EGZ	IWGZ	SC	BCDO	DCBO	WCB	Mottled/Partially Recrystallized	Secondary Microfractures	Truncation Boundary	Dissolution Front	Microbreccia	Homogenous	Pinch outs	Gangue Minerals	Opaque minerals	Site
RH24		qz2	none	anhedral	bright										X		X				3
		qz3	none	euhedral	bright to moderate	X	X							X							3
		qz4	none	euhedral	moderate	X									X						3
		qz5	none	anhedral	dark											X			ser		3
	A1	qz1	none	subhedral	moderate							X							ser, ksp	py	5
		qz2	none	subhedral	bright to dark		X								X						5
		qz3	none	anhedral	dark								X			X			ser	mo	5
TMC7-1089 P	B	qz1	none	subhedral	light to moderate	X		X					X							mo	2
		qz2	none	euhedral	dark	X							X								2
	B	qz1	none	anhedral	moderate		X				X	X			X	X	X			3 gen of mo	3
	B	qz1	ser	euhedral	moderate	X															5
		qz2	none	euhedral	dark	X															5
	B	qz1	ser	subhedral	moderate		X	X			X									mo, py	7
	B	qz1	ser	subhedral	moderate	X		X					X						ser, brt, xtm	mo, py, sp	8
		qz2	ser	euhedral	dark	X															8
TMC7-1089-CL-A	B	qz1	ser	anhedral				X												mo, py	1
		qz2	ser	euhedral	moderate	X		X					X								1
TMC12-1071	B	qz1	none	subhedral	bright to moderate		X					X	X		X	X			rt, zr, xtm, mnz, ser	mo, py	3
		qz2	none	anhedral	dark												X				3
	B	qz1	none	subhedral	bright	X	X			X					X				ser, anh, ap, brt, framboid	mo, py, cp	4

Sample	Vein Type	Mineral	Halo	Morphology	CL Intensity	EGZ	IWGZ	SC	BCDO	DCBO	WCB	Mottled/Partially Recrystallized	Secondary Microfractures	Truncation Boundary	Dissolution Front	Microbreccia	Homogenous	Pinch outs	Gangue Minerals	Opaque minerals	Site
TMC12-1071		qz2	ser	anhedral	moderate	X									X	X					4
	D1	qz1	ser	anhedral	moderate		X			X	X	X	X		X					py, mo	8
		qz2	ser	anhedral	dark												X				8
TMC12-1075-Cl-A	B	qz1	none	subhedral	bright to moderate		X	X		X			X						rt, xtm	mo, py	1
		qz2	none	euhedral	bright to dark	X		X							X						
TMC14-31b-CL-A	A1	qz1	none	anhedral	moderate						X	X								mo, py	1
	A1	qz1	ser?	subhedral	moderate		X	X					X				X		rt, alu, fsp		2b
	UST	qz1	none	subhedral	bright	X	X	X								X					3
		qz2	none	subhedral	moderate to dark	X	X						X		X	X					3
		qz3	none	anhedral	dark								X			X					3
	UST	qz1	none	euhedral	bright to moderate		X						X							mo	4
	UST	qz1	none	euhedral	bright to moderate	X		X			X				X					mo	4
		qz2	none	euhedral	dark											X				mo	4
	A1	qz1	none	anhedral	bright to moderate		X		X		X		X		X	X			anh, ser, rt	cp	5
	UST	qz1	none	anhedral	moderate		X					X	X						rt, zrn, alu		6
	A2	qz1	none	subhedral	moderate to dark		X					X									FI1
		qz2	none	anhedral	dark																FI1
	UST	qz1	none	euhedral	bright to moderate	X															FI2
		qz2	none	subhedral	dark		X		X				X								FI2
	UST	qz1	none	euhedral	bright to moderate	X	X						X		X						FI3

Sample	Vein Type	Mineral	Halo	Morphology	CL Intensity	EGZ	IWGZ	SC	BCDO	DCBO	WCB	Mottled/Partially Recrystallized	Secondary Microfractures	Truncation Boundary	Dissolution Front	Microbreccia	Homogenous	Pinch outs	Gangue Minerals	Opaque minerals	Site
TMC14-31b-CL-A		qz2	none	euhedral	moderate to dark		X														FI3
		qz3	none	anhedral	dark								X								FI3
	B	qz1	none	anhedral	bright to moderate		X		X		X	X	X		X				rt, ser	mo, py	FI7
		qz2	none	anhedral	moderate		X						X				X				FI7
		qz3	none	euhedral	bright	X															FI7
		qz4	none	euhedral	dark	X															FI7
		qz5	none	anhedral	bright to dark											X					FI7
	B	qz1	none	subhedral	bright to moderate			X	X		X	X	X		X						FI1
		qz2	none	subhedral	moderate						X	X									FI1
		qz3	none	euhedral	bright	X	X														FI1
		qz4	none	euhedral	dark	X	X									X				mo, py	FI1
TMC14-380	A1	qz1	none	anhedral	moderate to bright		X														2
	B	qz1	none	anhedral	bright										X		X				2
		qz2	none	euhedral	moderate	X								X							2
		qz3	none	euhedral	moderate	X									X						2
		qz4	none	anhedral	moderate							X									2
		qz5	none	anhedral	bright										X					mo, py	2
		qz6	none	anhedral	dark									X							2
	D	qz1	none	subhedral	moderate					X		X	X								3
TMC14-1173 P	D1	qz1	ser	anhedral	moderate		X						X				X		rt, ser, ap, hem	py, cal, bis	2

Sample	Vein Type	Mineral	Halo	Morphology	CL Intensity	EGZ	IWGZ	SC	BCDO	DCBO	WCB	Mottled/Partially Recrystallized	Secondary Microfractures	Truncation Boundary	Dissolution Front	Microbreccia	Homogenous	Pinch outs	Gangue Minerals	Opaque minerals	Site
TMC14-1173 P	Qz Eye	qz1	none	anhedral	moderate								X				X				3
	B	qz1	none	subhedral	moderate		X					X					X		rt, anh	py, mo	4
	D2	qz1	none	anhedral	moderate		X	X				X	X						framboid	py	7
		qz2	none	anhedral	dark								X								7
TMC14-1173-CL-A	B	qz1	none	subhedral	moderate	X							X		X		X			mo, py	3
		qz2	none	euhedral	moderate to dark	X			X	X			X								3
		qz3	none	euhedral	moderate to dark	X														py	3
	B	qz1	none	euhedral	moderate to bright	X							X		X		X			mo	4
		qz2	none	euhedral	moderate to dark	X			X		X		X							py, mo	4
		qz3	none	anhedral	dark			X					X								4
	A2	qz1	none	anhedral	moderate	X		X				X					X				5
		qz2	none	anhedral	dark	X															5
	A1	qz1	none	anhedral	moderate		X					X					X				6
		qz2	none	anhedral	dark	X														py	6
	A2	qz1	none	anhedral	moderate							X	X				X				7
TMC17-88	A1	qz1	none	subhedral	moderate		X				X	X	X							py	1
	A2	qz1	none	subhedral	moderate	X						X	X							py	2
	A2	qz1	none	eu	moderate	X							X								4
		qz2	none	euhedral	bright to moderate	X							X								4
	D1	qz1	ser	anhedral	bright		X		X						X				ser	py	6
		qz2	ser	euhedral	dark	X				X									ser, rt	py	6

Sample	Vein Type	Mineral	Halo	Morphology	CL Intensity	EGZ	IWGZ	SC	BCDO	DCBO	WCB	Mottled/Partially Recrystallized	Secondary Microfractures	Truncation Boundary	Dissolution Front	Microbreccia	Homogenous	Pinch outs	Gangue Minerals	Opaque minerals	Site
TMC17-1245	D1	qz1	ser	anhedral	moderate		X										X				1
TMC18-187	D1	qz1	ser	subhedral	bright to moderate					X		X	X								6
		qz2	none	euhedral	dark	X														py, cp, cc	6
TMC19-32A P	B	qz1	ser	subhedral	moderate							X	X							mo, py, po, cp, cc	1
TMC25-136	D1	qz1	ser	anhedral	bright		X			X											5
		qz2	ser	anhedral	bright to dark		X			X										py, po, cp	5
	Kaol	qz1	none	anhedral	bright to moderate	X									X				kaol		6
		qz2	none	euhedral	dark												X				6
	D1	qz1	ser	euhedral	moderate to bright	X				X					X		X				8
		qz2	none	anhedral	dark	X										X				py	8
TMC25-733	A1	qz1	ser	subhedral	moderate		X									X			rt, zir, bar	py, cp	1
	A2	qz1	ser	euhedral	bright to moderate	X							X		X				anh	py, mo	2
	A1	qz1	ser	subhedral	moderate		X													mo	3
TMC25-1176	D2	qz1	none	euhedral	moderate to dark	X	X		X						X				rt	py, sp, hem	1
	A1	qz1	none	subhedral	bright to moderate		X						X							mo	2
	B	qz1	none	subhedral	bright to moderate		X					X	X							mo	3
	B	qz1	none	subhedral	bright	X	X						X								4
		qz2	none	anhedral	dark		X													mo	4
	A1	qz1	none	subhedral	bright to moderate		X													mo	5

Glossary

Mineral Abbreviation	Mineral Name
alu	alunite
anh	anhydrite
ap	apatite
bar	barite
bis	bismuthinite
bn	bornite
bt	biotite
cal	calcite
cc	chalcocite
chl	chlorite
cov	covellite
cp	chalcopyrite
ep	epidote
fsp	feldspar
gn	galena
grt	garnet
jar	jarosite
hem	hematite
hbl	hornblende
kaol	kaolinite
ksp	K-feldspar
mnz	monazite
mo	molybdenite
mt	magnetite
or	orthoclase
pl	plagioclase
po	pyrrhotite
py	pyrite
qz	quartz
rt	rutile
ser	sericite
sp	sphalerite
xtm	xenotime
zrn	zircon

References

Adams, D.C., and Keller, G.R., 1996, Precambrian basement geology of the Permian basin region of west Texas and eastern New Mexico: A geophysical perspective: AAPG Bulletin, v. 80, p. 410–431.

Alpers, C.N., and Brimhall, G.H., 1988, Middle Miocene climatic change in the Atacama Desert, northern Chile: Evidence from supergene mineralization at La Escondida: Bulletin of the Geological Society of America, v. 100, p. 1640–1656.

Ammon, W.L., 1981, Geology and plate tectonic history of the Marfa Basin, Presidio County, Texas, *in* Pearson, B. t. ed., Marathon-Marfa region of WestWest Texas: Permian Basin Section, Society of Economic Paleontologists and Mineralogists, Symposium and guidebook, p. 75–102.

Anderson, C.A., 1955, Oxidation of copper sulfides and secondary sulfide enrichment: Economic Geology 50th Annivesary Volume, Part 1, p. 324–340.

Anthony, E.Y., and Titley, S.R., 1994, Patterns of element mobility during hydrothermal alteration of the Sierrita porphyry copper deposit, Arizona: Economic Geology, v. 89, p. 186–192.

Barker, D.S., 1987, Tertiary alkaline magmatism in Trans-Pecos Texas: Geological Society, London, Special Publications, v. 30, p. 415–431.

Beane, R.E., 1974, Biotite Stability in the Porphyry Copper Environment: Economic Geology, v. 69, p. 241–256.

Beane, R.E., and Bodnar, R.J., 1995, Hydrothermal fluids and hydrothermal alteration in porphyry copper deposits: Arizona Geological Society Digest, v. 20, p. 83–93.

Berge, T.B., 1982, Structural evolution of the Northeastern Chihuahua tectonic belt: Geologic Studies of the Cordilleran Thrust Belt1, v. I, p. 451–457.

Blahd, K.W., 1982, The formation of goethite, jarosite, and alunite during the weathering of sulfide-bearing felsic rocks: Economic Geolgy, v. 77, p. 176–184.

Blanchard, R., 1968, Interpretation of leached outcrops: Nevada Bureau of Mines Bulletin, v. 66, p. 196.

Bodnar, R.J., 1995, Fluid inclusion evidence for a magmatic source for metals in porphyry copper deposits: Mineralogical Association of Canada Short Course Series, v. 23, p. 152.

Bogle, L.L., 2000, Depositional environments and paleogeography of the Permian of the Shafter , Texas area: Sul Ross Sate University.

Burnham, C.W., 1962, Facies and types of hydrothermal alteration: Economic Geology, v. 57, p. 768–784.

Burnham, C.W., 1997, Magmas and hydrothermal fluids, *in* Barnes, H.L. ed., Geochemistry of hydrothermal ore deposits, New York, John Wiley & Sons, p. 63–123.

Cameron, K., and Cameron, M., 1986, Whole-rock/groundmass differentiation trends of rare earth elements in high-silica rhyolites: Geochimica et Cosmochimica Acta, v. 50, p. 759–769.

Candela, P.A., and Holland, H.D., 1984, The partitioning of copper and molybdenum between silicate melts and aqueous fluids: Geochimica et Cosmochimica Acta, v. 48, p. 373–380.

Cannell, J., Cooke, D.R., Walshe, J.L., and Stein, H., 2005, Geology , Mineralization , Alteration , and Structural Evolution of the El Teniente Porphyry Cu-Mo Deposit: Economic Geology, v. 100, p. 979–1003.

Castro, A., Moreno-Ventas, I., and De La Rosa, J.D., 1991, Multistage crystallization of tonalitic enclaves in granitoid rocks (Hercynian belt, Spain): implications for magma mixing: Geologische Rundschau, v. 80, p. 109–120.

Cepeda, J.C., 1977, Geology and geochemistry of the igneous rocks of the Chinati Mountains, Presidio County, Texas: The University of Texas at Austin.

Cepeda, J.C., and Henry, C.D., 1983a, Oligocene Volcanism and Multiple Caldera Formation in the Chinati Mountains, Presidio County Texas: v. Report of, p. 1–29, doi: Report of Investigations No. 135.

Cepeda, J.C., and Henry, C.D., 1983b, Oligocene volcanism and multiple caldera formation in the Chinati Mountains, Presidio County, Texas:, No. NP–4900626 p.

Chavez, W.X.J., 2000, Supergene oxidation of copper deposits: Zoning and distribution of copper oxide minerals: Society of Economic Geologists Newsletter, v. 3, p. 9–21.

Cline, J.S., and Bodnar, R.J., 1991, Can economic porphyry copper mineralization be generated by a typical calc□alkaline melt? Journal of Geophysical Research: Solid Earth, v. 96, p. 8113–8126.

Cloos, M., and Sapiie, B., 2013, Porphyry copper deposits: strike–slip faulting and throttling cupolas: International Geology Review, v. 55, p. 43–65.

Cloos, M., Sapiie, B., Quarles van Ufford, A., Weiland, R.J., Warren, P.Q., and McMahon, T.P., 2005, Collisional delamination in New Guinea: the geotectonics of subducting slab breakoff: Geological Society of America Special Paper, v. 400, p. 1–51.

Company, R.G.M., 1997a, Outline of proposed Red Hills copper mining & processing operation:, 1–16 p.

Company, R.G.M., 1995, Red Hill copper molybdenum prospect, Shafter Texas:, 5 p.

Company, R.G.M., 1997b, Red Hills copper/molybdenum property, Presidio County, Texas; prefeasibility study – III; 0.49% or 0.44% Big Pits or 0.62% in 3 small pits or 0.73%, 0.55%, 0.37% staged pit and pre-feasibility study – IIIA; staged 7 year pit – 0.73%, 0.55%, 0.37% or Stage: , p. 1–206.

Coney, P., 1978, Mesozoic-Cenozoic cordilleran plate tectonics: Geological Society of America Memoirs, v. 152, p. 33–50.

Coney, P.J., 1987, The regional tectonic setting and possible causes of Cenozoic extension in the North American Cordillera: Geological Society, London, Special Publications, v. 28, p. 177–186.

Cooke, D.R., Hollings, P., and Walshe, J.L., 2005, Giant porphyry deposits: characteristics, distribution, and tectonic controls: Economic Geology, v. 100, p. 801–818.

Corp, B., 1997, Annual financial report (10-KSB):.

Dill, H.G., Bosse, H.-R., Henning, K.-H., Fricke, A., and Ahrendt, H., 1997, Mineralogical and chemical variations in hypogene and supergene kaolin deposits in a mobile fold belt the Central Andes of northwestern Peru: Mineralium Deposita, v. 32, p. 149–163.

Enders, M.S., 2000, The evolution of supergene enrichment in the Morenci porphyry copper deposit, Greenlee County, Arizona.

Evans, T.J., 1975, Gold and silver in Texas: University of Texas at Austin, Bureau of Economic Geology, Mineral Resource Circular, p. 35.

Field, C.W., 1966, Sulfur isotopic method for discriminating between sulfates of hypogene and supergene origin: Economic Geology, v. 61, p. 1428–1435.

Fitz-Gerald, J.J., 1983, No Title: , p. 1.

Gardien, V., Thompson, A.B., and Ulmer, P., 2000, Melting of Biotite + Plagioclase + Quartz Gneisses: the Role of H2O in the Stability of Amphibole: Journal of Petrology, v. 41, p. 651–666.

Gilmer, A., 2001, Age and characterization of the Red Hills porphyry copper-molybdenum deposit and its relationship to the Chinati Mountains Caldera, Presidio County, Texas: Jackson School of Geosciences, University of Texas at Austin.

Gilmer, A.K., Kyle, J.R., Connelly, J.N., Mathur, R.D., and Henry, C.D., 2003, Extension of Laramide magmatism in southwestern North America into Trans-Pecos Texas: Geology, v. 31, p. 447.

Goetz, L.K., and Dickerson, P.W., 1985, A Paleozoic transform margin in Arizona, New Mexico, west Texas and northern Mexico: Structure and tectonics of TransPecos Texas: West Texas Geological Society, Field conference guiebook, v. 85, p. 173–184.

Götze, J., 2009, Chemistry, textures and physical properties of quartz – geological interpretation and technical application: Mineralogical Magazine, v. 73, p. 645–671.

Gruen, G., Heinrich, C.A., and Schroeder, K., 2010, The Bingham Canyon porphyry Cu-Mo-Au Deposit . II . Vein geometry and ore shell formation by pressure-driven rock extension: Economic Geology, v. 105, p. 69–90.

Gustafson, L.B., and Quiroga, J., 1995, Patterns of Mineralization and Alteration below the Porphyry Copper Orebody at El Salvador, Chile: Economic Geology, v. 90, p. 2–16.

Gustavson, L.B., and Hunt, J.P., 1975, The porphyry copper deposit at El Salvador, Chile: Economic Geology, v. 70, p. 857–912.

Harris, A.C., Golding, S.D., and White, N.C., 2005, Bajo de la Alumbrera copper-gold deposit: Stable isotope evidence for a porphyry-related hydrothermal system dominated by magmatic aqueous fluids: Economic Geology, v. 100, p. 863–886.

Head, J.A., 2002, Stratigraphic and structural controls of Permian carbonate-host Silver (Pb-Zn) Mineralization, Shafter, Presidio County, Texas: The University of Texas at Austin.

Hemley, J.J., and Jones, W.R., 1964, Chemical aspects of hydrothermal alteration with emphasis on hydrogen metasomatism: Economic Geology, v. 59, p. 538–569.

Henry, C.D., 1998, Basement-controlled transfer zones in an area of low-magnitude extension, eastern Basin and Range province, Trans-Pecos Texas: Geological Society of America, v. 323, p. 75–88.

Henry, C.D., 1992, Geology of the Infiernito caldera and magmatic evolution of the Chinati Mountains, Trans-Pecos Texas:.

Henry, C.D., and Price, J.G., 1986, Early Basin and Range development in Trans-Pecos Texas and adjacent Chihuahua: magmatism and orientation, timing, and style of extension: Journal of Geophysical Research, v. 91, p. 6213–6224.

Holland, H.D., 1972, Granites, solutions, and base metal deposits: Economic Geology, v. 67, p. 281–301.

Horak, R., 1985, Trans-Pecos tectonism and its effect on the Permian basin: Structure and tectonics of trans-Pecos Texas: West Texas Geological Society Field Conference, publication., p. 85–81.

Jacobs, D.C., and Parry, W.T., 1979, Geochemistry of biotite in the Santa Rita porphyry copper deposit, New Mexico: Economic Geology, v. 74, p. 860–887.

James, E.W., and Henry, C.D., 1993, Pb isotopes of ore deposits in Trans-Pecos Texas and Northeastern Chihuahua, Mexico: Basement, igneous, and sedimentary sources of metals: Economic Geology, v. 88, p. 934–947.

Keppler, H., and Wyllie, P.J., 1991, Partitioning of Cu, Sn, Mo, W, U, and Th between melt and aqueous fluid in the systems haplogranite-H 2 O− HCl and haplogranite-H 2 O− HF: Contributions to Mineralogy and Petrology, v. 109, p. 139–150.

Van den Kerkhof, A.M., Kronz, A., Simon, K., and Scherer, T., 2004, Fluid-controlled quartz recovery in granulite as revealed by cathodoluminescence and trace element analysis (Bamble sector, Norway): Contributions to Mineralogy and Petrology, v. 146, p. 637–652.

Kirkham, R.V., and Sinclair, W.D., 1988, Comb quartz layers in felsic intrusions: Special Volume - Canadian Institute of Mining and Metallurgy, v. 39, p. 50–71.

Klemm, L.M., Pettke, T., and Henrich, C.A., 2007, Hydrothermal evolution of the El Teniente deposit, Chile: Porphyry Cu-Mo ore deposition from low-salinity magmatic fluids: Economic Geology, v. 102, p. 1021–1045.

Knox, W.P., 1983, Correspondence from Gold Fields Mining Corporation to Duval Corporation regarding controlled-source audio magnetotelluric surveying of the Red Hills area: , p. 1.

Kyle, J.R., 2012a, Laramide magmatism in Trans-Pecos Texas: geologic history of the Red Hills intrusive center, Presidio County, Texas: Geological Society of America Abstract South-Central Section 46th Annual Meeting, p. 2012.

Kyle, J.R., 2012b, Laramide magmatism in Trans-Pecos Texas: geologic history of the Red Hills intrusive center, Presidio County, Texas: Geological Society of America Abstracts with Programs, v. 44.

Landtwing, M.R., and Pettke, T., 2005, Relationships between SEM-cathodoluminescence response and trace-element composition of hydrothermal vein quartz: American Mineralogist, v. 90, p. 122–131.

Leeman, W.P., MacRae, C.M., Wilson, N.C., Torpy, A., Lee, C.-T. a, Student, J.J., Thomas, J.B., and Vicenzi, E.P., 2012, A study of cathodoluminescence and trace element compositional zoning in natural quartz from volcanic rocks: mapping titanium content in quartz.: Microscopy and microanalysis : the official journal of Microscopy Society of America, Microbeam Analysis Society, Microscopical Society of Canada, v. 18, p. 1322–41.

Linnen, R.L., and Williams-Jones, A.E., 1990, Evolution of aqueous-carbonic fluids during contact metamorphism, wall-rock alteration, and molybdenite deposition at Trout Lake, British Columbia: Economic Geology, v. 85, p. 1840–1856.

Long, K.R., 1992, Reserves and production data for selected ore deposits in the United States found in the files of the Anaconda Copper Company: U.S. Department of the Interior. U.S. Geological Survey., v. Open-File , p. 1–20.

Luff, G.C., 1981, A brief overview and oil and gas potential of the Marfa Basin: Marathon-Marfa region of West Texas, Symposium & Guidebook, Permian basin Section, SEPM, p. 111–130.

McCandless, T.E., Ruiz, J., and Campbell, A.R., 1993, Rhenium behavior in molybdenite in hypogene and near-surface environments : Implications for Re-0s geochronometry: Geochimica et Cosmochimica Acta, v. 57, p. 889–905.

Mercer, C.N., and Reed, M.H., 2013, Porphyry Cu-Mo stockwork formation by dynamic , transient hydrothermal pulses : Mineralogic insights from the deposit at Butte , Montana: Economic Geology, v. 108, p. 1347–1377.

Moore, W.J., and Lanphere, M. a., 1971, The age of porphyry-type copper mineralization in the Bingham Mining District, Utah: a refined estimate: Economic Geology, v. 66, p. 331–334.

Mosher, S., 1998, Tectonic evolution of the southern Laurentian Grenville orogenic belt: Geological Society of America Bulletin, v. 110, p. 1357–1375.

Muehlberger, W.R., 1980, Texas lineament revisted: New Mexico Geological Society Guidebook, v. 31st Field, p. 113–122.

Muehlberger, W.R., and Dickerson, P.W., 1989, A tectonic history of Trans-Pecos Texas: Structure and Stratigraphy of Trans-Pecos Texas: El Paso to Guadalupe Mountains and Big Bend July 20-29, 1989, p. 35–54.

Müller, A., Herrington, R., Armstrong, R., Seltmann, R., Kirwin, D.J., Stenina, N.G., and Kronz, A., 2010, Trace elements and cathodoluminescence of quartz in stockwork veins of Mongolian porphyry-style deposits: Mineralium Deposita, v. 45, p. 707–727.

Müller, A., Wiedenbeck, M., van den Kerkhof, A.M., Kronz, A., and Simon, K., 2003, Trace elements in quartz – a combined electron microprobe, secondary ion mass spectrometry, laser-ablation ICP-MS, and cathodoluminescence study: European Journal of Mineralogy, v. 15, p. 747–763.

Muntean, J.L., and Einaudi, M.T., 2001, Porphyry-Epithermal Transition: Maricunga Belt, Northern Chile: Economic Geology, v. 96, p. 743–772.

Naylor, R.G., 1982a, Gold Fields/Duval joint venture, Shafter, Presidio County, Texas; monthly exploration report, October, 1982: , p. 1–3.

Naylor, R.G., 1982b, Gold Fields/Duval joint venture, Shafter, Presidio County, Texas; monthly exploration report, September, 1982: , p. 1–3.

Penniston-Dorland, S.C., 2001, Illumination of vein quartz textures in a porphyry copper ore deposit using scanned cathodoluminescence : Grasberg Igneous Complex , Irian Jaya , Indonesia: American Mineralogist, v. 86, p. 652–666.

Peterson, W.C., 1973, Hinton project: , p. 40.

Peterson, W.C., 1972, Possible outline of best copper mineralization: , p. 1–3.

Price, J.G., and Henry, C.D., 1982, Porphyry copper-molybdenum deposit as- sociated with the Chinati Mountains caldera, Trans-Pecos Texas: Geological Society of America Abstracts with Program, v. 14, p. 593.

Price, J.G., and Henry, C.D., 1984, Stress orientations during Oligocene volcanism in Trans-Pecos Texas : Timing the transition from Laramide compression to Basin and Range tension: Geology, v. 12, p. 238–241.

Price, J.G., Henry, C.D., Barker, D.S., and Parker, D.F., 1987, Alkalic rocks of contrasting tectonic settings in Trans-Pecos Texas: Geological Society of America Special Papers, v. 215, p. 335–346.

Price, J.G., Henry, C.D., Parker, D.F., and Barker, D.S., 1986, Igneous Geology of Trans-Pecos Texas: Field Trip Guide and Research Articles, *in* Austin, p. 1–359.

Proffett, J.M., 2003, Geology of the Bajo de la Alumbrera Porphyry Copper-Gold Deposit , Argentina: Economic Geolgy, v. 98, p. 1535–1574.

Rempel, K.U., Migdisov, A.A., and Williams-Jones, A.E., 2006, The solubility and speciation of molybdenum in water vapour at elevated temperatures and pressures: Implications for ore genesis: Geochimica et Cosmochimica Acta, v. 70, p. 687–696.

Rix, C.C., 1953, Geology of Chinati Peak quadrangle, Trans-Pecos Texas: The University of Texas at Austin.

Ross, C.P., 1943, Geology and ore deposits of the Shafter mining district, Presidio County, Texas: , p. 45–125.

Ross, C. a., 1986, Paleozoic evolution of southern margin of Permian basin: Geological Society of America Bulletin, v. 97, p. 536–554.

Rozelle, J.W., and Tschabrun, D.B., 2008, Shafter silver project, Presidio County, Texas USA: , p. 1–61.

Rusk, B.G., 2012, Cathodoluminescene and trace elements in hydrothermal quartz, *in* Götze, J. and Möckel, R. eds., Quartz: Deposits, Mineralogy and Analytics, Berlin, Springer, p. 307–329.

Rusk, B., 2004, Compositions of magmatic hydrothermal fluids determined by LA-ICP-MS of fluid inclusions from the porphyry copper-molybdenum deposit at Butte, MT: Chemical Geology, v. 210, p. 173–199.

Rusk, B.G., Lowers, H.A., and Reed, M.H., 2008, Trace elements in hydrothermal quartz: Relationships to cathodoluminescent textures and insights into vein formation: Geology, v. 36, p. 547.

Rusk, B., and Reed, M., 2002a, Scanning electron microscope – cathodoluminescence analysis of quartz reveals complex growth histories in veins from the Butte porphyry copper deposit , Montana: Geology, v. 30, p. 727–730.

Rusk, B., and Reed, M., 2002b, Scanning electron microscope–cathodoluminescence analysis of quartz reveals complex growth histories in veins from the Butte porphyry copper deposit, Montana: Geology, v. 30, p. 727.

Rusk, B.G., Reed, M.H., and Dilles, J.H., 2008, Fluid inclusion evidence for magmatic-hydrothermal fluid evolution in the porphyry copper-molybdenum deposit at Butte, Montana: Economic Geology, v. 103, p. 307–334.

Sarg, J.F., Markello, J.R., and Weber, L.J., 1999, The sequence stratigraphy, sedimentology, and economic importance of evaporite–carbonate transitions: a review: Sedimentary Geology, v. 140, p. 9–34.

Seedorff, E., Dilles, J.H., Proffett, Jr, J.M., Einaudi, M.T., Zurcher, L., Stavast, W.J.A., Johnson, D.A., and Barton, M.D., 2005, Porphyry Deposits: Characteristics and Origin of Hypogene Features, *in* Economic Geology 100th Anniversary Volume, p. 251–298.

Seo, J.H., Guillong, M., and Heinrich, C. a., 2012, Separation of molybdenum and copper in porphyry deposits: The roles of sulfur, redox, and pH in ore mineral deposition at bingham canyon: Economic Geology, v. 107, p. 333–356.

Shelton, K.L., and Rye, D.M., 1982, Sulfur isotopic compositions of ores from Mines Gaspe, Quebec: an example of sulfate-sulfide isotopic disequilibria in ore-forming fluids with applications to other porphyry-type deposits: Economic Geology, v. 77, p. 1688–1709.

Shepard, T.M., and Walper, J.L., 1982, Tectonic evolution of Trans-Pecos, Texas: Gulf Coast Association of Geological Societies Transactions, v. 32, p. 165–172.

Sillitoe, R.H., 2010, Porphyry Copper Systems: Economic Geolgy, v. 105, p. 3–41.

Silver, L.T., and Anderson, T.H., 1974, Possible left-lateral early to middle Mesozoic disruption of the southwestern North American craton margin: Geological Society of America Abstracts with Programs1, v. 6, p. 955–956.

Sinclair, W.D., 2007, Porphyry Deposits, *in* Goodfellow, W.D. ed., Mineral deposits of Canada: a synthesis of major deposit-types, district metallogeny, the evolution of geological provinces, and exploration methods, St. John's, Newfoundland, p. 223–243.

Smith, J.C., 2011, Shafter mining district: Handbook of Texas online (http://www.tshaonline.org/handbook/online/articles/gps02), Texas State Historical Association,.

Smith, R.W., Norman, D.I., and Popp, C.J., 1980, Calculated solubility of molybdeniite in hydrothermal solutions: J Geological Society of America Abstract Programs, v. 12.

Stoffregen, R.E., Alpers, C.N., and Jambor, J.L., 2000, Alunite-Jarosite Crystallography, Thermodynamics, and Geochronology: Reviews in Mineralogy and Geochemistry, v. 40, p. 453–479.

Taylor, R., Hammarstrom, J., Piatak, N., and Seal, R., 2010, Arc-Related Porphyry Molybdenum Deposit Model: USGS Scientific Investigations Report 2010-5070-D, p. 1–42.

Tietz, P.G., 2012, Updated Technical Report on the Red Hills Project Presidio County , Texas Mine Development Associates Mine Engineering Services.

Titley, S.R., 1975, Geological Characteristics and Environment of Some Porphyry Copper Occurrences in the Southwestern Pacific: Economic Geology, v. 70, p. 499–514.

Titley, S.R., and Marozas, D.C., 1995, Processes and products of supergene copper enrichment, *in* Southwestern North America, in Pierce, FW, Bolm, JG (eds.), Porphyry Copper Deposits of the American Cordillera: Tucson, Arizona Geological Society Digest 20, p. 156–168.

Udden, J., 1904, The geology of the Shafter silver mine district: Von Boeckmann-Jones Company, State printers.

Vasyukova, O., Goemann, K., Kamentetsky, V.S., MacRae, C.M., and Wilson, N.C., 2013, Cathodoluminescence properties of quartz eyes from porphyry-type deposits : Implications for the origin of quartz: American Mineralogist, v. 98, p. 98–109.

Vernon, R.H., 1984, Microgranitoid enclaves in granites—globules of hybrid magma quenched in a plutonic environment: Nature, v. 309, p. 438–439.

Weis, P., Driesner, T., and Heinrich, C. a, 2012, Porphyry-copper ore shells form at stable pressure-temperature fronts within dynamic fluid plumes.: Science (New York, N.Y.), v. 338, p. 1613–6.

Westra, G., and Keith, S.B., 1981, Classification and genesis of stockwork molybdenum deposits: Economic Geology, v. 76, p. 844–873.

Wetherill, G.W., 1965, Discordant uranium-lead ages: Eos, Transactions American Geophysical Union, v. 37, p. 320–326.

White, W.H., Bookstrom, A.A., Kamilli, R.J., Ganster, M.W., Smith, R.P., Ranta, D.., and Steininger, R.C., 1981, Character and Origin of Climax Type Molybdenum Deposits: Economic Geology, p. 270–316.

Whitney, M., 1982a, Duval joint venture; September monthly report (August 27 – September 26): , p. 1.

Whitney, M., 1982b, Shafter-Duval exploration report (April – August, 1982): , p. 1–2.

Vita

Stefanie N. Frelinger was raised in Bakersfield, California where her childhood interest in Earth science led her to Colorado School of Mines, where she earned her B.S. in Geological Engineering, Exploration tract. After her undergraduate career, she worked for the industrial minerals company Imerys in France and Alabama where she developed skill sets in 3-D geologic modeling and mine planning. In August of 2012, she began her graduate career at The University of Texas at Austin in the Department of Geological Sciences where she interned with petroleum company, QEP during the summer of 2013.

Permanent email: sfreling11@gmail.com

This thesis was typed by Stefanie Naoko Frelinger.